9-2020

Tidal Wetland Inundation and Vegetation Phenology from Space: A Synthesis of Approaches for Characterizing Ecological Status and Inundation Dynamics in Tidal Wetlands with Remote Sensing Observations

Brian T. Lamb
The Graduate Center, City University of New York

TIDAL WETLAND INUNDATION AND VEGETATION PHENOLOGY FROM SPACE. A SYNTHESIS OF APPROACHES FOR CHARACTERIZING ECOLOGICAL STATUS AND INUNDATION DYNAMICS IN TIDAL WETLANDS WITH REMOTE SENSING OBSERVATIONS

by

BRIAN THOMAS LAMB

A dissertation submitted to the Graduate Faculty in Earth and Environmental Sciences in partial fulfillment of the requirements for the degree of Doctor of Philosophy, The City University of New York

2020

Tidal Wetland Inundation and Vegetation Phenology from Space. A Synthesis of Approaches for Characterizing Ecological Status and Inundation Dynamics in Tidal Wetlands with Remote Sensing Observations

by

Brian Thomas Lamb

This manuscript has been read and accepted for the Graduate Faculty in Earth and Environmental Sciences in satisfaction of the dissertation requirement for the degree of Doctor of Philosophy.

__________________	________________________________
Date	Maria Tzortziou
	Chair of Examining Committee
__________________	________________________________
Date	Monica Varsanyi
	Executive Officer

Supervisory Committee:

Kyle McDonald (Co-Advisor) (City College of New York)

Dorothy Peteet (Columbia University)

Andrew Reinmann (CUNY Advanced Science Research Center)

THE CITY UNIVERSITY OF NEW YORK

ABSTRACT

Tidal Wetland Inundation and Vegetation Phenology from Space. A Synthesis of Approaches for Characterizing Ecological Status and Inundation Dynamics in Tidal Wetlands with Remote Sensing Observations

by

Brian Thomas Lamb

Advisor: Professor Maria Tzortziou

This dissertation focuses on the monitoring and characterization of tidal marshes using remote sensing-based approaches. Chapter 1 introduces the topics of wetland ecology and remote sensing. Chapters 2-4 are the main research chapters of the dissertation covering the topics of tidal marsh mapping, tidal marsh vegetation characterization, and assessment of tidal marsh inundation patterns. Chapter 5 summarizes the preceding chapters and highlights future research directions.

The primary research objective of Chapter 2 is the mapping and study of tidal marshes of the Chesapeake and Delaware Bays. This chapter also features a thematic focus on the evaluation of various forms of satellite imagery for wetlands studies in general. In this chapter, Chesapeake and Delaware Bay tidal marshes were mapped with producer's accuracy greater than 88% and user's accuracy greater than 83% using a random forest classification. A second classification effort focused on the mapping of wetlands vegetation at the Jug Bay wetlands complex in the Patuxent River. This classification, which also utilized the random forest

technique, yielded accuracies of greater than 90% for all mapped wetlands vegetation types. These two classifications made use of SAR and optical/IR satellite imagery as input layers. Post-classification analysis demonstrated that optical/IR images were most useful for providing accurate classifications for Chesapeake Bay tidal marshes while the SAR images were most useful for classifying different wetlands vegetation at Jug Bay. This highlights the importance of SAR-optical/IR fusion for providing flexibility in achieving accurate classifications when mapping diverse wetlands types with a single classifier.

Chapter 3 builds on many of the findings from the evaluation portion of Chapter 2. In Chapter 3, a mapping methodology utilizing SAR-optical/IR fusion is used to expand tidal marsh mapping beyond the Chesapeake and Delaware Bays and into the entire Mid-Atlantic region. Chapter 3 also seeks to map not only tidal marshes, and distinguish them from freshwater marshes, but also map marshes that have been invaded by *Phragmites australis*. These three types of marshes were all mapped with greater than 80% user's and producer's accuracy in the Mid-Atlantic region. This marsh mapping effort was also carried out in the Gulf Coast region, where marshes were mapped with greater than 91% user's accuracy and 95% producer's accuracy, although the three individual marsh classes were often confused with one another. In addition to effectively mapping *Phragmites australis* with supervised classification approaches in the Mid-Atlantic region, a decision tree-based approach was developed to map invasive aquatic water chestnut (*Trapa natans*) with greater than 96% accuracy. This decision tree approach utilized multitemporal Sentinel-1 C-band SAR imagery. The same decision tree classification was utilized to map non-persistent emergent vegetation, an indicator of tidal freshwater wetlands, with greater than 93% accuracy.

Chapter 4 seeks to assess tidal marsh inundation patterns. In this chapter, numerous satellite image-based inundation products were developed and validated using in-marsh water level observations from study sites. In this chapter, optical/IR, C-band SAR, and L-band SAR inundation products are validated with water level sensors and assessed for overall performance. This validation suggest that L-band inundation products offered the best performance for mapping tidal marsh inundated area with 90% accuracy. L-band inundation products were developed using backscatter intensity thresholding-based approaches which were derived empirically. Radiometric modeling efforts were also utilized to elucidate changes in scattering mechanisms in support of empirical image analyses. The radiometric modeling efforts and empirical image analyses demonstrate that C-band and L-band SAR backscatter tends to decrease in response to inundation in tidal marshes. However, an important distinction that the radiometric modeling efforts revealed was that C-band signals interact much more strongly with vegetation, while L-band signals respond more strongly with the surface underlying vegetated canopies. Further, L-band signals decrease to a greater magnitude in response to inundation making L-band imagery much more effective for assessing tidal marsh inundation state than C-band imagery. These findings are also supported by image-based polarimetric decompositions which capture similar scattering shifts in response to inundation as those demonstrated by radiometric modeling efforts at L-band frequencies.

Chapter 5 summarizes the previous chapters and discusses the launch of three satellites that are anticipated to advance the study of tidal marsh systems. The most relevant of which is the NISAR satellite which will operate at an L-band frequency with an anticipated 12-day revisit time. The findings of this dissertation demonstrate the utility of L-band SAR for characterizing tidal marsh inundation state, combined with a 12-day revisit, NISAR imagery should greatly improve the characterization of tidal marsh inundation patterns.

ACKNOWLEDGEMENTS

The research in this dissertation was not developed in a vacuum. Several related research projects have provided the support and inspiration for this dissertation work. As a first year PhD student, I was fortunate to be involved in a NASA Carbon Cycle Science (CCS) Program-funded project (NNX14AP06G, Lead PI: M. Tzortziou) on wetland-estuary carbon cycling, working on the tidal wetland remote sensing component of this project. Involvement in this project served as inspiration for many of the research questions developed in this dissertation and eventually led to a publication on remote sensing-based wetland characterization of the Chesapeake and Delaware Bays in the journal *Remote Sensing* (Lamb et al. 2019). This publication makes up the majority of the second chapter of this dissertation focusing on technological assessment of satellite remote sensing in wetland characterization.

A second research project that greatly influenced this dissertation is a NASA Interdisciplinary Studies (IDS) Program-funded project (80NSSC17K0258, Lead PI: M. Tzortziou) seeking to understand human impacts on wetlands and estuarine waters of the Long Island Sound. Again, I was fortunate to be involved in this research project working on the wetland remote sensing component. Studying the wetlands of the western Long Island Sound also allowed me to conduct comparative studies on the wetlands of the Hudson River. Even though all wetlands sites in the Chesapeake Bay, Long Island Sound, and Hudson River are tidal systems in a similar climatic setting (i.e. the Mid-Atlantic U.S.), they exhibited pronounced differences in hydrology and vegetation phenologies. The comparison between these three site locations provided two very important lessons. The first lesson is that satellite image analysis needs to be guided by site knowledge and ground surveys. The second lesson is that multiple forms of satellite imagery are often needed to accurately characterize wetland systems. Much of

this combined work on the Long Island Sound, Hudson River, and Chesapeake Bay served as the third chapter of this dissertation which seeks to answer science questions about the distribution of tidal wetlands and wetland vegetation characteristics in the Mid-Atlantic U.S. and also expands into the Gulf Coast U.S.. The majority of the third chapter of this dissertation is presented in a publication planned for submission to the journal *Remote Sensing*.

My PhD thesis research was also supported by a NASA National Earth and Space Science Fellowship (NESSF) (80NSSC17K0365) I received from 2017 to 2020. The NESSF proposed research topics included tidal wetland vegetation characterization and tidal wetland inundation assessments using satellite remote sensing. Although the tidal wetland inundation assessments were informed and inspired by work on the Chesapeake Bay CCS project and Long Island Sound IDS project, they became much more refined in the NESSF fellowship. The NESSF research proposed the development of tidal wetland inundation detection algorithms, which were developed and validated using a three-way approach combining satellite imagery, *in situ* inundation sensors, and radiometric modeling. This research serves as the fourth chapter of this dissertation.

I feel fortunate that each of the three research projects I was involved in as a PhD student served as a primary influence on each of the main research chapters of my dissertation. I owe my participation in each of these projects to my PhD advisors, Dr. Maria Tzortziou and Dr. Kyle McDonald, both of whom facilitated my initial involvement in the Chesapeake Bay CCS project, supported my participation in the Long Island Sound IDS project, and supervised the formulation of my NESSF PhD fellowship. The thesis research that follows has been shaped by their mentorship. For their involvement, constructive criticism, and support I am truly grateful.

The most direct support for this dissertation research came in the form of mentorship

from my PhD advisors, thoughtful suggestions from dissertation committee members Dorothy Peteet and Andrew Reinmann, generous funding from NASA, and academic and financial support from the CUNY Graduate Center. However, there are several institutions and individuals that provided additional support for this research as well.

In terms of institutions, substantial acknowledgement and thanks is owed to NASA, USGS, JAXA, and ESA for their provisions of open-access satellite imagery. It is my belief that providing satellite imagery to researchers free of charge is one of the best ways advance Earth science research as rapidly as possible, as this allows the greatest amount of research participation by removing financial barriers to entry. This is especially true for students and early career scientists interested in Earth observation-based research. For this particular dissertation, a great number of satellite images were used in the analysis. This analysis simply would not have been possible without access to free of charge satellite imagery. The precedent of providing satellite imagery free of charge was set by the United States with the earliest Landsat missions, and it has been wonderful to see this practice adopted by other space agencies as well. The continuation of this practice in conjunction with the launch and operation of a greater number of Earth observing satellites makes me optimistic about the future of Earth science.

There are a number of individuals who provided direct support for this dissertation research, especially with regard to wetlands access. Patrick Megonigal and James Holmquist were tremendously generous with their insights and help with access at Kirkpatrick Marsh. Patricia Delgado was equally helpful in facilitating fieldwork at the Jug Bay Wetlands Sanctuary. The Connecticut Coastal Audubon Society was extremely helpful in providing access to Wheeler Marsh. Without ground validation, the value of remote sensing analysis is reduced tremendously, I'd like to thank all of you for your help with wetlands access. Additionally, I'd like to thank

Matthew Whitbeck of the USFWS for providing water level timeseries for Blackwater NWR which proved critical in being able to calibrate estuary NOAA tide gauges to in-marsh water levels. Dean Hively of the USGS is owed a debt of gratitude for his mentorship on the topic of optical/IR remote sensing of agricultural systems. Many of the vegetation characterization approaches used in agricultural studies proved very effective for wetland-based studies in this dissertation.

My lab mates were also invaluable in supporting me through this research effort, whether it was conducting fieldwork, discussing specific research, discussing science in general, and/or things completely unrelated. Kat Jensen, Aaron Davitt, Andrea Gomez, Derek Tesser, Michael Brown, Jessica Rosenqvist, Alana Menendez, Brice Grunert, Fang Cao, Liz Corbett, and adopted lab mate Luis (Lou) Ortiz Uriarte all made up a group of people I feel truly grateful and lucky to have had as lab mates, and have as friends.

Most importantly, I'd like to thank my family for all their support throughout the years. My wonderful parents have inspired and cultivated my interest in the natural world from as early as I can remember. Whether it was through fossil hunting, fishing, camping, or gardening, my Mom and Dad had more influence on my path into Earth science than anyone else. I'd also like to thank my Sister, a very promising and capable young scientist, for all her support and discussions on research that have always stretched the bounds of my scientific understanding. Lastly, but certainly not least, I'd like to thank my Wife and her family for their support throughout a long period of graduate school. I couldn't have made it this far without you all. To my lovely Wife in particular, you have been the foundation of support throughout my graduate research. As this PhD chapter ends, I look forward to starting another new chapter in our lives together.

TABLE OF CONTENTS

LIST OF TABLES

Table 4.5. Sentinel-1 (S1) and PALSAR/PALSAR-2 correlation with tidal stage (shown as R-values).

LIST OF FIGURES

CHAPTER 1

INTRODUCTION

1.1 Wetland Importance Background

Wetlands are among the most productive and important ecosystems on Earth. Wetlands are defined by their high frequency and long duration of inundation relative to other ecosystems, possessing hydric soils, and possessing vegetation that is uniquely adapted to thrive in these wet conditions (Mitsch and Gosselink 2007). Wetlands have tremendously high rates of gross primary productivity (GPP) and are extremely efficient at carbon sequestration; this is especially true of tidal wetlands (McLeod et al. 2011; Hinson et al. 2017; Milligan et al. 2019; Feagan et al. 2020). Howard et al. (2017) demonstrated that tidal marshes and mangroves have carbon sequestration rates orders of magnitude higher than tropical rainforests on a per-area basis. Although tidal wetlands generally act as carbon sinks on aggregate, they are also important sources of carbon-rich and humic dissolved organic matter to adjacent waters (Tzortziou et al. 2008). Tidal wetlands also provide a plethora of ecosystem services including coastal flood protection, sediment capture, denitrification, and water filtration (Barbier et al. 2011; EPA 1996). The ensemble of ecosystem services that tidal wetlands provide is becoming increasingly important as coastal regions become more populated and more people depend on these ecosystem services. However, wetlands are being lost at a rapid rate globally (Mitsch and Gosselink 2007). Tidal wetlands in particular are vulnerable to loss through eutrophication (Deegan et al. 2012) and development (Pendleton et al. 2012). Further, the location of tidal wetlands means they are impacted by the transport of excessive nutrients and pollutants from connected freshwater aquatic systems, as well as by the encroachment of rising sea levels from connected estuarine aquatic systems. Although it is well established that rising sea level will inevitably change the distribution of tidal wetlands, it is unknown how wetlands will respond to changes in sea level (Ross and Adam 2013; Tabak et al. 2016; Kirwan et al. 2016). However, several studies have indicated that changes in salinity have pronounced impacts on wetland vegetation community composition (Howes et al. 2010; Sutter et al. 2013; Turner et al. 2019). In addition to alterative physical impacts on native wetland vegetation, tidal wetlands are also impacted by the presence of invasive vegetation that form monospecific stands, greatly reducing wetland biodiversity and ecological function (Bertness 2002).

It is critical to have tools for monitoring and characterizing tidal wetlands. However, global estimates of herbaceous tidal wetlands (i.e. tidal marshes) distributions remain poor compared to other wetland systems, including woody tidal wetland systems like mangroves (Pendleton 2012; Bunting et al. 2018; Thomas et al. 2018). A study by Mcowen et al. (2017) has produced a global tidal marsh inventory by aggregating disparate tidal marsh surveys conducted at the national level. However, the Mcowen product does not provide a spatiotemporally harmonized and gap filled tidal marsh product and does not provide monitoring capabilities. In this thesis research, I seek to improve estimates of tidal marsh extent by implementing methodologies that are suitable not just for estimating tidal marsh distributions but monitoring tidal marsh distributions through time. In addition to focusing on assessment of tidal marsh distributions, this research effort also seeks to provide assessments of tidal marsh vegetation characteristics and inundation dynamics, as these are all indicators of the ecological status of tidal marshes. Marsh vegetation characteristics and tidal inundation extents also influence tidal biogeochemical exchanges at wetland-estuarine interfaces which has significant implications for coastal and global carbon cycling (Tzortziou et al. 2008; Logozzo et al. 2020).

This research effort focuses on the study of tidal wetlands of the Mid-Atlantic and Gulf of Mexico coastal regions of the United States. Two regions with high population and tidal wetland densities, and two regions that are at increasingly significant risk for tidal flooding during high tides and storms (Feagan et al. 2020; Dahl et al. 2017). The Mid-Atlantic and Gulf of Mexico study regions were also selected due to the fact they contain some of the highest densities of tidal freshwater marshes in the United States (Leck et al. 2009). Tidal freshwater marsh ecosystems are generally defined as having low average salinities less than 0.5 parts per thousand (PPT) while still being strongly hydrologically influenced by tidal forcing from connected estuarine-ocean waters (Odum 1988; Leck et al. 2009). Compared to brackish and salt marshes, tidal freshwater marshes have vastly different vegetation characteristics (Odum 1988; Leck et al. 2009). Thus, remotely sensed identification of tidal freshwater marsh vegetation presents a potentially powerful monitoring tool for assessing salinities of deepwater systems connected to wetlands and monitoring impacts of climate change, sea level rise, and seawater intrusion on coastal habitat, plant species composition and carbon fixation and mineralization (Herbert et al. 2018).

Tidal wetlands play an important role in coastal flood protection by decreasing the velocity of flood pulses and serving as temporary storage areas for flood waters (EPA 1996). Despite the importance of tidal wetlands in mitigating the impacts of coastal flooding, sea-level rise has also contributed to a loss of tidal wetlands in the United States and globally (Becket et al. 2016; Ross and Adam 2013). Subsequently, the loss of tidal wetlands leaves developed coastal regions more vulnerable to the impacts of flooding from coastal storms (Costanza et al. 2008). In the context of coastal flood vulnerability assessment, tidal marshes may be some of the first coastal systems to exhibit signs of change in long-term average sea levels. These changes are evidenced by permanent inundation (ponding) on the marsh interior and by the loss of vegetation (Gangu et al. 2013). A suite of monitoring tools that allows for assessment of tidal marsh distribution, vegetation characteristics, and inundation dynamics provides a powerful set of indicators for assessment of wetland ecological status.

Tidal marshes can be large in extent, highly heterogenous, and difficult to access. These factors limit the ability to monitor and characterize wetlands using field studies alone. Satellite remote sensing provides synoptic observations of wetlands and direct observations of biophysical attributes that define wetlands, including surface hydrology (inundation state), hydrophilic vegetation, and hydric soils (Kulawardhana et al. 2007; Mitsch and Gosselink 2007). Many studies have utilized remote sensing to study abiotic and biotic wetland processes (Lang et al. 2008; Schmitt and Brisco 2013; Kim et al. 2014; Moser et al. 2016; Brisco et al. 2017; Byrd et al. 2018), and to inventory wetlands (Whitcomb et al. 2009; Clewley et al. 2015; Hird et al. 2018). These remote sensing-based research efforts enable wetland studies to be carried out on much larger scale than field study-based efforts. However, tidal wetland systems, and tidal marshes in particular, have been understudied with remote sensing approaches compared to other wetlands. This may be due, in part, to challenges in accurately characterizing high frequency tidal variability in tidal marshes when assessing inundation dynamics. Especially since this tidal variability may interfere with assessments of tidal wetland vegetation characteristics and even tidal marsh distribution assessments. While understudied compared to other wetland systems, there have been many important remote sensing-based tidal marsh research efforts (Barlett and Klemas et al. 1981; Kearney 2002; Oliver-Cabrera and Wdowinski 2016; Ramsey et al. 2012; Ramsey et al. 2014; Ramsey et al. 2016; Rangoonwala et al. 2016; Slatton et al. 2008). These efforts highlight the challenges of working in tidally influenced systems and have largely focused on brackish and salt marsh systems. Remote sensing-based studies of freshwater tidal marshes in contrast, have been extremely limited (Elmore 2008). This thesis specifically seeks to improve the large-scale study of freshwater tidal wetlands which serve as important indicators of ecological conditions and demarcate freshwater marshes and brackish marshes.

Overall, it is clear that satellite remote sensing is unparalleled in wetland monitoring in terms spatial capabilities, but how well can current satellite observations resolve tidal marsh dynamics? This thesis research seeks to address that question and ideally overcome some of the challenges that exist in utilizing remote sensing to study tidal marshes.

1.2 Remote Sensing Theory Background

At the most fundamental level, remote sensing is the process of determining properties of a target at a physical distance from it. The vast majority of remote sensing systems utilize electromagnetic (EM) radiation, commonly referred to as light, for the identification of target properties. Early attempts to describe light scientifically date back to Ancient Greece and perhaps even earlier. However, in providing the foundations for modern remote sensing, three scientists provided precise descriptions of light that are fundamental to the field. The first of them is Christiaan Huygens who was the first scientist to mathematically describe light as a wave. Huygens description of light as a wave lead to debates with Isaac Newton who had previously described light as streams of particles. Eventually, modern quantum mechanics would vindicate both Huygens and Newton by ultimately arriving at the concept of light's wave-particle duality. The second important figure in providing the physical foundations of modern remote sensing was Albert Einstein who provided the useful particle description of light as photons. Modern remote sensing requires both wave and particle descriptions of light (EM radiation). For example, remote sensing imaging systems that operate at visible to infrared (IR) (optical/IR) wavelengths (400 nm to 2500 nm) utilize arrays of photon detectors, while radar instruments that operate at microwave wavelengths (1 mm to 30 cm) measure EM wave intensity with antennae. The equations below show the general wave equation (1), equation for photon energy (2), and equation for the speed of light (3). The wave equation term k describes the wavenumber which inversely relates wavelength to the wave frequency. Like the wave equation (1), the photon equation (2) also contains a wavelength term (λ) and demonstrates that the energy of a given photon is inversely proportional to wavelength. Equation 3 relates the constant speed of light to wavelength and frequency which has important significance when describing light's interaction with media.

$$\psi(z,t) = A\sin(kz - \omega t + \phi_0) \tag{1}$$

$$E = \frac{hc}{\lambda} \tag{2}$$

$$c = \lambda\upsilon \tag{3}$$

where A is wave amplitude, k describes the wavenumber which inversely relates wavelength to the wave frequency, ω represents angular frequency, and ϕ_0 represents the wave phase in general wave equation 1. In equation 2, E denotes energy. In equations 2 and 3, λ denotes wavelength, h is Plank's constant, c is the speed of light in a vacuum, and υ is frequency.

The third scientist to contribute greatly to modern remote sensing, and arguably the most important in a fundamental sense, was James Clerk Maxwell. Maxwell was the first physicist to fully describe the intertwined nature of the electric and magnetic properties of light in a series of four succinct equations which includes the research of Carl Friedrich Gauss and Michael Faraday. Maxwell's equations (4-7) below describe interactions between light's electric and magnetic fields in free space.

$$\nabla \cdot \mathbf{E} = \frac{\rho}{\varepsilon_0} \tag{4}$$

$$\nabla \cdot \mathbf{B} = 0 \tag{5}$$

$$\nabla \times \mathbf{E} = -\frac{\partial}{\partial t}\mathbf{B} \tag{6}$$

$$\nabla \times \mathbf{B} = \mu_0 \left(\mathbf{J} + \varepsilon_0 \frac{\partial}{\partial t}\mathbf{E}\right) \tag{7}$$

where **E** is the electric field, ρ is charge density, ε_0 is permittivity of free space, **B** is the magnetic field, μ_0 is the permeability of free space, and **J** is current density.

It is critical to note that Maxwell's equations describe not only light's intertwined electric and magnetic fields, but also describe the propagation of them in space. ε_0 and μ_0 describe the electrical permittivity and permeability of free space (a vacuum), respectively. Together these terms also describe the speed of light in a vacuum as shown in the equation 8 below. Like equation 3, equation 8 also describes the speed of light, but does so as a function of the properties of the free space in which light propagates rather than the inherent properties of the light itself.

$$c = \frac{1}{\sqrt{\varepsilon_0 \mu_0}} \tag{8}$$

The properties of a medium, rather than a vacuum, are described by the relative permittivity and relative permeability (ε_r and μ_r) which are dimensionless factors that relate permittivity and permeability of a medium (ε and μ) to their free space counterpart terms (ε_0 and μ_0) (shown in equations 9-10). Most Earth targets can be approximated as non-magnetic media; therefore, their relative permeability is equal to one, meaning their permeability will be equal to the permeability of free space. In contrast, permittivity values and the associated relative permittivity values can vary greatly. This is one of the most important concepts in both microwave and optical remote sensing. The relative permittivity of a given medium, which is often referred to as the dielectric constant, dictates many important interactions between EM radiation and media in which it propagates. These interactions include: Scattering, absorption, and transmission. These interactions are all of great importance to the field of remote sensing and will be discussed in greater detail in future sections. Equation 11 below demonstrates that the velocity of an EM wave is related to the medium's relative permittivity alone when the medium is non-magnetic. In remote sensing of Earth targets, EM waves will often pass between media with different dielectric values. When this occurs, the velocity (ν) of the wave will change as shown in equation 11, which results in a change in wave propagation direction, through a process known as refraction, a type of scattering. This is a very important concept in remote sensing at air-water interfaces and will be discussed in greater detail in following sections.

$$\mu = \mu_r \mu_0 \tag{9}$$

$$\varepsilon = \varepsilon_r \varepsilon_0 \tag{10}$$

$$\nu = \frac{1}{\sqrt{\varepsilon_r}\sqrt{\varepsilon_0 \mu_0}} = \frac{c}{\sqrt{\varepsilon_r}} \tag{11}$$

At this point, it is important to address a distinction between the microwave and optical remote sensing communities. The microwave community will generally refer to the dielectric properties of a medium while the optical community will refer to the refractive index of the medium. The refractive index (n) is simply the square root of the dielectric constant. The dielectric constant and refractive index are both complex terms with real and imagery parts. The real term refers to a medium's induced polarized orientation when impinged upon by an electric field, while the imaginary term refers to the loss of an electric field as it propagates through the medium. To a first approximation these properties control scattering and absorption, respectively. A medium's dielectric constant (or refractive index) will vary depending on the frequency of the EM wave propagating within it, as shown in equation 15 below.

$$n = \sqrt{\varepsilon_r} = \frac{c}{v} \tag{12}$$

$$n = n + ik \tag{13}$$

$$\varepsilon_r = \varepsilon'_r - i\varepsilon''_r \tag{14}$$

$$\varepsilon_r(\omega) = \varepsilon'_r(\omega) - i\varepsilon''_r(\omega) \tag{15}$$

where n refers to the refractive index and ε_r refers to the dielectric constant. The second terms in equations 13 and 14 denote the imaginary (loss/absorption) terms in the complex refractive index and dielectric constant, respectively. Equation 15 expresses the frequency-dependence of the dielectric constant which also applies to the refractive index.

Having developed some background on the physical properties of EM radiation and established the importance of the medium's dielectric constant in interaction with EM radiation, it is important to address a few remaining concepts. First, only interactions between EM radiation and media have been discussed thus far. However, it is important to note that many of the EM descriptions of media properties are also descriptions of particle properties (e.g. dielectric values). Second, the initial wave function in equation 1 defined only a one-dimensional wave with an arbitrary plane of oscillation. Maxwell's equations demonstrate that electric and magnetic fields are intertwined. For an EM wave, the electric and magnetic fields will oscillate in orthogonal planes with the same propagation direction. As previously mentioned, in Earth remote sensing the vast majority of targets are non-magnetic, therefore the magnetic fields of an EM wave will seldom change due magnetic interactions. Electric fields, in contrast, often change due to interaction with common Earth targets. This means that EM wave descriptions are often simplified using the electric field alone. The updated wave equation 16 below reflects this simplification, and also includes the description of the electric field's oscillation about the x-axis, with the z-axis remaining the direction of propagation. Note like equation 1, this updated wave equation describes wave propagation in time and space with the same wavenumber (k), angular frequency (ω), and phase terms (ϕ_0).

$$E_x(z,t) = E_{0x}\sin(kz - \omega t + \phi_0) = E_{0x}e^{i\phi} \tag{16}$$

The orientation of the electric field serves as a useful description for later sections when discussing radar polarization. Additionally, note that in contrast to the original wave equation 1, this updated wave equation has an imaginary term. This imaginary term is useful for representing a wave's phase along with the amplitude. This description becomes very useful in microwave remote sensing where wave amplitude and phase are often recorded together, while each provide unique information on target properties.

It is critical to be able to link the wave equation 16 defined above to the radiometric properties that remote sensing instruments measure or derive. Many remote sensing instruments record EM wave intensity rather than amplitude (E). To get to intensity, one must first convert to power (P) by squaring the EM wave amplitude. Intensity is a measure of time-average power (P) per-unit area (A). Intensity (I) is often express in units of Watts per square meter. Power and intensity equations are shown below.

$$P = |E(z,t)|^2 \tag{17}$$

$$I = \frac{\langle P \rangle}{A} \tag{18}$$

EM radiation intensity can be further described by whether it is incoming or outgoing relative to a target. When EM radiation of a given intensity is incoming, it is termed irradiance denoted by the letter *E* (note this term is different from electric field amplitude in equation 16). When EM radiation is exiting a target it is aptly termed exitance denoted by the letter *M*. Often in remote sensing, it is useful to define not just whether EM radiation of a given intensity is leaving or exiting a target, but to determine the precise direction from which the EM radiation originates. When EM radiation intensity is measured from a defined solid angle (steradian), this property is termed radiance denoted by the letter *L*. Radiance is defined as Watts per square meter per steradian. Most remote sensing instruments, especially optical/IR sensors, measure radiance rather than irradiance because imaging system detectors must be constrained to a very narrow field of view. The last concept needed to generally describe how satellite instruments observe EM radiation are spectral properties. Spectral irradiance is general measured in Watts per square meter per unit spectral wavelength (λ), spectral radiance includes the steradian term. Often the spectral wavelength units are micrometers (um) and nanometers (nm). The common units are shown below.

$$Irradiance = E\ (units = Wm^{-2})$$

$$Radiance = L\ (units = Wm^{-2}sr^{-1})$$

$$Spectral\ Irradiance = E_\lambda\ (units = Wm^{-2}nm^{-1})$$

$$Spectral\ Radiance = L_\lambda\ (units = Wm^{-2}sr^{-1}nm^{-1})$$

Nearly all satellites with optical imaging systems measure spectral radiance or derive spectral radiance as a radiometric property. Optical instruments are generally multispectral, with separate photon detectors corresponding to different spectral channels. These spectrally distinct photon detectors have a spectral response function that defines quantum detection efficiency for a given photon of a given wavelength. These photon detectors measure photon counts within a spectral range, commonly referred to as a spectral band. These spectral bands are generally recorded as digital number values which correspond to scaled photon counts. A single digital number value corresponds to a single spectral band's individual pixel. To generate multispectral images, optical instruments have both spatial and spectral detector arrays that are required to produce detailed imagery. The digital number values of pixels of a given image roughly correspond to scaled photon counts, but on their own are physically meaningless units. In order to produce physical units, optical satellites have accurately calibrated parameters (gains and offsets) that relate digital number values to physical units, most commonly spectral radiance. After spectral radiance values have been determined, top of atmosphere (TOA) reflectance imagery of the Earth's surface can be calculated from the ratio of upwelling spectral radiance observed by the satellite to downwelling spectral irradiance. Downwelling solar irradiance for a given satellite image can be calculated accurately based on sun-sensor geometry, date, time, and image location. Although defining TOA reflectance for optical imagery is conceptually simple, obtaining accurate estimates of Earth's surface reflectance is challenging. Atmospheric gases and particles interact strongly with EM radiation at optical wavelengths, perturbing both the downwelling irradiance incident on the Earth's surface and the reflected upwelling radiance reaching the satellite sensor. The process of correcting or compensating for these atmospheric effects is a topic that is not covered further in this thesis but is of critical importance to obtain an accurate characterization of the Earth's surface. For this reason, all optical imagery used in the thesis has been corrected to surface reflectance (Kaufman et al. 1997; Vermote et al. 2016).

In contrast to optical imaging systems, for longer wavelength microwave systems, the atmosphere is largely transparent (non-perturbing). Meaning that atmospheric correction is not required for long wavelength microwave remote sensing platforms. This thesis exclusively addresses active microwave instruments, namely imaging radar, for wetland characterization and observation. All radar imagery in this thesis has been acquired by synthetic aperture radar (SAR) imaging systems. SAR systems utilize the motion of an aircraft or satellite to produce a synthetically lengthened aperture (antenna) which has the effect of increasing the spatial resolution of acquired imagery after advanced signal processing. SAR signal processing and system design are important and complex topics, but are outside the scope of this thesis, and are not discussed further. Since SAR are active microwave instruments, they have a number of technical differences and complexities that differentiate them from passive optical sensors. SAR, being a form of radar, are active instruments that transmit their own EM signals of a known wave amplitude/intensity and measure the amplitude/intensity of the return signal. In doing so, radar instruments are essentially measuring the scattering efficiency of a target. This is termed the scattering cross section denoted by sigma (σ). The radar cross-section equation below further describes how σ is defined in the context of a radar imaging system.

$$\sigma = \frac{I_{rec}}{I_{inc}} \, 4\pi R^2 \tag{19}$$

where σ is the radar scattering cross section, I_{rec} and I_{inc} are received and incident intensity, respectively, and R is the range or distance between the radar and the target (Woodhouse 2006).

Radar systems can be monostatic when signal transmission and signal reception occurs on the same antenna or bistatic where separate antennae are dedicated to signal transmission and reception (Jensen et al. 2018). In the monostatic case, only direct backscattered signal from a target can be measured. In the bistatic case, theoretically any scattering direction relative to a target can be measured. The vast majority of spaceborne radar are monostatic, including all SAR satellites described in this thesis, thus every account of sigma (σ) from this point forward is referring to monostatic backscattered σ. In order to obtain a measure of the scattering cross section that is not dependent on a SAR imaging system's footprint or pixel size, it is necessary to normalize σ by an area as is shown in equation 20 for sigma naught (σ^0) below.

$$\sigma^0 = \frac{\sigma}{A} \tag{20}$$

Both σ and σ^0 often need to be described as a function of satellite view geometry (signal transmit and receive geometry for radar), even though σ^0 should be theoretically only be impacted by ground properties. SAR are side looking instruments with a view geometry that is off-nadir by approximately 20-50 degrees. When this off-nadir view geometry is taken into consideration with the fact that many Earth targets are anisotropic scatterers in the microwave region, it becomes even more essential to account for this view geometry. The first reason for this is the fact that the Earth's surface is seldom flat (topographically invariant) even at the resolution of a single image pixel, which can vary widely from < 10 m to > 50 km. When a SAR instrument images topographically variant targets, the total scattering area changes as a function of the Earth's topography in relation to sensor view geometry, even when the SAR imaging system's resolution cell remains constant. Equations 21 and 22 (reproduced from Woodhouse 2006) describe radar backscatter in the slant range geometry which accounts for slanting topography in an image resolution cell.

$$\gamma = \frac{\sigma^0}{\cos \theta_i} \tag{21}$$

$$\beta^0 = \frac{\sigma^0}{\sin \theta_i} \tag{22}$$

where γ is slant range scattered intensity observed by the sensor normalized by sensor view angle relative to topography and β^0 is slant range scattered intensity normalized by ground area.

Terrain correction is required to accurately convert slant range geometry backscatter (γ and β^0) to ground range geometry backscatter (σ^0) which best describes target properties. Because wetlands are largely topographically invariant, this terrain correction is a fairly straightforward process, and is not discussed further. It should be noted that equation 23 introduces a theta term for sensor view angle. This view angle is important to account for, even considering topographically invariant targets like wetlands, as backscatter changes as a function of view angle for certain targets types like wetland vegetation.

$$\sigma^0(\theta) = \frac{\sigma(\theta)}{A} \tag{23}$$

Sigma naught radar imagery can at times be difficult to interpret as the dynamic range of the imagery may not sufficiently capture intermediate brightness levels (intermediate backscatter values). For this reason, it is often helpful to convert sigma naught (σ^0) values to decides (dB) as shown in equation 24.

$$dB = 10 * log_{10}(\sigma^0) \tag{24}$$

In addition to being differentiated from optical sensors by the fact they are active sensors, radar have many other differentiating factors from optical sensors. Radar not only measure wave amplitude/intensity but also wave phase. The phase information proves very useful in many more complex SAR processing techniques that are discussed in later sections. Another distinction between radar and optical instruments is the fact that radar measure wave polarization. Currently, no operational optical satellites designed for Earth surface imaging have polarimetric observational capabilities. Lastly, radar instruments are largely distinguished from optical instruments not only by their microwave wavelengths, but the fact that these microwave wavelengths are monochromatic rather than multispectral. In this thesis, two types of monochromatic radar are used for wetland observation and characterization, these are C-band radar (5.55 cm wavelength) and L-band radar (23.5 cm wavelength). This is contrasted with the optical/IR imagery used in this thesis that is multispectral.

In summarizing the previous sections, a critical takeaway is that σ^0 is a measure of scattering efficiency of a target which largely depends on the target's dielectric properties ($\varepsilon_r(\omega)$) in combination with target geometry. Further, it is the relative geometry of the target (if anisotropic) in relation to the satellite's view geometry that influences σ^0. Although not previously discussed, it is crucial to note that σ^0 is also dictated by the physical size of the target (or targets) in a resolution cell relative to the radar signal's transmitted wavelength. This has important implications for comparative physical responses of C-band scattering, L-band scattering, and optical/IR reflectance for wetland targets. In the following section we discuss the dielectric properties of several common wetland targets, while noting that the relative size of the wavelength compared to the physical target(s) size and satellite view-target scattering geometry are also largely influential factors in dictating the value of σ^0.

1.3 Wetland Target Dielectric Properties

Wetlands are defined by the presence of hydrophilic vegetation, hydric soils, and periodic water presence (generally surface water). Water's dielectric properties are some of the most unique of any naturally occurring material on Earth which presents numerous opportunities in being able to separate wetland targets from drier targets and study wetland hydrological processes when using EM-based approaches. At optical/IR wavelengths, the real part of the dielectric constant (ε'_r) is approximately 1.79 at ultraviolet-blue wavelengths (400 nm), 1.77 at red edge wavelengths (700 nm), and 1.73 at the 1000 nm transition between the near infrared (NIR) and shortwave infrared (SWIR) (Pope and Fry, 1997; Segelstein 1981). The imaginary part of the dielectric constant ($i\varepsilon''_r$) has a value of 2.62e^{-20} at 400 nm, 1.21e^{-15} at 700 nm, and 1.21e^{-12} at 1000 nm (Pope and Fry, 1997; Segelstein 1981). When considering the fate of optical/IR EM radiation propagating in a medium of water, the relative spectral difference in the imaginary part of the dielectric constant has great implications for spectrally dependent absorption, and thus how much signal returns to a multispectral optical sensor imaging a water target. NIR and SWIR EM signals are more strongly attenuated than visible EM signals along the same geometric path length. At the interface of two media like air and water, some radiation will undergo scattering (mostly specular reflectance) dictated by ε'_r. However, the relative differences between the real dielectric values at visible and NIR-SWIR wavelengths are relatively small, and thus surface scattering spectral differences at the air-water interface are small. Further, optical satellites are generally designed with a view geometry that minimizes the observation of the specular reflectance that dominates this surface scattering for water targets (namely sun glint). This sun glint minimization means that a significant portion of optical EM signals will be upwelling radiance from within the water medium rather than from the water's surface. As previously stated, the spectrally dependent absorption has important implications here, with significantly higher levels of visible EM radiation returning to the sensor than NIR-SWIR EM radiation. This important difference has manifested in the development of many effective multispectral-based approaches for identifying surface water targets. One very commonly used approach is the development of spectral indices, the normalized difference water index (NDWI) and modified difference normalized water index (mNDWI) which make use of normalized differences of green and NIR bands, and green and SWIR bands, respectively (McFeeters 1996; Du et al. 2016). These water indices have addition utility in wetland characterization because they effectively respond to relative percent covers of vegetation and open water, as vegetation produces higher scattering in the NIR and SWIR relative to the visible (McFeeters 1996; Du et al. 2016; Jones 2019). This means that these water index responses are spectrally opposite for open water and vegetation, providing a sufficient range to allow estimation of vegetation cover and open water. Several surface water products exist that derive surface water extents from spectral indices or similar spectral band combinations, with the European Commission Joint Research Centre (JRC) Global Surface Water (GSW) product being one of the most commonly used products for moderate-high (30-meter) spatial resolution surface water mapping (Pekel et al. 2016). More recently, the U.S. Geological Survey released a Dynamic Surface Water Extent (DSWE) 30-meter resolution product utilizing a sophisticated decision tree classification incorporating several water indices and vegetation indices that classifies surface water probabilities in addition to potential wetlands (Jones 2019).

These optical indices and their associated derived products are limited in several ways compared to radar-based estimates of wetland inundation state and soil hydrologic properties. Compared to the small wavelengths of optical EM radiation, microwave EM radiation provides far greater penetration into vegetated canopies, allowing SAR to characterize the sub-canopy surface water or soil hydrologic state more effectively than optical sensors. Secondly, because SAR are side looking instruments, they observe not only the tops of vegetated canopies, but a more geometrically integrated canopy response, allowing not only assessment of upper canopy vegetation properties, but structural biomass as well. Third, the physical responses of microwaves to not only the presence, but the geometric distribution, of water in wetland systems is far stronger than optical EM responses. The remainder of this thesis chapter focuses on descriptions of microwave EM responses in characterizing wetland targets, which have been underutilized relative to optical approaches despite numerous technical advantages.

At microwave frequencies the dielectric properties of water are even more extreme than at optical wavelengths. At L-band wavelengths water reaches an ε'_r of ~80, while the $i\varepsilon''_r$ reaches value of ~20 (depending on temperature) (Ulaby and Long, 2015). At C-band wavelengths water reaches an ε'_r of ~70, while the $i\varepsilon''_r$ reaches value of ~25 (depending on temperature) (Ulaby and Long, 2015). Thus, at these microwave wavelengths there is tremendously strong scattering and high absorption, with minimal transmission of EM radiation into water. The seemingly narrow focus on the water's dielectric properties is not without reason. In the context of radar-based characterization of wetlands, vegetation and soils also contain high water contents. Based on the extremely high dielectric values of water at microwave wavelengths, it can be accurately summarized that it is the geometric distribution of water that dictates scattering from vegetation and soil targets in addition to open water. It is for this reason that many microwave radiometric models approximate vegetation as a water cloud (Ulaby and Long 2015). The importance of water's dielectric properties is further evidenced in the work by Duan and Jones (2017) summarizing previous research by Ulaby and El-Rayes (1987) and Lam et al. (2008) which estimated a dry (dead) marsh grass dielectric of 3.2 + i.79i and a wet (live) marsh grass dielectric of 13.62 + 4.83i. This difference in the real and imagery dielectric between live and dead marsh vegetation manifests in important scattering and absorption differences. Research by Atwood et al. (2020) found that a dielectric of 6.5 + 0.5i originally measured in corn stalks provided an effective analogue to *Typha* (cattail) stems in wetland microwave radiometric modeling efforts. Ellison et al. (2017) measured 2.45 GHz dielectric values of energy cane, tallow tree, and live oak vegetation matter with water contents below 12%, finding that all vegetation types exhibited similar real dielectric values of 2.13 on average, while imaginary dielectric values were less than 0.1. These studies clearly illustrate the important role that water plays in dictating the microwave dielectric values of wetland vegetation. Noting the importance of the dielectric constant variability in wetland targets, this factor is discussed in the following section as it pertains to microwave scattering and the backscatter that is observed by radar instruments.

1.4 Wetland Target Radar Scattering Responses

In wetland systems, vegetation, surface waters, and moist or saturated soils all contribute to an integrated radar backscatter response in a single resolution cell or image pixel. Scattering responses from these three primary targets vary and depend on dielectric properties and geometry in relation to the SAR sensor. For instance, backscatter from open water will vary as a function of both water's roughness from wind and wave activity and the SAR incidence angle (Vachon and Wolf 2011). Soils will generally act as rough surfaces when wet, scattering SAR signals somewhat anisotropically. However, as moisture increases and soils transition from moist to inundated, a more specular scattering response occurs (Woodhouse 2006). Vegetation backscatter responses are the most complex of all these three targets, as vegetation scattering varies as a function of: vegetation water content, stem and leaf density, stem and leaf orientation, canopy height, and whether vegetation is herbaceous or woody (Ulaby and Long, 2015). The complex scattering responses from vegetation also produce unique scattering signatures that allow vegetation to be distinguished from other targets. The first unique response is a tendency for leaves and stems to produce a volume scattering response in SAR signals. Volume scattering has the effect of depolarizing a SAR signal as many scattering events occur (Woodhouse 2006). The volume scattering response is captured in a relative difference between the polarization of the transmitted signals and polarization difference in the return signal. For instance, it is common for the Sentinel-1a SAR satellite to transmit a vertically polarized signal and measure vertically (VV) and horizontally (VH) polarized returns, with the first letter denoting transmitted polarization and the second denoting the received polarization. The PALSAR and PALSAR-2 satellites will commonly transmit a horizontally polarized signal and measure horizontal (HH) and vertical (HV) polarized returns. In both the Sentinel-1 and PALSAR/PALSAR-2 cases, the relative backscatter intensity differences between the co-polarized (VV, HH) and cross-polarized (VH, HV) signals will provide a relative assessment of vegetation-induced volume scattering. In general, the less degree of difference in the co-polarized and cross-polarized backscatter, the greater the occurrence of volume scattering.

Wetland vegetation produces an additional unique scattering response when the sub-canopy is inundated known as the double bounce effect. This response occurs as a result of two strong corner reflections off water's surface and then off a trunk(s) or stem(s) (or vice-versa). These two scattering events have the combined effect of producing a strong (high intensity) backscatter response. The double bounce effect is most pronounced if the scatterers (e.g. trunks or stems) have a geometry opposite the SAR signal (Ulaby and Long, 2015). In most wetland systems, both woody (e.g. swamps) and herbaceous (e.g. marshes), trunks and stems will have an approximately vertical orientation, meaning that the double bounce scattering effect will be most pronounced in SAR signals with horizontal polarization (HH). The double bounce effect in the co-polarized VV backscatter will be reduced relative to HH backscatter in wetlands with such vertically structured vegetation. In general, the double bounce scattering mechanism is largely thought to be absent from cross-polarized channels (HV, VH). Still, some studies have indicated the existence of helical scatterers in wetland systems that produce depolarized coherent scattering in the VH, HV channels. This cross-polarized coherent scattering mechanism is generally believed to have a minor contribution to backscatter and is best detected by polarimetric phase analyses (Hong and Wdowinski 2013; Hong et al. 2015). A more thorough discussion of phase-based SAR approaches for wetland monitoring will be discussed in later sections. The remainder of this section discusses SAR backscatter intensity. Figure 1.1 showcases the double bounce and volume scattering effects for C-band and L-band sensor backscatter. Note that soil and vegetation penetration depth differ for C-band L-band sensors, and that the degree of double bounce scattering changes as a function of wavelength relative to the physical size of the scatterer (e.g. herbaceous vegetation, tree, etc.). In the next section an in-depth assessment of existing literature and assessment of current SAR technologies for wetland characterization and observation is provided.

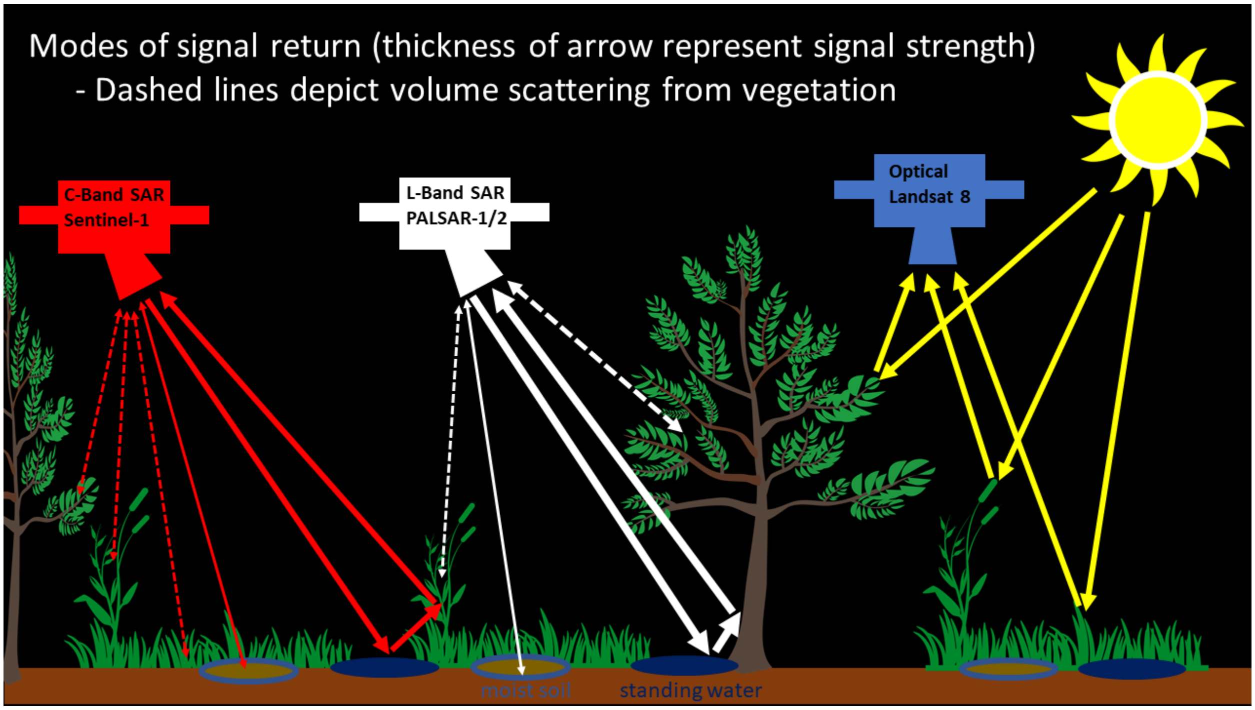

Figure 1.1. Depiction of SAR scattering and optical/IR reflectance in wetland systems for three most utilized satellite sensors in the following chapters of this thesis. Note when vegetated canopies are dense, signal penetration depth is a function of sensor wavelength. Interaction between satellite signals and wetland targets is dependent on the target's physical size relative to wavelength. Notably the double bounce effect is more pronounced for herbaceous vegetation with C-band signals, while inundated trees will produce a strong double bounce effect at L-band wavelengths. All depicted signal differences are based on backscatter or reflectance intensity, not signal phase which is discussed in later sections.

1.5 Radar-Based Wetland Characterization and Limitations to Address

Numerous studies have demonstrated the utility of SAR in wetland monitoring and characterization. Many of these studies have focused on inland wetlands. However, there are a number of SAR remote sensing studies focusing on tidal marshes specifically (Oliver-Cabrera and Wdowinski 2016; Ramsey et al. 2012; Ramsey et al. 2013; Ramsey et al. 2015; Rangoonwala et al. 2016; Kasischke and Bourgeau-Chavez 1997; Tannis et al. 1994). These studies largely focus on tidal marsh inundation monitoring with L-band and C-band SAR. These studies generally produce empirical and theoretical findings that tidal marsh SAR backscatter tends to decrease in the presence of tidal inundation, with the amount of backscatter decrease being a function of inundation depth. Some of the most comprehensive comparative studies of L-band imagery and C-band imagery for tidal marsh inundation characterization come from Ramsey et al. (2012) and Ramsey et al. (2013). These studies point to L-band PALSAR imagery being more effective in tidal marsh inundation mapping when using threshold-based approaches compared to C-band ASAR imagery (91% vs. 67% inundation classification accuracy). Oliver-Cabrera and Wdowinski (2016) found that PALSAR L-band Interferometric SAR (InSAR) image pairs acquired over inundated tidal marshes of the Gulf Coast tended to produce much higher interferogram coherence than RADARSAT-2 C-band InSAR image pairs acquired at similar tidal stages. This indicates that L-band scattering responses to tidal inundation state was more consistent across the tidal marsh study domain. Findings from Kasischke and Bourgeau-Chavez (1997) indicate some of the complexities of C-band imagery (ERS-1) in assessing inundation state. In their Southwest Florida study domain, both brackish tidal marsh and freshwater marsh ERS-1 backscatter increased transitioning from dry periods to wet periods, which was attributed to vegetation growth. Tannis et al. (1994), in contrast, found consistent ERS-1 C-band backscatter decreases for brackish marshes comparing low tide images to high tide.

It is not until the freshwater marsh SAR inundation studies are evaluated that a more well-supported assessment of C-band and L-band marsh inundation characterization performance becomes clear. Pope et al. (1997) found backscatter increases in HH and VV channel C-band imagery of the SIR-C instrument when high biomass herbaceous wetlands inundated, while Kasischke et al. (2003) found that freshwater herbaceous wetland backscatter decreased in response to inundation when imaged with the ERS-1 satellite's VV channel. These results are not necessarily inconsistent, but rather point to the combined influence of herbaceous vegetation biomass variability and inundation state in influencing C-band backscatter directional change. Although the combined influence of inundation state and marsh vegetation structure clearly have an impact on C-band backscatter response, the scattering mechanisms are not fully described by empirical analyses.

Radiometric model-based SAR scattering studies do help to elucidate scattering mechanisms when assessed in tandem with empirical image analysis. Tannis et al. (1994) and Kasischke and Bourgeau-Chavez (1997) found that SAR backscatter from the ERS-1 satellite was best fit to radiometric modeling efforts by describing herbaceous marshes as non-double bounce scattering, while woody wetlands were descried as double bounce scattering. Equations 25 and 26 are reproduced from Kasischke and Bourgeau-Chavez (1997) showcasing total wetland backscatter contributions (${\sigma^0}_t$) from different sources with and without the double bounce mechanism.

$$ {\sigma^0}_{t-w} = {\sigma^0}_c + {\tau^2}_c \ {\tau^2}_t \ ({\sigma^0}_m + {\sigma^0}_t \ {\sigma^0}_s + {\sigma^0}_d) \tag{25} $$

$$ {\sigma^0}_{t-h} = {\sigma^0}_c + {\tau^2}_c \ ({\sigma^0}_m + {\sigma^0}_s) \tag{26} $$

where ${\sigma^0}_c$ is backscatter from the vegetation crown. ${\tau^2}_c$ is the transmission coefficient of the vegetation canopy. ${\tau^2}_t$ is the transmission coefficient of the trunk. ${\sigma^0}_m$ is multiple path scattering between vegetation and ground. ${\sigma^0}_t$ is direct scattering from trunks. ${\sigma^0}_s$ is direct surface scattering from the ground. ${\sigma^0}_d$ is double bounce scattering between trunks and ground

Equations 25 and 26 effectively showcase scattering contributions from different sources and showcase how these radiative transfer equations are written with and without the double bounce mechanism present. Although the equation 25 terms ${\tau^2}_t$, ${\sigma^0}_t$, and ${\sigma^0}_d$ refer to trunk scattering contributions, these terms could readily be modified to represent stem scattering contributions if stems have a sufficient diameter and water content (high dielectric values) to contribute to strong double bounce scattering. The importance of the identification of the double bounce mechanism in assessing tidal marsh inundation state differs depending on approach. A comparison of the backscatter thresholding in Ramsey et al. 2013 and InSAR analysis in Oliver-Cabrera and Wdowinski (2016) serve as fine examples of the difference in approach. When using SAR backscatter approaches (returned signal intensity), the consistent L-band backscatter decreases as a function of inundation depth indicate that as marsh vegetation submerges, forward specular scattering dominates the total scattering response (${\sigma^0}_s$), while backscatter contributions from the vegetation canopy (${\sigma^0}_c$) decrease. However, scattering from vegetation canopies generally tend to scatter SAR signals incoherently (Woodhouse 2006). Thus, effective InSAR studies assessing tidal inundation state, must necessarily isolate the existence coherent scattering mechanisms like the double bounce effect or even coherent multiple path scattering (${\sigma^0}_m$) between marsh canopy and ground. This is not possible with incoherent scattering of non-inundated marsh vegetation, high biomass vegetation where no sub-canopy scattering occurs, or open water (Brisco et al. 2017). In the case of an inundating marsh, even though the backscatter intensity decreases as a function of water height as vegetation submerges as forward scattering dominates, so long as non-volume scattering vegetation structures like large stems remain present to produce coherent scattering, the retuned backscatter signal phase may remain coherent, even if the backscatter intensity is lowered.

Perhaps the most effective approach for isolating scattering mechanisms associated with marsh inundation state is by making use of polarimetric phase information in SAR imagery (PolSAR), rather than comparing the phase differences in separate image pairs as InSAR does.

Studies by Hong and Wdowinski (2013) and Hong et al. (2015) found that when marshes inundate, phase coherence between the VV and HH channels remains high, pointing to the presence of the double bounce scattering mechanism. These studies also found that cross-polarized channel and co-polarized phase difference coherence also remained high in many cases, pointing to the existence of coherent volume scattering. Similar findings of the existence of coherent volume scattering were also obtained by Atwood et al. (2020) in *Typha.* dominated marshes. PolSAR approaches not only detect the coherent scattering from double bounce and/or other coherent scattering mechanisms, but also identify comparative relative contributions of volume scattering and surface scattering when using physical scattering model-based polarimetric decompositions like Van Zyl and Yamaguchi approaches. Further, PolSAR approaches have the advantage of being useful for assessing marsh inundation state and vegetation characteristics for X-band, C-band, and L-band SAR (Hong and Wdowinski 2013; Hong et al. 2015; Ramsey et al. 2015). In contrast, L-band InSAR approaches are demonstrated as much more accurate in assessing marsh inundation state than C-band (Kim et al. 2014; Oliver-Cabrera and Wdowinski 2016). In thesis Chapters 2 and 3, backscatter-based approaches for tidal marsh inundation assessment and vegetation characterization are utilized. In Chapter 4 these approaches are compared to PolSAR-based approaches and radiometric models to better elucidate scattering mechanisms. Currently, studies that fully assess marsh SAR scattering through a combination of backscatter, polarimetric phase, and radiometric modeling analyses are limited (Kim et al. 2014; Atwood et al. 2020; Kasischke et al. 2003). Only Tannis et al. (1994) and Slatton et al. (2008) have combined such analyses in tidal marsh inundation assessments. Further, no studies (to the best of my knowledge) have provided comparative analyses using recent PALSAR-2 L-band imagery and Sentinel-1 C-band imagery.

Although the vast majority of these aforementioned studies illustrate the importance of accurate vegetation characterization in the context of assessing tidal marsh inundation state with SAR (particularly C-band SAR), few studies have specifically assessed tidal marsh vegetation characteristics using SAR imagery (Ramsey et al. 2015; Ramsey et al. 2016; Rangoonwala et al. 2014; Jensen et al. 2019). Literature reviews on the topic of remote sensing of tidal marsh vegetation illustrate that optical/IR remote sensing is more commonly utilized for tidal marsh vegetation assessment (Bartlett and Klemas 1981; Campbell et al. 2015; Hurd et al. 2005; Klemas et al. 2013; Langely and Megonigal 2012; Feagan et al. 2020). The nature of these respective SAR and optical/IR studies reveal differences in capabilities, where the SAR studies characterize tidal marsh vegetation structure and biomass while optical/IR studies focus on assessment of vegetation greenness and identification of specific vegetation by utilizing multispectral mapping and classification approaches. These differences however, do point to the potential underutilization of SAR in tidal wetland vegetation classifications, especially considering the complementary nature of these approaches and fact that SAR-optical fusion has been demonstrated as a powerful approach for freshwater marsh wetland vegetation classifications (Bourgeau-Chavez et al. 2013; Bourgeau-Chavez et al. 2015). Additionally, SAR imagery has been identified as very useful in the identification of functional wetland classes, including tidal marshes (Whitcomb et al. 2009; Clewley et al. 2015).

1.6 Current Challenges and Opportunities in Wetland Remote Sensing

The preceding sections illustrate numerous areas of potential research development in the remote sensing of tidal wetlands. A number of these specific research opportunities align well with the general objectives of this thesis, namely, to improve the monitoring and characterization of tidal marsh extent, vegetation characteristics, and inundation state. In the following thesis Chapter 2, an evaluation of current remote sensing technologies is carried out and assessed in the context of wetland characterization for the Chesapeake Bay-Delaware Bay region of the Mid-Atlantic United States. An empirical assessment of tidal marsh inundation characterization capabilities using PALSAR L-band imagery and Sentinel-1 C-band imagery is performed over two brackish tidal marsh study sites. Additionally, a SAR-optical fusion approach is used for the classification of tidal marshes and the classification of specific tidal wetland vegetation characteristics over a tidal freshwater marsh system with a diverse vegetation community composition. As previously noted, remote sensing-based studies of tidal freshwater marshes are very limited. In Chapter 2, assessment of vegetation identification is carried out with both SAR and optical imagery. Chapter 2 concludes with a similar evaluation study for the Long Island Sound region of the Mid-Atlantic United States and findings are contrasted with those from the Chesapeake Bay.

In Chapter 3 of this thesis, the approaches developed in Chapter 2 are utilized to identify tidal marshes throughout the Mid-Atlantic and Gulf Coast regions using SAR-optical fusion approaches that were demonstrated successful in Chapter 2. Chapter 3 highlights the importance of the identification of tidal freshwater marshes in the context of their role as indicators of ecological setting, especially of abiotic ecological factors like salinity and hydrology, and in being able to delimit boundaries between brackish and freshwater areas. The identification of tidal freshwater marshes is carried out through identification of non-persistent vegetation unique to freshwater and freshwater tidal marsh systems that is not found in brackish and salt marsh systems (Odum 1988). Chapter 3 includes applied studies on the identification of the invasive tidal marsh species *Phragmites australis* (common reed) and invasive *Trapa natans* (water chestnut) which is often found in deepwater areas adjacent to freshwater tidal marshes. This chapter focused on the separation of *Trapa natans* from non-persistent emergent vegetation as the phenologies of these different types of vegetation are similar, but were accurately separated from one another in Mid-Atlantic tidal marshes and deepwaters (> 93% accuracy). This vegetation mapping effort is the first of its kind identifying tidal freshwater marsh and aquatic vegetation utilizing primarily Sentinel-1 SAR imagery which was found to have a more effective structural phenological response than optical imagery.

Chapter 4 of this thesis involves an in-depth assessment on the current state of SAR-based tidal marsh inundation mapping approaches at study sites in the Mid-Atlantic and Gulf Coast regions of the United States. SAR-based inundation product development is also compared to existing optical inundation products. This analysis is carried out with a combination of C-band and L-band SAR imagery, *in situ* validation, and radiometric modeling efforts. This research effort transitions into Chapter 5 which provides a summation of Chapters 1-4 in the context of future opportunities and challenges that exist in tidal marsh remote sensing. This final chapter specifically highlights opportunities that exist with the anticipated launch of three new satellites all of which provide unique and potential ground-breaking opportunities in the field of tidal wetland remote sensing. These three satellite launches include the NASA-ISRO SAR Mission (NISAR), the Surface Biology and Geology Mission (SBG) Designated Observable, and the Geostationary Littoral Imaging and Monitoring Radiometer (GLIMR) Earth Venture Instrument (EV-I) mission. These three satellites represent technological advances in radar, hyperspectral, and geostationary remote sensing, respectively and will be discussed in the context of thesis research conclusions in Chapter 5.

CHAPTER 2

EVALUATION OF SATELLITE IMAGERY FOR WETLAND CHARACTERIZATION

2.1 Introduction to Chapter and Chesapeake Bay Study Site

The following chapter focuses on the evaluation of current era satellite imagery for the purpose of wetland observation and characterization. Sections 1.4 and 1.5 of the previous chapter addressed potential advances in SAR and optical wetland remote sensing in the context of EM theory, addressing scattering and absorption, dielectric constant, sensor-target geometry, and similar topics. Building on that theoretical groundwork, this chapter takes a more applied focus, evaluating the capabilities of specific satellite and aircraft imagery for wetland observation and characterization. This chapter then addresses how these observational capabilities align with the challenges and opportunities addressed in the theoretical context. Section 2.2 of this chapter addresses specific characteristics of remote sensing platforms and the imagery they produce.

The wetland remote sensing evaluation study described herein is set in Chesapeake and Delaware Bays. This region of the Mid-Atlantic has some of the highest wetland densities on the eastern seaboard, a significant portion of which are tidal marshes. The initial inception of this work came from a NASA funded project assessing wetland-estuarine carbon cycling in the Chesapeake Bay region (NNX14AP06G, PI: Tzortziou). The research on this NASA project uncovered many additional research questions that are partially answered here in Chapter 2 but are further addressed in Chapters 3 and 4. Sections 2.2 through 2.6 can be found in publication form under the title “Evaluation of Approaches for Mapping Tidal Wetlands of the Chesapeake and Delaware Bays” in the journal *Remote Sensing* (Lamb et al. 2019). This chapter concludes with Section 2.7 which contains a similar wetland remote sensing evaluation approach for the Long Island Sound region (NASA Grant 80NSSC17K0258, PI: Tzortziou).

2.2. Background on Current Remote Sensing Capabilities in Wetland Observation

Many studies have utilized remote sensing to study abiotic and biotic wetland processes (Lang et al. 2008; Schmitt et al. 2013; Kim et al. 2014; Moser et al. 2016; Brisco et al. 2017; Byrd et al. 2018), and to inventory wetlands (Whitcomb et al. 2009; Clewley et al. 2015; Hird et al. 2017). For wetland process studies, polar orbiting optical and synthetic aperture radar (SAR) satellites with spatial resolutions of 5–250 meters have generally represented a compromise in terms of spatial resolution and temporal resolution (revisit time), which are both important for monitoring wetland dynamics. Satellite imagery with spatial resolutions finer than five meters is more suited to characterizing wetland spatial variability and producing detailed wetland maps (Gilmore et al. 2008; Klemas et al. 2013; Campbell et al. 2017). However, many of the satellites acquiring this high spatial resolution imagery are commercial, requiring users to purchase imagery and at times also requiring tasking of the satellites for image acquisition over a given study site. Further, commercial imagery generally lacks the large-scale regional coverage in space and time needed for mapping a wetland's extent and inundation dynamics over large areas. Publicly available high spatial resolution aerial photography, such as the United States Department of Agriculture Farm Service Agency National Aerial Imagery Program (NAIP) provides an alternative to high spatial resolution commercial satellite imagery and provides growing season imagery for the entire United States every two to three years. The United States Fish and Wildlife Service produces its National Wetlands Inventory (NWI) by manually digitizing wetland boundaries using NAIP and other high spatial resolution aerial photography (Cowardin et al. 1979; FGDC 2013). Although manual digitization is effective for wetland mapping (Smith 2013), these mapping efforts are labor intensive, preventing frequent updates of associated datasets. As a result, the NWI and similar products may at times be out of date by several years or even decades (Lang et al. 2008). In contrast to wetlands mapping efforts utilizing aerial photography, which often relies on manual digitization, satellite imagery-based mapping efforts have generally relied on supervised and unsupervised automated classification approaches (Kulawardhana et al. 2007). When the wetlands being classified are large in extent, automated classification approaches with 30-m resolution satellite imagery can achieve classification accuracies greater than 95%, which is similar to accuracies obtained from classifications with 1-m resolution imagery recommended by the Federal Geographic Data Committee (FGDC) for wetlands mapping (Frohn et al. 2009). Use of satellite imagery for wetlands characterization and mapping also provides the ability to fuse optical imagery with SAR imagery, which each have unique and complementary observational capabilities (Ozesmi and Bauer 2002).

Optical satellite imagery has been widely used for characterizing wetland vegetation. The visible red to near infrared spectral angle provides a combined measure of vegetation greenness, leaf area index, and upper canopy structure, integrated within an image pixel. This spectral angle is often leveraged to produce spectral ratios and indices that relate to the aforementioned vegetation properties (Tucker 1979; Prabhakara et al. 2015). SAR satellites operate at microwave wavelengths, achieving greater signal penetration in vegetated canopies and more accurate characterization of vegetation structural biomass and inundation below canopies than optical spectral ratios and indices. C-band SAR (5.56-cm wavelength) is particularly suitable for separating/identifying emergent marsh vegetation based on biomass. Ramsey et al. (2015) and Dabrowska-Zielinska et al. (2016) both demonstrated strong statistical relationships between leaf area index (LAI) and cross-polarized C-band backscatter in emergent marsh wetlands. With an increasing biomass of shrubs and trees, C-band signals saturate, limiting their ability to differentiate high biomass emergent marsh vegetation from forest- and shrub-dominated wetlands (Woodhouse 2006). L-band SAR (23-cm wavelength) can effectively separate emergent marsh vegetation from shrubs and trees. The differences in vegetation canopy interaction between optical, C-band SAR, and L-band SAR make these forms of imagery complementary in wetland mapping in general, and particularly useful in mapping the tidal wetlands of the Chesapeake and Delaware Bays, which are largely classified as estuarine emergent (i.e., tidal marsh) by the NWI and dominated by emergent species of moderate biomass.

Just as the characterization of vegetation structure remains critical in mapping emergent tidal marshes, so is the characterization of wetland hydrology. SAR and optical datasets can both accurately assess surface water extent (Clewley et al. 2015; White et al. 2015; Behnamian et al. 2017; Bioresita et al. 2018; Kuenzer et al. 2015; McFeeters 2013; Du et al. 2016). SAR-based surface water mapping generally relies on backscatter thresholding approaches (Behnamian et al. 2017; Bioresita et al. 2018). Optical surface water mapping generally relies on the derivation of spectral indices and subsequent thresholding or the thresholding of several multispectral bands. The normalized difference water index (NDWI) with green and near infrared bands and the modified normalized difference water index (mNDWI) with green and shortwave infrared bands (McFeeters 2013; Du et al. 2016) are two commonly used optically-based surface water indices.

Because microwave signals penetrate vegetation canopies, SAR is able to detect inundation under vegetated canopies more effectively than optical imagery. Several studies have utilized SAR imagery for inundation mapping in vegetated wetlands (Lang et al. 2008; Kim et al. 2014; Ramsey et al. 2012). SAR backscatter intensity may increase or decrease when vegetated wetlands become inundated depending on the relative contributions of: 1) double-bounce scattering between vegetation and the underlying water surface, which increases like-polarized backscatter; 2) multiple scattering by vegetation, which enhances cross-polarized backscatter; and 3) forward specular scattering from open water, which greatly decreases backscatter (Woodhouse 2006; Pope et al. 1997; Kasischke et al. 2003). The double-bounce scattering mechanism is most present in co-polarized backscatter, σ^0_{HH} and σ^0_{VV} (with the first $_H$ or $_V$ representing the polarization of the transmitted signal and second $_H$ or $_V$ representing polarization of the return signal). Volume (multiple) scattering from vegetation is best characterized with the cross-polarized backscatter, σ^0_{HV} and σ^0_{VH}. As the inundation level increases in wetlands, moist soil transitions to standing water and double-bounce scattering enhances co-polarized backscatter, while cross-polarized backscatter decreases monotonically as vegetation exposed above the water level decreases. This opposite behavior of co- and cross-polarized backscatter can be used to identify inundated vegetation provided sufficient vegetation remains present above the water level. These scattering responses also vary in magnitude and sensitivity with SAR wavelength (e.g., C-band vs. L-band frequency).

In this study we examine the characterization of inundation dynamics and vegetation characteristics of target wetland study sites in the Chesapeake Bay using SAR and optical satellite imagery. We explore and evaluate the capabilities of SAR and optical imagery and use this to guide layer selection for a fused SAR-optical-Digital Elevation Model (DEM) classification based on the random forest algorithm (Breiman 2001), mapping the tidal wetlands of the Chesapeake and Delaware Bays for 2017. In this regional scale wetlands classification, we separated estuarine emergent wetlands from palustrine emergent wetlands. This separation corresponded to a general split between freshwater marshes and brackish/salt marshes. Our approaches utilized multitemporal satellite imagery from a single year and can be updated on an annual basis to provide annual assessments of change in tidal wetlands distribution. Our regional scale wetlands mapping effort leveraged the temporally dense record of publicly accessible satellite imagery including Sentinel-1A, Sentinel-2A, Landsat 8, and Advanced Land Observing Satellite (ALOS) – Phased Array type L-band Synthetic Aperture Radar 1 & 2 (PALSAR/PALSAR2) imagery.

2.3 Materials and Methods

2.3.1 Methods Overview

Due to the fact we are attempting to provide assessments of wetland extent, wetland vegetation characteristics, and wetland inundation dynamics in a single study, the methods we employed were by their very nature multifaceted and at times complex. For these reasons, we provide an ordered overview of the methods sections here to provide clarity to the reader. Section 2.3.2 describes the satellite datasets we evaluated and successively employed for wetland characterization and subsequent mapping. Section 2.3.3 describes the target wetlands study sites we selected for this evaluation. Section 2.3.4 describes wetland vegetation characterization in terms of both field studies and previous datasets utilized for vegetation characterization in addition to remote sensing-based methods employed for vegetation characterization. Section 2.3.5 describes wetland inundation characterization and is split into Subsection 2.3.5.1, which discusses the field studies and previous datasets used for the hydrologic characterization of study sites, and Subsection 2.3.5.2, which describes the remote sensing-based methods employed for inundation characterization. The methods section concludes with Sections 2.3.6 and 2.3.7, which describe mapping efforts employing random forest classifications. Section 2.3.6 describes a classification of vegetation within a target study site wetlands complex using both SAR-only and

SAR-optical-DEM image stacks as classification inputs. In Section 2.3.6, we describe the use of a post-classification importance assessment for the SAR-only and SAR-optical-DEM classifications to determine which forms of imagery were most important for improving classification accuracy. Section 2.3.7 describes the methods for mapping general wetlands classes in a regional scale classification for the Chesapeake and Delaware Bays using the same SAR-optical-DEM image stack used in Section 2.3.6. Section 2.3.7 concludes with a post-classification importance assessment of the SAR-optical-DEM regional scale wetlands classification, which was then compared to the SAR-optical-DEM wetland vegetation classification described in Section 2.3.6.

2.3.2 Satellite Image Selection and Processing

We evaluated L-band PALSAR and PALSAR-2, and C-band Sentinel-1A SAR imagery, as well as Sentinel-2A and Landsat 8 optical imagery for the characterization of wetland vegetation and inundation state, as well as mapping of overall tidal wetland extent, at three target study sites. We then utilized these satellite datasets to map palustrine emergent, estuarine emergent, and forested wetlands throughout the Chesapeake and Delaware Bays for 2017 in a regional scale classification. The aforementioned satellites provided data with revisit intervals of 48, 48, 12, 10, and 16 days, respectively. There was sufficient temporal overlap between the satellite datasets from 2016 through to 2017 to evaluate satellite performance in the characterization of vegetation phenology and inundation extent over a range of tidal stages. This was the timeframe for which we performed the majority of our analysis. The exception to this rule was the PALSAR satellite, which operated between 2006 and 2011. We used Google Earth Engine (GEE) for the majority of our image data assembly (Gorelick et al. 2017). GEE is a cloud-based image processing platform that has been effective for computationally demanding image processing and classification applications, such as large-scale agricultural mapping, forest monitoring, and wetlands mapping (Hird et al. 2017; Shelestov et al. 2017). The majority of our classification work employed SAR and optical satellite imagery; however, we also made extensive use of the Shuttle Radar Topography Mission (SRTM) Digital Elevation Model (DEM) in our regional scale classification efforts. We accessed Sentinel-2A and Landsat 8 optical imagery and the SRTM DEM through GEE. Sentinel-2A imagery was available on GEE as a top of atmosphere (TOA) reflectance product, while Landsat 8 was available as a surface reflectance product. All optical imagery was quality and cloud masked in GEE prior to the analysis and classification.

Sentinel-1A imagery accessed through GEE was processed with the European Space Agency's Sentinel Applications Platform (SNAP) toolbox in a processing sequence in which ground range detected SAR imagery undergoes the following processes: orbit correction, border noise removal, thermal noise removal, radiometric calibration, and terrain correction with an SRTM DEM. Although SAR terrain correction tools can be variable in performance, the flat terrain of the Chesapeake and Delaware Bay regions was unlikely to produce significant differences in processed SAR imagery based on the choice of SAR terrain correction tool; however, this is a non-trivial consideration in topographically complex study areas. PALSAR-2 imagery was available on GEE in the form of annual mosaics. These annual mosaics were assembled by the Japan Aerospace Exploration Agency (JAXA). JAXA produced the PALSAR-2 annual mosaics by orthorectifying PALSAR-2 image strips from a given year, applying a slope correction with the 90-m SRTM DEM, and then mosaicking the image strips and applying a destriping process. PALSAR imagery was the only satellite dataset not available through the GEE platform. We used PALSAR imagery provided and processed by the Alaska Satellite

Facility (ASF) through an agreement with JAXA. ASF processed the PALSAR imagery to a ground-range-detected, terrain-corrected, level 1.5 product, which we downloaded from ASF's VERTEX online interface. PALSAR and PALSAR-2 L-band imagery was available for HH polarization, and at times HV polarization as well, while Sentinel-1A C-band imagery was available for both VV and VH polarizations.

Processing of imagery outside of the GEE environment for target wetlands site vegetation and inundation analysis and development of training/validation data for the regional scale classification were performed using Quantum GIS (QGIS), Python, and the R programming language (R Core Team 2017).

2.3.3 Study Site Selection

We selected three target wetlands study sites for the evaluation of satellite imagery for vegetation and inundation characterizations and to inform our regional scale wetlands mapping effort for the Chesapeake and Delaware Bays. These sites were chosen based on their high wetland densities and distinct ecological characteristics relative to one another. The three target sites included the Smithsonian Global Change Research Wetland (GCReW), or Kirkpatrick Marsh (hereafter referred to as Kirkpatrick Marsh), the Blackwater National Wildlife Refuge (hereafter referred to as Blackwater NWR), and the Jug Bay Wetlands Sanctuary (hereafter referred to as Jug Bay) (Figure 2.1).

Kirkpatrick Marsh, in the Rhode River sub-estuary along the northwestern shoreline of the Chesapeake Bay, is classified as an estuarine, emergent, persistent, and irregularly flooded marsh (E2EM1P) according to the National Wetlands Inventory (NWI) 2013 update. Kirkpatrick Marsh is noted as being high elevation by previous studies (Correll and Jordan 1991; Langley and

Megonigal 2012; Nelson et al. 2017). The vegetation composition is typical of a high elevation marsh in the Mid-Atlantic region of the United States with dominant species including: *Scirpus americanus (*also known as *Schoenoplectus), Spartina patens*, *Iva frutescens*, and *Phragmites australis*. These are all persistent species with significant amounts of non-photosynthetic plant material remaining present on the marsh surface during the non-growing season.

Blackwater NWR and its connected wetlands comprise the largest estuarine wetlands complex in the Chesapeake Bay (Figure 2.1). Situated along the eastern shoreline of the Chesapeake Bay, this site contains several classes of individual wetlands, the vast majority of which are estuarine, emergent, persistent, and irregularly flooded marshes (E2EM1P) according to the NWI 2013 update. Blackwater NWR also contains estuarine, emergent, persistent, and regularly flooded marshes (E2EM1N). The low elevation of Blackwater's marsh surface, combined with sea-level rise, sediment deficits, and marsh destruction by nutria, have resulted in significant wetland degradation with more than 5000 acres of tidal marsh being converted to open water since 1938 (Kearney et al. 2002; Scott et al. 2009; Ganju et al. 2013; Ganju et al. 2017). Thus, even though Blackwater NWR shares the same NWI wetland class as Kirkpatrick Marsh, it is a very different system in terms of its geomorphology. These differences are further evidenced by the presence of low marsh species like *Spartina alterniflora*, which is largely absent from Kirkpatrick Marsh. Blackwater NWR also contains *Spartina patens* and *Distichlis spicata*, which are common high marsh species. These three dominant species of Blackwater NWR are all persistent graminoid emergents.

Located along the Patuxent River in southern Maryland, Jug Bay is a tidal freshwater wetlands complex containing several NWI wetland classes (Figure 2.1). The most common wetland classes include estuarine, emergent, persistent, and irregularly flooded marsh (E2EM1P), estuarine, emergent, persistent, and regularly flooded marsh (E2EM1N), as well as various deepwater, shrub, and forested wetlands according to the NWI 2013 update. The salinity differences between Jug Bay relative to Kirkpatrick Marsh and Blackwater NWR facilitates pronounced differences in vegetation characteristics (Odum et al. 1984; Odum 1988). Jug Bay, like other Mid-Atlantic tidal freshwater systems, contains a significant amount of non-persistent vegetation types including: *Nuphar lutea* (spatterdock), *Peltandra virginica* (green arrow arum), and *Pontederia cordata* (pickerelweed) (Leck et al. 2009; Swarth et al. 2013). Jug Bay also contains substantial amounts of *Zizania aquatica* (wild rice), which is semi-persistent in nature, losing its leaves at the end of the growing season, while its stems persist on the marsh surface either standing or in a horizontal mat during the non-growing season. Jug Bay contains significant amounts of persistent *Typha spp.* (cattail) as well. We surveyed the Jug Bay Wetlands Sanctuary during all four seasons and performed vegetation inventories during each of these visits (6/7/2016, 5/1/2017, 23/6/2017, 13/9/2017, 14/9/2017, 5/12/2017, 6/12/2017, and 13/4/2018). We observed that dominant vegetation was fairly well zonated, forming stands that were largely monospecific. We observed that *Nuphar lutea* was by far the most dominant non-persistent vegetation in Jug Bay.

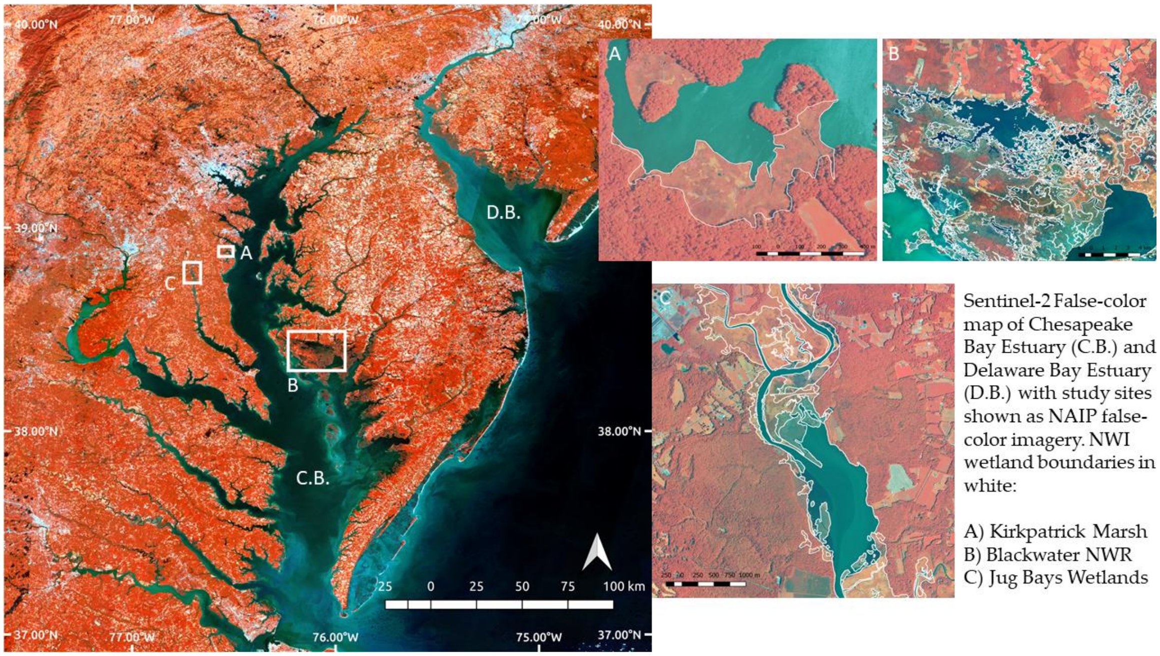

Figure 2.1. False-color rendering of Sentinel-2 near infrared imagery of Chesapeake Bay and Delaware Bay study region with Kirkpatrick Marsh, Blackwater National Wildlife Refuge (NWR), and Jug Bay Wetlands target study sites shown in the right panel with false-color National Aerial Imagery Program (NAIP) aerial photography and National Wetlands Inventory (NWI) boundaries in white.

2.3.4 Marsh Vegetation Characterization Using Field Surveys and Satellite Images

Kirkpatrick Marsh and Jug Bay were selected as evaluation sites for vegetation characterizations with SAR and optical satellite imagery. We were particularly interested in evaluating the differences between persistent and non-persistent vegetation types within these study sites and determining whether their presumed phenological differences would be captured using multitemporal satellite imagery. Previous vegetation inventories existed for Kirkpatrick Marsh (Lu, Williams, and Megonigal, 2016) and Jug Bay (Swarth et al. 2013). In order to update these surveys to correspond to the 2016–2017 satellite imagery datasets, we visited both target sites and performed GPS-based transects in July 2016, recording dominant vegetation types. These transects were then referenced with 2015 NAIP imagery, as well as the original Lu, Williams, and Megonigal and Swarth et al. shapefile-based vegetation inventories in order to perform updates to the dominant vegetation boundaries (Figure 2.2). We performed this manually digitized update in QGIS, changing the boundaries of dominant species only where clearly identifiable shifts in the spatial distribution of dominant vegetation had occurred relative to the 2015 NAIP imagery. In many cases, the Lu, Williams, and Megonigal survey for Kirkpatrick Marsh and Swarth et al. survey for Jug Bay needed only minor spatial adjustments.

These updated surveys were then ingested into Google Earth Engine (GEE). Within GEE, we accessed collections of Sentinel-1A, Sentinel-2A, and Landsat 8 imagery in order to evaluate whether optical vegetation indices or SAR backscatter timeseries exhibited unique temporal signatures that could be utilized for the identification of different classes of vegetation. We computed the normalized difference vegetation index (NDVI) and triangular vegetation index (TVI) for optical imagery (Tucker 1979; Prabhakara et al. 2015).

NDVI is one of the more commonly used indices for characterizing wetland vegetation (Kulawardhana et al. 2007; Langley and Megonigal 2012; Kearney et al. 2002). TVI is less commonly utilized but it has been demonstrated to be more effective for characterizing vegetation in high biomass ranges in agricultural studies. After evaluating the temporal and spatial coverage of Landsat 8 and Sentinel-2A imagery, we elected to only use Sentinel-2A vegetation indices as they provided a denser timeseries of cloud-free imagery over both target sites. Following this evaluation, Sentinel-2A NDVI and TVI, as well Sentinel-1A VV- and VH-polarized backscatter (σ^0_{VV} and σ^0_{VH}) spatial averages, were computed for each vegetation class for Kirkpatrick Marsh and Jug Bay. These timeseries were then exported from GEE and analyzed with Python and R.

$$\mathrm{NDVI} = \frac{(\mathrm{NIR} - \mathrm{Red})}{(\mathrm{NIR} + \mathrm{Red})} \quad (1)$$

$$\mathrm{TVI} = 0.5[120(\mathrm{NIR} - \mathrm{Green}) - 200(\mathrm{Red} - \mathrm{Green})] \quad (2)$$

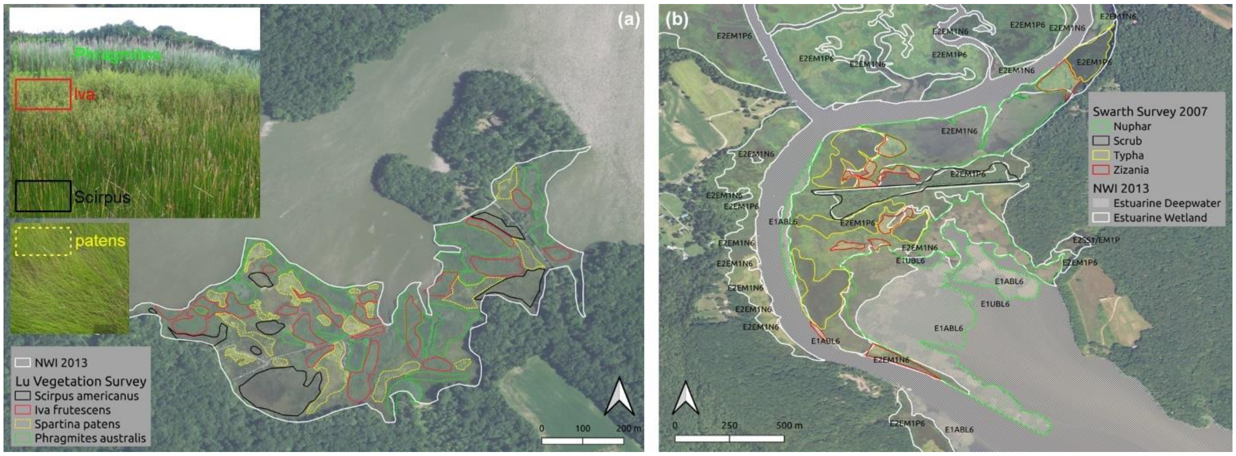

Figure 2.2. 2015 NAIP natural-color site maps of Kirkpatrick Marsh (**a**) and Jug Bay (**b**). 2013 NWI boundaries shown in white. The color shapefile boundaries show the updated Swarth et al. (2013) and Lu, Williams, and Megonigal (2016) vegetation survey boundaries.

2.3.5. Marsh Inundation Characterization and Approaches

2.3.5.1. Field Measurements of Marsh Inundation

To evaluate how differences in geomorphology (i.e., marsh elevation) impact marsh inundation regimes and our ability to detect inundation using different remote sensing tools, our remote sensing assessment and mapping of marsh inundation focused on Kirkpatrick Marsh and Blackwater NWR. Kirkpatrick Marsh consists of almost entirely high marsh, is less frequently inundated than low marsh systems, and the mean tidal amplitude of the adjacent Rhode River sub-estuary is 0.3 meters (Langley and Megonigal 2012; Jordan et al. 1986; Tzortziou et al. 2008). This presented a unique opportunity to determine how effectively inundation events of low water depth (less than 0.5 meters) that occurred below dense vegetated canopies could be detected using satellite imagery, particularly in regions dominated by the high biomass and densely growing *Phragmites australis*. The Blackwater NWR system is a mix of a low and high marsh. We surveyed a sub-region of the Blackwater NWR site on 15 October 2015 (see GPS locations in Figure 2.3). We noted that major sections of the surveyed area were dominated by *Spartina alterniflora*. During this survey, we observed that major regions of the marsh inundated during regular high tides (approximate tidal range of 0.6 meters in the connected estuary).

To assess the capability of the satellite imagery in characterizing tidal inundation within these study sites, tidal stage water level timeseries were acquired from nearby National Oceanic and Atmospheric Administration (NOAA) tidal stations and matched with satellite overpass times. The NOAA tidal gauge closest to Blackwater NWR is Bishop's Head (Station ID: 8571421). The tidal gauge closest to Kirkpatrick Marsh is Annapolis (Station ID: 8575512). No time-based or water level-based adjustments were made to the Bishop's Head tidal timeseries because reliable estimates of in-marsh water heights were not available over Blackwater NWR. In the case of Kirkpatrick Marsh, water level adjustments were made by leveraging the findings from previous studies that characterized the hydrology of the marsh in detail (Correll and Jordan 1991; Nelson et al. 2017). Nelson et al. determined that a water depth of 0.89 meters or greater in a major tributary draining Kirkpatrick Marsh was needed to reach a bankfull depth, at which point the marsh platform begins to inundate (Nelson et al. 2017). The results from Nelson et al. were obtained using a SonTek Acoustic Doppler Current Profiler (ADCP) measuring water depth and velocity. Because the SonTek was only deployed for limited times, we performed an assessment of relationship between the SonTek and the nearby Annapolis NOAA tidal gauge to determine whether adjustments could be made to the Annapolis series to estimate the Kirkpatrick Marsh tidal creek water levels during all satellite overpasses. We performed this assessment by resampling the SonTek and Annapolis series to a common temporal resolution of one minute. A lagged correlation analysis (lag range of −120 minutes to +120 minutes) was performed for a time period of approximately one week for three separate seasons in 2016. These three selected periods were times when the SonTek was determined to be operating continuously. The three time periods were determined to have an average time offset of 34.33 minutes (with the SonTek water level changes preceding the Annapolis water level changes). The height offset was determined to be 0.4774 meters on average (with the Kirkpatrick Marsh tributary bottom where the SonTek was deployed being lower in elevation than the Annapolis tidal gauge). These parameters are shown in Table 1.

Table 2.1. Adjusted Annapolis stage parameters for estimating tidal creek stage of Kirkpatrick Marsh.

Date	n (minutes)	Max R-value	Time Offset (minutes)	Height Offset (meters)
June 2016	6000	0.9911	34	0.4856
October 2016	6000	0.9963	37	0.4769
December 2016	6000	0.9912	32	0.4696
Average	--	--	34.33	0.4774

2.3.5.2. Satellite-Based Inundation Mapping at Kirkpatrick Marsh and Blackwater NWR

After the adjusted water level series were obtained, GEE was used to derive optically-based water indices (NDWI and mNDWI) from Sentinel-2A and Landsat 8 imagery and to provide σ^0_{VV}, σ^0_{VH}, and $\sigma^0_{VV}/\sigma^0_{VH}$ ratio timeseries from Sentinel-1A, covering Kirkpatrick Marsh between 2016–2017. We evaluated the $\sigma^0_{VV}/\sigma^0_{VH}$ ratio as a potential normalized inundation indicator as σ^0_{VV} tends to increase as marshes inundate from enhanced double-bounce scattering, while σ^0_{VH} tends to decrease from reductions in volume scattering. The spatial means of the backscatter and water index values were computed over the Kirkpatrick Marsh (NWI class E2EM1P). The same process was used for the NWI-defined irregularly inundated estuarine marshes (E2EM1P) and regularly inundated marshes (E2EM1N) of the Blackwater NWR study site in addition to several less spatially extensive NWI wetland classes. The optical water index and SAR backscatter timeseries were computed in GEE, then exported for further analysis in Python and R. The Kirkpatrick Marsh and Blackwater NWR satellite timeseries were compared to the adjusted Annapolis tidal series and Bishop's Head tidal series, respectively.

Pearson's correlation was used to determine the goodness of fit between the Sentinel-1A backscatter and the Sentinel-2A water index variability and tidal stage in both Kirkpatrick Marsh and Blackwater NWR. These relationships were also plotted using both ordinary least squares and second order polynomials. Blackwater NWR had only one PALSAR image acquired at high tide that was from the same orbit as a corresponding low tide image (ascending orbital path 136). This high tide–low tide image pair was used for comparison, in addition to the Sentinel-1A and Sentinel-2A image timeseries, providing an assessment of optical, C-band SAR, and L-band SAR for inundation characterization at the Blackwater NWR site (Figure 2.4). No PALSAR imagery was available for the stage height above the bankfull depth in Kirkpatrick Marsh, thus no corresponding assessment of inundation mapping could be performed. Above the bankfull depth, Landsat 8 images were also limited. As a result, only Sentinel-1A backscatter (σ^0_{VV}, σ^0_{VH}, and $\sigma^0_{VV}/\sigma^0_{VH}$ ratio) and Sentinel-2A NDWI and mNDWI could be assessed for their inundation mapping capabilities at Kirkpatrick Marsh.

$$\mathrm{NDWI} = \frac{(\mathrm{Green}-\mathrm{NIR})}{(\mathrm{Green}+\mathrm{NIR})} \tag{3}$$

$$\mathrm{mNDWI} = \frac{(\mathrm{Green}-\mathrm{SWIR})}{(\mathrm{Green}+\mathrm{SWIR})} \tag{4}$$

In Kirkpatrick Marsh, having a well-constrained estimate of the bankfull depth from a previous study (Nelson et al. 2017) allowed us to segment Pearson's correlation analysis of

Sentinel-1A backscatter and Sentinel-2A optical water indices into above- and below-bankfull depth categories. Within the above-bankfull depth (ABD) category, Sentinel-1A backscatter, particularly σ^0_{VV} and $\sigma^0_{VV}/\sigma^0_{VH}$ ratio exhibited the highest correlation with water level (tidal stage) and were subsequently selected for mapping the inundation extent (see the Results section for justification). Noting the relationships showing moderate to strong statistical relationships between the marsh-integrated σ^0_{VV} and $\sigma^0_{VV}/\sigma^0_{VH}$ ratio and water level above-bankfull depth, we utilized this relationship to map the inundation over Kirkpatrick Marsh at different tidal stages with a statistically based change detection approach. This approach relied on computing a below-bankfull depth (BBD) temporal mean image and BBD temporal standard deviation (SD) image for σ^0_{VV} and the $\sigma^0_{VV}/\sigma^0_{VH}$ ratio on a per-pixel basis for low tide Sentinel-1A imagery covering the marsh between 2016–2017. The full 2016–2017 imagery timeseries (above- and below-bankfull depth) was then classified as inundated for any pixel 2 SD below the mean for $\sigma^0_{VV}/\sigma^0_{VH}$ ratio or 2 SD above the mean for σ^0_{VV} (Equations (5) and (6)), representing a >95% confidence interval separation from the BBD σ^0_{VV} or $\sigma^0_{VV}/\sigma^0_{VH}$ temporal mean. We also evaluated 1 SD and 3 SD thresholds for inundation classification. Using a per-pixel change detection classification allowed us to control for spatial and temporal variability across the marsh due to variability in vegetation structure, biomass, and non-tidal hydrology to detect changes linked to high tide inundation events.

$$\text{Inundated pixel} = \sigma^0_{VV} > (\mu_{\_vv\_bbd} + 2SD_{\_vv\_bbd}) \tag{5}$$

$$\text{Inundated pixel} = \sigma^0_{VV}/\sigma^0_{VH} < (\mu_{\_vvvh\_bbd} - 2SD_{\_vvvh\_bbd}) \tag{6}$$

where σ^{0*} is the backscatter for a given image pixel location in full timeseries, $\mu_{\_*\_bbd}$ is the backscatter temporal mean for below-bankfull depth image series at a given pixel location, and $2SD_{\_*\_bbd}$ is two backscatter standard deviations for below-bankfull depth image series at a given pixel location.

At the Blackwater NWR site, we performed an additional analysis on a sub-region of the wetlands complex. We evaluated 2015 NAIP imagery in combination with an October 2015 ground survey and 2013 NWI polygons to determine which sections of the study site were consistently classified as tidal marsh, estuarine forest, upland forest, and open water. This was done to produce accurate regions of interest (ROIs) that could be used for pixel extraction of high tide and low tide satellite image pairs. Since only one PALSAR high tide–low tide pair existed, we could not perform a timeseries analysis, but rather performed a backscatter pixel distribution comparison between high tide and low tide imagery. The PALSAR image pair was acquired from the same ascending orbital path 136. The low tide image was acquired on 2006-12-05 03:30:00 GMT with a Bishop's Head tidal stage of 0.084 meters. The high tide image was acquired on 2010-03-15 03:32:00 GMT with a Bishop's Head tidal stage of 0.805 meters. Sentinel-1A high tide–low tide pairs from similar tidal stages were selected for comparison to PALSAR. Sentinel-1A low tide imagery was acquired on 2016-10-30 23:06:00 GMT with a Bishop's Head tidal stage of 0.238 meters, and high tide imagery was acquired on 2016-10-06 23:06:00 GMT with a tidal stage of 0.885 meters.

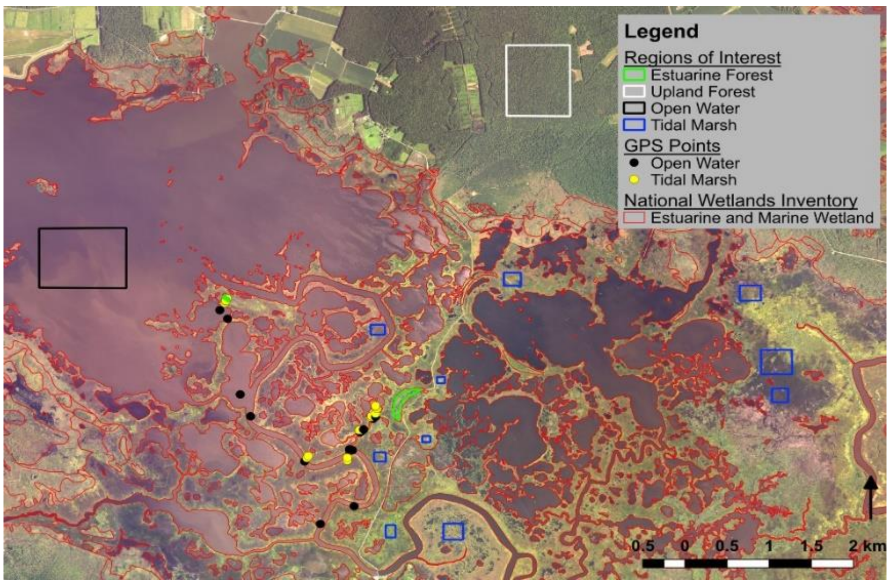

Figure 2.3. 2015 NAIP natural-color site map for a subsection of Blackwater NWR used for pixel extraction. NWI boundaries for the estuarine class are shown as red polygons. Pixel extraction regions of interest (ROIs) are noted in the legend. GPS points depict locations of the 15 October 2015 field survey.

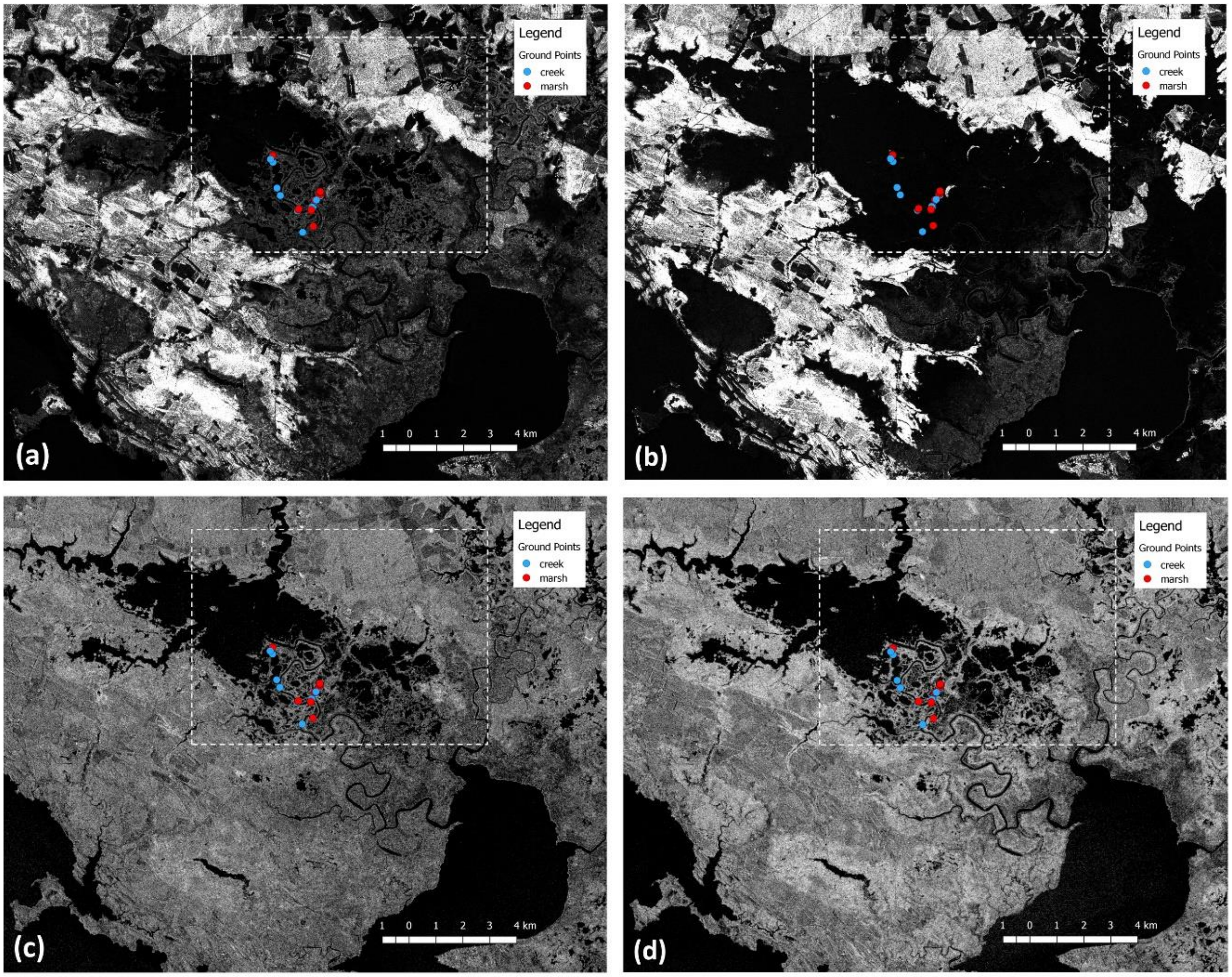

Figure 2.4. Blackwater October 2015 survey locations (points) and Figure 2.3 subregion (white box) overlaid on Synthetic Aperture Radar (SAR) imagery. Phased Array type L-band Synthetic Aperture Radar (PALSAR) L-band backscatter (σ^{0}_{HH}) images are shown in the upper panels with the left-side image (**a**) being low tide and the right-side image (**b**) being high tide. Sentinel-1A C-band backscatter (σ^{0}_{VV}) images are shown in the lower panels with the left-side being low tide (**c**) and the right-side image (**d**) being high tide. All SAR images are scaled between −5 dB and −20 dB.

2.3.6 Target Site Wetland Vegetation Mapping and Classification Overview

We selected Jug Bay as a wetland vegetation mapping site. We mapped specific wetland vegetation classes at Jug Bay described in the Swarth et al. survey and expanded the mapping effort into the surrounding Patuxent River region. We performed two classifications at Jug Bay, the first was a multitemporal SAR classification where the layer selection was informed by the vegetation timeseries analysis described in Methods Section 2.3.4 and the corresponding Results Section 2.4.2. A SAR-only classification was developed at Jug Bay to capitalize on pronounced differences in the SAR timeseries between vegetation classes. In an effort to capture these phenological differences in a classification, we created a 10-layer image stack with Sentinel-1A SAR temporal derivatives for both VV and VH polarizations including annual mean, annual standard deviation, summer mean (July–August), fall mean (September–October), and winter mean (November–December) layers.

We then classified this SAR-only image stack using a per-pixel supervised classifier based on the random forest algorithm (Figure 2.5). The random forest approach was also used in the regional scale classification described in Section 2.3.7. The random forest algorithm is a machine learning classification approach structured as an ensemble of decision trees that split predictor variable values at nodes and define a precited class based on votes across the decision trees (Breiman 2001). The random forest approach performs an internal validation and classification accuracy assessment using out-of-bag sampling (making cross-validation unnecessary), is robust to over-fitting, and has been demonstrated as effective in previous satellite image-based wetland classification efforts (Clewley et al. 2017; Breiman 2001). The random forest approach also provides a post-classification importance assessment of predictor variables (Breiman 2001). In the SAR-only random forest classification, we parameterized the classifier with three predictors sampled for splitting at each node in a given tree and used 200 trees, as performed in Clewely et al. (2017). We used the updated Swarth survey as training/validation data for the random forest classification at Jug Bay. Within the R environment, the “sp” package was used to define a stratified random sample of 500 points within each multipart polygon of a given Swarth survey vegetation class (and one open water class). These training/validation points were then used to extract associated predictor values from the SAR-only image stack, which was subsequently used to train and validate the random forest classification and classify the image stack using R's "randomForest" package.

To provide a comparison to the SAR-only Jug Bay wetland vegetation classification described above and to provide a second comparison to the regional scale wetlands classification described in the following Section 2.3.7, we performed a second per-pixel random forest classification of vegetation at Jug Bay using the same SAR-optical-DEM stack used in the regional scale classification. We parameterized this second random forest classifier with 200 trees and selected four predictors for splitting at each node. The comparison between the SAR-only and SAR-optical-DEM classifications were performed in order to evaluate the importance of layer selection in wetland mapping at Jug Bay. The second comparison of the SAR-optical-DEM classification at Jug Bay and the regional scale SAR-optical-DEM classification described in Section 2.3.6. was performed in order to provide a controlled evaluation of the satellite image importance in terms of characterizing vegetation within wetlands and separating wetlands from other land cover. The rationale for SAR-optical-DEM stack layer selection is described in the following section (2.3.7).

2.3.7 Regional Scale Wetland Mapping and SAR-Optical-DEM Layer Selection

Results from our satellite-based vegetation and inundation characterizations at target wetlands sites were used to guide the selection of input satellite imagery for the regional scale wetlands classification for the Chesapeake and Delaware Bays. The motivation was to carefully select image layers that provided information that could uniquely identify estuarine emergent wetlands (i.e., tidal marshes). For the regional scale classification, we also included additional wetland classes in the form of forested wetlands and palustrine emergent wetlands. Several common non-wetland classes were included in the regional scale classification in order to evaluate potential classification confusion with wetlands. These classes included: open water, urban, barren, grass, agriculture, shrub, and forest.

In order to perform the regional scale classification, we first created a training/validation dataset. The training/validation dataset of non-wetland classes were acquired directly from the 2011 National Land Cover Database (NLCD) (Jin et al. 2013). Training/validation dataset wetland classes were created by merging the National Wetlands Inventory (2013 update) and the 2011 NLCD to map the locations of emergent wetlands and forested wetlands. NWI wetlands polygons were assigned an integer value based on the wetland class, rasterized to a 10-m spatial resolution, then resampled and georegistered to the NLCD pixels at a matching 30-m spatial resolution. Only areas of overlap between the NWI and NLCD were used to define the wetland extent, culminating in a conservative estimate of wetland extent and reducing classification commission errors for wetland classes in the training of the random forest classifier. These data layers were merged together culminating in a final training raster.

GEE was used to process the optical imagery, SAR imagery, and topographic variables that served as inputs to the regional scale random forest classification. Within GEE, we stacked imagery by first selecting Sentinel-1A image paths. These paths were split between path 4 and path 106, which roughly divided the eastern and western sides of the Chesapeake Bay. The first layers we included in the GEE image stacks were the 2017 annual mean backscatter and standard deviation for Sentinel-1A σ^0_{VV} and σ^0_{VH} imagery. In this way, we could reduce the size of the Sentinel-1A image collection while preserving useful temporal information for the classifier and also temporally filter imagery to reduce SAR speckle noise (Quegan 2001). Sentinel-1A fall 2017 high tide–low tide difference layers for the σ^0_{VV}, σ^0_{VH}, and $\sigma^0_{VV}/\sigma^0_{VH}$ ratio images were also included in the GEE stacks since, as seen in Results Section 2.4.1.1 and 2.4.1.2, large differences between high and low tide imagery occurred during the fall season (September-November). Part of our evaluation process was to determine whether these tidal difference layers were particularly useful in classifying estuarine emergent marshes compared to all other classification layers. The 2017 PALSAR-2 annual mosaics with σ^0_{HH} and σ^0_{HV} images were also binned in the Sentinel-1A image paths within the GEE image stacks. Although our results demonstrated that PALSAR L-band imagery was highly effective for mapping inundation at the Blackwater NWR site (Results Section 2.4.1.1), multitemporal PALSAR-2 imagery coinciding with the 2016–2017 timeframe of our analysis was not available. However, the PALSAR results from Blackwater NWR also demonstrated that single date L-band imagery was important to include in the regional scale classification (namely PALSAR-2 imagery) because of its capability in the biomass-based separation of forested and emergent wetlands.

We computed vegetation indices (NDVI, TVI) and water indices (mNDWI) with cloud-masked Landsat 8 surface reflectance imagery for summer 2017 (June–August), fall 2017 (September–October), and winter 2017 (November–December). Several of these ranges contained multiple overlapping images, which we reduced by computing the temporal median index value. These spectral indices were acquired from various Landsat paths and were binned to the separate Sentinel-1A image paths in the GEE image stacks. Landsat 8 imagery was selected over Sentinel-2A imagery because it was available in GEE as a mature surface reflectance product (Vermote et al. 2016; USGS 2018). The Landsat 8 imagery also tended to be less cloudy at the regional scale than Sentinel-2A imagery. Like the temporal reductions of the Sentinel-1A imagery, the inclusion of Landsat 8 vegetation and water indices (over multispectral bands) was done in an effort to reduce the total number of input variables (layers) in the GEE image stacks. Topographic variables were included in the GEE image stacks in the form of elevation and slope derived from the SRTM DEM. The elevation and slope layers were also binned into the Sentinel-1A image paths. Topographic variables were included in the GEE image stacks because they have been demonstrated as being more important than optical or SAR imagery in supervised classifications by previous wetlands mapping studies (Clewley et al. 2017; Knight et al. 2013). The final GEE image stacks had nine SAR input layers, nine optical input layers, and two topographic input layers. The layers in the GEE image stacks varied in spatial resolution, with Sentinel-1A having a 20 × 22-m spatial resolution (resampled to 10 × 10-m pixel resolution in GEE), PALSAR-2 annual mosaics having a 25 × 25-m resolution, and SRTM DEM and Landsat 8 resolutions being 30 × 30 m. We resampled the GEE image stacks to the coarsest common resolution of 30 × 30 m. The GEE image stacks were exported to a local desktop. These SAR-optical-DEM image stacks for Sentinel-1A path 4 and path 106 were mosaicked using R's "Raster" package. The rationale for layer inclusion in the SAR-optical-DEM stack is described in Table 2.

The final SAR-optical-DEM image stack served as predictors for both the regional scale classification and the Jug Bay SAR-optical-DEM classification described in Section 2.3.6. For the regional scale classification, a random forest classification was performed by defining training data using QGIS to select random points within the training raster. This was done by performing a stratified random point sampling with 10,000 points per training class, and then performing a second random sample with 100,000 total points. These samples were then combined to produce a training dataset that represented a compromise between including underrepresented classes while also accounting for class prevalence. To assess the degree to which parameter tuning impacted the accuracy of the random forest classifier, we performed a series of regional scale classifications by adjusting the number of trees in the classifier by the following values: 10, 25, 50, 75, 100, 150, 200, 300, 400, and 500.

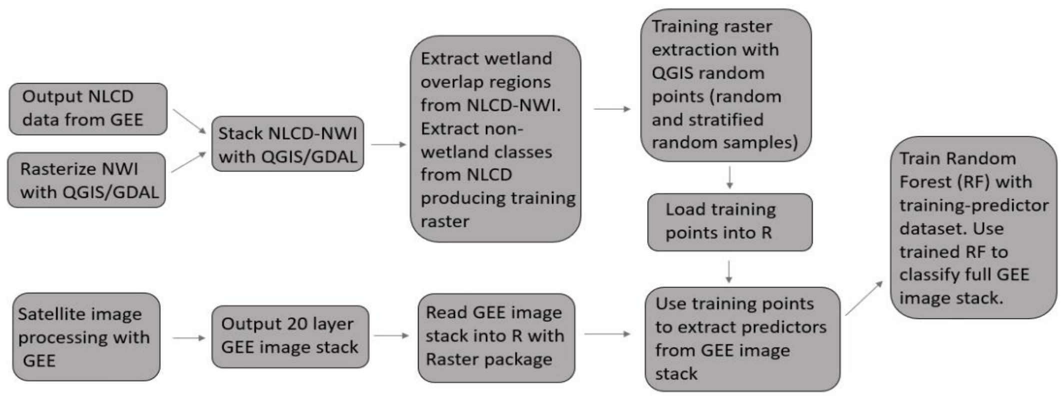

Figure 2.5. Schematic of regional scale random forest classification process in which the National Land Cover Database (NLCD) and the National Wetlands Inventory (NWI) are merged to produce a classification training raster and Quantum GIS (QGIS) and its associated Geospatial Data Abstraction Library (GDAL) are used to produce training polygons used to classify Google Earth Engine (GEE) image stacks in the R environment with R's Random Forest package.

Table 2.2. Description of input layers to regional scale random forest classification.

Layer in GEE Stack	Description	Rationale	Example
vv_mean	Sentinel-1 VV 2017 annual mean	Decreases SAR speckle noise while preserving resolution,	Jug Bay
vh_mean	Sentinel-1 VH 2017 annual mean	captures central backscatter tendency	
vv_sd	Sentinel-1 VV 2017 annual standard deviation	Provides separability between high annual temporal variability	Jug Bay
vh_sd	Sentinel-1 VH 2017 annual standard deviation	emergent estuarine wetlands and other landcover	
vv_tidal_diff	Sentinel-1 VV tidal difference (Fall 2017)	Captures tidal variability in emergent estuarine systems presumably absent from other landcover	Blackwater, Kirkpatrick
vh_tidal_diff	Sentinel-1 VH tidal difference (Fall 2017)		
vvvh_tidal_diff	Sentinel-1 VV/VH tidal difference (Fall 2017)		
hh	PALSAR-2 HH 2017 annual mosaic	Provides biomass-based backscatter separability between	Blackwater
hv	PALSAR-2 HV 2017 annual mosaic	between emergent and forested wetlands	
summer_tvi	Landsat 8 TVI (Summer 2017)	Captures wetland vegetation phenology (three seasons help	Kirkpatrick
fall_tvi	Landsat 8 TVI (Fall 2017)	separate emergent wetlands from crops); more biomass	
winter_tvi	Landsat 8 TVI (Winter 2017)	separability than NDVI	
summer_ndvi	Landsat 8 NDVI (Summer 2017)	Captures wetland vegetation phenology (three seasons help separate emergent wetlands from crops)	Kirkpatrick
fall_ndvi	Landsat 8 NDVI (Fall 2017)		
winter_ndvi	Landsat 8 NDVI (Winter 2017)		
summer_mndwi	Landsat 8 mNDWI (Summer 2017)	Captures fractional surface water in sparsely vegetated wetlands	Blackwater
fall_mndwi	Landsat 8 mNDWI (Fall 2017)		
winter_mndwi	Landsat 8 mNDWI (Winter 2017)		
elevation	SRTM DEM	Estuarine emergent wetlands close to sea-level	Sites low elevation
slope	SRTM DEM Gradient		

2.4. Results

2.4.1. Satellite-Based Marsh Inundation Characterization and Mapping

2.4.1.1. Blackwater NWR Inundation

We assessed the linear and non-linear empirical relationships between the tidal stage and SAR backscatter/optical water index values for several different wetland types (shown in Table 3). The Sentinel-1A $\sigma^0_{VV}/\sigma^0_{VH}$ ratio exhibited the highest correlation with the tidal stage compared to other imagery at the Blackwater NWR site for the dominant E2EM1P wetland class for both ordinary least squares and polynomial fits. In general, SAR-tidal stage correlation was greater than that of optical water indices. The mNDWI exhibited a moderate degree of correlation with the tidal stage for E2EM1P wetlands, which was significantly higher than the correlation for NDWI. Figure 2.6 depicts the ordinary least squares (OLS) fit and second order polynomial fit (Poly) relationships between the tidal stage and $\sigma^0_{VV}/\sigma^0_{VH}$ ratio for both major estuarine emergent wetland classes. The polynomial better modeled the data than the OLS, but neither was ideal. However, the increasing downward slope of the polynomial fit in the range of 0.4 to 0.6 meters did indicate the presence of a change point relationship, where backscatter only exhibited sensitivity to tidal stage above a certain level. Even though the polynomial behavior suggested the existence of a change point, without having a well-constrained estimate of water level bank full depth, we could not perform a piecewise regression analysis. However, we demonstrate how such an analysis was used in Section 2.4.1.2 for Kirkpatrick Marsh.

Table 2.3. Pearson's correlation (R-value) for Sentinel-1A (S1) and Sentinel-2A (S2) values and Bishop's Head tidal stage for the ordinary least squares (OLS) fit and polynomial (Poly) fit.

NWI Class	S1-VH OLS	S1-VH Poly	S1-VV OLS	S1-VV Poly	S1-VV/VH OLS	S1-VV/VH Poly	S2-NDWI OLS	S2-NDWI Poly	S2-mNDWI OLS	S2-mNDWI Poly	Total Area (km^2)
E2EM1N	−0.638	0.757	0.374	0.575	−0.705	0.889	0.314	0.378	0.460	0.468	12.01
E2EM1P	−0.689	0.761	0.581	0.666	−0.765	0.856	0.352	0.393	0.471	0.515	284.40
E2EM1P6	−0.450	0.541	0.368	0.378	−0.530	0.567	0.192	0.283	0.001	0.235	3.70
E2EM1Pd	−0.646	0.725	0.457	0.539	−0.684	0.772	0.407	0.412	0.560	0.669	15.38
E2SS4P	−0.189	0.422	0.395	0.403	−0.456	0.457	0.047	0.303	−0.065	0.080	13.92
E2FO4P	−0.089	0.357	0.360	0.381	−0.401	0.401	0.006	0.236	0.108	0.142	24.63

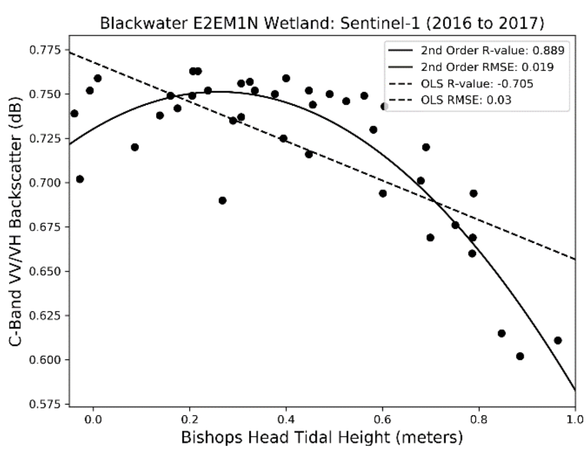

(**a**)

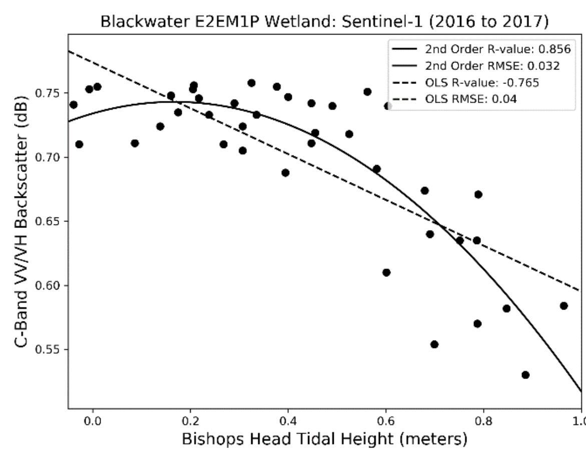

(**b**)

Figure 2.6. Relationships between the Sentinel-1A $\sigma^0_{VV}/\sigma^0_{VH}$ (VV/VH backscatter) ratio and tidal stage for dominant NWI wetland types in Blackwater NWR; both E2EM1N (estuarine emergent, persistent, regularly flooded) (**a**) and E2EM1P (estuarine emergent, persistent, irregularly flooded) (**b**) show similar relationships with the tidal stage.

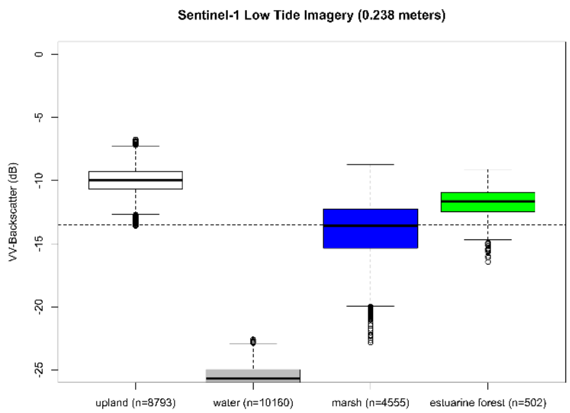

(a-1)

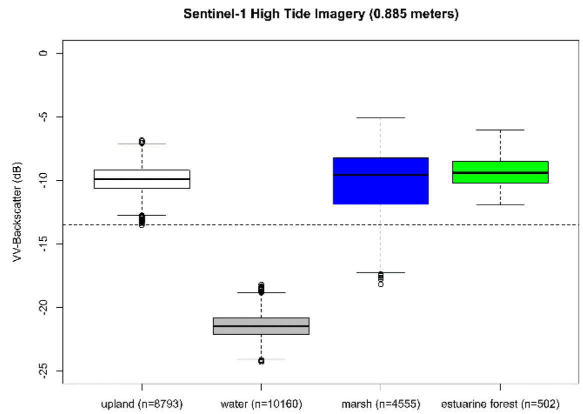

(a-2)

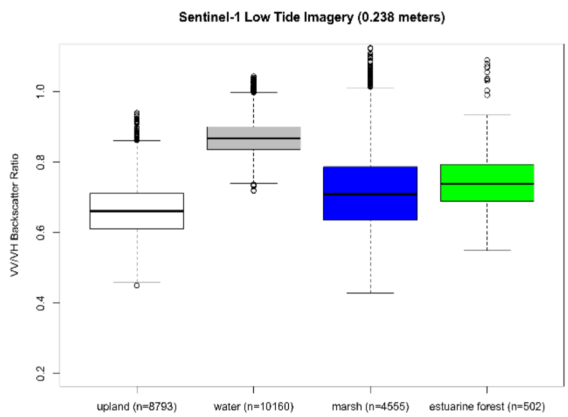

(b-1)

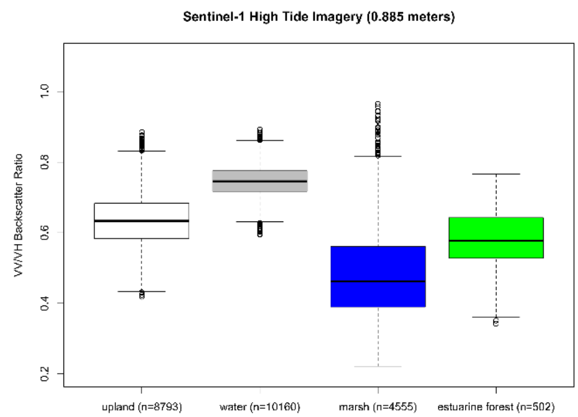

(b-2)

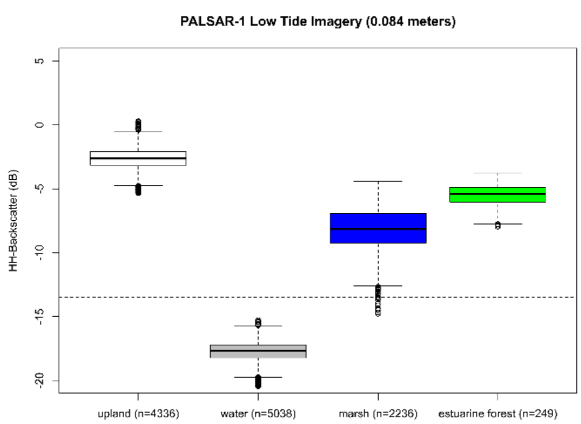

(c-1)

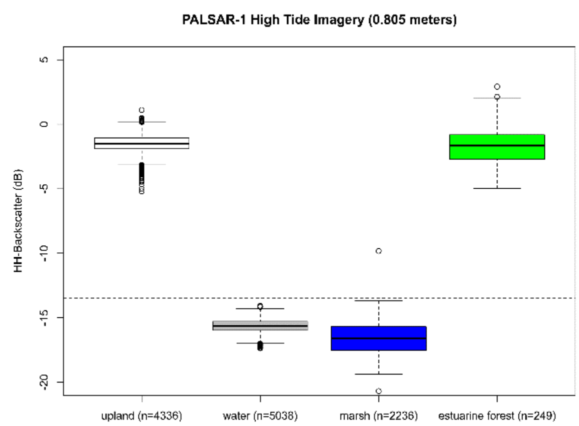

(c-2)

Figure 2.7. Comparison of the Sentinel-1A $\sigma^0_{VV}/\sigma^0_{VH}$ ratio (VV/VH backscatter ratio), Sentinel-1A σ^0_{VV} (VV backscatter), and PALSAR σ^0_{HH} (HH backscatter) for high tide and low tide imagery. Although the Sentinel-1A σ^0_{VV} (**a**) and $\sigma^0_{VV}/\sigma^0_{VH}$ ratio (**b**) effectively capture variability from tidal influence, they do not provide the clearly defined separability of PALSAR σ^0_{HH} (**c**) for threshold-based inundation classification of tidal marshes in Blackwater NWR.

Figure 2.7 illustrates that Sentinel-1A σ^0_{VV} and $\sigma^0_{VV}/\sigma^0_{VH}$ ratio distributions exhibited substantial change between high and low tide. The PALSAR high tide–low tide pair distributions for the σ^0_{HH} imagery exhibited even greater change and sufficient separability for an absolute threshold of −13.5 dB to be applied to the high tide and low tide imagery to classify tidal marsh inundation. The thresholded images were differenced to derive a marsh intertidal zone, as shown in Figure 2.8.

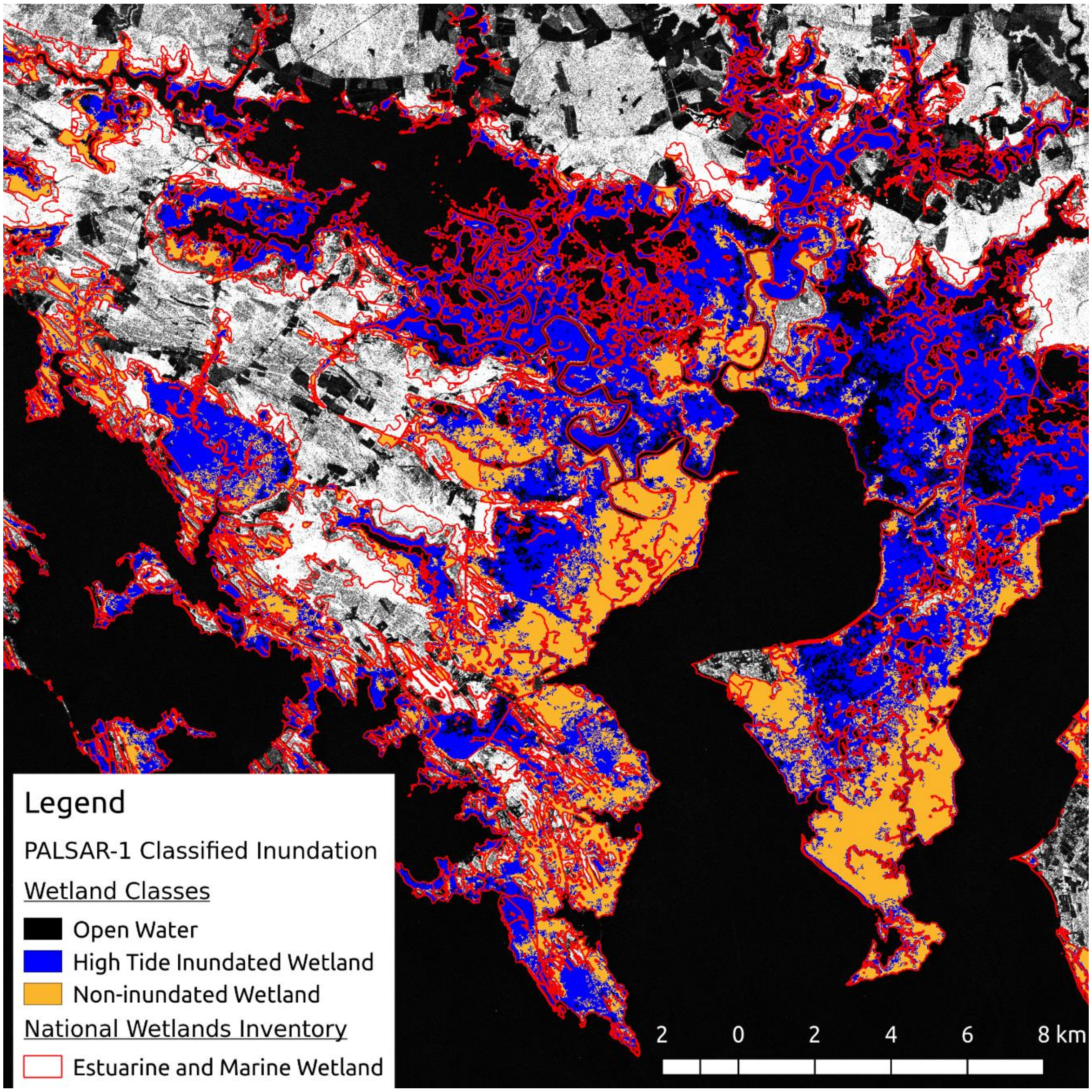

Figure 2.8. Blackwater NWR PALSAR high tide–low tide classified inundation extents based on absolute backscatter thresholds from PALSAR image pair differencing. Open water was classified as below −13.5 dB for both low tide and high tide imagery. The marsh intertidal zone was classified as below −13.5 dB at high tide and above −13.5 dB at low tide. This threshold was derived in Figure 2.7. Only NWI estuarine emergent wetlands and marine classes were classified as tidally inundated, non-tidally inundated, or open water (red polygons on map also include estuarine forest, which was not classified). Like estuarine forests, upland areas are also shown as grayscale SAR imagery from the high tide image.

2.4.1.2 Kirkpatrick Marsh Inundation

Second order polynomial and ordinary least squares relationships between satellite imagery and tidal stage were evaluated for Kirkpatrick Marsh as they were for Blackwater NWR with the exception that ordinary least squares was split into a BBD regression and an ABD regression, as determined by the Nelson et al. study that better constrained the hydrology of Kirkpatrick Marsh relative to Blackwater NWR. Figure 2.9 depicts similar relationships to Blackwater NWR where the start of the increasing downward slope of the polynomial existed in close proximity to the BBD–ABD split and tracked the two BBD and ABD regressions fairly well, demonstrating the potential utility of the polynomial for modeling backscatter over the full tidal range when known break points for a marsh bankfull depth cannot be obtained. These findings, shown in Table 4 and Figure 2.9, served as the impetus for use of the change detection-based inundation classification with the Sentinel-1A $\sigma^0_{VV}/\sigma^0_{VH}$ ratio shown in Figure 2.10. Figure 2.10 shows the Kirkpatrick Marsh inundated area for the four 2016–2017 Sentinel-1A images acquired at the four highest tidal stages using 1 SD, 2 SD, and 3 SD as change detection thresholds. Also shown in Figure 2.10 is an open-water estuary ROI demonstrating that the open water $\sigma^0_{VV}/\sigma^0_{VH}$ ratio did not change with the water level stage. Vachon and Wolfe (2011) demonstrated that C-band backscatter increases for all polarizations when open water becomes roughened by wind and wave activity. σ^0_{VV} was noted as being most sensitive to water surface roughness from wind. Wind and wave activity can influence the water level stage, especially when combined with peak tidal phases. However, our results demonstrate that the variability in the $\sigma^0_{VV}/\sigma^0_{VH}$ ratio was likely caused by scattering variability from marsh vegetation–inundation interaction, rather than roughness-based scattering changes to the water's surface on the inundated marsh, as evidenced by a lack of change in the estuary $\sigma^0_{VV}/\sigma^0_{VH}$ ratio. This scattering change on the marsh was likely due to increases in double-bounce scattering in σ^0_{VV} and decreases in volume scattering in σ^0_{VH} as the marsh inundated.

Table 2.4. Pearson's correlation (R-value) for Sentinel-1A and Sentinel-2A values for the full tidal range (polynomial only) and above-bankfull depth (ABD) for Kirkpatrick Marsh tidal creek water level.

Imagery Type	Full Poly	OLS (ABD)	Poly (ABD)	n (ABD)
S1-VH	0.326	−0.478	0.572	13
S1-VV	0.790	0.819	0.859	13
S1-VV/VH	0.897	−0.868	0.917	13
S2-mNDWI	0.280	0.335	--	4
S2-NDWI	0.473	−0.514	--	4

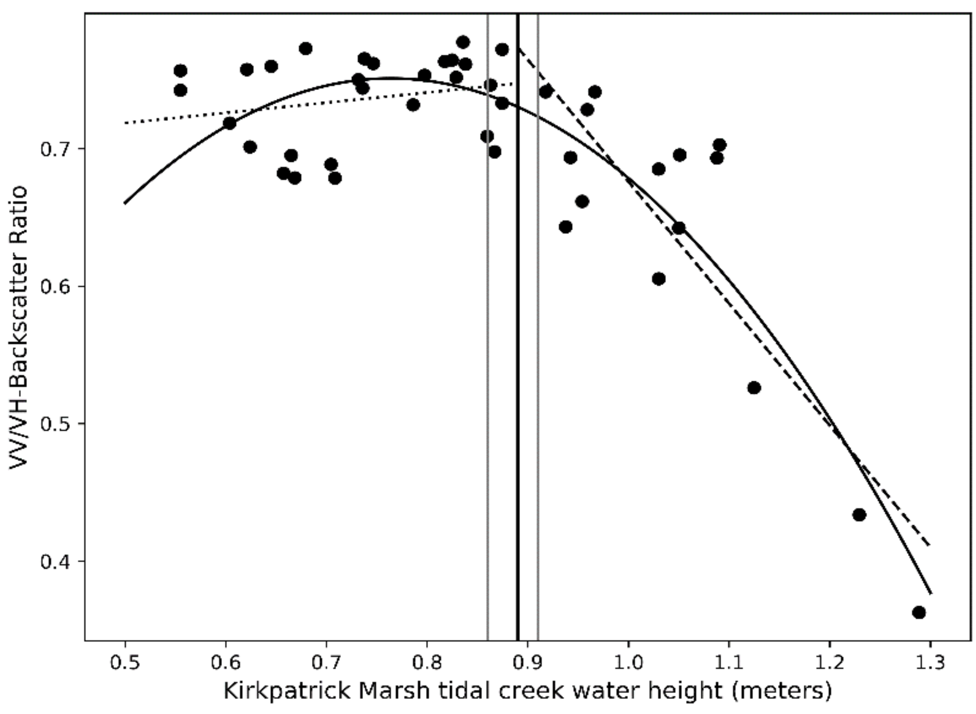

Figure 2.9. Kirkpatrick Marsh Sentinel-1A $\sigma^0_{VV}/\sigma^0_{VH}$ ratio with a full-range polynomial (solid black line), BBD regression (dotted line), ABD regression (dashed line), and Nelson et al. bankfull depth as the vertical black line with grey confidence intervals (95%).

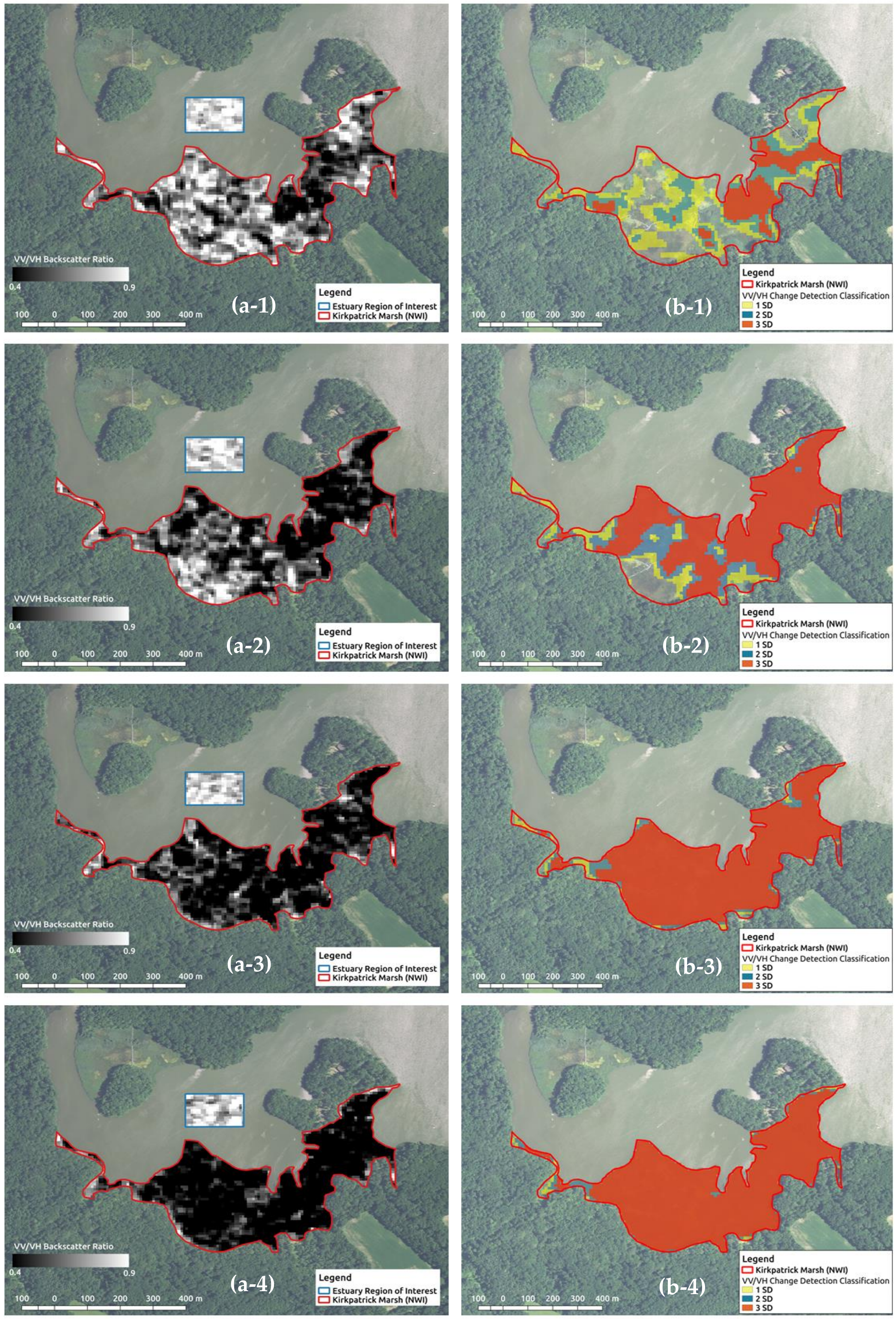

Figure 2.10. Change detection-based inundation products from the Sentinel-1A $\sigma^0_{VV}/\sigma^0_{VH}$ ratio for high tide imagery over Kirkpatrick Marsh: (**a**) $\sigma^0_{VV}/\sigma^0_{VH}$ ratio, and (**b**) the corresponding classified inundation. Tidal stage increases moving from the top of the figure to the bottom (1–4)

2.4.2 Satellite-Based Marsh Vegetation Characterization

2.4.2.1. Kirkpatrick Marsh Vegetation

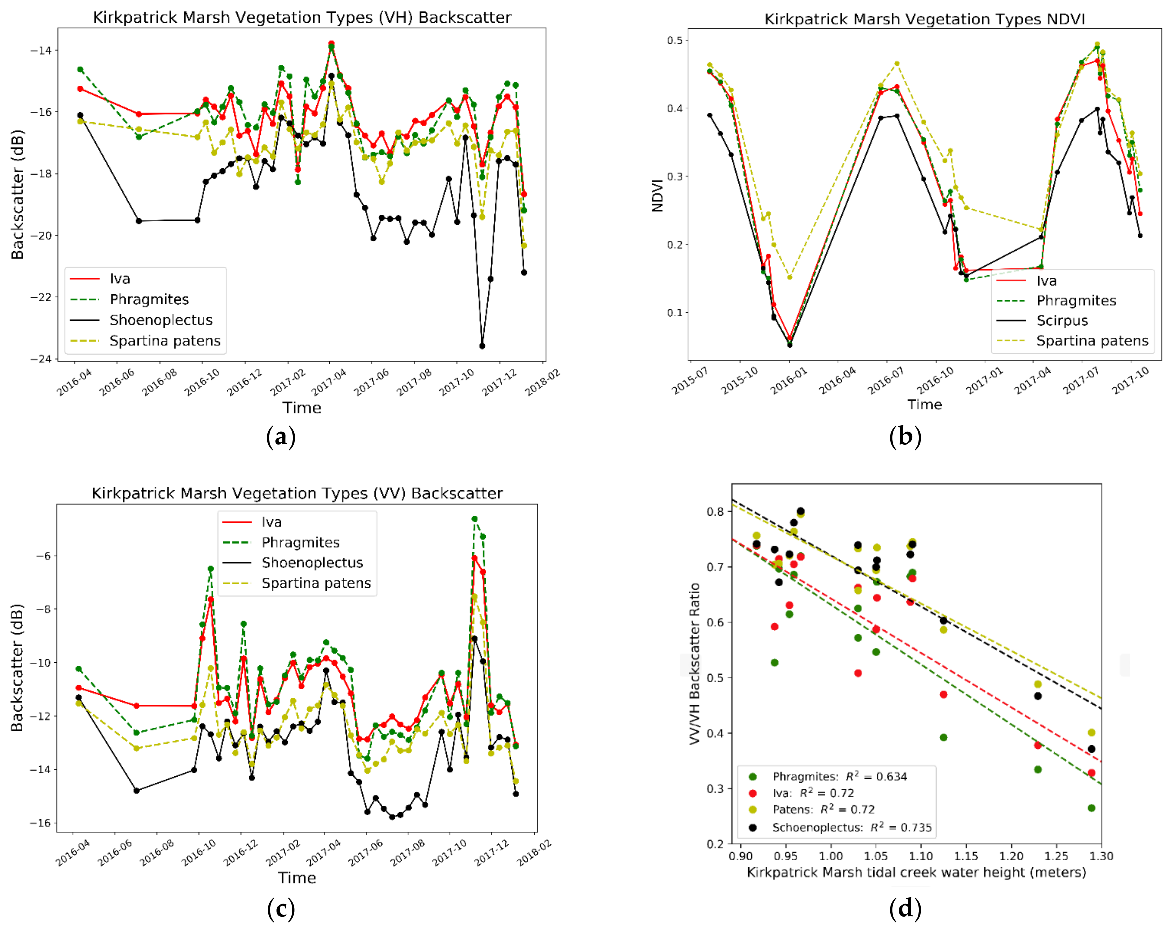

Figure 2.11. Timeseries plots for the spatial mean Sentinel-1A σ^0_{VH}, Sentinel-2A NDVI, and Sentinel-1A σ^0_{VV} for dominant vegetation species over Kirkpatrick Marsh (**a**,**b**,**c**, respectively). (**d**) The $\sigma^0_{VV}/\sigma^0_{VH}$ ratio for the above-bankfull depth for the dominant vegetation demonstrating a similar response to tidal inundation between all four species, albeit with a biomass offset.

The four dominant species of vegetation at Kirkpatrick Marsh exhibited similar temporal directional tendencies for Sentinel-1A σ^0_{VV} and σ^0_{VH} and Sentinel-2A NDVI. NDVI captured a predictable greenness phenology for two full growing seasons. *Scirpus americanus* (also called *Schoenoplectus*) vegetation exhibited a lower NDVI than the other species, likely owed to its more vertical structure and more open canopy (Langley and Megonigal 2012). *Spartina patens*, which is the most horizontally oriented vegetation and forms dense mats of many small stems and leaves, had a consistently higher NDVI than even *Phragmites australis* and *Iva frutescens*, despite having a lower biomass. The response of TVI (not shown in Figure 2.11) was very similar to the NDVI, despite findings of TVI being less prone to biomass-based saturation (Schmitt et al. 2013). This indicates that the optical vegetation indices were responsive to the upper canopy structure, especially canopy closure, as well as greenness, but provided little capability in separating vegetation based on biomass.

Sentinel-1A σ^0_{VV} and σ^0_{VH} imagery captured biomass-based offsets between species, with *Phragmites australis* and *Iva frutescens* exhibiting an offset backscatter from *Scirpus* and *Spartina patens*, indicating stability in biomass separation between the species. Sentinel-1A σ^0_{VH} showed lower backscatter for *Scirpus* compared to the other vegetation during the growing season. Both Sentinel-1A σ^0_{VV} and σ^0_{VH} tended to decrease during the growing season for all four species. Several times during the fall seasons in 2016 and 2017, σ^0_{VV} increased greatly and σ^0_{VH} decreased greatly. Exploring the divergence between σ^0_{VV} and σ^0_{VH} with the $\sigma^0_{VV}/\sigma^0_{VH}$ ratio showed this was likely the result of tidal influence as the $\sigma^0_{VV}/\sigma^0_{VH}$ ratio for the four dominant species all showed strong inverse relationships when the $\sigma^0_{VV}/\sigma^0_{VH}$ ratio was regressed against the water level above bankfull depth (Figure 2.11).

2.4.2.2. Jug Bay Wetlands Vegetation

Different classes of vegetation at Jug Bay had pronounced differences in vegetation structural phenology. The two most common classes of vegetation, *Typha spp.* and *Nuphar lutea*, exhibited very different Sentinel-1A σ^0_{VV} signatures (Figure 2.12, left panel). These backscatter changes were consistent with differences in the seasonal structural changes that occurred between persistent and non-persistent vegetation (Figure 2.12, right panel). Persistent *Typha spp.* exhibited backscatter increases in fall that were similar to the persistent species at Kirkpatrick Marsh. Correlation of the 2016–2017 Sentinel-1A σ^0_{VV} timeseries between *Typha spp.* from Jug Bay and Kirkpatrick Marsh *Scirpus americanus*, *Spartina patens*, *Iva frutescens*, and *Phragmites australis* produced R-values of: 0.86, 0.76, 0.80, and 0.85, respectively. Indicating that Kirkpatrick Marsh and Jug Bay likely share a similar tidal hydrology given that most of the variability in Sentinel-1A σ^0_{VV} in tidal marshes with persistent vegetation was explained by variability in tidal stage. The similar temporal variability in backscatter between persistent vegetation across study sites is contrasted by the temporal backscatter variability differences between persistent and non-persistent species at Jug Bay. These differences are captured in the 2017 σ^0_{VV} annual standard deviation map shown in the central panel of Figure 2.13. Note that the Sentinel-1A backscatter (σ^0_{VV}) annual standard deviation effectively depicted the locations of non-persistent *Nuphar lutea.* These findings were the impetus for inclusion of VV-polarized backscatter (σ^0_{VV}) annual standard deviation as one of the several input layers included in the SAR-only and SAR-optical-DEM Jug Bay classifications.

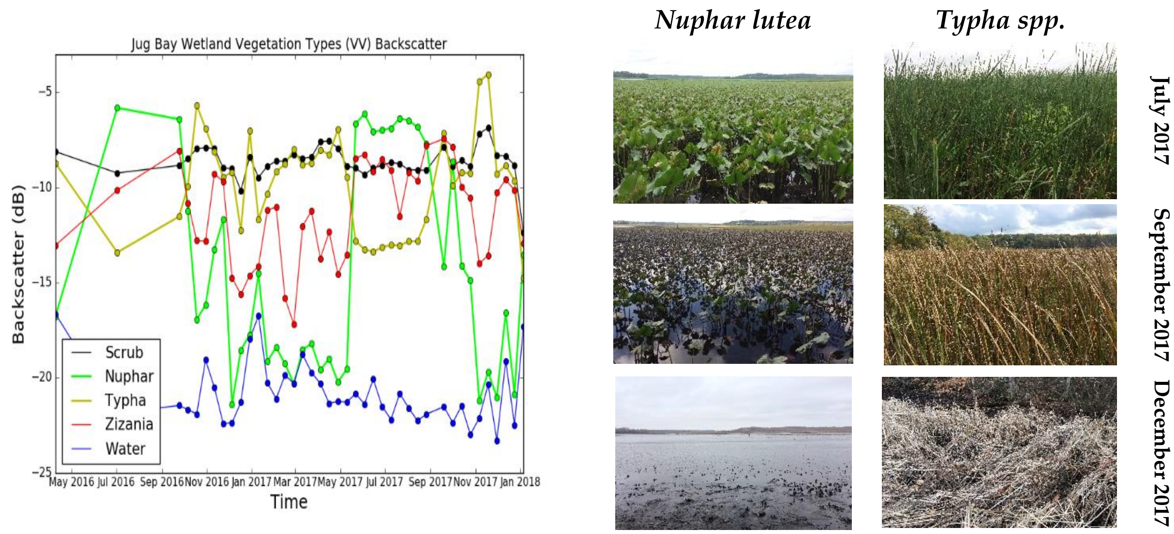

Figure 2.12. Timeseries plots for spatial mean Sentinel-1A σ^0_{VV} according to Jug Bay vegetation type (left panel). Right panel shows site photos of general summer to winter phenological changes in non-persistent *Nuphar lutea* and persistent *Typha spp.*, which were effectively captured by the SAR timeseries.

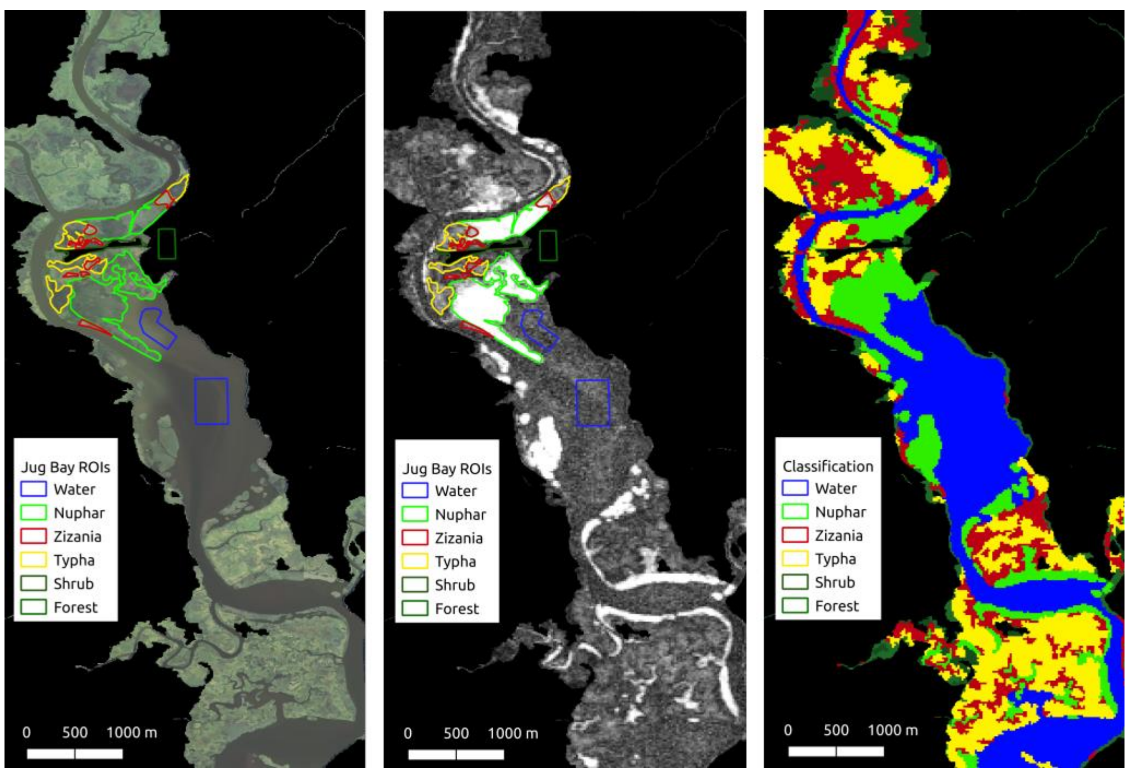

(a) **(b)** **(c)**

Figure 2.13. Jug Bay random forest classification. ROIs from the Swarth survey overlaid on the 2015 NAIP imagery and Sentinel-1A σ^0_{VV} 2017 annual standard deviation imagery (**a** and **b**, respectively). (**c**) SAR-only random forest classification. Note that Sentinel-1A σ^0_{VV} annual standard very effectively highlighted locations of non-persistent *Nuphar lutea*, which was not clearly distinguished in the natural color NAIP imagery.

Table 2.5. Jug Bay random forest classification confusion matrix for SAR-only classification. Diagonal matches between observed (Reference) and predicted (Classification) classes are bolded.

		Classification						
		Water	Nuphar	Zizania	Typha	Shrub	Forest	Producer's Accuracy (%)
Reference	Water	**495**	0	0	0	0	0	100.00
	Nuphar	0	**464**	31	2	0	0	93.36
	Zizania	0	17	**469**	14	5	0	92.87
	Typha	0	1	14	**481**	9	2	94.87
	Shrub	0	1	6	10	**471**	5	95.54
	Forest	0	0	0	0	3	**480**	99.38
	User's Accuracy (%)	100.00	96.07	90.19	94.87	96.52	98.56	
								Overall Accuracy %
								95.97

Table 2.6. Jug Bay random forest classification confusion matrix for SAR-optical-DEM classification.

		Classification						
		Water	Nuphar	Zizania	Typha	Shrub	Forest	Producer's Accuracy (%)
Reference	Water	**500**	0	0	0	0	0	100.00
	Nuphar	1	**481**	19	6	0	1	94.69
	Zizania	0	8	**477**	5	3	0	96.75
	Typha	0	1	10	**483**	10	0	95.83
	Shrub	0	0	0	9	**491**	0	98.20
	Forest	0	0	0	0	0	**496**	100.00
	User's Accuracy (%)	99.80	98.16	94.27	96.02	97.42	99.80	
								Overall Accuracy %
								97.57

Table 2.7. Jug Bay random forest layer importance assessment for SAR-only classification. Columns 2–7 represent the decrease in accuracy predicting a given class when removing the input layer (predictor) in column 1. For example, the removal of the VV_mean layer (σ^0_{VV} annual mean) decreased the accuracy by 0.2193 when classifying a given pixel as water. Thus, higher values of accuracy decrease represent layer importance. Columns 8–9 represent the decrease in accuracy for all classes and decrease in the Gini coefficient. Top three layer classification improvements for each vegetation/landcover class prediction (columns) are bolded.

Layer Type	Water	Nuphar	Zizania	Typha	Shrub	Forest	MeanDecreaseAccuracy	MeanDecreaseGini
VV_mean	**0.2193**	0.0763	0.0942	0.0789	**0.3221**	0.1573	0.1573	216.4184
VH_mean	0.1671	0.0706	0.1209	0.1133	0.2701	0.2326	0.1618	258.9103
VV_SD	0.0019	**0.2059**	0.1683	**0.1864**	**0.3489**	**0.4963**	**0.2331**	**319.5366**
VH_SD	0.0004	0.0905	**0.2567**	0.0511	0.2171	**0.3411**	0.1588	200.7394
VV_summer	**0.2306**	0.0858	0.1430	0.1562	0.1402	0.1806	0.1559	273.6167
VH_summer	**0.1981**	0.0437	0.0859	0.1374	0.1381	0.2040	0.1340	226.1407
VV_fall	0.0406	0.0028	0.0693	0.0252	0.1007	0.1058	0.0571	99.9647
VH_fall	0.0112	0.0357	0.1531	0.0456	**0.2795**	0.1928	0.1190	194.1971
VV_winter	0.0223	**0.2752**	**0.2119**	**0.1622**	0.2436	0.2148	**0.1884**	**316.4512**
VH_winter	0.0191	**0.2163**	**0.2981**	**0.1751**	0.2679	**0.3360**	**0.2186**	**365.0655**

Table 2.8. Jug Bay random forest layer importance assessment for SAR-optical-DEM classification.

Layer Type	Water	Nuphar	Zizania	Typha	Shrub	Forest	MeanDecreaseAccuracy	MeanDecreaseGini
VV_mean	**0.2189**	0.1184	0.1087	0.1070	0.1862	0.0334	**0.1288**	**219.2148**
VH_mean	**0.2468**	**0.1930**	**0.1906**	**0.1637**	**0.3262**	0.0269	**0.1910**	**328.2239**
VV_SD	0.0150	**0.2690**	0.0967	**0.1428**	**0.2534**	0.0179	**0.1331**	**236.3179**
VH_SD	0.0028	**0.1636**	**0.1873**	0.1304	**0.2292**	0.0158	0.1215	189.5208
VV_tidal_diff	0.0002	0.0044	0.1148	**0.1492**	0.0166	0.0003	0.0475	79.6682
VH_tidal_diff	0.0004	0.0031	**0.1957**	0.0228	0.0181	0.0121	0.0415	71.2645
VVVH_tidal_diff	0.0002	0.0060	0.0429	0.0849	0.0123	0.0010	0.0245	44.7473
HH	0.0213	0.0034	0.0276	0.0101	0.0206	0.0007	0.0138	15.6724
HV	0.0019	0.0033	0.0378	0.0130	0.0204	0.0005	0.0127	16.6604
summer_tvi	0.0581	0.0417	0.1470	0.0880	0.0595	0.0256	0.0698	111.7885
summer_ndvi	0.0685	0.0502	0.1196	0.0666	0.1002	**0.2178**	0.1034	182.2881
summer_mndwi	**0.2041**	0.0604	0.1324	0.0817	0.0573	0.0613	0.0991	180.2152
fall_tvi	0.0140	0.0861	0.1052	0.0406	0.0556	0.0324	0.0558	85.8827
fall_ndvi	0.0379	0.0601	0.1414	0.0978	0.1428	**0.2085**	0.1146	192.8352
fall_mndwi	0.1262	0.1097	0.1422	0.1020	0.1038	0.0411	0.1041	184.5659
winter_tvi	0.0065	0.0325	0.0798	0.0477	0.0254	0.1041	0.0492	70.8000
winter_ndvi	0.0054	0.0212	0.0871	0.0444	0.0320	0.0529	0.0404	67.6125
winter_mndwi	0.0738	0.0049	0.0959	0.0436	0.0186	0.0337	0.0448	40.8471
DEM	0.0213	0.0386	0.0593	0.0559	0.0533	**0.2899**	0.0862	142.0544
DEM_grad	0.0014	0.0029	0.0199	0.0121	0.0175	0.0001	0.0090	13.8682

The random forest classification for Jug Bay achieved accurate results using 10 timeseries Sentinel-1A input layers as predictors (>95%). The 20 input layers from the SAR-optical-DEM stack achieved slightly higher accuracies (>97%). In the SAR-optical-DEM stack, SAR layers were the most important predictor layers for increasing classification accuracy. In the SAR-only classification, the $\sigma^0{}_{VV}$ annual standard deviation and $\sigma^0{}_{VV}$ and $\sigma^0{}_{VH}$ winter mean (November–December) imagery were the most useful predictors. All vegetation classes within this wetland system and open water were classified with accuracies greater than 90% for both user's accuracy (commission error) and producer's accuracy (omission error) (Tables 5 and 6). Tables 7 and 8 illustrated that each of the layers were uniquely useful for classifying individual classes in both the SAR-only and SAR-optical-DEM classifications. For both *Nuphar lutea* and

Typha spp., the σ^0_{VV} standard deviation and winter σ^0_{VV} and σ^0_{VH} imagery were the most useful predictors in the SAR-only classification. In the SAR-optical-DEM classifications, the σ^0_{VV} standard deviation was also a useful predictor for *Nuphar lutea* and *Typha spp.* The σ^0_{VV} tidal difference layer was uniquely important for the classification of *Typha spp.*

2.4.3 Regional Scale Wetlands Mapping

Informed by the findings from the vegetation and inundation characterizations at the target wetlands study sites, we mapped the wetlands of the Chesapeake Bay and Delaware Bay regions. This regional classification is shown in Figure 2.14. Open water was mapped with the greatest accuracy (user's accuracy and producer's accuracy >96%). Emergent estuarine wetlands were mapped with the next highest accuracy with user's and producer's accuracies of 83% and 88%, respectively. Emergent palustrine wetlands were mapped with a producer's accuracy of 65% and a user's accuracy of 79%. All other classes were mapped with lower accuracies (Table 9). We found that emergent estuarine wetlands and emergent palustrine wetlands were most often confused with one another in terms of classification accuracy and were often adjacent to each other in regions generally characterized as tidal freshwater wetlands by previous studies. When the palustrine and estuarine emergent classes were lumped into a single emergent class, classification accuracy improved to a user's accuracy greater than 86% and a producer's accuracy of greater than 90%. The overall accuracy of the regional scale classification was relatively low at 67%; however, much of this diminished accuracy was due to a confusion between upland classes, rather than inaccuracy in wetland classification which was the focus of this study.

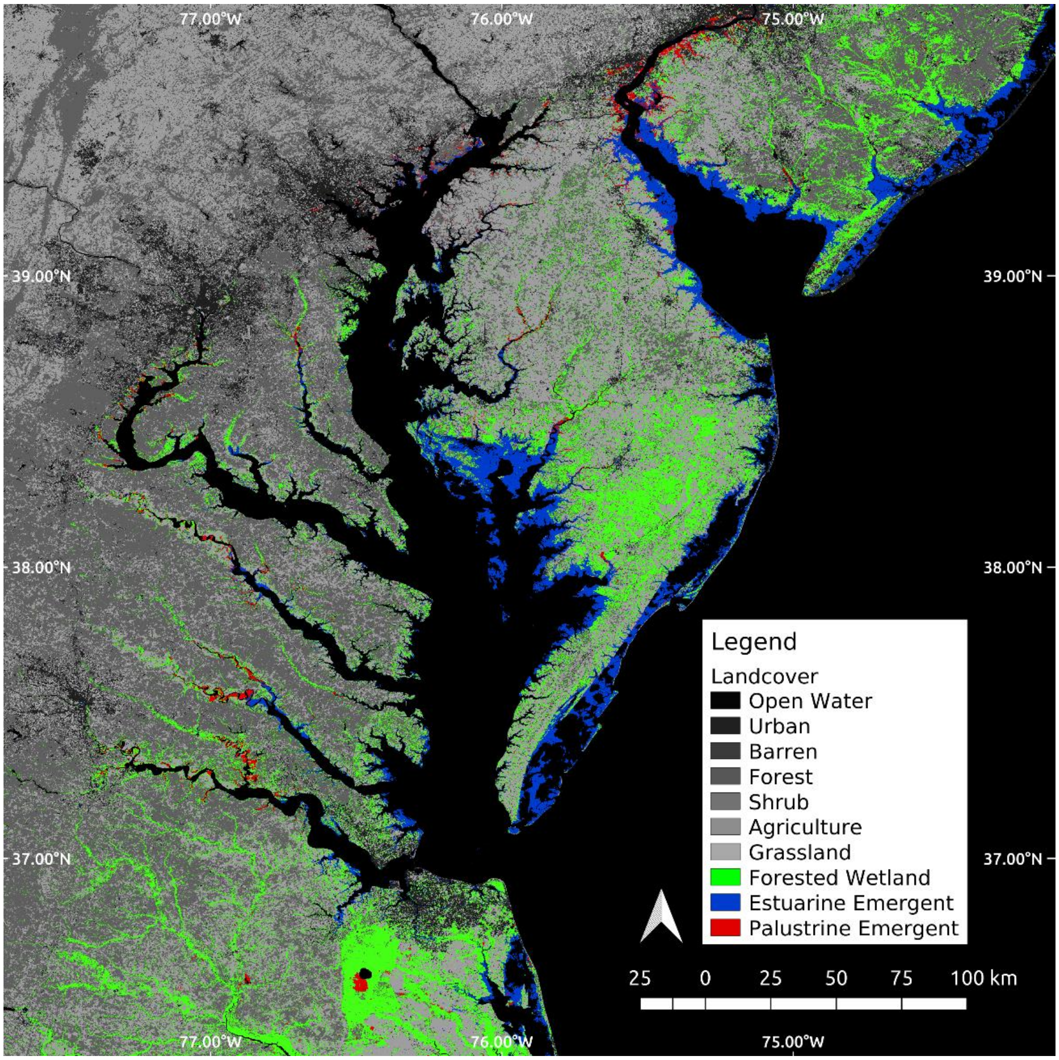

Figure 2.14. Random forest classification for Chesapeake Bay and Delaware Bay wetlands for 2017. Estuarine emergent wetlands are depicted in blue. Palustrine emergent wetlands are depicted in red. Forested wetlands depicted in green were classified less accurately than emergent wetlands.

Our random forest parameter tuning assessment revealed that increasing the number of trees made little difference in improving classification accuracy above a certain limit. We found that increasing the number of trees from 10 to 25 to 50 to 100 to 200 increased the overall classification accuracy from 58.13% to 63.38% to 65.43% to 66.53% to 67.04%. However above 200 trees, the accuracy remained asymptotically limited below 68%. For these reasons, we selected the 200-tree classifier for the final regional scale classification of the SAR-optical-DEM stack shown in Figure 2.14.

The importance assessment of the regional scale random forest classification is shown in Table 10. These findings illustrate that the SRTM DEM elevation was the most important layer in terms of increasing overall classification accuracy, as evidenced by both the mean decrease in accuracy from removing the SRTM DEM elevation layer as a classification predictor variable and in the Gini impurity index. Optical vegetation indices were more important for separating wetlands from non-wetland landcover than SAR layers. SAR layers were overall less important than the optical and SRTM DEM layers in the overall classification. Of the SAR layers, tidal difference layers were the least important of the SAR input layers. The Sentinel-1A σ^0_{VH} annual mean was the most important SAR layer in terms of the overall classification importance and Gini impurity index value in the regional scale classification as it had the third highest mean decreases in overall accuracy and the fifth highest Gini index value.

Table 2.9. Regional scale random forest classification confusion matrix. Diagonal matches between observed (Reference) and predicted (Classification) classes are bolded.

Reference	Classification											
	Water	Urban	Barren	Grass	Agriculture	Shrub	Upland Forest	Forested Wetland	Palustrine Emergent	Estuarine Emergent	Total	Producer's Accuracy %
Water	**22172**	80	263	37	51	2	75	51	87	260	23078	96.07
Urban	31	**11261**	637	1957	1061	50	449	164	61	105	15776	71.38
Barren	502	1522	**4473**	650	1575	233	669	221	107	290	10242	43.67
Grass	31	2410	208	**4449**	4835	696	3643	1031	65	78	17446	25.50
Agriculture	11	764	290	1666	**22852**	220	1699	615	113	31	28261	80.86
Shrub	16	311	106	1039	1486	**2853**	5059	1535	45	27	12477	22.87
Upland Forest	28	494	100	1431	1415	1343	**23427**	3374	30	7	31649	74.02
Forested Wetland	56	254	53	496	585	529	3662	**10732**	372	224	16963	63.27
Palustrine Emergent	93	75	73	116	1009	83	171	550	**5954**	950	9074	65.62
Estuarine Emergent	127	71	160	34	53	2	1	130	699	**9993**	11270	88.67
Total	23067	17242	6363	11875	34922	6011	38855	18403	7533	11965		
User's Accuracy %	96.12	65.31	70.30	37.47	65.44	47.46	60.29	58.32	79.04	83.52		**Overall Accuracy %**
												67.05

Table 2.10. Regional scale random forest layer importance assessment.

LayerType	Water	Urban	Barren	Grass	Ag.	Shrub	U. Forest	W. Forest	Palustrine	Estuarine	MeanDecreaseAccuracy	MeanDecreaseGini
vv	**0.286**	0.027	0.026	0.000	0.040	0.006	0.051	0.063	0.038	0.092	0.071	6792.088
vh	**0.282**	0.020	**0.074**	−0.003	**0.112**	0.020	**0.103**	**0.127**	0.069	0.116	**0.104**	10293.323
vv_sd	0.018	0.005	0.009	−0.002	0.022	0.001	0.026	0.024	0.029	0.016	0.016	4621.997
vh_sd	0.007	0.017	0.016	0.002	**0.075**	0.016	0.038	0.042	0.048	0.036	0.032	7285.724
vv_tidal_diff	0.000	0.003	0.002	0.000	0.004	0.000	0.005	0.004	0.003	0.005	0.003	3740.538
vh_tidal_diff	0.000	0.002	0.001	0.000	0.005	0.000	0.005	0.003	0.003	0.010	0.003	3897.383
vvvh_tidal_diff	0.001	0.001	0.002	0.000	0.005	0.001	0.002	0.001	0.002	0.005	0.002	3669.585
hh	0.027	0.017	0.005	−0.001	0.019	0.003	0.022	0.029	0.014	0.019	0.017	4689.331
hv	0.072	0.033	0.011	0.001	0.027	0.010	0.041	0.031	0.023	0.052	0.033	5633.296
summer_tvi	0.179	0.148	0.070	0.012	0.054	0.014	0.025	0.029	0.066	**0.292**	0.081	8488.662
summer_ndvi	0.184	**0.237**	**0.133**	**0.023**	0.028	0.026	**0.094**	**0.167**	**0.102**	0.268	**0.117**	**11751.909**
summer_mndwi	0.245	**0.174**	0.032	0.009	0.044	0.014	0.044	0.042	0.098	0.128	0.084	8987.405
fall_tvi	0.093	0.084	0.034	0.009	0.042	0.015	0.032	0.014	0.060	**0.290**	0.059	7603.245
fall_ndvi	0.148	**0.170**	**0.092**	**0.020**	0.036	**0.039**	0.078	0.066	0.095	0.235	0.091	11122.123
fall_mndwi	0.237	0.166	0.036	0.014	0.037	0.021	0.042	0.033	0.096	0.104	0.079	**12343.496**
winter_tvi	0.078	0.048	0.026	0.011	**0.062**	0.030	0.031	0.017	**0.110**	0.205	0.055	6736.456
winter_ndvi	**0.349**	0.081	0.063	0.010	0.034	**0.073**	0.046	0.043	0.090	0.072	0.090	8764.048
winter_mndwi	0.205	0.128	0.023	0.004	0.045	0.018	0.045	0.027	0.089	0.077	0.069	9277.989
dem	0.198	0.052	0.038	**0.025**	0.051	**0.039**	**0.171**	**0.120**	**0.243**	**0.451**	**0.130**	**14884.806**
dem_grad	0.274	0.008	0.011	0.000	0.006	0.001	0.029	0.005	0.008	0.016	0.045	4979.564

2.5 Discussion

Inundation mapping results from Blackwater NWR (Section 2.4.1.1) demonstrated that PALSAR L-band σ^0_{HH} high tide–low tide image pairs could be used to unambiguously separate inundated and non-inundated tidal marshes using absolute thresholding. The threshold value of −13.5 dB separating inundated and non-inundated marsh was similar to the −14.0 dB threshold used by Clewley et al. (2017) to map surface water with PALSAR imagery. Because the marshes surveyed in Blackwater NWR are dominated by emergent graminoid species of low to moderate biomass (e.g., *Spartina alterniflora*, *Spartina patens*, and *Distichlis spicata*), the close agreement with Clewley et al. was not surprising and was indicative of specular forward scattering dominating backscatter response when low–moderate biomass graminoid vegetation becomes submerged or partially submerged during high tide. Kim et al. (2014) evaluated C-band and L-band SAR for inundation detection in *Cladium sp.* (sawgrass)-dominated wetlands, which have a structure and biomass similar to *Spartina alterniflora*-dominated wetlands. Kim et al. (2014) found that L-band SAR backscatter exhibited a much stronger inverse relationship with the wetland water level than C-band SAR backscatter, likely indicating more specular forward scattering at longer wavelengths (lower backscatter) as moderate-biomass emergent vegetation submerges. Ramsey et al. (2013) performed a similar comparison, noting that L-band-based inundation maps had higher levels of agreement (91%) with *in situ* inundation measurements than C-band-based maps (67–71%) in *Spartina alterniflora* dominated wetlands. Consistent with these previous studies, our results demonstrate that L-band SAR imagery was more effective than C-band SAR imagery in detecting inundation in the moderate-biomass emergent wetlands of Blackwater NWR. It should be noted, however, that in our analysis, we compared C-band and L-band SAR imagery of different polarizations (Sentinel-1A C-band VV vs. PALSAR L-band HH), which limited a direct wavelength-based comparison of the imagery as polarimetric responses to inundation state can be variable as well (Brisco et al. 2011; Hong et al. 2013; Hong et al. 2015). These findings have relevance to the science objectives of the upcoming NASA-ISRO Synthetic Aperture Radar (NISAR) mission, which will operate at an L-band frequency and will have a nominal revisit of 12 days. The implementation of thresholding techniques for deriving inundation products from NISAR imagery could make for an effective and simple approach, which is important to consider given the anticipated computational demands for storing and processing NISAR imagery.

The single high tide–low tide PALSAR image pair provided effective backscatter separation in the Blackwater NWR study site. However, this particular threshold (and general approach of absolute thresholding) may not be applicable to inundation mapping in other wetlands dominated by higher biomass species like *Typha spp*. and *Phragmites australis*. Bourgeau-Chavez et al. (2013) and Bourgeau-Chavez et al. (2015) demonstrated that *Phragmites australis* and *Typha spp*. could be effectively distinguished from lower biomass emergent vegetation in wetlands mapping efforts, indicating that these higher biomass emergent species may not produce the same backscatter responses in L-band signals when inundated as the lower biomass emergent species of Blackwater NRW did. Although we did not acquire PALSAR imagery above the bankfull depth in Kirkpatrick Marsh, future work should focus on investigating differences in L-band backscatter response between *Phragmites australis* and lower biomass vegetation at this site. We are currently in the process of performing this analysis with multitemporal PALSAR-2 imagery.

In contrast to the PALSAR L-band results, classification of inundation using Sentinel-1A C-band imagery at Blackwater NWR was more challenging. The Sentinel-1A VV-polarized backscatter (σ^0_{VV}) and $\sigma^0_{VV}/\sigma^0_{VH}$ ratio did show substantial changes in distributions between high and low tide for tidal marsh ROIs, but these differences did not provide clear separability. For these reasons, we did not attempt to use Sentinel-1A imagery to classify inundation over Blackwater NWR. Our results suggest that detailed characterization of a wetland's tidal hydrology, such as that provided in Nelson et al. for Kirkpatrick Marsh, is important for constraining satellite-based inundation estimates and should be integrated into future efforts applying change detection approaches to classify inundation over Blackwater NWR.

At the Kirkpatrick Marsh site, we determined that increases in the Sentinel-1A σ^0_{VV} and decreases in the $\sigma^0_{VV}/\sigma^0_{VH}$ ratio were both strong indicators of the tidal inundation extent given the moderate–high goodness of fit between the site-adjusted tidal stage and marsh integrated backscatter above the bankfull depth as defined in Nelson et al. [48]. We found a clear separation between the marsh-integrated σ^0_{VV} and $\sigma^0_{VV}/\sigma^0_{VH}$ ratio at a Kirkpatrick Marsh tidal creek water level greater than 1.1 meters. These factors allowed us to map tidal inundation over a series of high tide images in this high marsh system (Figure 2.10). Utilizing imagery acquired every 12 days from the Sentinel-1A satellite allowed us to effectively implement temporal change detection approaches to map inundation, which would not have been possible with imagery from SAR satellites with longer revisit times. The change detection approaches we implemented could be used for inundation mapping with timeseries imagery from the future L-band NISAR mission, which will also have a 12-day revisit.

At both Kirkpatrick Marsh and Blackwater NWR, Sentinel-1A imagery acquired at the highest tidal stages was acquired during fall. Higher tidal stages were correlated with a higher σ^0_{VV} and a lower $\sigma^0_{VV}/\sigma^0_{VH}$ ratio. Pope et al. (1997) suggested that C-band VV-polarized backscatter enhancement in emergent wetlands during high water periods could be attributed to reductions in the overall attenuation of vertically oriented SAR signal by vertically oriented vegetation. However, the findings by Pope et al. (1997) suggest that only high biomass emergent vegetation exhibits an increase in σ^0_{VV} for C-band imagery. In contrast, our results demonstrated that all four dominant vegetation types of Kirkpatrick Marsh exhibited backscatter increases during inundated conditions, despite having pronounced differences in biomass and structure. This may be attributed to the collapse of vertical stems and leaves during fall, resulting in increasingly horizontally structured vegetation, which enhances double-bounce scattering in vertically polarized SAR signals when the underlying marsh surface is inundated. It is also likely that the change in vegetation structure combined with senescing vegetation becoming saturated with saline water during or following high tide (but not submerged) may have increased backscatter by increasing the dielectric constant of the partially collapsed vegetation, which was also acting a rough surface, thus increasing the direct σ^0_{VV} response. These are all potential explanations for the observed Sentinel-1A σ^0_{VV} enhancement in fall, but they are by no means definitive. To further investigate the causal mechanisms of this fall backscatter enhancement, measurements with a grid of water level sensors were recently deployed across Kirkpatrick Marsh at sites with different vegetation characteristics, which will allow us to assess how the interaction of inundation and vegetation phenology contribute to this observed enhancement in Sentinel-1A σ^0_{VV}. Such a water level sensor grid will also serve to validate Sentinel-1A change detection-based inundation products for Kirkpatrick Marsh and validate future PALSAR-2 inundation mapping efforts as well.

In the case of the SAR-based inundation mapping work, both the results from Kirkpatrick Marsh and Blackwater NWR proved useful in informing the regional scale wetland classification. The pronounced tidal responses in both Sentinel-1A σ^0_{VV} and $\sigma^0_{VV}/\sigma^0_{VH}$ ratio was the impetus for including high tide-low tide difference layers in the regional scale classification. Although L-band high tide-low tide image pairs covering the Chesapeake Bay would have been optimal to include in this classification, this imagery was not available for 2017. However, the results from Blackwater NWR also demonstrated the capability of L-band imagery in separating forested and emergent wetlands, which was the impetus for including PALSAR-2 annual mosaics in the regional scale classification. Wetland inundation could not be mapped with optical water indices because relationships between tidal stage and water index value were weak at both Kirkpatrick Marsh and Blackwater NWR. Although the mNDWI is demonstrated as being effective for mapping surface water (Du et al. 2016), it is less effective for inundation detection under vegetated canopies than SAR imagery. However, multi-season mNDWI imagery was included in the regional scale classification to provide a characterization of open water extent as a complement to the SAR imagery characterizing wetland inundation extent.

Comparing Sentinel-1A σ^0_{VV} timeseries for Kirkpatrick Marsh and Jug Bay showed that σ^0_{VV} variability was very similar between different vegetation types at Kirkpatrick Marsh, but also very similar to *Typha spp.* at Jug Bay. This is likely indicative of phenological and inundation changes combining in a distinct way to enhance backscatter for all persistent vegetation types in fall. Potential causal factors of this fall backscatter enhancement have already been discussed. Our results demonstrated that persistent vegetation maintained a backscatter increase from summer to fall/winter, while non-persistent vegetation exhibited a backscatter decrease, which was of a greater relative magnitude as well. The reason for the decrease in non-persistent vegetation backscatter was well-evidenced by site photos depicting the loss of biomass as *Nuphar lutea* decayed at the end of the growing season, which was effectively tracked with decreases in the C-band SAR backscatter (Figure 2.12).

The use of timeseries-based Sentinel-1A SAR derivatives was highly effective for separating emergent vegetation classes at Jug Bay from one another and further separating them from shrub and forest classes. The Jug Bay SAR-only random forest classification achieved overall accuracies greater than 95%. The Jug Bay SAR-optical-DEM classification using the same layers as the regional scale wetland classification achieved accuracies greater than 97%. The Jug Bay random forest importance assessment revealed that the Sentinel-1A σ^0_{VV} backscatter annual standard deviation layer was one of the most important layers in terms of improving classification accuracy in both SAR-only and SAR-optical-DEM classifications. Qualitatively, it was clear that this layer was effective at depicting locations of non-persistent vegetation (Figure 2.13). The implementation of timeseries approaches for mapping functional vegetation classes could be used for mapping non-persistent vegetation outside of the Chesapeake Bay region. The Sentinel-1A imagery that was acquired nearly every 12 days in 2017 provided consistent observations of the phenological changes over the Jug Bay site that were not provided using cloud-obscured optical imagery. The reliability of SAR with stable operating modes was clearly demonstrated in this case as the consistency of SAR observations allowed for successful detection of phenological changes in persistent and non-persistent vegetation. The extent of non-persistent vegetation in coastal emergent wetlands is indicative of regions that are tidal freshwater, rather than brackish or saline (Odum 1988). The continued monitoring of these tidal freshwater wetlands serves as a tool for assessing changes to salinity properties along the freshwater-brackish-saline continuum.

In the regional scale random forest classification of wetlands in the Chesapeake and Delaware Bays, we used nine optical layers, nine SAR layers, and two DEM layers as classification predictors. The overall classification accuracy of our regional scale mapping effort was 67%, which was relatively low. However, much of the overall classification error was due to confusion between different non-wetland landcover classes. The overall goal of this effort was to map estuarine emergent wetlands (i.e., tidal marshes), which was done with relatively high accuracies (user's and producer's accuracies of 83% and 88%, respectively). We found that palustrine emergent wetlands were classified with a lower accuracy than estuarine emergent wetlands and noted that these two classes were most often confused with one another. When these classes were grouped into a single emergent wetland class, classification accuracy improved to a user's accuracy greater than 86% and a producer's accuracy of greater than 90%. All predictor layers used in this regional scale classification were carefully selected based on the findings from our target wetland site studies or a rationale that supported the separation of wetlands from other sites (i.e., use of multi-season NDVI and TVI to separate emergent wetlands from crops). We used the C-band SAR backscatter temporal mean and standard deviation to capture emergent wetland central tendency and temporal variability, the latter of which tended to be higher in emergent wetlands than other landcover types. We used multi-season mNDWI in the regional scale classification to aid in surface water identification, although the importance assessment of the regional scale classification demonstrated that summer NDVI, DEM gradient (slope), and Sentinel-1A σ^0_{VV} and σ^0_{VH} annual means were more useful variables for mapping the locations of open water. Sentinel-1A SAR high tide low tide image pairs for the fall season were included in an attempt to isolate estuarine emergent wetlands. Although the target wetland study sites showed well-defined changes in Sentinel-1A backscatter corresponding to tidal stage, the tidal difference layers proved to be some of the least useful layers for improving regional scale random forest classification accuracy overall, and for the estuarine emergent wetland class in particular. This was somewhat surprising but is likely the result of the SAR standard deviation layer capturing much of the similar variance that the tidal differences layers were, thus providing little additional useful information to the random forest classifier. Optically based vegetation indices proved to be some of the most useful layers in the regional scale wetland classification. This was likely because multi-season optical imagery aids the random forest classifier in separating emergent wetlands from crops, and because the peak TVI and NDVI values of emergent wetlands tend to be lower than upland vegetated systems as a result of less canopy closure (more vertically structured vegetation) and more near infrared attenuation by surrounding water compared to upland systems. The overall finding that the topographic variables (elevation and slope) were the most useful predictor layers in the regional scale classification was consistent with Clewley et al. (2015) and Knight et al. (2013). Overall, our results from the regional scale random forest classification highlighted the increasing relative importance of SAR, optical, and elevation data in overall wetland classification, consistent with Knight et al. (2013).

Our results demonstrate the existence of somewhat of a paradox: In our regional scale classification, optical imagery was superior for wetland mapping in terms of separating wetlands from other landcover. However, in our inundation and vegetation characterizations and vegetation mapping efforts at Jug Bay, SAR imagery proved more important for these characterizations. The use of the same SAR-optical-DEM stack in the regional scale classification and Jug Bay vegetation classification provided a direct comparison of layer importance for these different mapping efforts shown in Tables 8 and 10. These differences in the regional scale wetland classification and the Jug Bay vegetation classification were likely the result of timeseries optical imagery showcasing consistent differences between wetlands and other landcover, while the temporal and spatial variability within wetlands that timeseries SAR effectively captured may essentially act as noise in a statistically-based classifier when attempting to separate wetlands from upland landcover classes in the regional scale classification effort.

2.6. Conclusions

We used a combination of ground surveys and optical and SAR imagery to characterize tidal inundation patterns at two estuarine marsh study sites and vegetation characteristics at an estuarine marsh and a tidal freshwater marsh complex. Informed by the findings from these target wetlands sites, we mapped wetland vegetation for an expanded region in the Patuxent River with a very high accuracy (>95% overall) by utilizing timeseries SAR imagery and fused

SAR-optical-DEM imagery. The SAR-optical-DEM classification relied on the same layers used in our regional scale wetlands classification for emergent estuarine wetlands in the Chesapeake and Delaware Bays. In this way we produced two classifications, one providing a detailed classification of vegetation types within a wetlands complex and another separating wetlands from other landcover. Even when relying on the same input layers, these classifications produced very different post-classification importance assessments, with SAR layers being more useful for the detailed vegetation classification and DEM and optical being more useful for separating wetlands from other landcover classes.

Temporal SAR derivatives were used here, for the first time, to map non-persistent vegetation in the Patuxent River. Our approach provides a straightforward, yet powerful tool for mapping tidal freshwater systems through the identification of indicator non-persistent vegetation, which can lead to improved management of tidal freshwater systems. Critical to this approach is the ability to now leverage the consistent 12-day repeat C-band SAR observations provided by Sentinel-1A, which rarely changed its operating mode over our study region. The combination of Sentinel-1A's temporal fidelity and spatial resolution is unprecedented in SAR remote sensing and presents numerous opportunities and applications in wetland mapping and characterization. However, our findings suggest that L-band SAR is more useful than optical or C-band SAR for inundation mapping in tidal marshes. Future work should include assessments of inundation mapping with imagery from the fully polarimetric L-band Uninhabited Aerial Vehicle Synthetic Aperture Radar (UAVSAR) mission in conjunction with radiometric modeling, which will support the objectives of the upcoming NISAR mission (L-band frequency and 12-day revisit).

Remote sensing imagery was also used here to map estuarine emergent wetlands in the

Chesapeake and Delaware Bays with Google Earth Engine. The emergence of cloud-based remote sensing analysis platforms present opportunities to expand mapping efforts like the one described here to much larger extents, potentially globally. Global estimates of tidal marsh extent are poor (Pendleton et al. 2012). However, recent efforts by Mcowen et al. (2017) have aggregated national tidal marsh inventories into a global tidal marsh inventory. This global inventory likely underestimates the extent of tidal marshes since it aggregates national inventories that are often themselves incomplete. However, there is potential to improve these estimates of tidal marsh extent by utilizing tidal marsh inventories as training data for remote sensing-based tidal marsh classifications at the global scale. With the advent of cloud computing remote sensing platforms, such mapping efforts are now highly feasible.

2.7. Long Island Study Comparative Study

2.7.1 Introduction

The following section (2.7) serves as a follow on for the majority of Chapter 2 covering the Chesapeake Bay. Here, a similar satellite image evaluation is carried out for tidal marsh sites in the Long Island Sound (LIS). This includes an evaluation of both Sentinel-1A SAR and optical/IR imagery (Landsat 8 and Sentinel-2) as performed for the Chesapeake Bay study in Sections 2.2-2.6. Additionally, for this study covering the LIS, a more thorough evaluation of PALSAR/PALSAR-2 L-band imagery was carried out as there was a greater availability of PALSAR-2 imagery over LIS study sites and a greater number of PALSAR scenes available covering a range of tidal stages.

When this study was carried out, there were limited vegetation surveys, and for that reason the National Wetlands Inventory (NWI) was used as the primary dataset to identify particular wetlands and assess multitemporal satellite imagery. The analysis in this section mainly focuses on the assessment of satellite image response to tidal inundation variability which provides the groundwork for Chapter 4 focusing on the development of tidal marsh inundation products. This section (2.7) does not focus extensively on tidal marsh vegetation characterization which is covered extensively in Chapter 3. In this section, additional results from Chesapeake Bay study sites are included to provide comparisons between the Chesapeake Bay and LIS tidal marshes. The major general difference between these regions is the tidal range, with the LIS having a tidal range approximately 2.5 times greater than that of the Chesapeake Bay.

2.7.2 Long Island Sound Study Sites

Several LIS study sites were selected for this evaluation (Figure 2.16). Three sites were more intensively studied: Wheeler Marsh, Great Meadows Marsh, and the Nissequogue River. The Wheeler Marsh system contains three NWI classes (E2EM1P, E2EM1N, E2SS1P). At the Wheeler Site, these NWI classes correspond to irregularly flooded tidal marsh, regularly flooded tidal marsh, and tidal shrub-scrub wetlands according to the NWI. Site visits to Wheeler Marsh revealed that these three wetlands are better described as a sparsely vegetated low marsh, densely vegetated low marsh, and high marsh, respectively. The Great Meadows Marsh system contains two primary NWI classes (E2EM1N, E2EM1P) which also more accurately correspond to sparsely vegetated low marsh and densely vegetated high marsh, respectively. The Nissequogue River site contains six wetland classes. Three of the Nissequogue classes are emergent tidal marshes (E2EM1P, E2EM1N, E2EM5P) corresponding to correspond to irregularly flooded tidal marsh, regularly flooded tidal marsh, and *Phragmites australis*-dominated tidal marsh, according to the NWI. Unlike Great Meadows and Wheeler Marsh sites, we were not able to verify the split between E2EM1P and E2EM1N classes with extensive field studies at Nissequogue, but did verify that these classes were both native marsh, and were effectively split from the accurately classified *Phragmites australis*-dominated tidal marsh class (E2EM5P) with limited field studies. The Nissequogue River site also contain non-tidal marsh wetland and deepwater classes, including; one intertidal aquatic bed wetland class (E2ABN), one intertidal mudflat class (E2SUS3N), and one tidally influenced shrub-scrub class (E2SS1P).

LIS Tidal Wetland Study Sites (Intensive Study in Yellow)

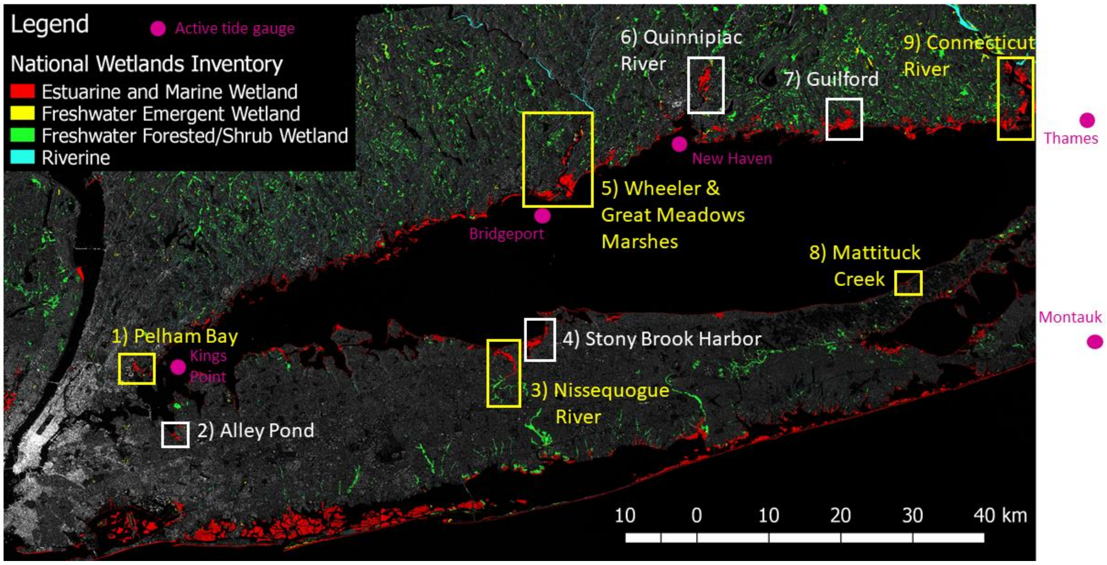

Figure 2.15. Long Island Sound study region and study sites. Approximate NOAA tidal gauge locations shown in magenta. Background grayscale image is Sentinel-1 SAR. Color polygon overlays are National Wetlands Inventory classes shown in upper left legend.

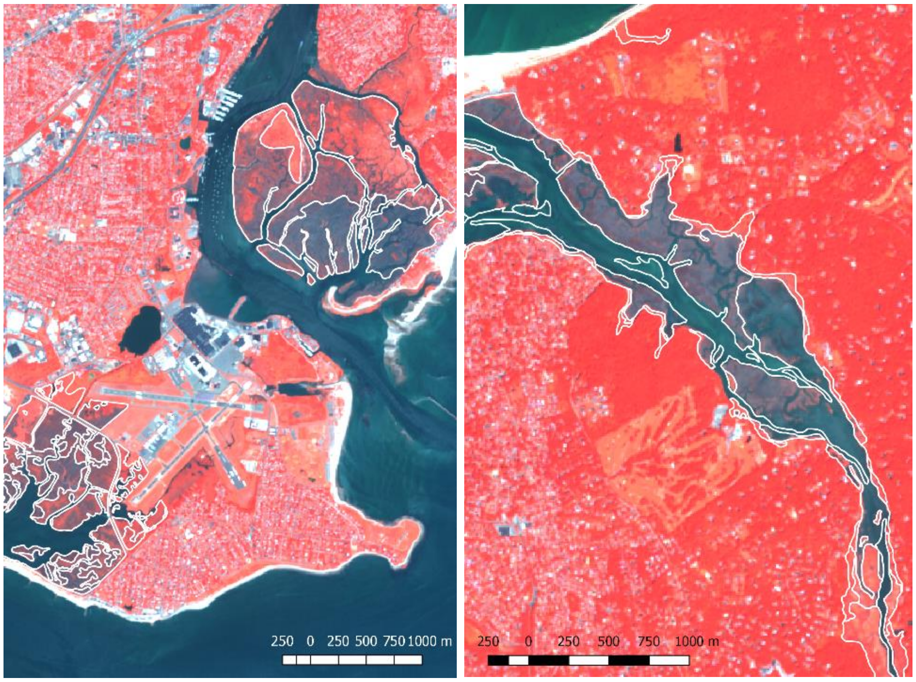

Figure 2.16. Sentinel-2 optical growing season false-color RGB image (Near Infrared, Green, Blue). Left panel Wheeler Marsh (Northeast) and Great Meadows (Southwest). Right panel shows the Nissequogue River. Note that white NWI boundaries shown varying NIR reflectance that corresponds to canopy closure and canopy density. This NIR variability is apparent over the three wetland classes at Wheeler Marshes. At the Nissequogue site, the southeast portion of the map shows high NIR reflectance corresponding to *Phragmites australis* and shrub dominated wetlands. The lower reflectance in the center and northwest portion of the map correspond to native tidal marsh, aquatic beds, and mudflats.

2.7.3 Methods & Results

Over the three intensive study sites, Sentinel-1 backscatter was extracted by wetland class and compared to local tidal stage. Over Wheeler Marsh, Sentinel-2 optical water indices and PALSAR/PALSAR-2 backscatter were also compared to tidal stage, culminating in a comparison between optical water indices, C-band SAR, and L-band SAR over this site. Previous results over the Chesapeake Bay demonstrated that optical indices were limited in performance compared to C-band and L-band SAR approaches over the Blackwater N.W.R. site which is the largest tidal marsh complex in the Chesapeake Bay. Wheeler Marsh represents a tidal marsh system with similar vegetation characteristics, but a greater tidal range.

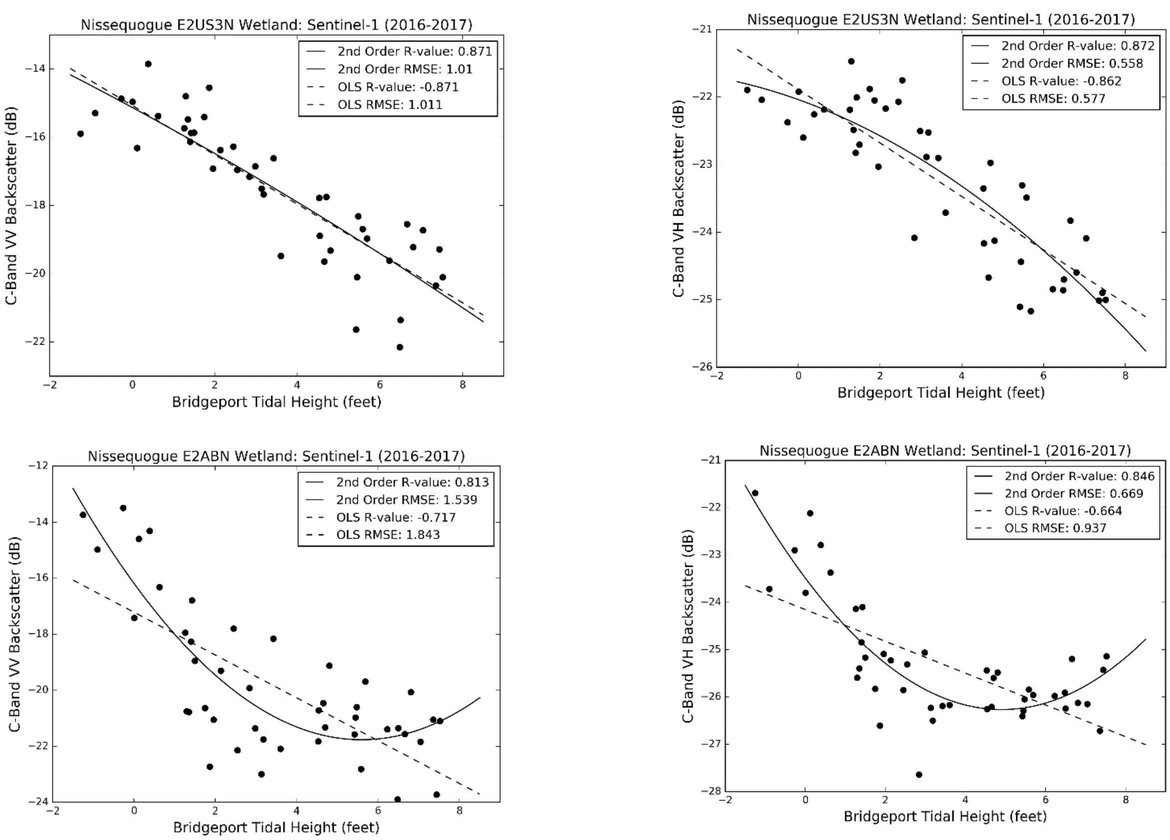

Figure 2.17. Sentinel-1 VV (left) and VH (right) backscatter vs. tidal stage for Nissequogue River deepwater NWI classes. Note that both the intertidal mudflat (E2US3N) and intertidal aquatic bed (E2ABN) both show backscatter decreases corresponding to increasing tidal stage. This decrease is present in both polarimetric channels.

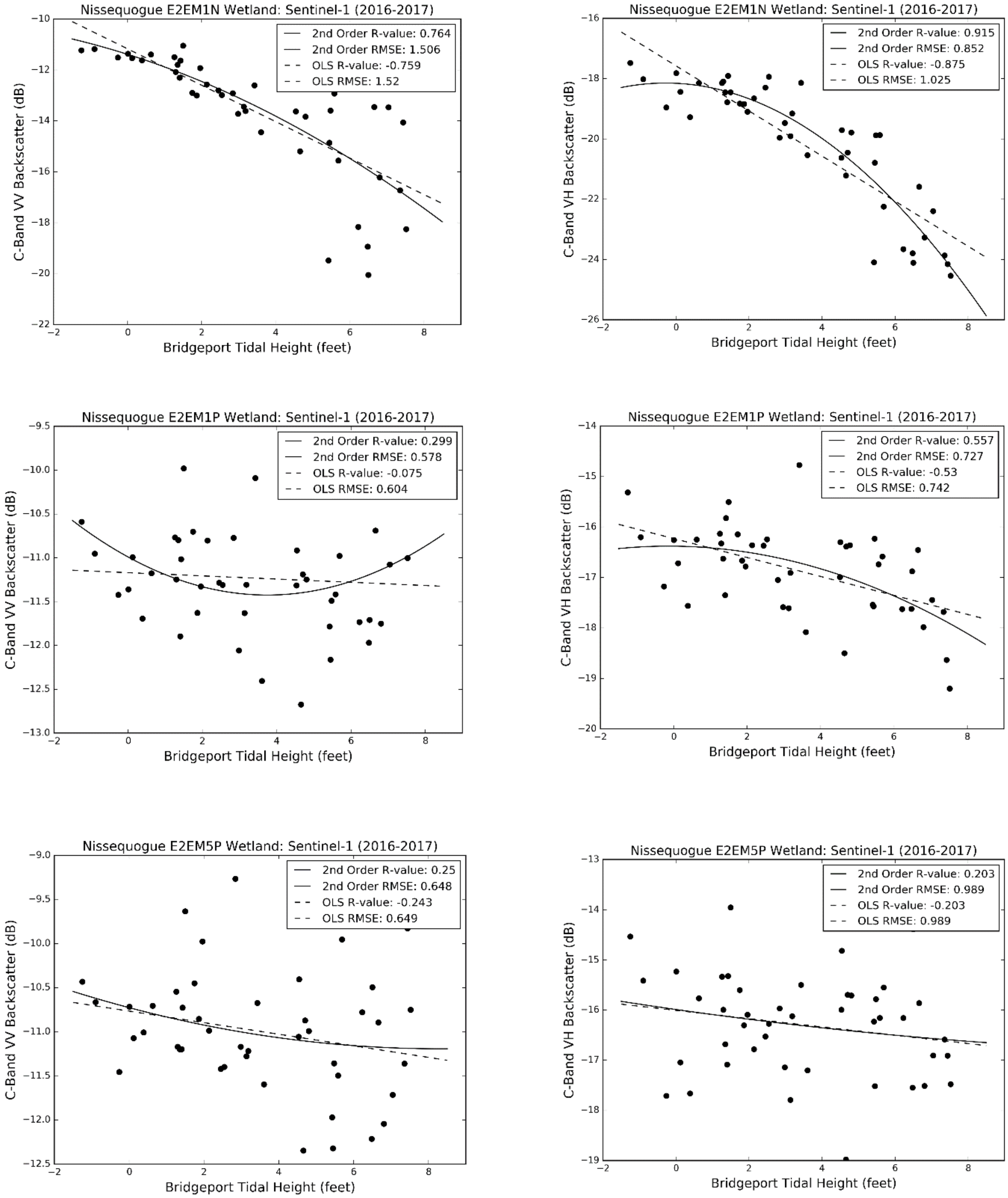

Figure 2.18. Sentinel-1 backscatter vs. tidal stage for Nissequogue River emergent NWI classes. Note that the sparsely vegetated low tidal marshes (E2EM1N) show high R-values when regressed against tidal stage. With greater canopy biomass of the densely vegetated low tidal marshes (E2EM1P) and Phragmites-dominated marshes (E2EM5P), statistical agreement with tidal stage lessens. Overall, the VH channel shows greater agreement between backscatter and tidal stage.

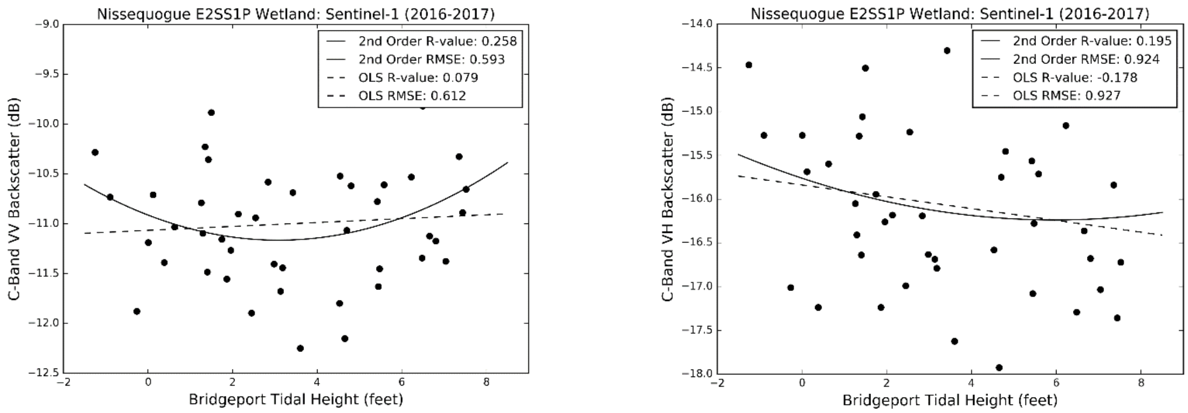

Figure 2.19. Sentinel-1 backscatter vs. tidal stage for Nissequogue River shrub NWI class (E2SS1P). Note that tidal stage and backscatter have minimal statistical agreement for this wetland type for both VV and VH channels.

For the Nissequogue River wetlands, it was apparent that as the wetland biomass increased there was less response to the underlying surface state (as indicated by tidal stage). This finding was consistent with previous studies reviewed in thesis Sections 1.4 and 1.5 showing that C-band SAR responds strongly to vegetation structure. The same patterns can be observed in Figures 2.20 and 2.21 below for Great Meadows tidal marsh wetlands.

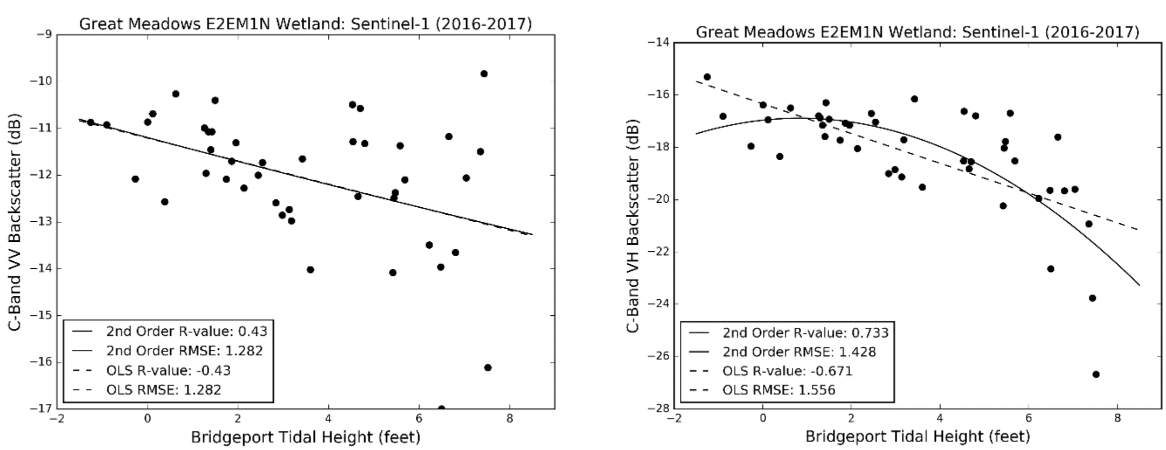

Figure 2.20. Great Meadows Sentinel-1 backscatter-tidal stage relationships for sparsely vegetated tidal marsh.

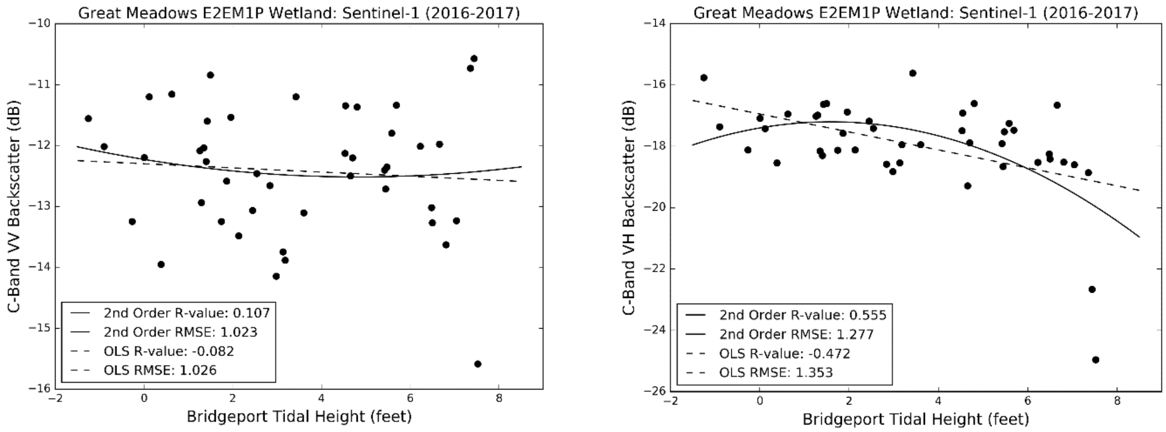

Figure 2.21. Great Meadows Sentinel-1 backscatter-tidal stage relationships for densely vegetated low tidal marsh.

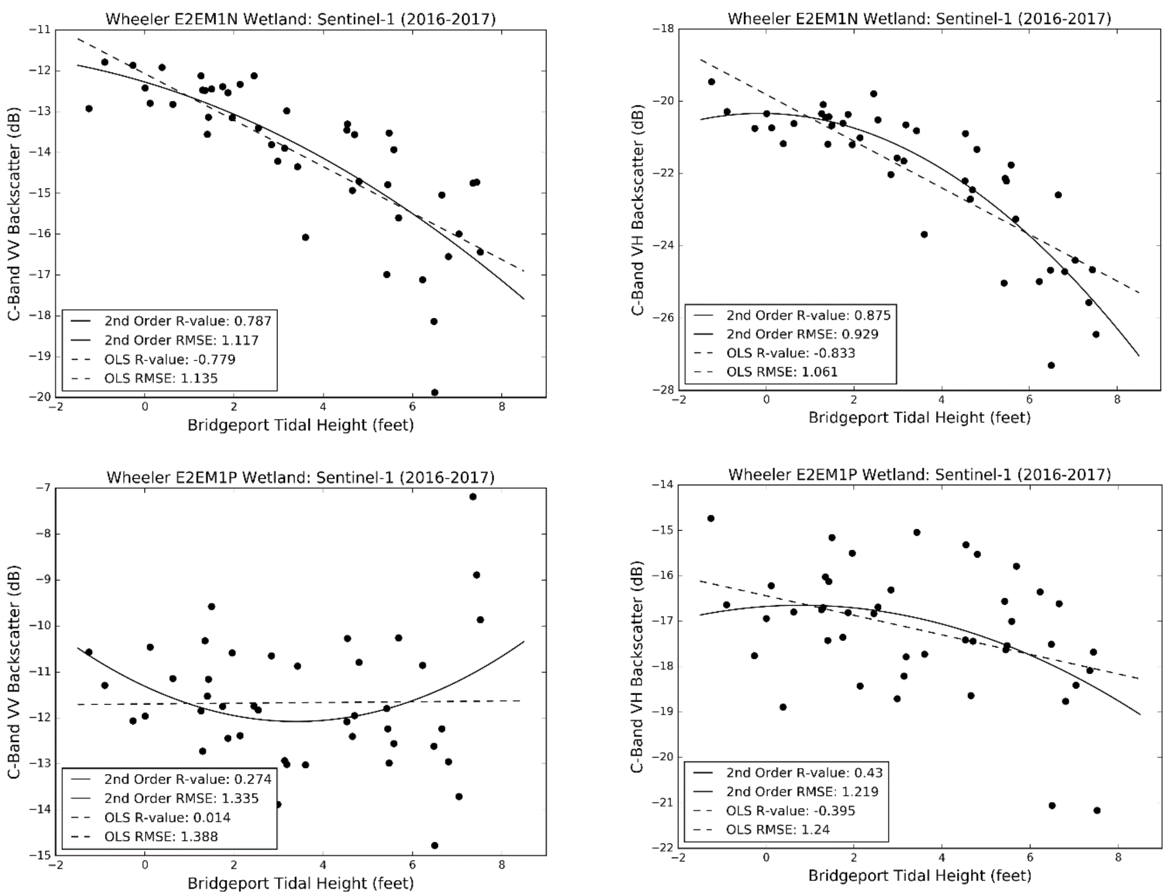

Figure 2.22. Wheeler Marsh Sentinel-1 backscatter-tidal stage relationships for sparsely vegetated low tidal marsh (upper panels) and densely vegetated low tidal marsh (lower panels).

Sentinel-1 C-band backscatter-tidal stage relationships varied by wetland type. One pattern that does emerge from this analysis, is the fact that in all cases (across all three study sites and wetland and deepwater classes), VH channel backscatter decreased in response to increasing tidal stage, although the degree of statistical fit and magnitude of change varied greatly for both the VV and VH channels. VV/VH ratio channels were also assessed, as the previous section (2.2-2.6) demonstrated this ratio to have a strong response to tidal stage in both the Blackwater NWR and Kirkpatrick Marsh sites in the Chesapeake Bay (Figures 2.6 and 2.9).

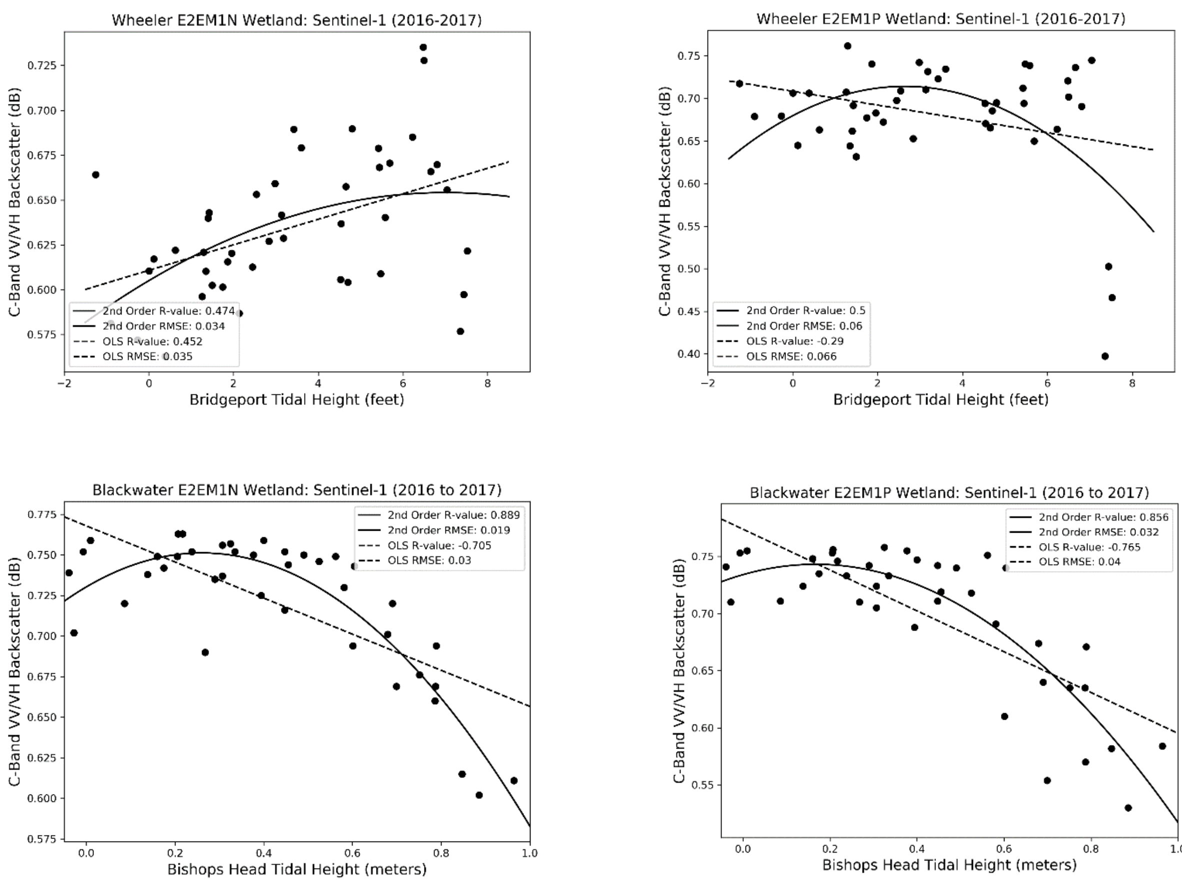

Figure 2.23. Sentinel-1 VV/VH backscatter ratio-tidal stage comparison for Wheeler Marsh (upper panels) and Blackwater NWR (lower panels) for E2EM1N and E2EM1P wetland classes. Note tidal stage units on for Wheeler are feet, Blackwater NWR units are meters.

The Wheeler Marsh site was the only site to have a full comparison of C-band SAR, L-band SAR, and optical water indices. L-band SAR, optical indices, and C-band SAR had the greatest R-values when correlated against tidal stage, respectively. For the densely vegetation low tidal marsh class (E2EM1P), only L-band SAR had high correlations with tidal stage (R-value > 0.8). The Sentinel-1 C-band VV/VH ratio that exhibited the strong statistical relationships with tidal stage at Chesapeake Bay sites was limited for Wheeler Marsh and Great Meadows Marsh LIS sites, comparatively (R-value < 0.46).

L-band backscatter consistently decreased with increasing tidal stage for all LIS tidal marsh sites. Although comparable PALSAR/PALSAR-2 timeseries imagery was not available for Blackwater NWR, the decrease in L-band backscatter is consistent with high tide-low tide PALSAR image comparisons over Blackwater NWR tidal marshes, where high tide and low tide imagery exhibited complete separability at a backscatter threshold of -13.5 dB.

Table 2.11. Expanded correlation matrix comparing satellite imagery to tidal stage. Blackwater NWR (B), Wheeler Marsh (W), Great Meadows (GM), and Nissequogue River (N). Columns represent Sentinel-1 polarimetric channels (S1), Landsat and Sentinel-2 optical water indices (NDWI and mNDWI), and PALSAR L-band correlation with tidal stage. Ordinary least squares (OLS) and second order polynomial (Poly) relationships are both assessed.

NWI Class	S1-VH OLS	S1-VH Poly	S1-VV OLS	S1-VV Poly	S1-VV/VH OLS	S1-VV/VH Poly	NDWI OLS	NDWI Poly	mNDWI OLS	mNDWI Poly	PALSAR-HH OLS	PALSAR-HH Poly	PALSAR-HV OLS	PALSAR-HV Poly
E2EM1N-B	−0.638	0.757	0.374	0.575	−0.705	**0.889**	0.314	0.378	0.460	0.468	--	--	--	--
E2EM1P-B	−0.689	0.761	0.581	0.666	−0.765	**0.856**	0.352	0.393	0.471	0.515	--	--	--	--
E2EM1P6-B	−0.450	0.541	0.368	0.378	−0.530	0.567	0.192	0.283	0.001	0.235	--	--	--	--
E2EM1Pd-B	−0.646	0.725	0.457	0.539	−0.684	0.772	0.407	0.412	0.560	0.669	--	--	--	--
E2SS4P-B	−0.189	0.422	0.395	0.403	−0.456	0.457	0.047	0.303	−0.065	0.080	--	--	--	--
E2FO4P-B	−0.089	0.357	0.360	0.381	−0.401	0.401	0.006	0.236	0.108	0.142	--	--	--	--
E2EM1N-W	**-0.833**	**0.875**	-0.779	0.787	0.452	0.474	**0.911**	--	**0.912**	--	**-0.845**	**0.878**	**-0.917**	**0.978**
E2EM1P-W	-0.395	0.430	0.014	0.274	-0.290	0.500	0.562	--	0.701	--	**-0.806**	**0.955**	-0.625	**0.924**
E2EM1N-GM	-0.671	0.733	-0.430	0.430	-0.251	0.413	--	--	--	--	**-0.817**	**0.937**	-0.717	**0.897**
E2EM1P-GM	-0.472	0.555	-0.082	0.107	-0.376	0.497	--	--	--	--	-0.716	**0.872**	-0.666	**0.824**
E2EM1N-N	**-0.833**	**0.875**	-0.759	0.764	--	--	--	--	--	--	-0.670	0.744	**-0.843**	**0.947**
E2EM1P-N	-0.395	0.430	-0.075	0.299	--	--	--	--	--	--	-0.544	0.684	-0.446	**0.854**

The findings of strong statistical agreement between PALSAR/PALSAR-2 backscatter and tidal stage motivated the generation of backscatter-tidal stage plots that also assessed backscatter distributions in the context of evaluation of separability between L-band backscatter images in tidal sequence. This is shown in Figure 24. The findings from these plots motivated the generation of thresholds in the HH and HV channels at -14.0 dB and -23.0 dB, respectively. These thresholds were used to develop tidal inundation product maps that are shown in Figure 25. Note that these threshold value for the HH channel is very similar to that obtained for the Chesapeake Bay at -13.5 dB.

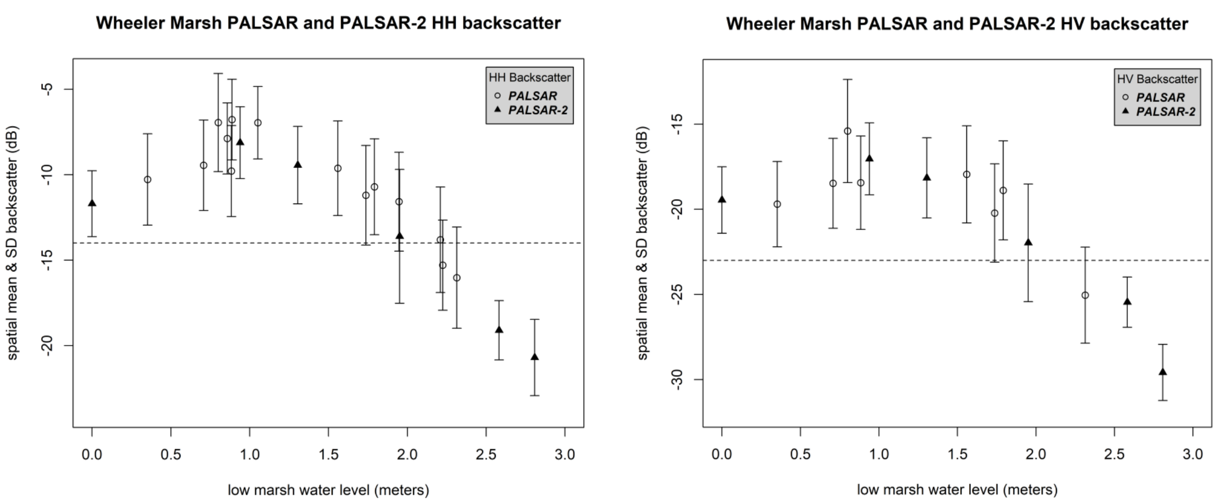

Figure 2.24 PALSAR and PALSAR-2 comparison with tidal stage. Distributions of pixels (+/- 1 SD) over the Wheeler Marsh site show that distributions fall below the threshold range used for classification of tidal marsh inundation over the Chesapeake Bay Blackwater NWR when tidal stage is sufficiently high.

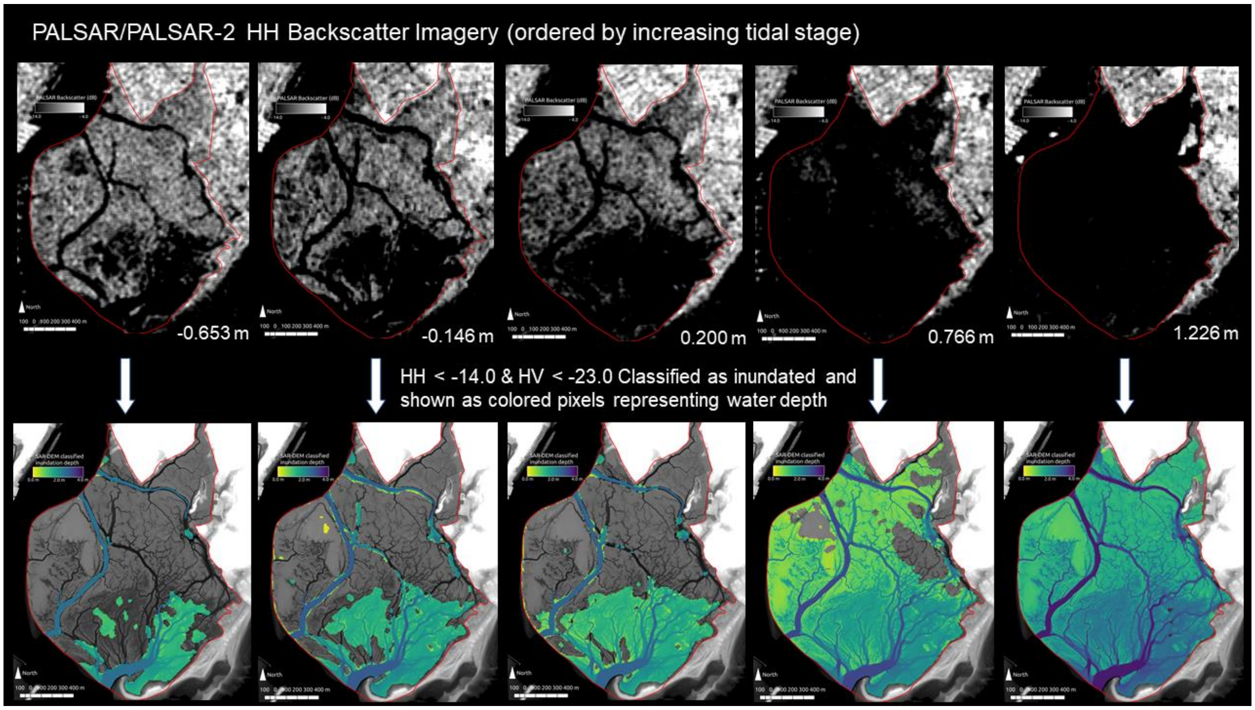

Figure 2.25. PALSAR/PALSAR-2 HH imagery ordered by tidal stage in upper panel. The lower panel shows classified inundation using thresholding approach over Wheeler Marsh site.

2.7.4 Discussion and Conclusions

The Methods and Results sections demonstrated that C-band SAR responses are not as broadly applicable to characterizing wetland inundation state as L-band SAR. Additionally, the Sentinel-1 C-band VH channel generally proved more responsive to tidal inundation state than the VV channel. L-band SAR showed a consistent response to tidal inundation state over LIS tidal marsh study sites with decreases in backscatter being similar to those over Chesapeake Bay tidal marshes. This was evidenced by the comparison of tidal stage correlations in Table 11. The Sentinel-1 VV/VH ratio that was demonstrated as statistically effective for detecting tidal marsh inundation in Blackwater NWR and Kirkpatrick Marsh was far less effective for LIS sites. This may largely be the result of differences in tidal stage between these sites. Especially given that vegetation communities between Blackwater NWR, Wheeler Marsh, and Great Meadows are very similar, with all these sites being dominated by the low marsh species *Spartina alterniflora* and secondary communities of *Spartina patens* and *Distichlis spicata* in adjacent marsh of higher elevation. With a much lower tidal range, high tide inundation events may not submerge the majority of vegetation biomass at Blackwater NWR, whereas Wheeler Marsh and Great Meadows sites show significant vegetation submergence as evidenced by site visits.

The findings here largely agree with previous literature demonstrating the L-band scattering response varies primarily in response to surface hydrologic state in tidal marsh systems (Ramsey et al. 2012; Ramsey et al. 2013; Kim et al. 2014). In contrast C-band SAR, is more sensitive to the combination of vegetation characteristics and surface hydrologic state (e.g. the degree of submergence of marsh vegetation). In Chapter 3, we further explore the use of Sentinel-1 C-band SAR for tidal wetland vegetation characterization, which this chapter demonstrates produces strong interactions with vegetation but varies in directional backscatter response. In Chapter 4, we leverage some of the empirical findings in this chapter to further develop and validate C-band and L-band-based tidal marsh inundation products with the use of *in situ* observations and radiometric modeling efforts. We also utilize radiometric modeling efforts to determine which specific scattering mechanisms led to the generally varied C-band backscatter responses across different wetlands, and generally consistent L-band backscatter responses across different wetlands.

CHAPTER 3

ASSESSMENT OF WETLAND VEGETATION CHARACTERISTICS

3.1. Introduction

Blue carbon ecosystems such as tidal marshes, mangroves, and seagrass meadows are among the most productive ecosystems on the planet and far surpass all other ecosystems in carbon sequestration on a per-area basis (Mcleod et al. 2011; Howard et al. 2017; Hinson et al. 2017). Global mangrove distributions have been effectively mapped with efforts like the Global Mangrove Watch (GMW) (Thomas et al. 2017; Bunting et al. 2018). However, estimates of tidal marsh extent remain poor (Pendelton et al. 2012; Mcowen et al. 2017). Further, very few research efforts have attempted to assess marsh vegetation characteristics over large scales, in spite of the important role that marsh vegetation plays in trapping sediments and contributing organic matter to soil carbon stocks. As noted in thesis Chapter 2, tidal marsh vegetation can vary greatly in terms of biomass, structural phenology, and seasonal persistence. These differences necessarily contribute to differences in carbon dynamics in addition to numerous other factors such as storm surge attenuation capabilities, resiliency to sea level rise impacts, habitat suitability, and influence on aquatic biogeochemical. (Barbier et al. 2011)

In this chapter, we build on the findings from Chapter 2 to characterize tidal marsh extent and vegetation characteristics for the Mid-Atlantic Coast and Gulf of Mexico (Gulf Coast) of the United States, two regions of high wetland density and importance (Feagan et al. 2020). By leveraging the expanding opportunities that exist in open-access satellite image processing, we develop a flexible methodology that enables potential mapping of tidal marshes, palustrine marshes, and deepwater habitats outside of our study regions. Within identified wetlands and deepwaters, we further refine our wetland identification methodology to separate between wetlands with persistent and non-persistent vegetation, as this separation is critical for accurately characterizing wetland biodiversity, ecological processes and biogeochemical cycles. In tidal marshes, the presence of non-persistent vegetation serves as an indicator of low salinity tidal freshwater settings (Odum 1988). Thus, the monitoring of tidal freshwater marsh vegetation can provide critical indicators of changing salinity regimes in coastal settings. In assessing overall wetland status, it is critical to not only characterize wetland distributions, carbon dynamics, and hydrologic settings, but ecological function and habitat suitability as well. Invasive species presence remains a primary factor in reducing wetland ecological function in addition to human modification (Bertness et al. 2002). For this reason, we develop tools to identify common invasive species in United States wetlands and deepwaters including the common reed (*Phragmites australis*) and water chestnut (*Trapa natans*).

3.1.1 Prior Wetlands Mapping and Vegetation Characterization Efforts

In the United States, several wetlands mapping products exist that provide accurate delineation of wetlands and deepwaters at the national scale. Although these large-scale products characterize wetland functional classes specifically, they also provide a general assessment of wetlands vegetation. The United States Fish and Wildlife Service (USFWS) National Wetlands Inventory (NWI) is the most commonly used wetland product for the conterminous United States. The technical details of NWI development are discussed in the preceding chapter. The NWI is very spatially detailed and provides accurate wetland-upland classifications (Kudray and Gale 2000). However, we have noted instances where classifications of wetlands are incorrect over our study sites, especially with regards to vegetation characterization. In addition to potential inaccuracies, the NWI classification scheme has potential issues when performing wetland characterization with satellite imagery in conjunction with NWI data. The NWI uses the Cowardian classification within which wetlands are defined by the presence of hydrophilic vegetation, hydric soils, and/or temporary inundation. The NWI defines deepwaters as permanently inundated regions situated below the deepwater boundary of wetlands (Cowardin et al. 1979). It should be noted that deepwaters and wetlands are only differentiated by the permanence of surface waters and that deepwaters can be vegetated. In the context of remote sensing-based research, a deepwater habitat with aquatic vegetation emerging from the water's surface may be indistinguishable from a flooded wetland with similar vegetation. Because we implement a modified version of the Cowardin classification in this research effort, it is critical to note the differences between wetlands and deepwaters . In addition to being a stand-alone data product, the NWI is also the source for the United States tidal marsh assessment used in the Mcowen global tidal marsh inventory (Mcowen et al. 2017), the Feagan blue carbon Gross Primary Productivity (GGP) product (Feagan et al. 2020), and the National Landcover Database (NLCD) which is produced by several federal agencies under the auspices of the United States Geological Survey (USGS). The NLCD relies on the NWI for wetlands classification training data (Homer et al. 2015; Yang et al. 2018). The last version of the NLCD was produced for 2016 (Yang et al. 2018). Although the NLCD is based on moderate spatial resolution imagery (30-m), it is only released as a standalone product every five years (Homer et al. 2015; Yang et al. 2018). Because tidal marshes are highly dynamic, a five year temporal fidelity may not be sufficient to resolve short-term changes in wetlands extent which can occur on an annual basis, especially as related to wetlands losses that occur as a result of extreme storm events (Campbell et al. 2017; Howes et al. 2010; Turner et al. 2019). Having monitoring tools that support mapping of wetlands vegetation at a one to two year resolution would enable more effective habitat assessments, ecological forecasting, greenhouse gas inventory production, assessment of carbon cycling and storage, and wetlands migration/loss assessment due to sea level rise (Becket et al. 2016; Byrd et al. 2018; Holmquist et al. 2018; Ross and Adam 2013; Tobias and Neubauer 2009). In this research effort, we present a methodology that enables large-scale wetlands mapping and vegetation characterization at an annual resolution by fusing Landsat 8 imagery with Sentinel-1 Synthetic Aperture RADAR (SAR) imagery. This approach enables production of wetlands products that can be updated more frequently than the NWI and NLCD, and has the potential for global applicability, which we evaluate herein. In addition to detailed wetlands vegetation assessments that can be used to validate the NWI.

3.1.2 Rationale for Developed Satellite-Based Mapping

To assess the spatial distribution of tidal marshes, we focused the development of our wetlands mapping methodology on meeting two keys objectives. The first objective is accurate mapping of wetlands and deepwaters in the Gulf Coast and Mid-Atlantic regions using an approach based on satellite remote sensing that is scalable to global application. The second objective is the assessment of vegetation characteristics within these identified wetlands. One of the most fundamental and important assessments of emergent herbaceous wetland (i.e. marsh) vegetation characteristics is the identification of persistent and non-persistent vegetation types. Persistent vegetation has a significant portion of biomass that remains conspicuously present outside of the growing season, while non-persistent vegetation is readily decomposed at the end of the growing season (Cowardin et al. 1979; Odum 1988). In general, non-persistent vegetation is found only in emergent wetlands below a certain salinity threshold meaning this non-persistent vegetation serves as a salinity indicator for open water systems (i.e. streams, rivers, lakes, and estuaries) connected to wetlands (Odum 1988). According to the Cowardian classification, these open water systems are deepwaters habitats, but they are distinguished from deepwaters with above surface or at surface vegetation. From this point forward, we make the distinction between open water systems which are non-vegetated and vegetated deepwater systems (at or above surface), both of which are distinct from wetlands that are only temporarily flooded or inundated. The identification of non-persistent vegetation in tidally influenced wetlands is critical as it serves as an indicator of the tidal freshwater zone with low salinity, < 0.5 PPT on average. Tidal freshwater wetlands have some of the highest levels of biodiversity found in temperate regions and their presence serves as a sea level rise indicator (Leck et al. 2009). In spite of their importance very few remote sensing studies have focused on tidal freshwater wetland monitoring (Elmore 2008). In addition to vegetation persistence being an indicator of salinity of open water systems connected to wetlands, the accurate characterization of non-persistent and persistent wetland extents is also important for assessment of ecological setting and wetlands ecosystem services. Non-persistent and persistent vegetation have vastly different carbon cycling characteristics, geomorphological traits, and storm surge attenuation capabilities (Herbert et al. 2018; Odum 1988; Howes et al. 2010). A major applied focus of this research effort is the identification of invasive vegetation in wetlands and deepwater habitats which we carried out in concert with the two major research objectives.

To achieve the first research objective, we carried out a general wetlands classification which we term the level-1 classification. In the level-1 classification, we use the random forest machine learning approach to classify estuarine emergent wetlands (tidal marshes), palustrine emergent wetlands (non-tidal freshwater marshes), *Phragmites australis* dominated emergent wetlands, woody wetlands, non-vegetated wet regions (mudflats and sandbars), and open water (Breiman 2001). These classes are all found within the combined wetlands and deepwaters categorization described in Cowardin et al. (1979). Although *Phragmites australis* is a specific wetland vegetation class rather than a functional class like other level-1 classes, *Phragmites australis* possesses several traits that significantly differentiate it from other species of emergent wetlands vegetation, including a higher biomass, unique phenology, tendency to form monospecific stands, and a tendency to occupy distinct locations in a wetlands complex (general high elevations and along edges) (Prisloe et al. 2006; Smith 2013; Bertness et al. 2002). We surmised that multi-season satellite imagery would capture these unique traits allowing effective distinction from common wetland vegetation like *Spartina spp.* in estuarine wetlands and *Typha spp.* in palustrine wetlands as was demonstrated in Bourgeau-Chavez et al. (2013). Following the level-1 classification, we performed a level-2 classification of specific vegetation functional classes within the level-1 classified emergent wetlands and deepwaters. To develop our level-2 classification approach, we first evaluated timeseries satellite imagery across a range of wetland study sites with well-established wetland vegetation inventories to determine what forms of satellite imagery are most useful for deriving a decision tree-based mapping approach. We ultimately derived a decision tree approach making use of the same multi-temporal SAR and optical imagery used in the level-1 random forest classification, enabling identical pixel colocation between the level-1 and level-2 classifications and maximizing computational efficiency in image processing.

3.2. Materials and Methods

3.2.1 Study Sites

The target wetlands study sites we established included general study sites and intensive study sites. The general study sites cover large regions, while the intensive study sites cover smaller regions and have associated ground surveys which we conducted over many seasons in most cases. The motivation in selection of study sites was to exercise classification techniques over a wide variety of coastal wetlands systems. In the Mid-Atlantic region, general study sites include the Hudson River (NY-NJ), Housatonic River/ Long Island Sound (CT-NY), Delaware River (NJ-DE), Patuxent River (MD), and Choptank River (MD). The Gulf Coast general study sites included the Sabine River (TX), the Wax Lake Delta (LA), and Mississippi River wetlands including the Breton Sound and the Bird's Foot Delta (LA). These systems vary greatly in terms of geomorphology, hydrology, and salinity gradients.

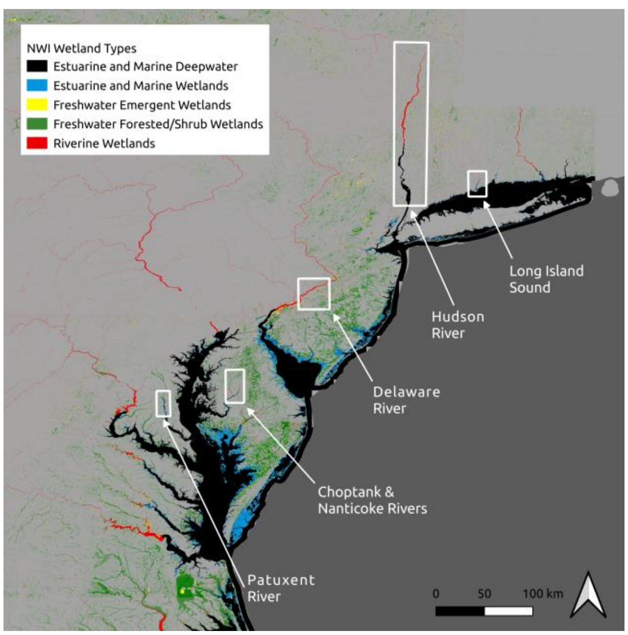

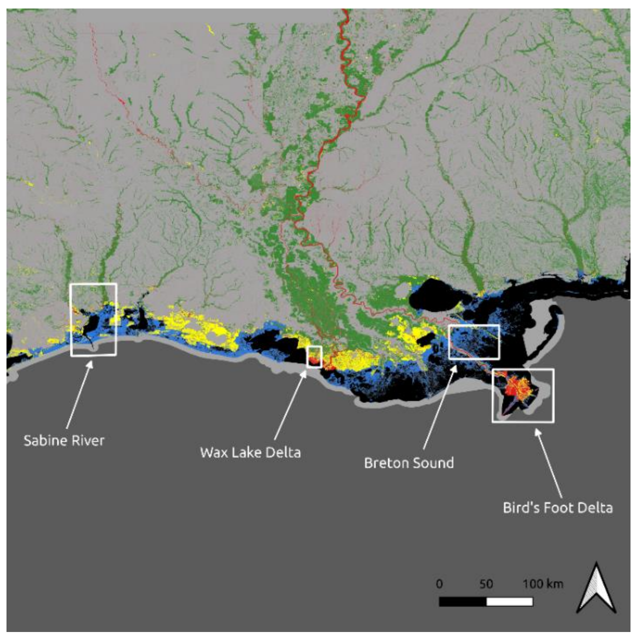

Figure 3.1. General study sites in the Mid-Atlantic (left) and Gulf Coast (right)

We selected the Jug Bay Wetlands Sanctuary as the intensive study site in the Patuxent River, the Wheeler Marsh system as a Long Island Sound intensive study site, and Beacon Bridge wetlands (not an official name) and Constitution Marsh sites as Hudson River intensive study sites. Jug Bay was selected as a study site as it possesses a mix of persistent and non-persistent emergent vegetation which is typical of tidal freshwater marshes throughout both the Gulf and Atlantic Coasts (Odum 1988; Leck et al. 2009; Swarth et al. 2013). The Wheeler Marsh system was chosen as an intensive study site due to the fact it is meso-saline brackish and thus possesses only persistent emergent vegetation, but also has a high frequency and magnitude of tidal inundation relative to other sites. This presents the potential for confusion between vegetation phenological variability and hydrologic variability when characterizing wetlands with timeseries SAR imagery, a potential challenge we explicitly sought to address in this effort. The Hudson River wetlands sites were selected as intensive study sites because they are tidal freshwater and possess a mixture of persistent and non-persistent vegetation types. The final datasets used for analyses are a blend of our own ground surveys, wetland surveys from other studies, the NWI, and our analysis of recent aerial photography. At Jug Bay we developed a final dataset from a survey by Swarth et al. (2013), which represents a more accurate classification than the NWI which in certain areas incorrectly classified the non-persistent emergent vegetation species *Nuphar lutea* as either persistent emergent tidal marsh or aquatic bed dominated deepwaters (as shown in Figure 3.2). At Constitution Marsh, a New York State Tidal Wetlands Inventory (NYS-TWI) covering the Hudson River Estuary (HRE) is used to more accurately identify vegetation than the NWI, although we did not note incorrect NWI classifications of functional wetlands at this site. In the Beacon Bridge wetlands, we used NWI and also note areas of confirmed *Trapa natans* expansion based on our ground surveys, and suspected *Trapa natans* based on 2017 aerial photo identification. In general, the NWI accurately classified *Trapa natans* as aquatic beds in Hudson River sites but did not cover certain areas of recent expansion. For Wheeler Marsh, we use NWI boundaries, but have updated the wetland classes based on ground survey confirmation shown in parentheses in Figure 3.2. For Wheeler Marsh the "low marsh" class represents sparse *Spartina alterniflora* and mudflat, "mid marsh" represents dense *Spartina alterniflora*, and "high marsh" represents *Spartina patens* and *Distichlis spicata* mix. The NWI E2SS1P class is incorrect and represents an estuarine system with scrub-shrub vegetation, however our site visits indicate this NWI boundary is best represented by an estuarine high marsh class as shown in the site photos in Figure 3.3.

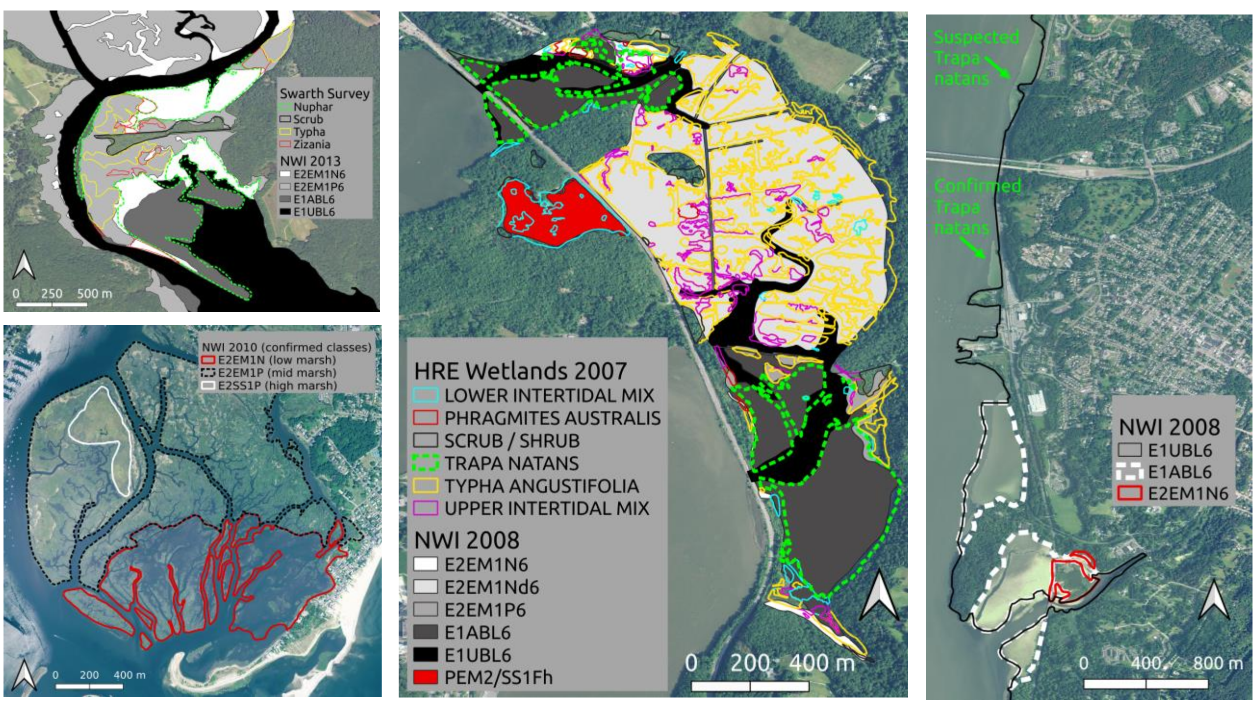

Figure 3.2. Intensive study sites with final wetland vegetation inventory datasets; Jug Bay, Constitution Marsh, Beacon Bridge wetlands (not an official name), and Wheeler Marsh. Wheeler Marsh ground-confirmed classes are shown in parentheses. Note there are several cases where NWI classifications do not match more detailed wetlands inventories or ground surveys.

Figure 3.3. Site photo examples of wetland vegetation for the Beacon Bridge wetlands, Constitution Marsh, Jug Bay, and Wheeler Marsh. Note in many of the photos connected surface waters and aquatic beds are shown adjacent to wetlands. Constitution Marsh presents a clear demonstration of the fine elevation gradients that zonate moderate elevation marsh wetland vegetation like *Typha* from low elevation marsh wetland vegetation like *Nuphar* from floating aquatic deepwater vegetation like *Trapa natans*. Wheeler Marsh shows a common zonation of persistent vegetation types in a brackish tidal marsh complex.

3.2.2 Satellite Image Assembly and Selection Rationale

Sentinel-1 C-band SAR, Landsat 8 optical/IR, and Sentinel-2 optical/IR imagery were initially evaluated for application to wetlands vegetation characterization. After initial testing, we focused this timeseries analysis on Sentinel-1 SAR imagery due to its more frequent revisit (when considering cloud impacts on optical imagery), lack of atmospheric impacts, and enhanced capabilities in characterizing vegetation structural phenology. Initial qualitative comparative assessments of Sentinel-1 SAR imagery between Jug Bay and the Hudson River sites indicated similar temporal signatures. Upon more detailed investigation it was determined that Jug Bay's non-persistent satellite signatures were attributed to the presence of rooted emergent vegetation (defined as wetlands), while the Hudson River signatures were primarily attributed to the presence of a non-persistent floating aquatic species of invasive water chestnut (*Trapa natans*) (defined as deepwaters). While carrying out this research effort, it became apparent that it was critical to distinguish between floating aquatic non-persistent vegetation and rooted non-persistent emergent vegetation. This was crucial in a general technical sense regarding development of accurate mapping tools differentiating wetlands from deepwaters, as well as in a more specific sense of monitoring invasive vegetation in the Hudson River.

We evaluated Sentinel-1 SAR backscatter for different wetlands vegetation classes between 2017 and 2019, extracting spatial mean backscatter for each class and tracking changes from 2017 to 2019 at a 12-day resolution (Sentinel-1a revisit time). We used Google Earth Engine (GEE) for initial image processing in this timeseries assessment (Gorelick et al. 2017). Water level observations in the Wheeler Marsh and Jug Bay wetlands sites were also assessed. After performing this timeseries assessment, we processed imagery using GEE for the purpose of mapping emergent wetlands for the Gulf and Mid-Atlantic Coasts and with the objective of developing a globally scalable classification methodology. Although we focused our timeseries assessment on Sentinel-1 SAR imagery, we also noted the importance of optical imagery in assessment of vegetation greenness. To assess vegetation greenness, we used the Normalized Difference Vegetation Index (NDVI), which has remained one of the most well-known and effective indices for assessing the presence of vegetation, vegetation greenness, and can assess vegetation biomass in certain instances (Tucker 1979; Prabhakara et al. 2015). NDVI and NDVI variants, have been demonstrated as especially useful in assessing marsh vegetation greenness and canopy closure (Bartlett and Klemas 1981; Langley and Megonigal 2012; Lopes et al. 2020). The NDVI summer temporal median (June through August) was computed from Landsat 8 surface reflectance, cloud masked imagery (Vermote et al. 2016; Zhu et al. 2015) in GEE. The importance of optical-SAR fusion in wetlands characterization was highlighted in Chapter 2, where SAR imagery was found to be more useful than optical in classifying different vegetation types within wetlands, while optical imagery and digital elevation models (DEMs) were more important than SAR for separating wetlands from other landcover types. Based on our findings from the satellite image timeseries assessment (results section 3.1) and previous efforts, we performed classifications using an 8-band SAR-optical-DEM stack consisting of Sentinel-1 VV annual mean, VH annual mean, VV annual standard deviation (SD), VV Spring mean, VV Summer mean, VV Fall mean, Landsat 8 Summer NDVI, and the Shuttle Radar Topography Mission (SRTM) DEM. These particular layers represent a selection of layers most useful for carrying out both the level-1 and level-2 classifications as described in the following sections. Further, the temporal mean compositing of Sentinel-1 imagery serves to reduce speckle compared to single date SAR imagery (Yu and Quegan 2001).

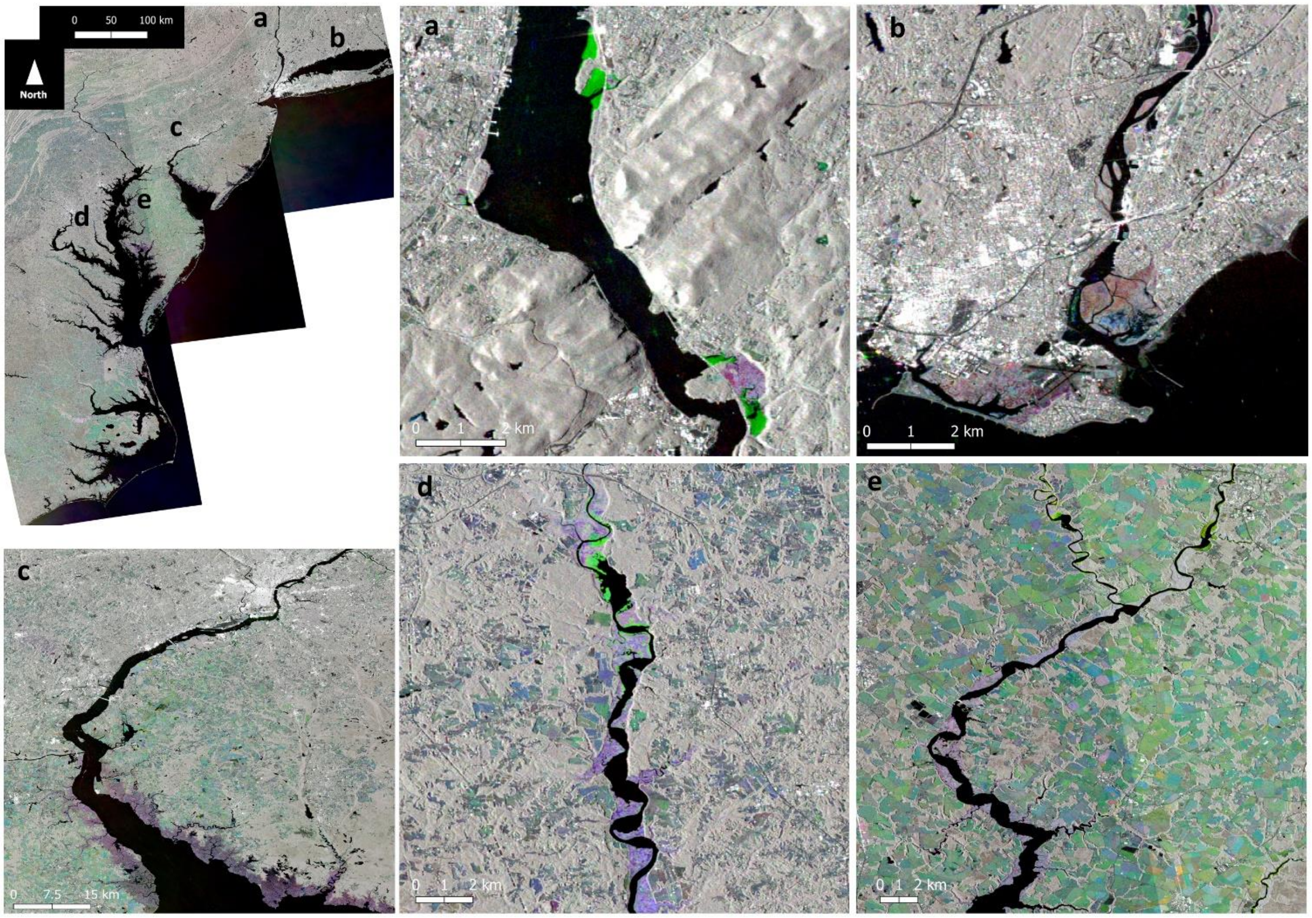

Figure 3.4. Sentinel-1 multi-season VV imagery over Mid-Atlantic study sites. RGB channels correspond to spring, summer, and fall backscatter layers, respectively. Tidal marshes dominated by persistent emergent vegetation in Wheeler Marsh (b) and Delaware Bay (c) show enhanced backscatter in spring and fall (as shown by red, blue, purple colors). Hudson River (a), Patuxent River (d), and Choptank River (e) show enhanced backscatter during summer for non-persistent vegetation in bright green, with a mix of persistent scattering (purple color) throughout the study sites. Note the mountainous areas of the Hudson River Highlands do not exhibit temporal differences in backscatter while the agricultural regions of the Choptank watershed show enhanced backscatter during the summer growing season. Urban areas in all sites exhibit high and temporally invariant backscatter shown as white pixels.

3.2.3 Level-1 Classification of Functional Wetlands Classes

The objective of the level-1 classification was to accurately map tidal wetlands of the Gulf Coast and Mid-Atlantic United Sates using supervised classification approaches. We utilized the random forest classifier for this purpose (Breiman 2001). Following Lamb et al. (2019), we created a merged training-validation dataset by combining the NWI with the 2016 NLCD and selecting wetland training points only where the classes matched (e.g. herbaceous NLCD wetlands code 95 must match one of NWI estuarine emergent classes like E2EM21P, E2EM1N to produce a valid training point). Classes of non-wetland landcover were selected directly from the 2016 NLCD. The generated training-validation dataset consisted of ten million points. We reduced this dataset to approximately 400,000 training-validation points by performing two random samples with approximately half of the points coming from a stratified random sample with an equal number of points per cover class, and the other half coming from a random sample. This culminated in a final training-validation dataset that weighted class prevalence while preserving a baseline representation of uncommon classes. The aforementioned NLCD training-validation layer was generated in GEE by exporting NLCD layers from 2016 along with the respective SAR-optical-DEM image stacks for the Gulf Coast and Mid-Atlantic regions. This approach ensured that training-validation layers and the satellite image stacks were georegistered. After the training-validation dataset was generated and the SAR-optical-DEM image stack was exported from GEE and downloaded to a local computer, we used the R programming language to ingest the SAR-optical-DEM stacks along with the training-validation sets. Within the R environment, we used the Random Forest package to perform supervised classifications of the SAR-optical-DEM stack with the training-validation dataset. We parameterized the random forest (RF) classifier with 500 trees. In the level-1 classification we identified open water, estuarine emergent wetlands, palustrine emergent wetlands, *Phragmites australis* dominated emergent wetlands, and woody wetlands. We assessed classification accuracy using both confusion matrices and post-classification layer importance assessments.

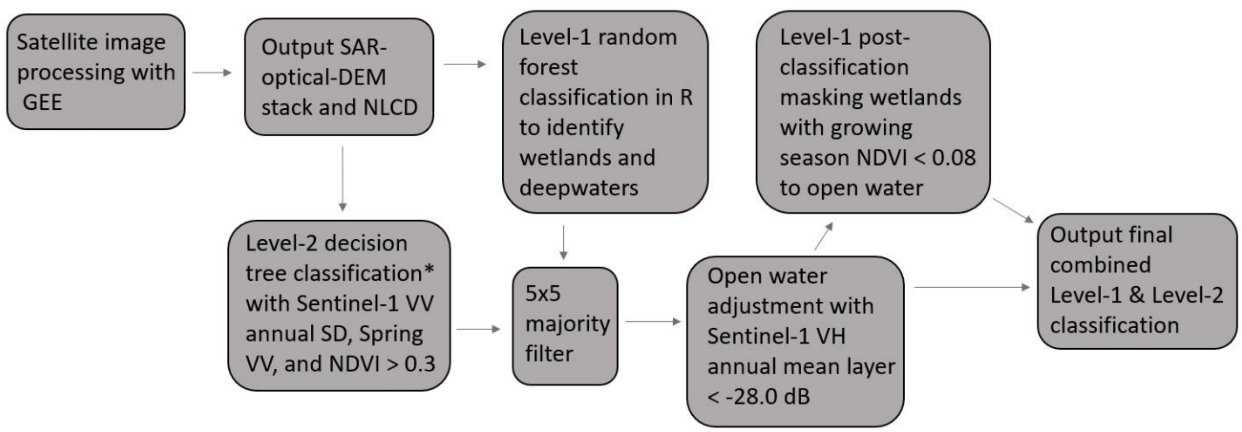

Figure 3.5. Schematic of image processing, classification, and post classification adjustments. * Level-2 decision tree classification final derivation is depicted in the following section (Figure 3.6).

3.2.4 Level-2 Classification of Wetland Vegetation

The objective of the level-2 classification was to develop a rule-based approach employing decision tree and thresholding to accurately identify persistent and non-persistent vegetation within the emergent wetlands and deepwaters identified in the level-1 classification and to the further objective of separating non-persistent emergent vegetation from non-persistent floating aquatic vegetation. Lamb et al. (2019) demonstrated that Sentinel-1a VV backscatter annual standard deviation (SD) was one of the more critically important image layers in allowing the separation of non-persistent *Nuphar lutea* from all other wetland vegetation (both woody and persistent emergent) at the Jug Bay study site when using a supervised random forest classification (overall classification accuracy > 95%). However, this prior mapping effort did not attempt to develop rule-based approaches with the potential for being applied across multiple wetlands systems and across multiple regions, nor did it provide a comparison between emergent wetland non-persistent vegetation and floating aquatic deepwater non-persistent vegetation. In this study we included *Nuphar lutea* and *Trapa natans* dominated sites to determine if they could be first identified as a single non-persistent class, and then split based on differences in biomass, which we surmised the C-band SAR backscatter would be sensitive to. In selecting these types of vegetation, our goal was to apply timeseries C-band SAR and the associated Sentinel-1 VV backscatter annual SD to classify non-persistent vegetation within a relatively wide biomass range. Another objective of this study was to determine which seasonally averaged Sentinel-1 VV layers would be useful for separating non-persistent emergent vegetation from *Trapa natans*. Guided by the findings in results section 3.1.2, we developed a decision tree classification by applying a threshold of 4.7 dB to Sentinel-1 annual SD imagery to split persistent and non-persistent vegetation classes and then splitting persistent emergent vegetation from *Trapa natans* by applying a -17.25 dB threshold to Sentinel-1 Spring VV imagery (see results section 3.1.2 for justification).

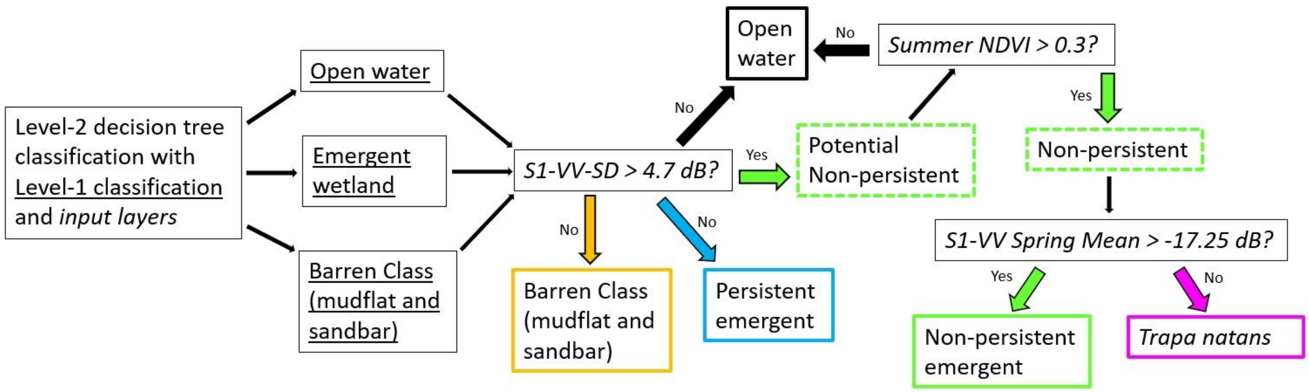

Figure 3.6. Final level-2 classification for the Mid-Atlantic for 2017. The Gulf Coast level-2 classification utilizes the same methodology but does not separate between aquatics (e.g. *Trapa natans*) and non-persistent emergents because we do not have sufficiently detailed wetland surveys to effectively evaluate this split.

3.2.5 Post-Classification Accuracy Assessment & Processing

To correct classification errors, a post-classification adjustment was produced using the Sentinel-1 VH annual mean layer to convert any wetland class to open water if backscatter was lower than -28 dB. A second post classification adjustment that utilizes growing season vegetation index thresholding (NDVI) was produced to mask classified wetlands to open water if NDVI values were below 0.08. Because mixed pixels along both wetland-water edges and barren class (rock, sand, mud areas)-water edges were post-classified as open water, this necessarily creates a slight positive biasing of the open water class prevalence and a slight negative biasing of the barren class. However, these adjustments were critical to obtain well-constrained estimates of emergent wetland extent, which is the primary focus of this research effort. We adjusted both the level-1 and level-2 classification layers with a 5x5 majority filter which reduced erroneous classifications of single pixels and small pixel clusters, a common issue with per-pixel classifiers like random forest. The combined, post-classified level-1 and level-2 wetlands mapping results are presented in Figures 3.13 and 3.14 for the Mid-Atlantic and Gulf Coast regions, respectively.

3.2.6 Study Site-Based Classification Performance Assessment

We evaluated the level-1 and level-2 classification results using independent datasets at three study sites. This in-depth performance assessment served two purposes. The first purpose is to showcase how the developed methodologies can be directly applied to wetlands ecological assessments and the identification of invasive vegetation. The second purpose of this assessment is to provide an in-depth performance assessment with high quality independent datasets. In the first performance assessment, we evaluated the performance of level-2 classification in detecting *Trapa natans* in the Hudson River. We used the Hudson River Submerged Aquatic Vegetation (HRSAV) dataset produced by the Hudson River National Estuarine Research Reserve, New York State Department of Environmental Conservation, and the Cornell Institute for Resource Information Services, as an external validation source for this performance assessment. The HRSAV does not map emergent wetlands as the 2007 New York State Tidal Wetlands Inventory does, but does track *Trapa natans*, with the most recent HRSAV release in 2018. In this Hudson River case study, we also assess which level-1 classes were most associated with identified *Trapa natans* aquatic beds, which have potential to be classified as open water, mudflats, and even emergent wetlands. In the second performance assessment we evaluated level-1 and level-2 classification performance in mapping emergent wetlands in the Choptank River. To assess performance of the level-1 and level-2 classifications we develop an independent evaluation dataset with 2017 Summer National Aerial Imagery Program (NAIP) imagery. We digitize the boundaries of persistent and non-persistent vegetation identified in the NAIP imagery and then assessed the performance comparison between the NAIP wetland dataset and level-1 and level-2 classifications. In the third performance assessment, we evaluated level-1 and level-2 classification performance in the Wax Lake Delta. In this case we use the NWI as a performance evaluation dataset. Although we used NWI data for training the level-1 classification, the dataset we used in the Wax Lake Delta is still considered independent because it is from the riverine wetland class, which we had excluded in the level-1 classification to enable mapping of wetland systems based on vegetation community composition and salinity rather than location in a riverine setting. The NWI data for the Wax Lake Delta was updated in 2017 and includes four riverine NWI classes. These classes are: R1ABT (riverine, tidal, aquatic bed, semi-permanently flooded), R1AB3V (riverine, tidal, aquatic bed, rooted vascular, permanently flooded), R1AB3T (riverine, tidal, aquatic bed, rooted vascular, semi-permanently flooded), and R1AB4V (riverine, tidal, aquatic bed, floating vascular, permanently flooded). Carle et al. (2015) noted that vegetation in the Wax Lake Delta generally exhibited species zonation as a function of elevation. Mixed grasses and forbs dominate intermediate elevations while lower elevation mudflats are generally dominated by non-persistent emergent species like *Nelumbo lutea* and *Sagitarria spp.*. The lowest elevation vegetated regions are dominated by non-persistent floating-leaved *Potamogeton nodosus*. We evaluated the use of the level-2 classification in identifying these non-persistent species using the range of the four tidally influenced NWI classes described above. Because Carle et al. (2015) did not note the presence of *Trapa natans* in this system, we evaluated only the presence of the general non-persistent class which includes both emergent wetland vegetation and aquatic deepwater vegetation. All three independent performance validation datasets (HRSAV, NAIP, and NWI) were shapefile-based datasets which were buffered inward by 30-m to reduce the influence of edges and mixed pixels in assessing the performance of the 30-m level-1 and level-2 classifications. Ideally, this inward buffer distance would be 60-m to 90-m to provide certainty of edge removal and account for satellite geolocation errors. However, we found a 60-m buffer to be too spatially restrictive for smaller shapefile polygons in all these datasets. Ultimately, a 30-m buffer was chosen as a compromise for the HRSAV and NWI datasets for the Hudson River and Wax Lake Delta. The even smaller area of the NAIP-based evaluation dataset for the Choptank River prohibited the use of a buffer.

3.3. Results

3.3.1. Study Site Assessments

We compared the spatial mean Sentinel-1 backscatter for wetlands vegetation classes within each of the Mid-Atlantic intensive study sites shown in Figure 3.2 maps. The VV and VH backscatter timeseries analyses for each study site are shown in Figures 3.7-3.10. The timeseries comparison showed that persistent vegetation classes exhibited reduced backscatter variability associated with vegetation phenology as compared to non-persistent vegetation classes which exhibited well-defined backscatter seasonality over three years of analysis for both VV and VH polarizations. The backscatter response of persistent vegetation was largely dependent on SAR polarization, vegetation density, marsh soil surface elevation, and the combination of water level change and seasonal vegetation structural change. For instance, the E2EM1P class representing dense *Spartina alterniflora* at Wheeler Marsh in Figure 3.7 showed consistent VV backscatter increases around September of each year where satellite overpasses also happened to correspond with high tides. Similarly, the Jug Bay *Typha spp*. series in Figure 3.8, showed similar VV backscatter increases in the fall season during high tide events. Field visits to both sites confirmed that both *Spartina alterniflora* and *Typha spp*. exhibit changes in structure during the fall season when leaf and stem orientations transition from a primarily vertical orientation to a more random orientation. Combined with high water events that increase the inundated wetlands area, this may result in increased backscatter via the double bounce scattering mechanism where increasingly horizontal leaves and stems more efficiently backscatter the opposite polarized VV SAR signal. The backscatter decrease in the VH channel is also indicative of increases in inundated wetland area which reduces volume scattering. The influence of seasonal processes on backscatter is also apparent in the Jug Bay *Typha spp*. series during summer, where backscatter decreases consistently during the summer season over the three years. This response was especially notable for the VV polarization. In contrast to the dense canopies and moderate wetland elevations represented by the *Typha spp*. series in Figure 3.8 and E2EM1P class representing dense *Spartina alterniflora* in Figure 3.7, the Wheeler Marsh E2EM1N class in Figure 3.7 represents a lower elevation and a less dense canopy. Outside of the fall season when the E2EM1N class exhibits slight backscatter increases (or relative stability), throughout the majority of the timeseries, backscatter values decrease as a function of tidal stage. The VH polarization showed fairly consistent decreases as a function of tidal stage. Occupying a similar low elevation, the non-persistent *Nuphar lutea* series from Jug Bay in Figure 3.8 shows VV and VH backscatter decreases that correspond to tidal stage, especially in the fall when this vegetation is decomposing. From late fall through spring *Nuphar lutea* matches the open water series VV and VH backscatter very closely. The similar VV and VH backscatter between open water and non-persistent *Trapa natans* from Constitution Marsh can be observed in Figure 3.9. Although, the backscatter timeseries between *Trapa natans* and *Nuphar lutea*, suggest *Trapa natans* has a substantially shorter growing season as shown in Figures 3.9 and 3.10. Another key distinction between these non-persistent vegetation classes is that *Nuphar lutea* exhibits fairly large backscatter temporal variability in the fall season that, along with vegetation senescence, may be caused by high water levels partially or completely submerging these rooted plants. The fact that *Trapa natans* is floating rather than rooted may explain why backscatter decreases gradually outside of the growing season, since water level changes do not impact the amount of *Trapa natans* exposed above the water's surface.

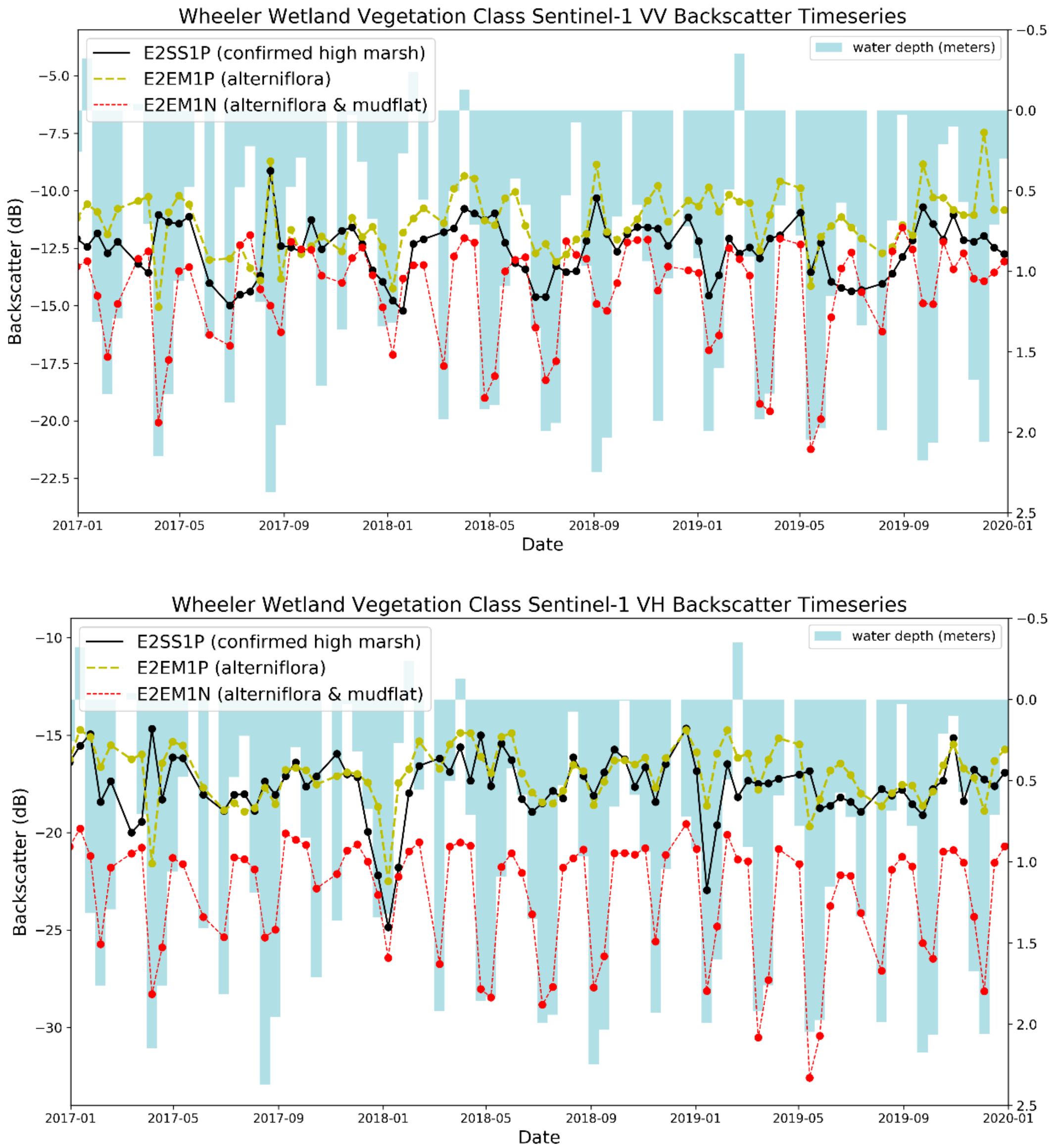

Figure 3.7. Wheeler Wetland Vegetation Class Sentinel-1 VV and VH Backscatter Timeseries (upper and lower panels, respectively). Water depth (in meters) is the NOAA tide gauge at Bridgeport (ID: 8467150) calibrated to in-marsh water level changes observed with Onset HOBO sensors from August 2018 to December 2018. Calibrations include time and water depth adjustments. E2EM1N (red dotted series) represents low elevation portion of wetland complex with sparse *Spartina alterniflora* and mudflat backscatter series. E2EM1P (gold dashed series) represents middle elevation marsh with dense *Spartina alterniflora*. E2SS1P (black series) is high marsh dominated by *Spartina patens*, *Distichlis spicata*, and short-form *Spartina alterniflora*. For both E2EM1P and E2SS1P some *Phragmites australis* is present along wetland-open water and wetland-upland edges.

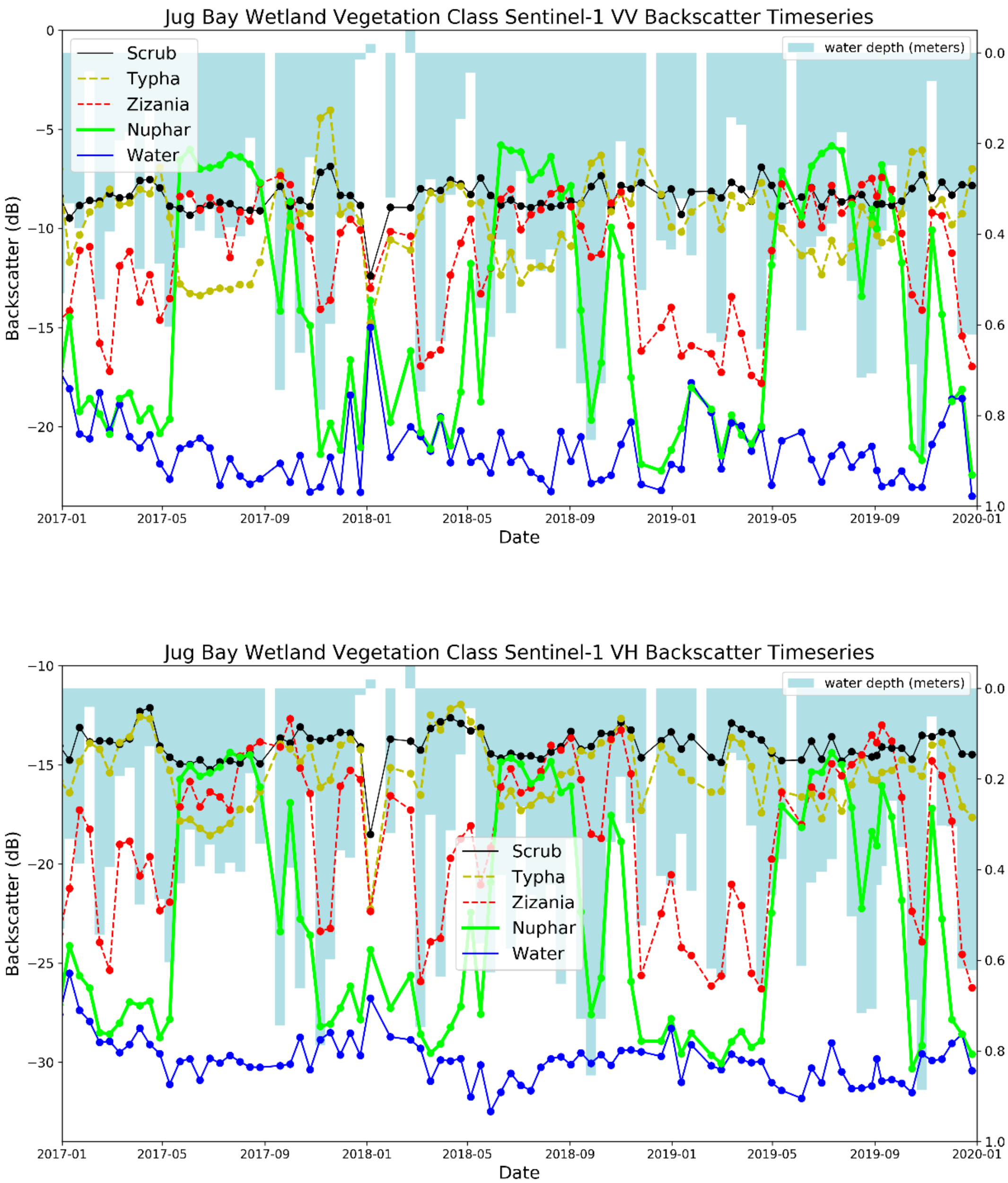

Figure 3.8. Jug Bay Wetland Vegetation Class Sentinel-1 VV and VH Backscatter Timeseries (upper and lower panels, respectively). Water depth (in meters) is the NOAA tide gauge at Solomon's Island (ID: 8577330) calibrated to in-marsh water level changes observed with Onset HOBO sensors from October 2019 to December 2019. Calibrations include time and water depth adjustments. All series represent spatial mean backscatter from Jug Bay wetland classes originally published in Swarth et al. (2012) and updated in Lamb et al. (2019). The wetland classes are as follow: solid black series = shrub-scrub, dashed gold series = *Typha spp*., red dashed series = *Zizania aquatica*, solid green series = *Nuphar lutea*, solid blue = open water.

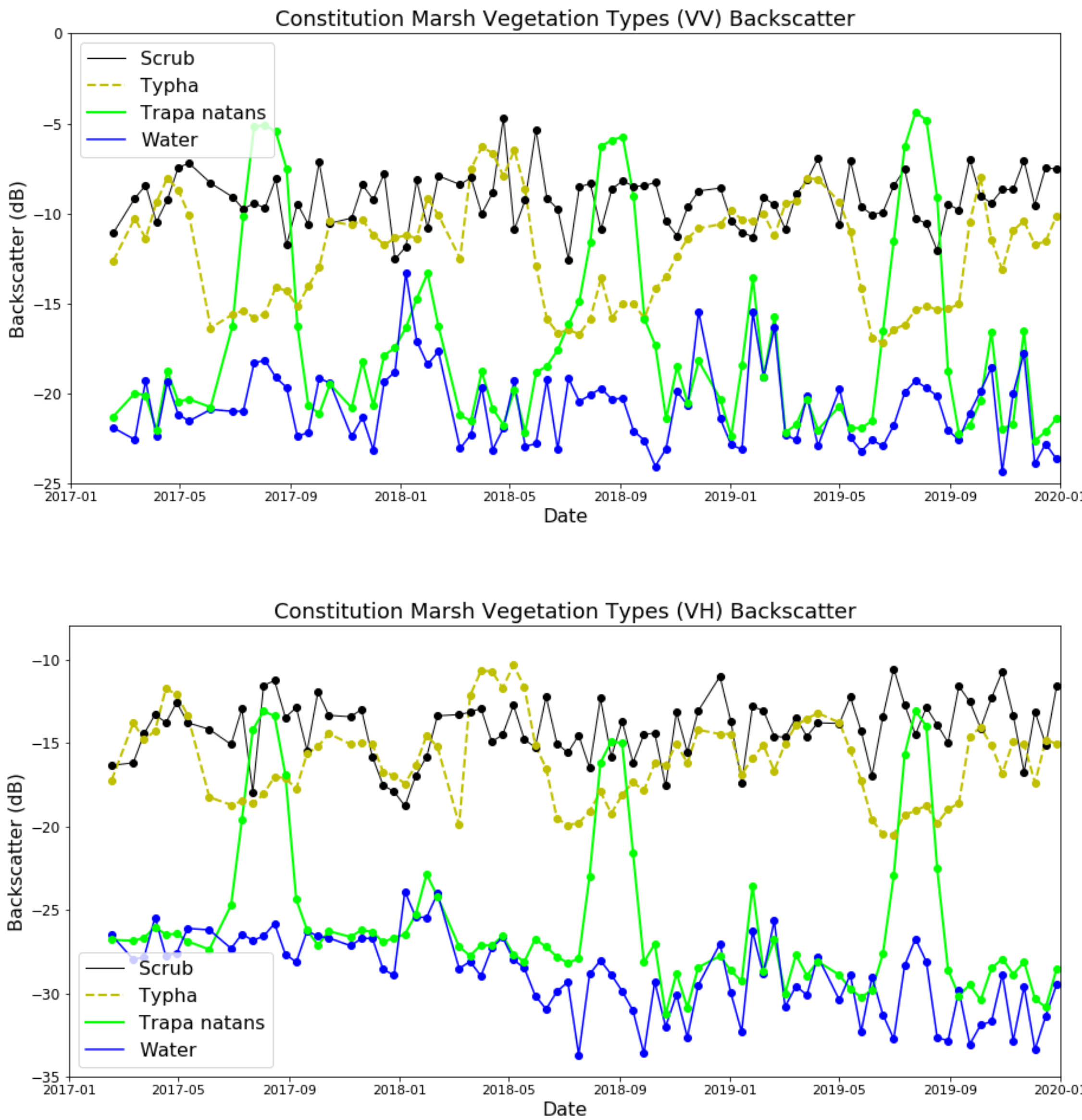

Figure 3.9. Constitution Marsh Vegetation Types Sentinel-1 VV and VH Backscatter Timeseries (upper and lower panels, respectively). Note that open water class (solid blue) and *Trapa natans* (solid green) exhibit similar backscatter changes outside of the growing season. *Typha spp.* series (dashed gold) tends to decrease in backscatter during the growing season, while *Trapa natans* backscatter peaks above both scrub series (solid black) and *Typha spp.* during the growing season.

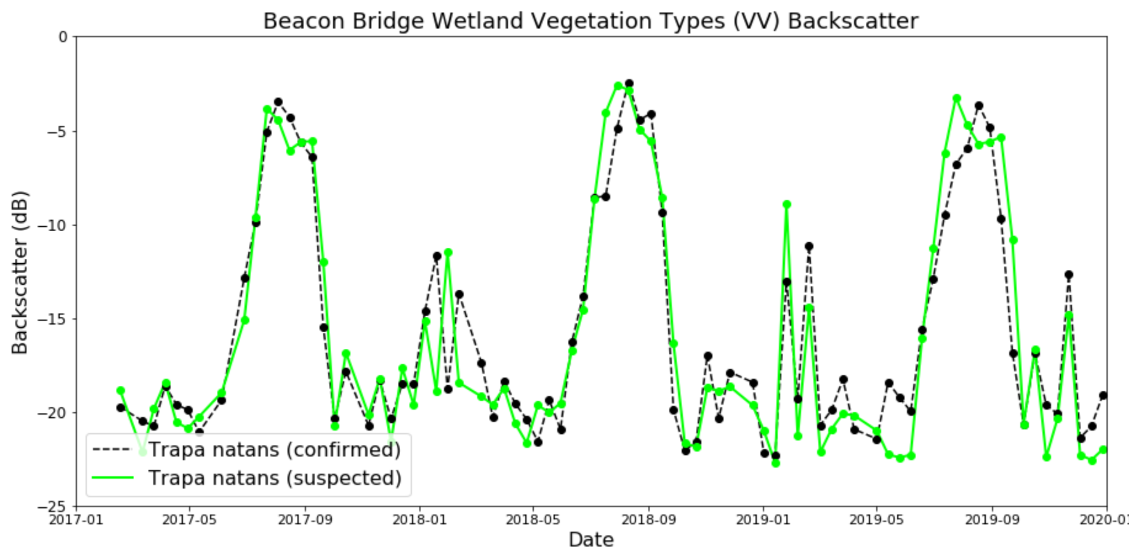

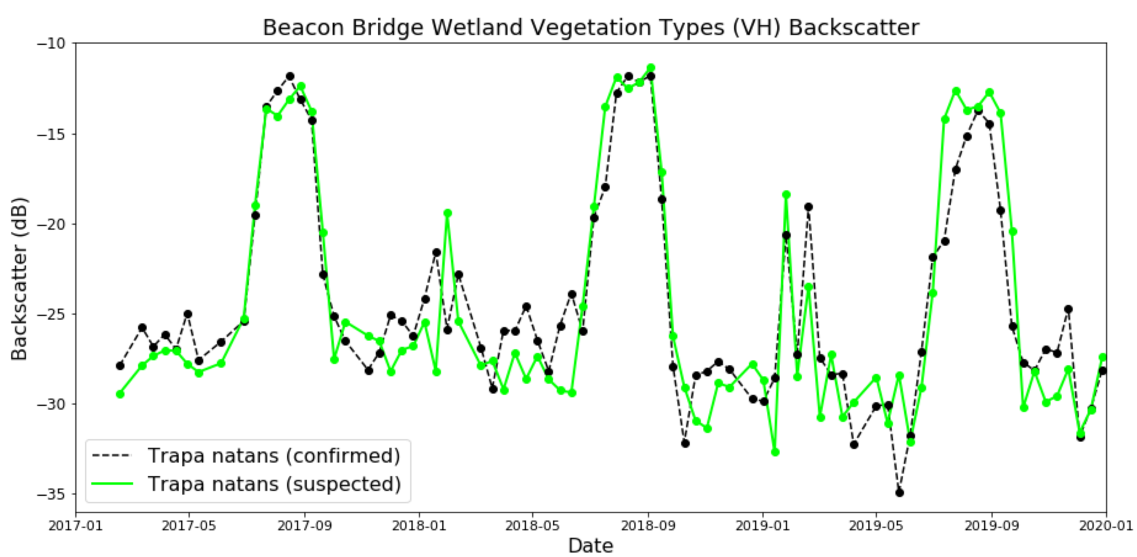

Figure 3.10. Beacon Bridge Wetland Vegetation Types Sentinel-1 VV and VH Backscatter Timeseries (upper and lower panels, respectively). The confirmed *Trapa natans* series (solid green) was verified with a site visit on June 2019. The suspected *Trapa natans* series (dashed black) was derived from digitized aerial photography noting similarity between the ground-identified *Trapa natans* (confirmed). The regions that these series cover are shown in Figure 3.2.

3.3.2 Assessment of Sentinel-1 Imagery for Level-2 Vegetation Classification

The high levels of backscatter variability tracking the growth phenology of the non-persistent vegetation classes (shown in Figures 3.7-3.10) facilitated the temporal reduction of the SAR dataset by computing the annual mean and standard deviation (SD) layers for Sentinel-1 VV and VH polarization timeseries imagery. For all non-persistent vegetation, the VV polarized backscatter exhibited higher peaks in the summer, and generally higher SD overall compared to VH polarized backscatter (Figures 3.7-3.10). For this reason, we utilized VV annual SD imagery for vegetation characterization rather than VH annual SD imagery. After observing high levels of spatial variability in 2017 VV annual SD imagery (hereafter referred to as VV-SD) comparing persistent and non-persistent vegetation types, we evaluated separability between the vegetation classes within each target wetland site by extracting all VV-SD pixels within the bounds of shapefiles corresponding to each wetland vegetation type. We then examined distributions to determine if a rule-based decision tree approach could be applied to split persistent and non-persistent emergent classes. We found that thresholding can effectively separate persistent and non-persistent vegetation using the VV-SD (annual standard deviation backscatter) layer at a threshold of 4.7 dB (green horizontal line in Figure 3.11). To further separate non-persistent aquatic vegetation from non-persistent emergent vegetation, we applied a separate threshold with VV mean imagery for the spring season (04/15/2017 to 06/15/2017) (hereafter referred to as VV-Spring), which allowed separation between *Trapa natans* and non-persistent emergents (Figure 3.11). These results informed our final derivation of the level-2 classification shown in methods section 2.4 and Figure 3.6).

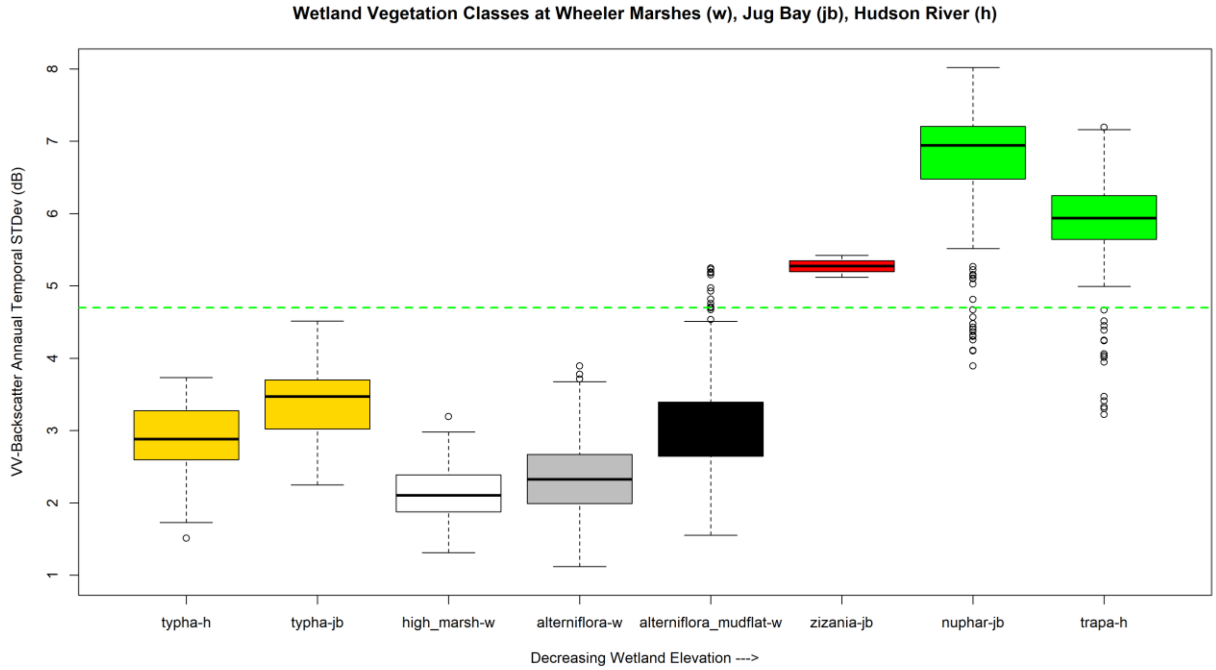

Figure 3.11. 2017 Sentinel-1 Annual Standard Deviation Layer by Wetland Vegetation Class at Wheeler Marshes (w), Jug Bay (jb), and Hudson River (h) sites. In boxes, first term represents wetland vegetation type and second term is location (e.g. "typha-h" is *Typha spp.* from Constitution Marsh at the Hudson River). All boxes represent VV-SD extraction for the wetland bounds shown in Figure 3.2 that were also used for time series spatial mean backscatter computation in Figures 3.7-3.10. Note that colors also correspond to vegetation type in Figures 3.7-3.10, except for Wheeler Marsh where grayscale box colors represent elevation gradient. Note threshold of 4.7 dB threshold separates persistent and non-persistent vegetation (horizontal dashed green line).

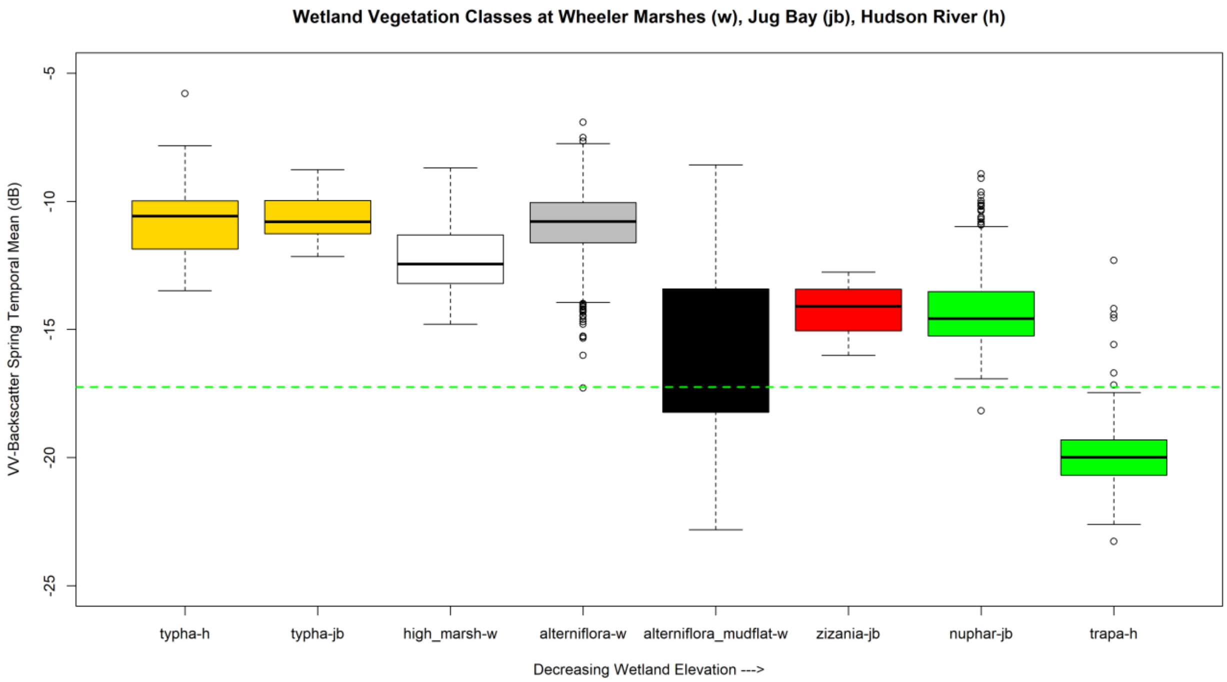

Figure 3.12. 2017 Sentinel-1 Spring Mean Backscatter by Wetland Vegetation Class at Wheeler Marshes (w), Jug Bay (jb), and Hudson River (h) sites. Naming convention, color schemes, and areas of extraction are the same as Figure 3.11. Note with the VV Spring layer, a threshold of 17.25 dB separates *Trapa natans* from other non-persistent vegetation (horizontal dashed green line).

3.3.3 Level-1 Classification Results and Accuracy Assessment

We performed the level-1 classifications separately for the Mid-Atlantic and Gulf Coast regions. After carrying out the classifications we quantitatively assessed performance accuracy via confusion matrices (Tables 3.1-3.2) and also post-classification variable importance assessment (Tables 3.3-3.4) as outputs from the random forest classification process. In addition to providing a regional scale classification as shown in Figure 3.12, we also demonstrate wetland classification performance over general study sites in the Hudson River, Housatonic River, Delaware River, Patuxent River, and Choptank River (Figure 3.13, sub-panels a-e). In part, these riverine regions were selected for performance assessment as they contain some well-defined salinity gradients to assess the split between palustrine emergent wetlands (non-tidal freshwater marshes) and estuarine emergent wetlands (tidal marshes). The Delaware River, Patuxent River, and Choptank River all exhibited very well-defined gradients that roughly occur along the freshwater tidal transition. *Phragmites australis* was mapped in all sites in Figure 3.13. *Phragmites australis* tended to occur along wetland-upland edges and along freshwater-brackish transitions. The level-1 extent of *Phragmites australis* agrees with previous publications in the Chesapeake Bay finding that *Phragmites australis* was most present on the Chesapeake Bay's Eastern Shore and most strongly associated with the presence of agriculture and moderate levels of disturbance (Sciance et al. 2016). The three emergent classes (estuarine emergent, palustrine emergent, and *Phragmites australis*) were all mapping with user's and producer's classification accuracies greater than 81% as shown in table 3.1. When these three emergent classes were aggregated into a single emergent wetland class, accuracy user's accuracy increased to 89.69% and producer's accuracy increased to 93.19%.

The level-1 classification performance in the Gulf Coast region was evaluated largely in the same manner as was the Mid-Atlantic described. Four general study sites with strong salinity gradients were chosen as assessment sites. These sites included the Sabine River wetlands, Wax Lake Delta wetlands, Brenton Sound wetlands, and Bird's Foot Delta wetlands (Figure 3.14, panels a-d). The mapped wetland distributions in these sites indicate the presence of salinity gradients which are strongly influenced by the presence of major river systems. For instance, the Brenton Sound and Bird's Foot Delta classified wetlands indicate the presence of palustrine wetlands closest to the Mississippi River and major freshwater diversions, whereas estuarine emergent marshes dominate away from major freshwater discharges. *Phragmites australis* was most present in the Bird's Foot Delta which largely agrees with descriptions of wetland vegetation in this area by the Audubon Society (Audubon). Overall classification accuracy of the three emergent classes is much lower than Mid-Atlantic sites at around 70% (Table 3.2). The aggregation of these three emergent classes into a single emergent class yields accuracies higher than the Mid-Atlantic with a user's accuracy of 91.81% and producer's accuracy of 95.02%.

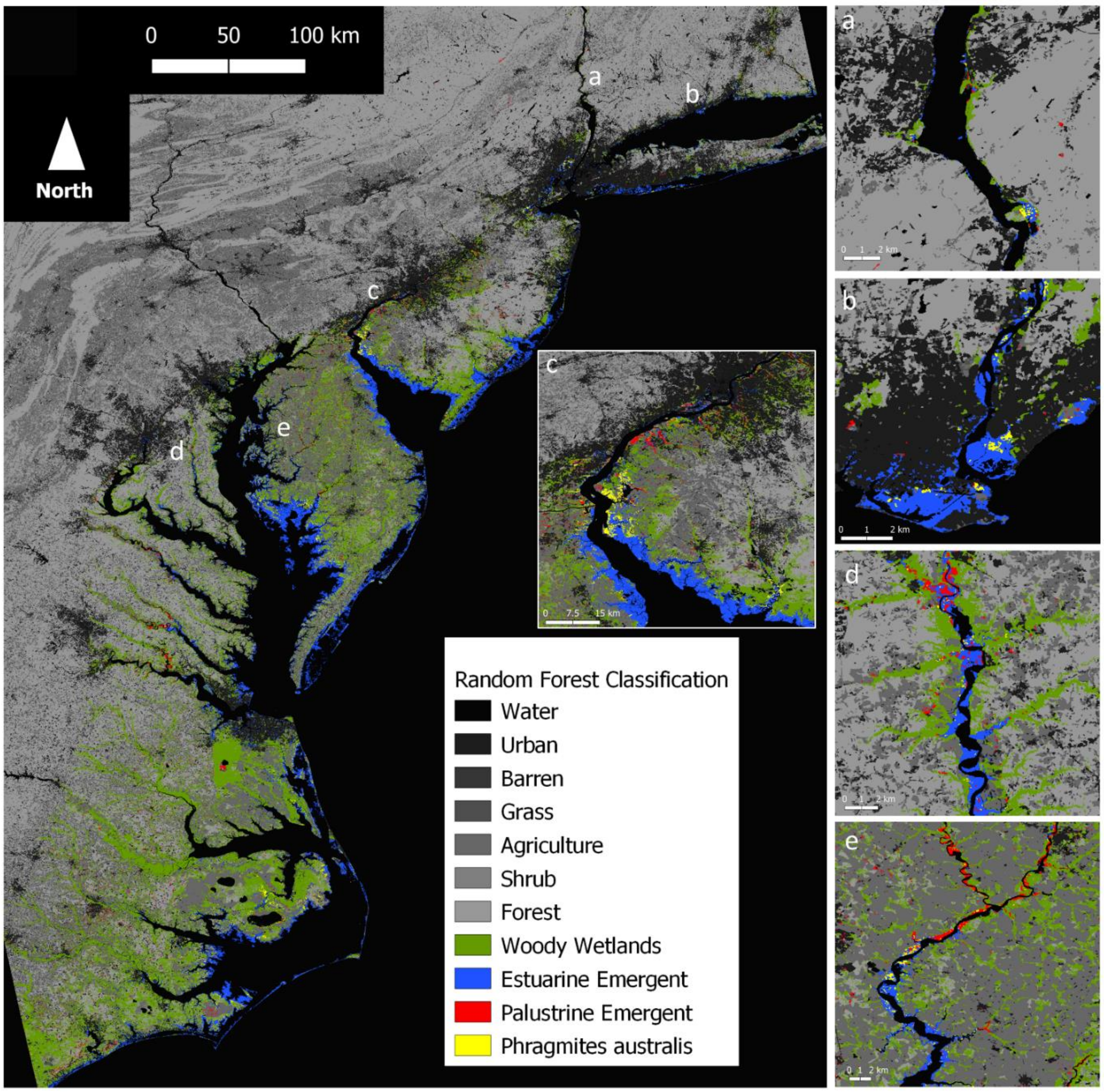

Figure 3.13. Mid-Atlantic Level-1 Random Forest Classification. Insets depict finer scale maps of the Hudson River wetlands (a), Housatonic River wetlands (b), Delaware River wetlands (c), Patuxent River wetlands (d), and Choptank River wetlands (e). The three separate emergent wetland classes are mapped with greater than 81% accuracy in all cases (see Table 3.1 confusion matrix). A clumped emergent wetland class was mapped with a user's accuracy of 89.69% and producer's accuracy of 93.19%.

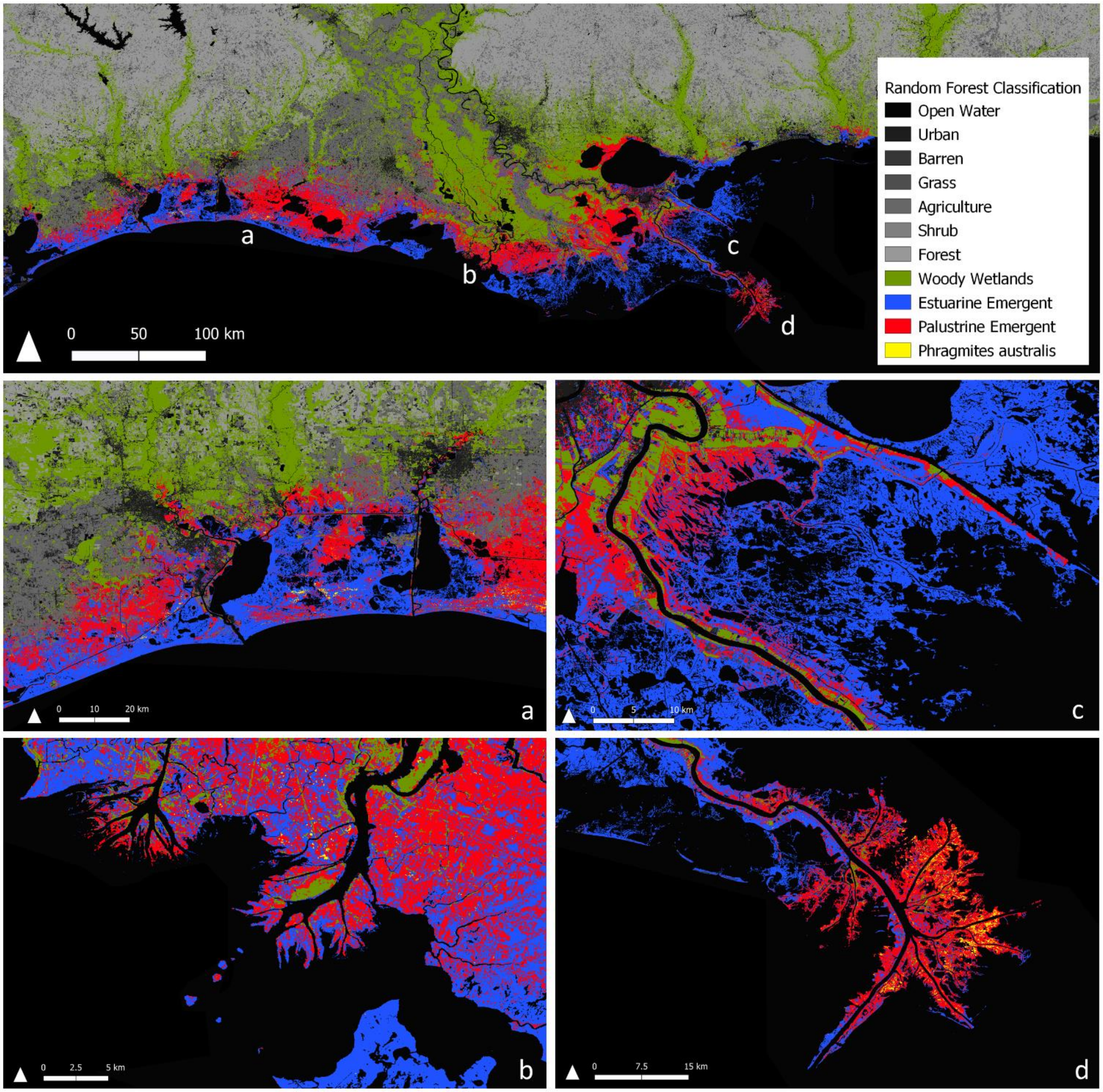

Figure 3.14. Gulf Coast Level-1 Random Forest Classification. Insets depict finer scale maps of the Sabine River wetlands (a), Wax Lake Delta wetlands (b), Brenton Sound wetlands (c), and Bird's Foot Delta wetlands (d). Classification accuracy of the three emergent classes is much lower than Mid-Atlantic sites at around 70% (see Table 3.2 confusion matrix). However, the aggregation of these three emergent classes into a single emergent class yields accuracies higher than the Mid-Atlantic with a user's accuracy of 91.81% and producer's accuracy of 95.02%.

Table 3.1. Confusion Matrix Mid-Atlantic.

		Classification												
		water	urban	barren	grass	agriculture	shrub	upland forest	woody wetlands	estuarine emergent	palustrine emergent	Phragmites australis	Total	Producer's Accuracy %
	water	**39538**	96	275	28	102	1	14	4	370	14	17	40459	97.72
	urban	53	**21874**	1722	3207	5789	517	2007	162	457	305	78	36171	60.47
	barren	561	3981	**8849**	839	3208	221	1587	155	1036	129	172	20738	42.67
	grass	18	5258	559	**6667**	10207	1174	11662	860	280	432	108	37225	17.91
	agriculture	23	3665	893	3092	**47904**	827	6661	563	515	899	183	65225	73.44
Reference	shrub	12	1991	206	2230	3359	**3121**	9460	1213	106	381	101	22180	14.07
	forest	13	1830	389	3148	5094	1327	**94643**	5119	28	164	64	111819	84.64
	woody wet.	3	286	11	526	349	408	9855	**12221**	33	101	101	23894	51.15
	estuarine	249	213	333	76	252	9	15	42	**19043**	312	1349	21893	86.98
	palustrine	49	167	72	175	1217	111	431	119	687	**16249**	549	19826	81.96
	Phragmites	18	49	18	28	154	14	30	25	840	95	**13729**	15000	91.53
	Total	40537	39410	13327	20016	77635	7730	136365	20483	23395	19081	16451	--	--
	User's Accuracy %	97.54	55.50	66.40	33.31	61.70	40.38	69.40	59.66	81.40	85.16	83.45	--	Overall Accuracy %
														68.49

Table 3.2. Confusion Matrix Gulf Coast.

		Classification												
		water	urban	barren	grass	agriculture	shrub	upland forest	woody wetlands	estuarine emergent	palustrine emergent	Phragmites australis	Total	Producer's Accuracy %
	water	35015	86	330	13	171	0	16	13	845	65	2	36556	95.78
	urban	35	13084	1354	2323	6877	103	1861	631	870	497	32	27667	47.29
	barren	681	2699	4899	1140	4996	45	876	353	874	175	23	16761	29.23
	grass	39	2723	606	8211	14099	598	9468	1185	437	162	16	37544	21.87
	agriculture	51	2630	561	4724	50487	475	7093	1695	1177	996	102	69991	72.13
Reference	shrub	7	689	116	2290	6227	1875	18641	1134	64	22	2	31067	6.04
	forest	10	861	128	3189	5163	829	77938	6290	13	36	0	94457	82.51
	woody wet.	15	590	24	289	1207	70	12264	23620	56	221	4	38360	61.57
	estuarine	1061	207	223	7	413	0	1	57	32073	5374	584	40000	80.18
	palustrine	373	197	59	24	666	3	99	328	6573	21294	384	30000	70.98
	Phragmites	5	48	8	3	132	0	10	4	3438	1478	3847	8973	42.87
	Total	37292	23814	8308	22213	90438	3998	128267	35310	46420	30320	4996	--	--
	User's Accuracy %	93.89	54.94	58.97	36.96	55.82	46.90	60.76	66.89	69.09	70.23	77.00	--	Overall Accuracy %
														63.13

Table 3.3. Random Forest Importance Assessment (Mid-Atlantic).

Layer/Class	water	urban	barren	grass	agriculture	shrub	upland forest	woody wetlands	estuarine emergent	palustrine emergent	Phragmites australis	Mean Decrease Accuracy	Mean Decrease Gini
dem	0.289	0.091	0.088	0.043	0.077	0.059	0.192	0.184	0.529	0.563	0.622	0.200	59933.873
vv_mean	0.295	0.115	0.067	0.019	0.088	0.010	0.148	0.125	0.146	0.318	0.307	0.140	41249.718
vh_mean	0.275	-0.014	0.119	0.011	0.194	0.057	0.271	0.237	0.142	0.488	0.388	0.198	54252.579
vv_sd	0.026	0.009	0.033	0.010	0.069	0.030	0.052	0.052	0.050	0.238	0.303	0.060	30873.451
vv_spring	0.052	0.052	0.049	0.011	0.057	0.022	0.109	0.078	0.125	0.244	0.266	0.085	33232.514
vv_summer	0.148	0.073	0.049	0.014	0.053	0.018	0.089	0.028	0.269	0.260	0.328	0.098	34889.631
vv_fall	0.513	0.062	0.027	0.012	0.036	0.020	0.081	0.041	0.070	0.186	0.247	0.110	35029.453
ndvi	0.371	0.193	0.171	0.055	0.058	0.061	0.275	0.222	0.311	0.489	0.480	0.223	67814.979

Table 3.4. Random Forest Importance Assessment (Gulf Coast).

Layer/Class	water	urban	barren	grass	agriculture	shrub	upland forest	woody wetlands	estuarine emergent	palustrine emergent	Phragmites australis	Mean Decrease Accuracy	Mean Decrease Gini
dem	0.108	0.089	0.060	0.079	0.106	0.066	0.185	0.169	0.413	0.400	0.283	0.173	67977.601
vv_mean	0.260	0.101	0.065	0.014	0.087	-0.022	0.116	0.243	0.185	0.112	0.129	0.119	45262.077
vh_mean	0.282	-0.002	0.094	0.036	0.166	0.021	0.164	0.211	0.126	0.045	0.189	0.132	52141.798
vv_sd	0.040	0.017	0.036	0.018	0.081	0.018	0.053	0.039	0.053	0.046	0.089	0.047	35667.538
vv_spring	0.140	0.070	0.027	0.015	0.038	0.004	0.066	0.057	0.108	0.097	0.106	0.064	36429.023
vv_summer	0.126	0.065	0.050	0.013	0.051	0.002	0.059	0.058	0.078	0.076	0.143	0.060	37290.038
vv_fall	0.077	0.049	0.039	0.011	0.031	0.002	0.050	0.025	0.076	0.030	0.128	0.042	32750.327
ndvi	0.486	0.147	0.142	0.057	0.083	0.042	0.209	0.265	0.138	0.184	0.196	0.177	71390.643

While the separation of estuarine emergent (tidal marshes), palustrine emergent (non-tidal freshwater marshes), and *Phragmites australis* dominated marshes were successful in the Mid-Atlantic region, the classifications results still highlight some limitations of approach. Notably that freshwater tidal wetlands are difficult to effectively map with a split between palustrine and estuarine emergent classes. This was indicated by the fact the tidal freshwater portions of the Choptank and Patuxent rivers were often classified as palustrine. Although a limitation of a discrete classification without an explicitly defined tidal freshwater wetland class, these results are not unexpected as non-tidal and tidal freshwater marshes often have similar vegetation types. The level-2 classification results in the next section present potential solutions to determining the location of tidal freshwater wetlands.

3.3.4 Level-2 Classification Results

After performing the level-1 classification we carried out the level-2 classification. The results of the level-2 classification in Mid-Atlantic are shown in Figure 3.15. Note that the classification of non-persistent emergent vegetation and *Trapa natans* is present in these products. In the Figure 3.15 level-2 classification, the Hudson River (panel-a) is the only system with significant *Trapa natans* identification. The Housatonic River/Wheeler Marsh classification (panel-b) shows no non-persistent vegetation indicating an accurate classification for a brackish marsh system. The freshwater tidal systems of the Delaware River, Patuxent River, and Choptank Rivers (panels c-e) all show the presence of non-persistent emergent vegetation in tributaries to the main river, all of which are less saline than the main river systems.

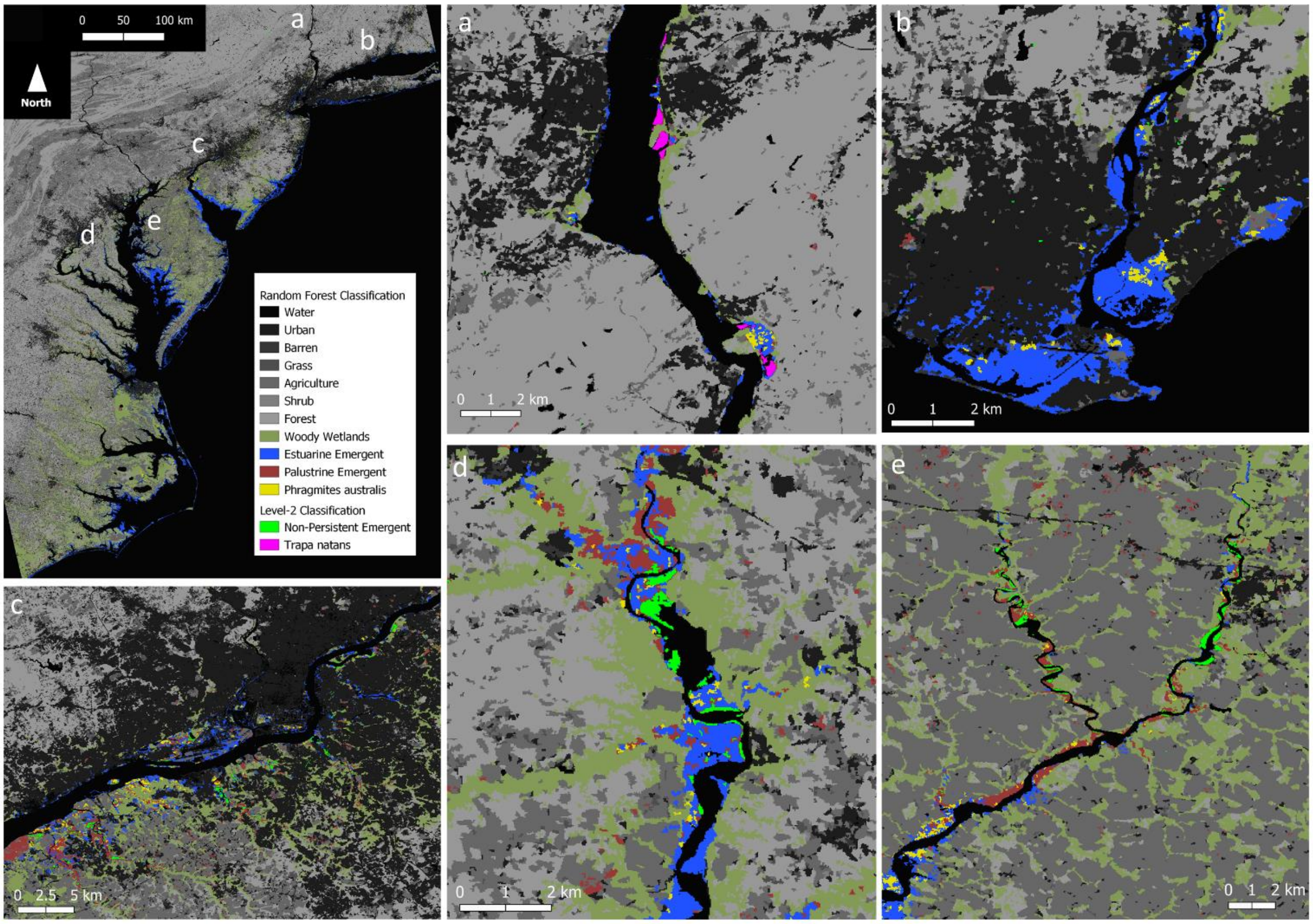

Figure 3.15. Maps of combined level-1 and level-2 classification with assessment at study sites over Mid-Atlantic. Level-1 random forest classification wetland colors have been muted to highlight non-persistent emergent wetlands in bright green and *Trapa natans* in magenta. Panels a-e correspond to the Hudson River, Housatonic River/Wheeler Marsh, Delaware River Patuxent River, and Choptank River, respectively.

The level-2 classification results for the Gulf Coast largely followed general expected patterns for the distribution of non-persistent emergent vegetation. Note that in this case there is one non-persistent class rather than a split between non-persistent emergent and non-persistent aquatic as there was for the Mid-Atlantic. Most mapped non-persistent emergent vegetation was associated with low salinity regions. In the Brenton Sound, the occurrence of non-persistent vegetation is minimal but tends to be associated with palustrine wetlands. The presence of non-persistent vegetation in the Wax Lake and Bird's Foot Delta wetlands is more expansive, but also tends to be associated with the presence of palustrine wetlands. In reality, these palustrine wetlands are likely tidal freshwater marshes. In the Bird's Foot Delta and Wax Lake Delta, classified non-persistent vegetation is indicative of the presence of *Sagittaria spp.* (Carle et al. 2015).

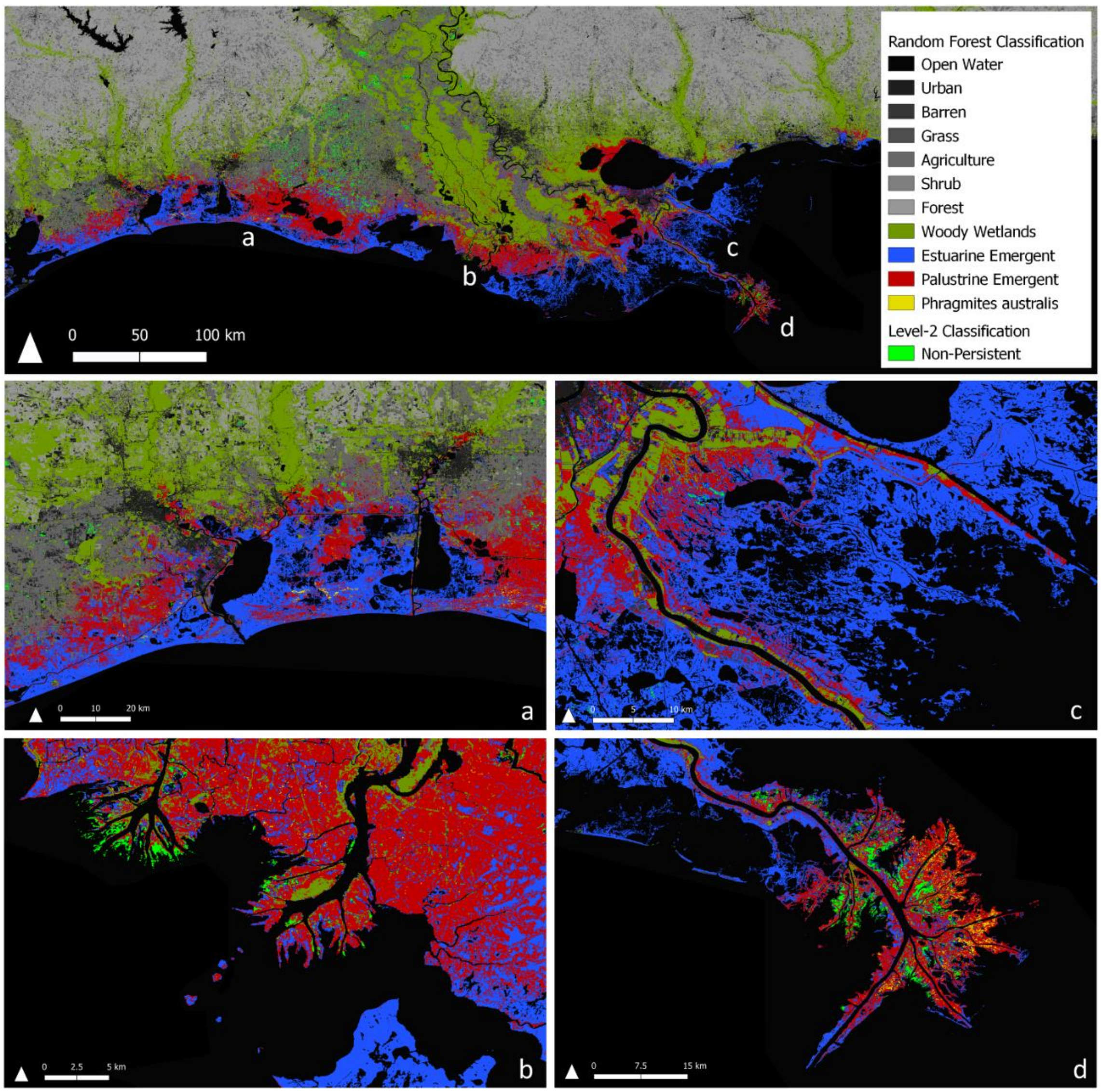

Figure 3.16. Maps of combined level-1 and level-2 classification with assessment at study sites over Gulf Coast. Panels a-d correspond to the Sabine River, Wax Lake Delta (and surrounding wetlands), the Brenton Sound, and the Bird's Foot Delta, respectively. Note that level-1 emergent wetland colors have been muted to highlight locations of non-persistent vegetation in the level-2 classification.

3.3.5 Level-2 Accuracy Assessment at Study Sites

We chose three sites for in-depth assessments of level-1 and level-2 combined classification accuracy. Each of these sites had a separate independent validation dataset. In the first validation study, we assessed the accuracy of *Trapa natans* in the Hudson River using the 2018 HRSAV dataset. Classification accuracy of level-2 *Trapa natans* as verified by the HSRAV dataset was 96.47% (n = 6882 pixels). Level-2 classified *Trapa natans* occurrence within level-1 random forest classification prior to masking level-2 classification to level-1 wet classes was 76.14% in barren class (includes mudflats), 15.66% in open water, 3.98% in estuarine emergent wetlands, 3.91% in palustrine emergent wetlands. All other level-1 classes exhibited a total occurrence with *Trapa natans* occurrence of less than 0.5%. The fact that all the level-1 classes included in the HRSAV dataset bounds were wet classes points to the effectiveness of the level-1 classification in the Hudson River.

In the second validation study we assessed combined level-1 and level-2 classification performance in the Choptank River with an independently derived validation dataset making use of digitized NAIP imagery. In the NAIP validation dataset, only non-persistent emergent and persistent emergent vegetation was observed, thus no aquatic beds (e.g. *Trapa natans*) should be detected over this site. Performance comparison between NAIP persistent emergent wetland bounds and classified wetlands (n = 1006 pixels) showed a 0% occurrence of *Trapa natans* and a 1.2% occurrence of non-persistent emergents. Level-1 class occurrence in NAIP persistent emergent bounds was: 3.71% woody wetlands, 1.10% estuarine emergent, 89.78% palustrine emergent, 4.91% *Phragmites australis*. When these three level-1 persistent emergent classes are clustered, this corresponds to a 95.79% accuracy. Performance comparison NAIP non-persistent emergent bounds and classified wetlands (n = 675 pixels) showed a 1.93% occurrence of *Trapa* *natans* and 93.60% occurrence of classified non-persistent emergents. Level-1 class occurrence in NAIP non-persistent bounds was: 22.37% open water, 1.19% woody wetlands, 8.15% estuarine emergent, and 68.15% palustrine.

The third validation study was based in the Wax Lake Delta and makes use of 2017 NWI data as a validation dataset for the combined level-1 and level-2 classification. Four riverine NWI classes (R1ABT, R1AB3V, R1AB3T, and R1AB4V) were used. Based on site vegetation maps and NWI-based wetland descriptions (Carle et al. 2015), these sites are presumed to be dominated by non-persistent vegetation, but because we do not have precise geolocations of exact vegetation types, we reference occurrences of classified pixels in NWI bounds rather than accuracies. In the R1ABT class, occurrence of level-2 non-persistent was 32.21%. The level-1 classification occurrence was 52.65% open water, 21.15% agriculture, 1.12% *Phragmites australis*, 8.33% estuarine emergent, and 16.14% palustrine emergent. For the R1AB3V, level-2 non-persistent occurrence was 47.37%. The level-1 classification occurrence was 57.69% open water, 17.05% agriculture, 0.15% *Phragmites australis*, 3.08% estuarine emergent, and 20.74% palustrine emergent. In R1AB4V, the level-2 occurrence was 14.08%. The level-1 class occurrence was 13.97% open water, 1.40% urban, 27.06% grassland, 0.13% *Phragmites australis*, 29.35% estuarine emergent, and 25.03% palustrine emergent. For the R1AB3T, the level-2 occurrence was 23.94%. The level-1 classification occurrence was 88.61% open water, 1.40% grassland, 7.18% estuarine emergent, and 1.81% palustrine emergent. Figure 3.19, panel b shows the Sentinel-1 VV annual standard deviation layer used to derive the level-2 classification which exhibits high levels of spatial variability within NWI validation classes (red polygons), highlighting the potential limitations of both our level-2 decision tree-based classification approach and/or issues with the NWI in accurately mapping wetlands and deepwaters vegetation communities.

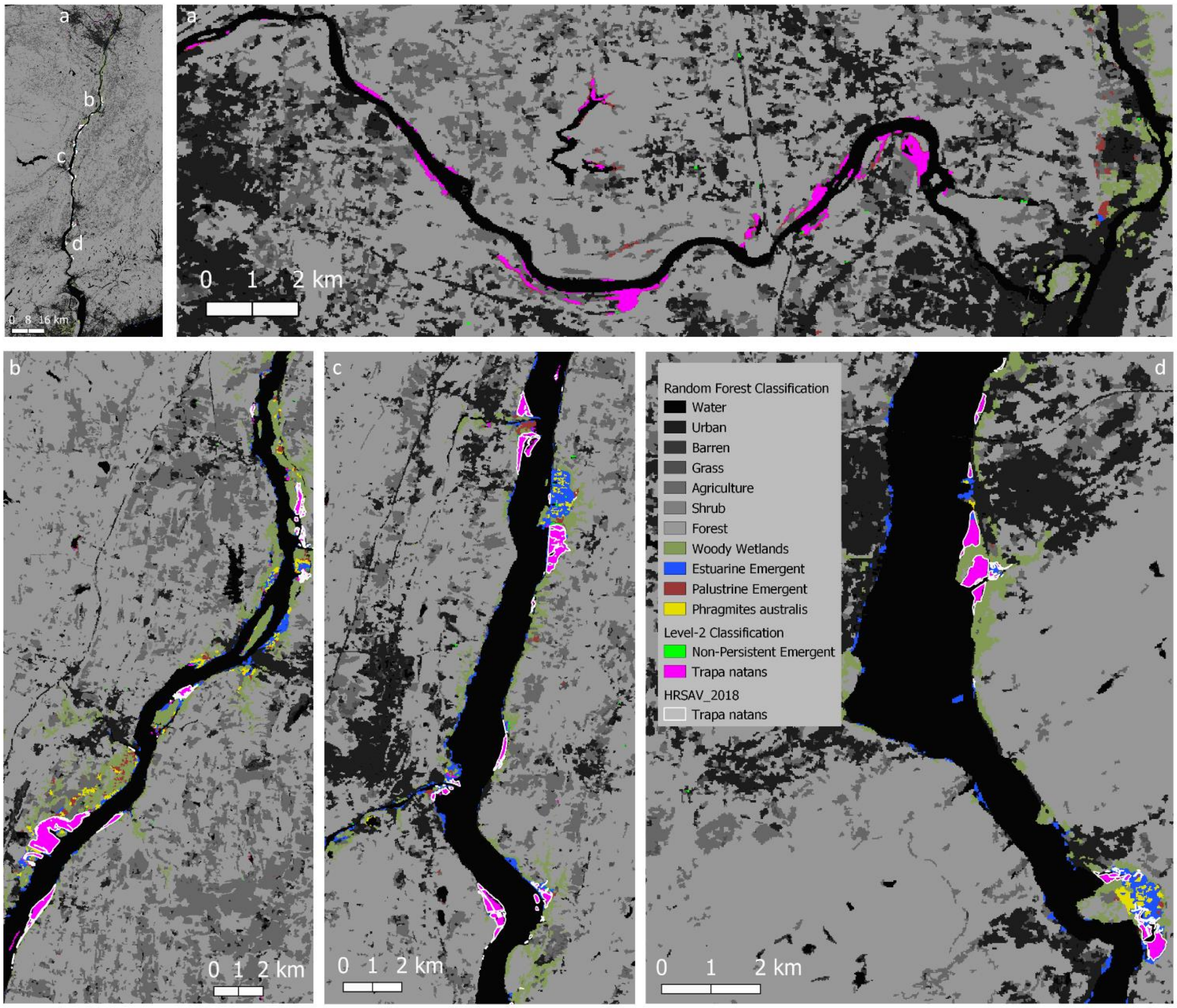

Figure 3.17. Comparison between Hudson River classified *Trapa natans* extents in level-2 classification and independent validation with 2018 HRSAV dataset. Small panned map in upper left corner shows Hudson River and locations of panels a-d. Panel a showcases classified *Trapa natans* extent in the Mohawk River, a tributary to the Hudson River, note that the HRSAV dataset does not cover this site. Panels b-d depict the common extents between the HRSAV *Trapa natans* extent in white polygons, while the magenta pixels showcase level-2 classified *Trapa natans* locations. Classification accuracy of level-2 *Trapa natans* was 96.47% (n = 6882 pixels)

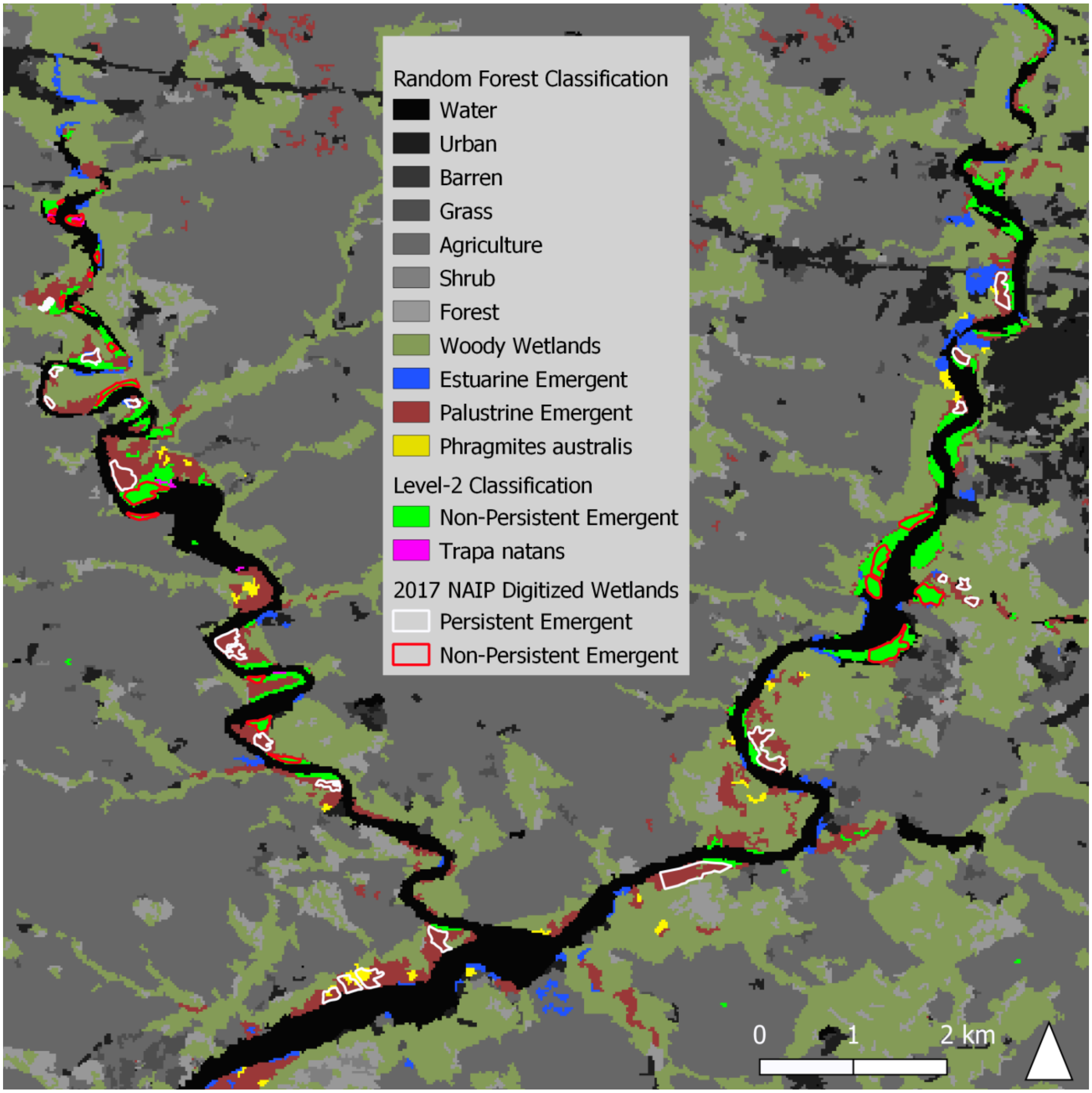

Figure 3.18. Comparison between Choptank River level-1 and level-2 classified wetland extents and independent validation with 2017 NAIP digitized wetland dataset. Identified non-persistent wetlands in the NAIP dataset were primarily *Nuphar spp*.. Utilizing the NAIP dataset as validation, the combined level-1 and level-2 classification accuracy was determined to be 93.60% for non-persistent emergent wetlands (n = 675 pixels) and 95.79% for persistent emergent wetland (n = 1006 pixels).

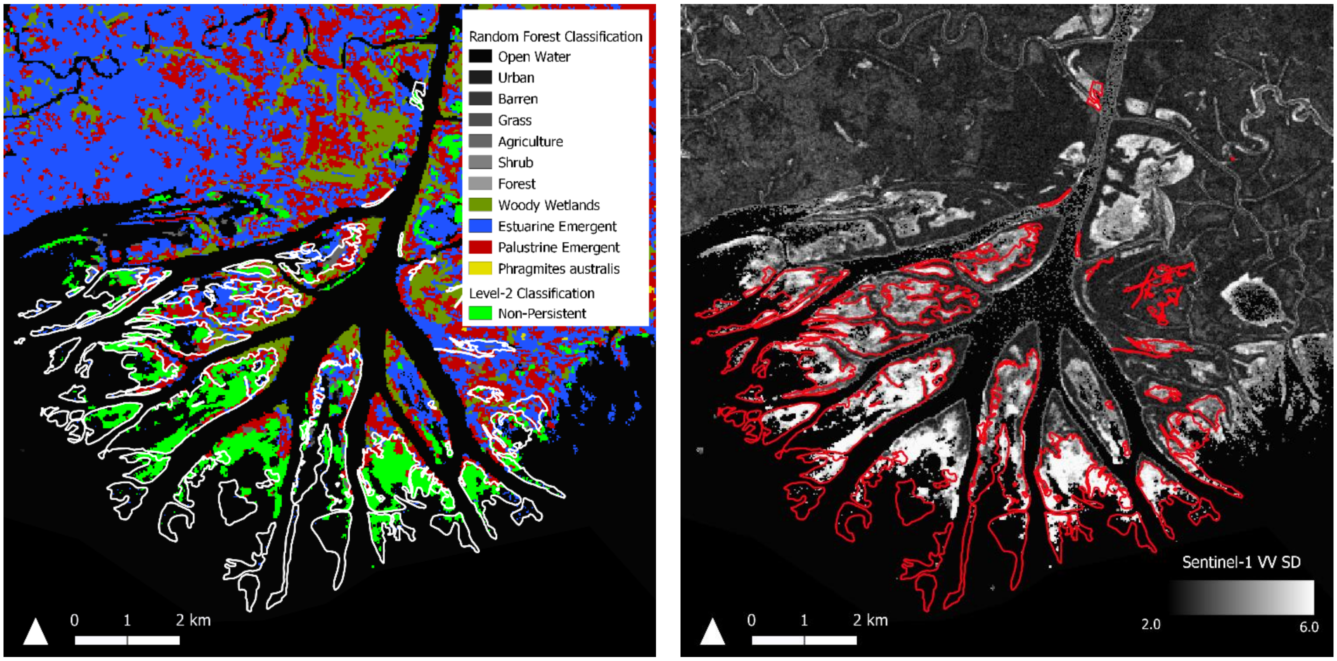

Figure 3.19. Left panel depicts classified level-1 and level-2 extents in 2017 NWI white polygons (white boundaries). Right panel depicts the Sentinel-1 VV annual standard deviation with same NWI polygons (red boundaries) showing that a number of regions in the NWI riverine polygons do not reach threshold of 4.7 dB for level-2 non-persistent classification indicating that vegetation communities may be mixed within NWI polygons. This also highlights the challenge of assessing classification accuracy without specific wetland vegetation surveys.

3.4. Discussion

The results of the level-1 classification demonstrate the utility of SAR-optical-DEM fusion in achieving relatively high emergent wetland classification accuracies. For both the Gulf Coast and Mid-Atlantic, emergent wetlands (i.e. marshes) (aggregation of estuarine emergent, palustrine emergent, and *Phragmites australis*) we achieved user and producer accuracies greater than 89%. The Gulf Coast combined emergent class user's accuracy was 91.81% and producer's accuracy was 95.02%. Application to the Mid-Atlantic coastline was slightly less accurate with user's accuracy of 89.69% and producer's accuracy of 93.19%. Combined with the findings of open water being mapped with accuracies greater than 93.89% in all cases, these results demonstrate that this methodology presents an effective tool for monitoring emergent wetland loss and gain through open water conversion with critical applications to both the Gulf Coast and Mid-Atlantic tidal wetlands (Turner et al. 2019; Ganju et al. 2017). The overall accuracies for identification of marshes (emergent wetlands) was comparable to NWI accuracy assessment studies generally finding accuracies exceeding 90% at the NWI class level (Handley and Wells 2009; Nichols 1994; Kudray and Gale 2000). It is critical to note however that no previous studies have performed an extensive validation of the NWI for the mapping of tidal marshes (estuarine emergent wetlands). Further within our study sites, we noted several instances where the NWI incorrectly classified estuarine emergent wetlands at Jug Bay and Wheeler Marsh. Thus, even the NWI accuracy assessment studies serve as a general classification accuracy goal, we do not have a direct assessment of tidal marsh classification accuracy.

The degree to which this methodology enabled us to distinguish between specific emergent wetland classes was variable. In the Mid-Atlantic, these classes were distinguished with better than 81% user's and producer's accuracy. Accuracies in the Gulf Coast were lower with user's accuracies ranging from 69.07% to 77.00% and producer's accuracies ranging from 41.87% to 80.18% for the three emergent wetland classes. These results suggest that the level-1 classification methodology should be used only for general emergent wetland mapping in the Gulf Coast. Application of this SAR-optical-DEM classification approach to two very different coastlines, the Gulf of Mexico and Mid-Atlantic coasts, revealed several important findings. The first is that in both the Gulf Coast and Mid-Atlantic classifications, the SRTM DEM was the most important layer in improving classification accuracy for all three emergent wetland classes (Tables 3.3 and 3.4). These findings agree with those from Knight et al. (2013). Growing season

NDVI was the second most important classification layer for both the Gulf Coast and Mid-Atlantic emergent classes. The third most important classification layer differed between the Gulf Coast and Mid-Atlantic with the VV annual mean being more important for the Gulf Coast emergent wetland classifications and VH annual mean being more important for the Mid-Atlantic (Table 3.3 vs. Table 3.4). This indicates potential vegetation structural/phenological differences and/or hydrological differences between wetlands in the respective regions, as Sentinel-1 VV and VH channel sensitivity to wetland vegetation and hydrologic state have been demonstrated as differing depending on these factors (Dabrowska-Zielinska et al. 2016) These differences in SAR polarimetric channel response need be considered when classifying diverse wetlands at large scales.

The level-2 classification was developed from timeseries analysis at Mid-Atlantic target sites demonstrating that persistent and non-persistent vegetation had sufficiently different phenological signatures that were effectively detected by C-band SAR. We initially sought to determine whether vegetation phenological SAR signatures could be distinguished from hydrologic influence on SAR signatures in these tidal wetland systems. Figures 3.7 and 3.8 demonstrated that water level variability does have a pronounced impact on SAR backscatter, especially for low elevation wetland vegetation like *Spartina alterniflora* and *Nuphar lutea*. When we temporally reduced Sentinel-1 image timeseries over our sites to compute VV annual standard deviation (SD) layers and VV-Spring layers, these layers were demonstrated as being primarily responsive to vegetation structural phenological changes rather than hydrologic variability. For those reasons, these layers became the basis of the level-2 classification, which proved to be quite accurate over Mid-Atlantic study sites. The accuracy of the level-2 classification results was greatest for the Hudson River detection of *Trapa natans* (> 96%).

Although *Trapa natans* detection was not a primary objective at the inception of this research effort, the results demonstrate the methods developed for detection of this invasive species were highly effective. Further, other sites where *Trapa natans* has not been observed (Jug Bay and Wheeler Marsh) did not show incorrect identifications, even with Jug Bay being dominated by large stands of non-persistent *Nuphar lutea* which shares a similar phenology. Initially, we suspected that *Trapa natans* and *Nuphar lutea* may be distinguished based on biomass-based backscatter differences during the growing season. However, the assessment of Sentinel-1 VV backscatter timeseries showed that during peak growth in July and August, both species had nearly identical peak backscatter values (-6 dB). This required us to separate these species based on phenological differences using the Spring-VV layer. The similarities in peak growth backscatter points to both species exhibiting strong surface scattering compared to a more canopy-based scattering response. This highlights the need to account for vegetation geometry when using C-band SAR for wetland and aquatic vegetation mapping.

The brackish wetlands of Wheeler Marsh and the surrounding lower Housatonic River, were largely absent of any classified non-persistent vegetation, indicating an accurate level-2 classification (Figure 3.15.b.). Level-2 classification accuracy at the Choptank River site was also highly accurate. In evaluating the level-2 classification accuracy in the Choptank River wetlands with the independent 2017 NAIP wetlands dataset, we noted only a 1.93% incorrect identification of *Trapa natans* in NAIP non-persistent emergent sites, while non-persistent emergent wetlands were correctly identified at a rate of 93.60%. The NAIP persistent emergent sites had no classified *Trapa natans* and a 1.20% incorrect identification of non-persistent emergents. The level-2 classification results for the Wax Lake Delta were far less accurate than the Mid-Atlantic sites where non-persistent vegetation was only identified with 47.37%.

However, it is important to note that the Wax Lake Delta NWI validation dataset in this case may not be as accurate as the Choptank NAIP-based validation dataset that was carefully digitized with expertise in separating persistent and non-persistent vegetation types in Mid-Atlantic systems, and the Hudson River HRSAV dataset that identified a single target species. Several studies have noted mixed stands of specific vegetation in the Wax Lake Delta wetlands (Carle et al. 2015; Elliton 2016; Olliver et al. 2020), which the NWI may not classify accurate.

The combined results of the level-1 and level-2 yielded some important findings with respect to differences between these classifications. In the level-2 accuracy assessment for the Hudson River (Figure 3.18), the overwhelming majority of identified non-persistent vegetation was *Trapa natans*. *Trapa natans* tended to occur most commonly in the level-1 classification barren class, which includes mudflats, at 76.14%. *Trapa natans* occurred in 15.66% of open water classified pixels, in 3.98% of classified estuarine emergent wetlands, and in 3.91% of classified palustrine emergent wetlands. This may be a level-1 classification inaccuracy due to confusion of shallow open waters with mudflats. This could also be due to the fact that mudflats may only be intermittently exposed depending on season and tidal stage. Field observations did suggest that *Trapa natans* tended to occur in very shallow waters. Given that this species is a floating aquatic there is also potential for clustering in very shallow waters and/or mudflats after riverine transport. However, these results speak to the importance of applying detection algorithms (e.g. level-2) over multiple types of "wet" cover classes (e.g. level-1). The level-2 classification results from the Choptank River showed a 1.93% false detection rate for *Trapa natans* and a 93.60% correct identification rate of non-persistent emergent vegetation compared to the NAIP validation dataset. Level-1 class occurrence in NAIP non-persistent bounds was: 22.37% open water, 1.19% woody wetlands, 8.15% estuarine emergent, and 68.15% palustrine emergent. Like the Hudson River results, this highlights the importance of applying detection algorithms similar to the level-2 classification over multiple “wet” classes. Interestingly, the Choptank level-2 non-persistent emergent class showed no occurrences with the level-1 barren class, which may be due to non-persistent emergents having a longer period of vegetated cover over the mudflats they grow in compared to *Trapa natans* which is more ephemeral in nature (Figure 3.8 vs. Figure 3.9). This may have resulted in a level-1 classification of palustrine emergent wetlands rather than the barren class representing mudflats. The results from the Choptank River demonstrated that persistent emergent wetlands were seldom incorrectly classified as non-persistent emergent by the level-2 classification with a 1.20% false identification rate. Choptank River persistent emergent wetlands identification was largely accurate with the level-1 classification showing occurrences of 3.71% woody wetlands, 1.10% estuarine emergent, 89.78% palustrine emergent, and 4.91% *Phragmites australis.* These results largely speak to the complementary nature of the level-1 and level-2 classifications and how machine learning and explicitly defined empirical classification approaches can complement and corroborate one another. Results from the combined level-1 and level-2 classification over the Wax Lake Delta suggested that challenges may exist in applying methodologies developed for the Mid-Atlantic to the Gulf Coast for identifying specific wetland vegetation classes, most likely due to structural and/or phenological differences between wetlands in the respective regions. In the Wax Lake Delta site, it was common for wetlands to be incorrectly identified as agriculture. In two NWI validation riverine aquatic bed wetlands, the level-1 classification of agriculture made up >17% and >23% of pixels within NWI wetland bounds. These errors likely occur because significant portions of the Gulf Coast have both rice production and aquaculture which are both classified as agriculture by the NLCD dataset used in level-1 training data. In future efforts, these specific forms of landcover would be split from conventional upland agricultural (i.e. corn, soy, wheat production) as this would provide future insights about how to better separate “wet” agriculture from natural wetlands. It should be noted that overall emergent wetland classification for the Gulf Coast was highly accurate (>90%), and it may be the lower elevation low marsh and aquatic vegetation that is particularly susceptible to erroneous classification as agriculture, especially given the prevalence of aquaculture and rice production in the Gulf Coast region.

3.5. Conclusions

We produced updated emergent wetlands and deepwaters maps for the Gulf Coast and Mid-Atlantic United States for 2017. Application of this approach to the Mid-Atlantic coast resulted in relatively high accuracies (> 80%) for the separation of tidal marshes, palustrine marshes, and *Phragmites* dominated marshes; yet the approach had lower accuracy in the Gulf Coast, most likely due to structural and/or phenological differences between wetlands in the respective regions. These phenological differences are important to consider when selecting temporally-based SAR imagery for classifications. This is especially true in the context of future potential development of a global tidal marsh product, as Sentinel-1 SAR, Landsat 8 optical, and SRTM DEM all provide the coverage for such a product, but may need to be tailored for specific regions based on *a priori* understanding of marsh structure, phenology, and hydrology. Differences in specific classification accuracy between the Gulf Coast and Mid-Atlantic also highlighted important considerations in proper training data selection for given regions, i.e. needing to include “wet” agricultural classes like rice production and aquaculture to better separate natural wetlands from other landcover. With regards to achieving a global tidal marsh product, training data availability may be a substantial issue, especially for training data selection for non-tidal wetland classes. Although the Mcowen tidal marsh inventory presents a potential training data set for global tidal marsh mapping efforts, the Mcowen product's integration of the NWI from the US and other disparate tidal marsh inventories from other countries presents numerous challenges. The foremost of which, that was identified in this research effort, is the fact that the NWI tidal marsh mapping accuracy has not been extensively tested and over some study sites showed incorrect classifications. Further, it is unclear if inventories akin to the Mcowen tidal marsh inventory exist for other wetland classes and non-wetland classes like rice production and aquaculture. Our results indicate that it is critical, at the very minimum, to have several non-wetland classes included in wetland classifications for confusion testing. It may be possible to use global products like the MODIS Land Cover product, GlobeLand30, or Copernicus Global Land Cover product as training data for herbaceous wetlands and all other non-wetland classes. These herbaceous wetland classes could be referenced with the Mcowen tidal marsh inventory to split tidal marshes from palustrine marshes, forming a global training dataset. Sentinel-1, Landsat 8, and SRTM DEM all provide global coverage in temperate regions where tidal marshes are present. Thus, input data availability is not an issue in these classifications, although training data quality needs to be further assessed.

Overall, the level-1 classification yielded fairly accurate results that point to applicability to global tidal marsh mapping. However, the novelty of this research effort lies in the level-2 classification which represents the first time C-band SAR was used to effectively map and separate persistent emergent, non-persistent emergent, and floating aquatic vegetation in wetland-deepwater systems. Previously, optically-based studies had been used to map similar vegetation classes (Villa et al. 2015; Villa et al. 2017). The findings in this research largely complement of those of Villa et al., especially given that SAR provides the ability to separate above- and below-water aquatic vegetation more effectively than optical approaches, while optical approaches have a clear advantage in assessing the presence and absence of below-surface aquatic vegetation. Overall, the level-2 classification results demonstrate that timeseries approaches with C-band Sentinel-1 SAR imagery presents numerous opportunities for emergent wetland characterization and monitoring. The approaches used in this particular research effort can be modified for use in different regions where emergent and floating aquatic vegetation have different phenologies as C-band SAR was demonstrably sensitive to phenological change for both floating and emergent vegetation, even more so than extreme water level changes (Figure 3.11). It is clear that emergent wetland characterization largely benefits from the regular observations from the Sentinel-1 SAR satellite operating at a C-band frequency.

With the anticipated launch of the NASA-ISRO Synthetic Aperture Radar (NISAR) satellite operating at the longer L-band wavelength (at times operating at S-band as well), fusion of vegetation response from Sentinel-1 C-band SAR with sub-canopy surface characterization from NISAR L-band SAR presents even further opportunities in wetland and deepwater monitoring and characterization. The inclusion of L-band imagery in classifications will likely greatly increase the classification accuracy of woody wetlands and provide better separation between woody and emergent wetlands (Clewely et al. 2015; Whitcomb et al. 2009). L-band imagery may also aid in providing a more standardized methodology for tidal marsh mapping at the global scale, as it will be more capable of detecting sub-canopy hydrologic variability than C-band SAR. This chapter indicates C-band backscatter is primarily responsive to emergent wetland and deepwater vegetation structure and phenology which can vary greatly across tidal marsh systems.

Chapter 4

TIDAL WETLAND INUNDATION PRODUCT DEVELOPMENT

4.1 Introduction

The accurate characterization of wetland inundation patterns is of critical importance for understanding wetland carbon cycling, biogeochemistry, habitat suitability, wetland restoration feasibility, flood vulnerability in wetland-adjacent areas, and potential wetland loss from sea level rise in coastal regions. Connected tidal marsh-estuary systems have been described as hotspots for biogeological exchange. For example, previous measurements in the Kirkpatrick and Blackwater NWR marsh-estuarine systems have shown that the amount of marsh-exported dissolved organic carbon varies temporally, but mainly in response to differences in tidal height and tidal range rather than seasonal variation in biological processes (Cao and Tzortziou 2020; Tzortziou et al pers. communication). Measurements of marsh-exported dissolved organic carbon (DOC) at the Kirkpatrick marsh showed a negative correlation with water-depth at low-tide ($n = 29$, $r =-0.75$), reflecting the extent to which marsh soil porewater (i.e. shallow groundwater) is exported into the tidal creek, a process that is most rapid during the lowest tides. Since low-low tides are often linked to high-high tides, this relationship also reflects the influence of the extent of marsh inundation, which determines how much marsh surface floods and interacts to provide soil dissolved organic matter (DOM) to surface flood waters. Because of the important role that inundation patterns play in mediating carbon exchange and other biogeochemical processes, it is critical to accurately characterize these inundation dynamics to understand both hydrological patterns and biogeochemical processes.

Over the past two decades major advances have been made in the study of wetland hydrology due to increases in the number of optical/IR and microwave remote sensing platforms capable of characterizing wetland inundation state. With optical/IR remote sensing platforms, the ability to detect water's strong absorption features in the near and shortwave infrared has led to the successful development of optical/IR inundation products (McFeeters 1996; Du et al. 2016; Pekel et al. 2017; Jones 2019). However, optical/IR inundation products are generally limited to characterization of surface water extent and can only assess wetland inundation state when wetland vegetated canopies are sufficiently sparse and/or submerged.

Active microwave instruments, including synthetic aperture radars (SARs), produce signals that penetrate vegetated canopies effectively and respond to the hydrologic state of the underlying surface. Further, SAR signals undergo unique forms of scattering that provide advantages over other remote sensing techniques when imaging inundated wetlands, like the so-called double bounce scattering that results from two successive scattering events (e.g. from the water surface then the stems/trunks) often producing enhanced backscatter intensity in SAR imagery. In high biomass woody wetlands like forested wetlands, the backscatter enhancements that occur because of this double bounce effect have been well established and have been used to map inundation patterns in woody wetlands and separate forested wetlands from upland forests when using L-band SAR imagery (J. Rosenqvist et al. 2020; Whitcomb et al. 2009). Comparatively, the double bounce scattering effect has generally been found to be less pronounced or negligible in emergent wetland systems dominated by herbaceous vegetation. Thus, the characterization of inundation state in emergent wetland systems becomes potentially more challenging than in woody wetlands. Several studies have found that herbaceous wetlands undergo varying degrees of backscatter increase and decrease when inundated (Pope et al. 1997;

Kasischke 2003; Ramsey 2013; Kim et al. 2014). Additionally, these studies have found differing backscatter responses at different wavelengths (C-band vs. L-band) and polarizations (HH, VV, and VH). However, few studies have fully linked empirical SAR image analyses to mechanistic analyses incorporating radiometric modeling to fully elucidate SAR scattering response to inundation state in emergent wetland systems. This has been particularly true of tidal marsh wetland systems where few such studies exist (Tannis et al. 1994; Kasischke and Bourgeau-Chavez 1997; Slatton et al. 2008). Compared to inland emergent wetlands systems, characterizing hydrological changes at tidal (approximately semi-diurnal) timescales in coastal wetlands systems is a challenge for aircraft and satellite remote sensing platforms as the temporal resolution of these observations (revisit time) is generally limited.

In this thesis chapter, we seek to overcome some of the challenges in characterizing tidal marsh inundation state by assessing the accuracy of previously developed SAR-based inundation products from Lamb et al. (2019) and Lamb et al. (2020) with two validation approaches; (1) an *in situ* empirical validation with water level sensor observations and (2) a radiometric modeling analysis. The radiometric modeling analysis makes use of the Michigan Microwave Canopy Scattering (MIMICS) model. MIMICS provides a physically-based elucidation of SAR backscatter and separates backscatter contributions from different scattering sources, in addition to providing a first principles-based validation of algorithms used in our prior inundation product development. In the first part of this research effort we assess the accuracy of previously established tidal marsh inundation products developed using single polarimetric and dual polarimetric SAR imagery from the ESA Sentinel-1a C-band SAR and JAXA Advanced Land Observing Satellite (ALOS) Phased Array type L-band Synthetic Aperture Radar (PALSAR and PALSAR-2). We then leverage the findings from radiometric modeling analysis to inform on the use of quad polarimetric-based approaches for characterization of inundation state using PALSAR-2 satellite imagery and aircraft imagery from the NASA-ISRO (NISAR) Uninhabited Aerial Vehicle Synthetic Aperture Radar (UAVSAR) AM/PM Campaign. The UAVSAR AM/PM Campaign has been acquiring quad-polarimetric SAR imagery since 2019 to support science objectives and product development related to the upcoming NISAR satellite mission. We specifically seek to address how well polarimetric decompositions utilizing polarimetric phase information compare to polarimetric backscatter-based approaches for assessing tidal marsh inundation state. This research effort is relevant to the upcoming NISAR satellite mission that will include a SAR sensor operating at L-band wavelengths, and generally, in dual polarimetric, and at times quasi-quad polarimetric, acquisition modes over the coastal United States. NISAR will acquire imagery at intervals comparable to the C-band Sentinel-1 satellites, generally a 12-day revisit, allowing the characterization of tidal marsh inundation state through C-band and L-band data fusion.

4.2. Materials and Methods

4.2.1. Study Sites and Water Level Sensor Deployment.

We established several wetlands study sites in the Mid-Atlantic and Gulf Coast United States where we had previously characterized wetland inundation with SAR imagery or did so in this research effort. These sites include Wheeler Marsh (CT), Kirkpatrick Marsh (MD), Blackwater NWR (MD), the Wax Lake Delta (LA), White Lake (LA), and Sabine River/Port Arthur (TX). For the purpose of validating remote sensing-based inundation products, we deployed grids of Onset HOBO U20L water level sensors (hereafter referred to as “water level sensors”) in Wheeler Marsh and Kirkpatrick Marsh (Figure 4.1). Water level sensors were deployed in these systems for several months to allow for a time offset and water level-based calibration with nearby NOAA tide gauges. After water level sensors had been deployed for several months, we performed a lagged correlation analysis between the in-marsh water level sensor series and the NOAA tide gauge series and established a time offset based on the lagged maximum R^2 value. After determining the best fit time offset, we performed a regression analysis to determine slopes and intercepts for in-marsh water level and NOAA tide gauge water level. Calibrations between the in-marsh water level sensors and NOAA tide gauge observations were accurate across marsh-deployed sensors ($R^2 >= 0.95$) as shown in Table 4.1. This enabled us to accurately estimate in-marsh water levels at each sensor location using calibrated water temporal offsets as well as water level slopes and intercepts from the longer-term NOAA tidal series. The accuracy of this calibration effort allowed us to extend the record of in-marsh water level estimates to that of our satellite record (2006-2020).

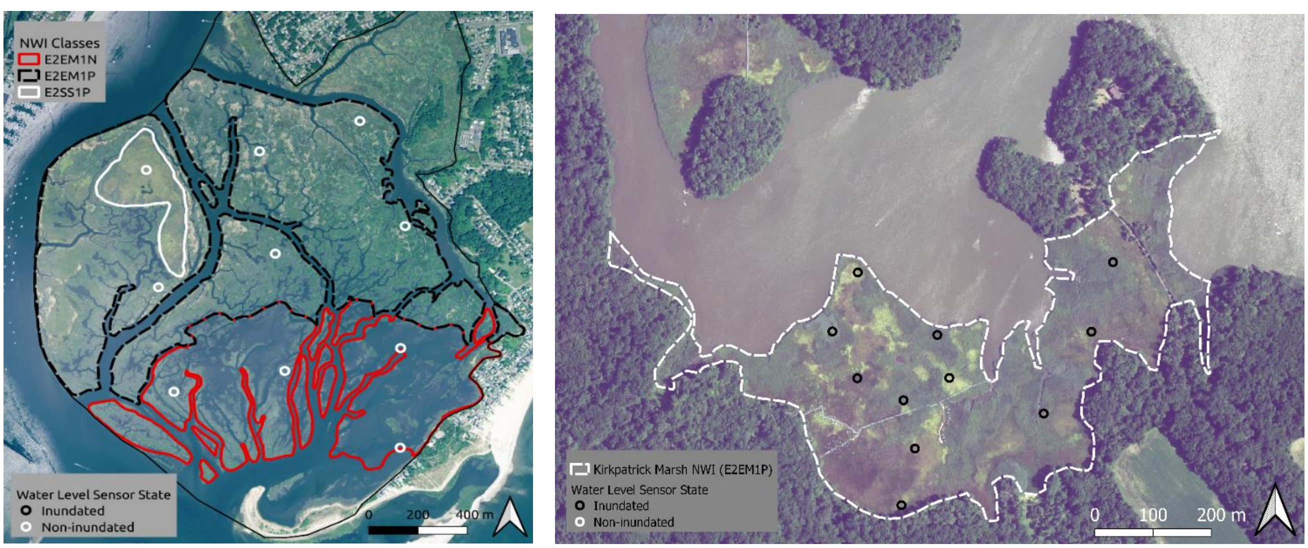

Figure 4.1. Natural color maps of Wheeler Marsh (left) and Kirkpatrick Marsh (right) sites with water level sensor grid deployments. Example water level sensor states show all non-inundated (white) for Wheeler Marsh and all inundated for Kirkpatrick (black) for demonstration only. Note that Kirkpatrick Marsh is a high marsh system, while Wheeler Marsh contains, low marsh-mudflat mix, low marsh, and high marsh corresponding to the red, black, and white, respective polygon bounds.

Table 4.1. Water level sensor grid calibration with long-term NOAA tidal stage observations. This includes the time offset between in-marsh and NOAA tidal water level series, the corresponding maximum R^2 value for this time offset, and the slopes and intercepts of those relationships. Note that the negative time offset for the Kirkpatrick Marsh site indicates that in-marsh water level changes precede those of the NOAA tide gauge in Annapolis, while in-marsh water levels for Wheeler Marsh lag those of the NOAA tidal gauge in Bridgeport. Index 5 shows the series for an in-marsh water level sensor deployed nearby a tidal creek where water level changes were previously estimated to precede those at the Annapolis NOAA station by 34.4 minutes (Lamb et al. 2019; Nelson et al. 2017), indicating good consistency of approach. Water level observations for Blackwater NWR were obtained by a USFWS YSI instrument deployment.

Index	Site	Sensor ID	Start Deployment	End Deployment	NOAA Gauge	Offset (minutes)	R^2 (max)	Slope	Intercept NAVD88 (feet)	Intercept MLLW (feet)	Vegetation
0	Kirkpatrick	20473575	11/28/2018	12/12/2019	Annapolis	-35	0.977	0.921	-1.361	-0.591	patens
1	Kirkpatrick	20473576	11/28/2018	12/12/2019	Annapolis	-22	0.978	0.971	-1.051	-0.281	Scirpus/Iva
2	Kirkpatrick	20473578	11/28/2018	12/12/2019	Annapolis	-28	0.972	0.919	-1.216	-0.446	Phragmites
3	Kirkpatrick	20473579	11/28/2018	12/12/2019	Annapolis	-23	0.978	0.971	-1.225	-0.455	Scirpus
4	Kirkpatrick	20473580	11/28/2018	12/12/2019	Annapolis	-22	0.978	0.919	-1.256	-0.486	patens
5	***Kirkpatrick***	*20473581*	*11/28/2018*	*12/12/2019*	***Annapolis***	***-33***	*0.98*	*0.938*	*-1.153*	*-0.383*	*Phragmites*
6	Kirkpatrick	20473582	11/28/2018	12/12/2019	Annapolis	-31	0.977	0.93	-0.951	-0.181	Phrag/Iva
7	Kirkpatrick	20473583	11/28/2018	12/12/2019	Annapolis	-29	0.976	0.93	-1.199	-0.429	Scirpus
8	Kirkpatrick	20473584	11/28/2018	12/12/2019	Annapolis	-20	0.981	0.941	-1.008	-0.238	Phrag
9	Kirkpatrick	20473585	11/28/2018	12/12/2019	Annapolis	-24	0.975	0.977	-1.309	-0.539	Scirpus/Typha
10	Kirkpatrick	20473586	11/28/2018	12/12/2019	Annapolis	-17	0.973	0.919	-1.39	-0.62	Mixed
0	Wheeler	20308250	8/8/2018	12/5/2018	Bridgeport	15	0.99	0.988	-4.221	-0.381	mudflat/alterniflora
11	Wheeler	20358449	8/8/2018	12/5/2018	Bridgeport	13	0.99	0.995	-4.448	-0.608	mudflat/alterniflora
12	Wheeler	20358450	8/8/2018	12/5/2018	Bridgeport	16	0.987	0.991	-4.171	-0.331	mudflat/alterniflora
13	Wheeler	20358451	8/8/2018	12/5/2018	Bridgeport	15	0.984	0.983	-5.608	-1.768	mudflat/alterniflora
21	Wheeler	20358452	8/8/2018	12/5/2018	Bridgeport	13	0.977	0.983	-6.891	-3.051	alterniflora
22	Wheeler	20358453	8/8/2018	12/5/2018	Bridgeport	15	0.975	0.982	-6.22	-2.38	alterniflora
23	Wheeler	20358454	8/8/2018	12/5/2018	Bridgeport	15	0.973	0.966	-6.394	-2.554	alterniflora
31	Wheeler	20358447	8/8/2018	12/5/2018	Bridgeport	9	0.949	0.933	-7.329	-3.489	patens/Distichlis
32	Wheeler	20358455	8/8/2018	12/5/2018	Bridgeport	17	0.967	0.971	-5.975	-2.135	alterniflora
33	Wheeler	20389462	8/8/2018	12/5/2018	Bridgeport	16	0.966	0.962	-6.575	-2.735	alterniflora
KM-Mean	**Kirkpatrick**	--	11/28/2018	12/12/2019	**Annapolis**	**-25.818**	--	0.94	-1.193	-0.423	--
WM-Mean	**Wheeler**	--	8/8/2018	12/5/2018	**Bridgeport**	**14.4**	--	0.975	-5.783	-1.943	--
BWNWR	**Blackwater**	USFWS-YSI	9/20/2016	10/31/2016	**Bishop's Head**	**186**	0.636	--	--	--	--

The water level observations over Blackwater NWR were obtained from a United States Fish and Wildlife Service (USFWS) monitoring effort that ran for two months in 2016 using a YSI instrument measuring water levels. This YSI water level timeseries was compared to the Bishop's Head NOAA station water level series using only lagged correlation analysis (slopes and intercepts were not computed). The maximum R^2 value of 0.636 was obtained at a time offset of 186 minutes. Although this correlation is lower than Wheeler Marsh and Kirkpatrick

Marsh, the difference is excepted given the hydrologic complexity of the Blackwater NWR system. These time offset findings do agree with a previous NOAA and USACE study for this site finding a 2.5 to 3-hour lag between the Shorter's Wharf region (where the YSI was deployed) and a less distant NOAA tidal station at McCready's Creek (Allen et al. 2001).

Gulf Coast sites were selected based on several criteria. First, they needed to be identified as having a high density of tidal marshes as identified in Lamb et al. (2020), have a sufficient number of UAVSAR AM/PM scenes, and have water level sensor sites within the wetland systems. All selected Gulf Coast study sites were deemed to have sufficient water level sensor observations from the State of Louisiana Coastal References Monitoring System (CRMS) network in addition to having ample wetland densities and numbers of UAVSAR AM/PM campaign scenes. The CRMS water level observations for select UAVSAR scenes at the time of image acquisition are shown in Table 4.4.

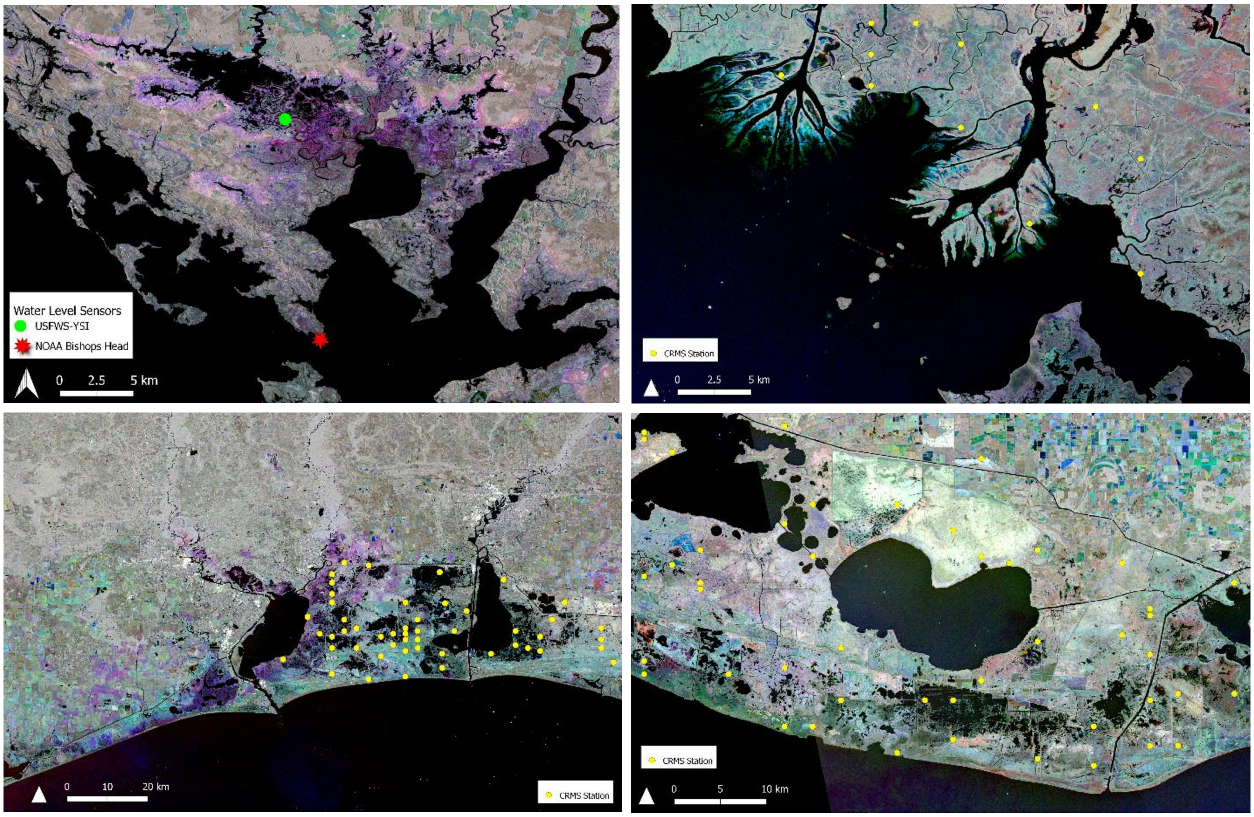

Figure 4.2. Sentinel-1a VV backscatter multi-season composites (R = spring, G = summer, B = fall) for study sites with water level sensors deployed by other research groups. Sites include Blackwater NWR, the Wax Lake Delta, Sabine River, and White Lake, respectively (left to right, top to bottom). The yellow points on Gulf Coast sites correspond to CRMS water level sensors. Blackwater NWR water level data was acquired from a USFWS YSI in the Shorter's Wharf region of Blackwater NWR between 2015-2016. The closest active NOAA tide gauge at Bishop's Head is also shown.

4.2.2 MIMICS Radiometric Model Parameterization

The Michigan Microwave Canopy Scattering (MIMICS) model provides the ability to model microwave scattering for various vegetated biomes, including wetlands. MIMICS allows flexible parameterization of vegetation canopies and the underlying surfaces. In this effort, our objective was to simulate radar scattering from tidal marshes with varying surface hydrologic states and vegetation characteristics. A generalized form of a tidal marsh was parameterized with vertically structured vegetation, a rough ground surface with varying soil moisture, and surface water with a salinity of 20 PPT. The vertical vegetation was modeled as a combination of cylinder-like stems and thin leaves. The rough ground surface, which we observed in many of the study sites, was parameterized with a root-mean-square height of 2 cm and a gaussian autocorrelation parameter length parameter of 10 cm. These values were identical to those used to represent a tidal marsh with a rough surface in a modeling effort by Duan and Jones (2017). In our effort, we represented marsh soil as equal proportions of sand, silt, and clay. Our modeling effort was most focused on the hydrologic variability influence on backscatter. To characterize change in hydrologic state, we varied marsh soil moisture from 0% to 100% in 5% increments. After a soil moisture of 100%, we replace the soil model with a water surface layer model, then iteratively changed the water height by successively lowering the marsh vegetation canopy into the water thereby effectively reducing the amount of vegetation exposed above the water level. This has the same effect as inundating/submerging marsh vegetation as tidal stage increases.

Parameterizing vegetation variability required a more nuanced approach than characterizing the marsh surface. Marsh vegetation types include grasses, rushes, and sedges which all have significant amounts of both stems and leaves. Stems were modeled as primarily vertically structured cylinders. Leaves were also modeled as primarily vertically structured. In order to provide more detailed parameterizations of marsh vegetation, we performed field surveys and sampling of marsh vegetation. These field studies included measurements of vegetation water content and the physical dimensions of vegetation, which are shown in the following Tables 4.2 and 4.3.

Table 4.2 Vegetation water contents from field sampling. In most cases green samples were acquired during the growing season while brown samples were acquired outside of the growing season. Vegetation was acquired across numerous Mid-Atlantic sites. Note vegetation % moisture remains fairly consistent between different vegetation types but varies largely depending on season.

Vegetation (Phenological State)	samples	% moisture
Typha (Green)	10	74.77
Typha (Brown)	3	9.61
alterniflora (Green)	9	75.09
alterniflora (Brown)	6	17.10
Phragmites (Green)	12	63.94
Phragmites (Brown)	21	12.38
Scirpus (Green)	11	68.58
Scirpus (Brown)	6	16.41
Scirpus (Brown-Wet)	4	37.41
patens (Green)	14	58.27
patens (Brown)	8	13.24
high marsh mix (Green)	10	64.40
high marsh mix (Brown)	9	28.04
cynosuroides (Green)	2	60.66
Average all samples (Green)	**68**	**66.57**
Average all samples (Brown)	**57**	**17.50**

Table 4.3 Vegetation dimensions field sampling. Canopy length (height) was measured in inches. Averages for tall, medium, and short canopies are calculated below. Tall-form *Spartina alterniflora* vegetation canopy height estimates were acquired from the USDA's Plants Database.

Date	Location	Species	Samples	Canopy Length (m)
20170916	Jug Bay	Typha	6	1.847
20190619	Connecticut River	Typha	2	1.702
20190412	Kirkpatrick	Phragmites	10	2.256
20190619	Connecticut River	Phragmites	3	1.727
20190412	Kirkpatrick	Scirpus	4	1.803
20190619	Connecticut River	Short-form Alterniflora	3	0.279
20190619	Connecticut River	High Marsh	3	0.229
USDA-Plants	Wheeler, Blackwater	Tall-form Alterniflora	NA	1.372 (0.610 to 2.137)
Average (tall)	--	--	25	**1.977**
Average (med)	--	--	NA	**1.372**
Average (short)	--	--	6	**0.254**

The vegetation sampling yielded very consistent vegetation moisture content values between different species. With average growing season vegetation moisture content being 66.57% and non-growing season average vegetation moisture being 17.50%. Vegetation canopy heights varied depending on species but were generally in the 2.0 meter range or 0.5 meter range. Although tall-form *Spartina alterniflora* vegetation samples were not obtained during our surveys, the USDA Plants Database was referenced and a value of approximately 1.0 meter was used to model this species (USDA). The final MIMICS radiometric model vegetation parameterizations were performed based on approximated marsh vegetation canopies rather than exact species or correspondence to a specific field sampling. This was done to select generalized vegetation heights with easily interpretable values and because field sampling of vegetation heights was limited compared to vegetation moisture content sampling. To provide generalized vegetation parameters, we parameterized the model with stems with a 1.5 cm diameter, length of 99 cm (maximum allowable value), and a vertical distribution to represent stems for marsh vegetation. Leaves were 2.5 cm in diameter and modeled as primary vertically oriented. The canopy was modeled with 50 stems per cubic meters and 200 leaves per cubic meter. The marsh canopies were then parameterized in MIMICS with canopy heights of 0.5, 1.0, and 2.0 meters. Compared to the generalized vegetation dimensions, more precise vegetation water content parameterizations were used, with 66.57% and 17.50% water contents being used to represent seasonal water content end-members in MIMICS. In total, six vegetation-based variants of the MIMICS model were parametrized with three vegetation height iterations and two water content iterations. We ran simulations for C-band scattering from the Sentinel-1 satellite and L-band scattering from the PALSAR/PALSAR-2 satellites for all six vegetation cases.

The MIMICS simulations produce outputs of both total backscatter intensity and backscatter contributions from various types of scatterers in the simulated environment which include ground scattering, direct vegetation scattering, and ground-vegetation scattering. Because our objective is to assess the sub-canopy hydrologic state of a simulated marsh, we focus our analysis of model outputs on the simulations with 2.0-meter canopy height and growing season vegetation water content (66.57%). By focusing on this particular simulation, we can assess C-band and L-band response to hydrologic state for a common high biomass marsh vegetation case where vegetation is most likely to interfere with radar's sub-canopy surface interaction, and thus, characterization. Utilizing MIMICS to fully assessing scattering mechanisms, we assess not only total backscatter intensity, but also the decomposition of scattering mechanisms which we compare to satellite-based analyses in later sections. Equation 1 that follows is reproduced from Kasischke and Bourgeau-Chavez (1997) with modified terms that better correspond to MIMICS first order solutions to the radiative transfer equation. MIMICS ground-crown and crown-ground terms correspond to double bounce scattering. MIMICS crown-ground-crown is approximated by the multiple path scattering term. MIMICS direct crown scattering and surface scattering are accurately represented by their original forms in equation 1.

$$\sigma^0{}_{t-h} = \sigma^0{}_c + \tau^2{}_c \ (\sigma^0{}_d + \sigma^0{}_m + \sigma^0{}_s) \tag{1}$$

where $\sigma^0{}_{t-h}$ is total herbaceous marsh backscatter. $\sigma^0{}_c$ is backscatter from the vegetation crown. $\tau^2{}_c$ is the transmission coefficient of the vegetation canopy. $\sigma^0{}_d$ is double bounce scattering between stems and ground (crown-ground and ground-crown). $\sigma^0{}_m$ is multiple path scattering (crown-ground-crown). $\sigma^0{}_s$ is surface scattering.

4.2.3 Description and Assembly of Datasets

We carried out an assessment of SAR satellite image capabilities in characterizing marsh inundation state from 2006-2020. PALSAR/PALSAR-2, UAVSAR, and Sentinel-1a imagery were all used in this assessment. Additionally, optical inundation products were compared to the SAR-based inundation products and assessed against *in situ* water level observations. Sentinel-1 imagery was acquired from Google Earth Engine (GEE) where it had been processed with ESA's SNAP toolbox for calibration and radiometric terrain correction prior to GEE ingestion. The SNAP toolbox was also used for the processing of PALSAR-2 imagery, performing calibration, multi-looking, speckle filtering, and radiometric terrain corrections. Multi-looking PALSAR-2 imagery was performed with the least number of looks required to produce a square pixel. Generally, this meant use of a 4x2 or 5x2 window. Multi-looking in this manner served to reduce speckle noise as well. Additional speckle filtering was then performed using a 5x5 Enhanced Lee filter. Radiometric terrain correction was performed with the 30-meter version of the SRTM DEM. PALSAR imagery was acquired from the Alaska Satellite Facility (ASF) at the 1.5 level where it had been previously calibrated and radiometric terrain corrected. After ASF acquisition, we speckle filtered PALSAR imagery with a 5x5 Enhanced Lee filter. UAVSAR imagery was accessed from ASF in Ground Projected Complex format and processed with ESA's PolSARpro software (v6.0) and ASF's MapReady software.

Sentinel-1 imagery was regularly acquired at 12-day intervals over the Mid-Atlantic study sites between 2015/2016 and 2020, which provided us with a very dense timeseries for analysis. PALSAR/PALSAR-2 and UAVSAR were acquired less frequently but were used more commonly in the proceeding analysis. For these reasons only PALSAR/PALSAR-2 and UAVSAR images are listed in Table 4.4.

Table 4.4 PALSAR/PALSAR-2 and UAVSAR acquisition table. Tidal stage represents the closest estimate of tidal stage for an image covering a study site. Wheeler, Kirkpatrick, and Blackwater NWR tidal stages have been time adjusted. Highlighted and underlined tidal values correspond to images used in analyses. Parenthesis represent the previous maximum tidal stage two days of fewer prior to image acquisition.

Sensor	Acquisition Time (GMT)	Site	Channels	Tidal Stage (meters)
PALSAR	2006-12-24 03:16:00	Wheeler	HH	0.857
PALSAR	2007-09-26 03:16:00	Wheeler	HH, HV	**2.313**
PALSAR	2007-12-27 03:15:00	Wheeler	HH	1.052
PALSAR	2008-06-28 03:13:00	Wheeler	HH, HV	0.707
PALSAR	2009-08-16 03:18:00	Wheeler	HH, HV	**0.884**
PALSAR	2009-10-01 03:18:00	Wheeler	HH, HV	1.791
PALSAR	2010-01-01 03:18:00	Wheeler	HH	2.224
PALSAR	2010-04-03 03:17:00	Wheeler	HH	0.887
PALSAR	2010-05-19 03:17:00	Wheeler	HH, HV	0.800
PALSAR	2010-07-04 03:17:00	Wheeler	HH, HV	0.352
PALSAR	2010-10-04 03:15:00	Wheeler	HH, HV	1.558
PALSAR	2010-11-19 03:15:00	Wheeler	HH, HV	**1.737**
PALSAR	2011-01-04 03:14:00	Wheeler	HH	1.947
PALSAR	2011-02-19 03:13:00	Wheeler	HH	2.209
PALSAR-2	2015-03-02 17:02:00	Wheeler	HH, HV	no data
PALSAR-2	2016-02-29 17:02:00	Wheeler	HH, HV	0.939
PALSAR-2	2016-04-25 17:02:00	Wheeler	HH, HV	**1.951**
PALSAR-2	2017-04-24 17:03:00	Wheeler	HH, HV	**1.305**
PALSAR-2	2017-04-27 4:40:00	Wheeler	HH, HV, VH, VV	**2.582**
PALSAR-2	2017-11-06 17:02:00	Wheeler	HH, HV	**2.807**
PALSAR	2006-12-05 03:30:00	Blackwater	HH	**0.128 (0.561)**
PALSAR	2007-10-28 15:36:00	Blackwater	HH	0.032
PALSAR	2008-10-30 15:35:00	Blackwater	HH	-0.327
PALSAR	2010-03-15 03:32:00	Blackwater	HH	**0.579 (1.164)**
PALSAR	2011-03-25 03:16:10	Blackwater	HH,HV,VH,VV	0.686
PALSAR-2	2015-05-10 4:56:00	Blackwater	HH,HV,VH,VV	**0.302**
PALSAR-2	2015-09-27 4:53:00	Blackwater	HH,HV	0.732
PALSAR-2	2016-09-02 5:03:00	Blackwater	HH,HV	0.232
PALSAR-2	2016-09-25 04:53:00	Blackwater	HH,HV	0.765
PALSAR-2	2017-01-02 5:03:00	Blackwater	HH,HV	0.655
PALSAR-2	2017-05-07 4:52:00	Blackwater	HH,HV,VH,VV	**0.777**
UAVSAR	2019-06-21 21:11:00	Wax Lake	HH,HV,VH,VV	--
UAVSAR	2019-07-02 23:27:27	Wax Lake	HH,HV,VH,VV	--
UAVSAR	2019-07-17 21:34:43	Wax Lake	HH,HV,VH,VV	--
UAVSAR	2019-07-17 21:34:43	Wax Lake	HH,HV,VH,VV	--
UAVSAR	2019-07-26 21:26:54	Wax Lake	HH,HV,VH,VV	--
UAVSAR	2019-08-13 21:56:25	Wax Lake	HH,HV,VH,VV	--
UAVSAR	2019-09-23 12:54:41	Wax Lake	HH,HV,VH,VV	--
UAVSAR	2019-10-01 21:59:22	Wax Lake	HH,HV,VH,VV	--
UAVSAR	2019-10-29 13:20:22	Wax Lake	HH,HV,VH,VV	--
UAVSAR	2019-07-01 14:02:30	White Lake	HH,HV,VH,VV	**0.780 (0.924)**
UAVSAR	2019-07-16 12:47:28	White Lake	HH,HV,VH,VV	**0.808 (1.716)**
UAVSAR	2019-07-25 13:21:57	White Lake	HH,HV,VH,VV	**0.738 (.744)**
UAVSAR	2019-06-06 14:17:10	Sabine River	HH,HV,VH,VV	--
UAVSAR	2019-07-16 13:03:21	Sabine River	HH,HV,VH,VV	--
UAVSAR	2019-07-25 13:40:18	Sabine River	HH,HV,VH,VV	--
UAVSAR	2019-08-12 13:42:28	Sabine River	HH,HV,VH,VV	**0.497**
UAVSAR	2019-09-23 13:21:08	Sabine River	HH,HV,VH,VV	**0.939**
UAVSAR	2019-09-30 13:40:41	Sabine River	HH,HV,VH,VV	**0.719**
UAVSAR	2019-10-29 13:50:13	Sabine River	HH,HV,VH,VV	--

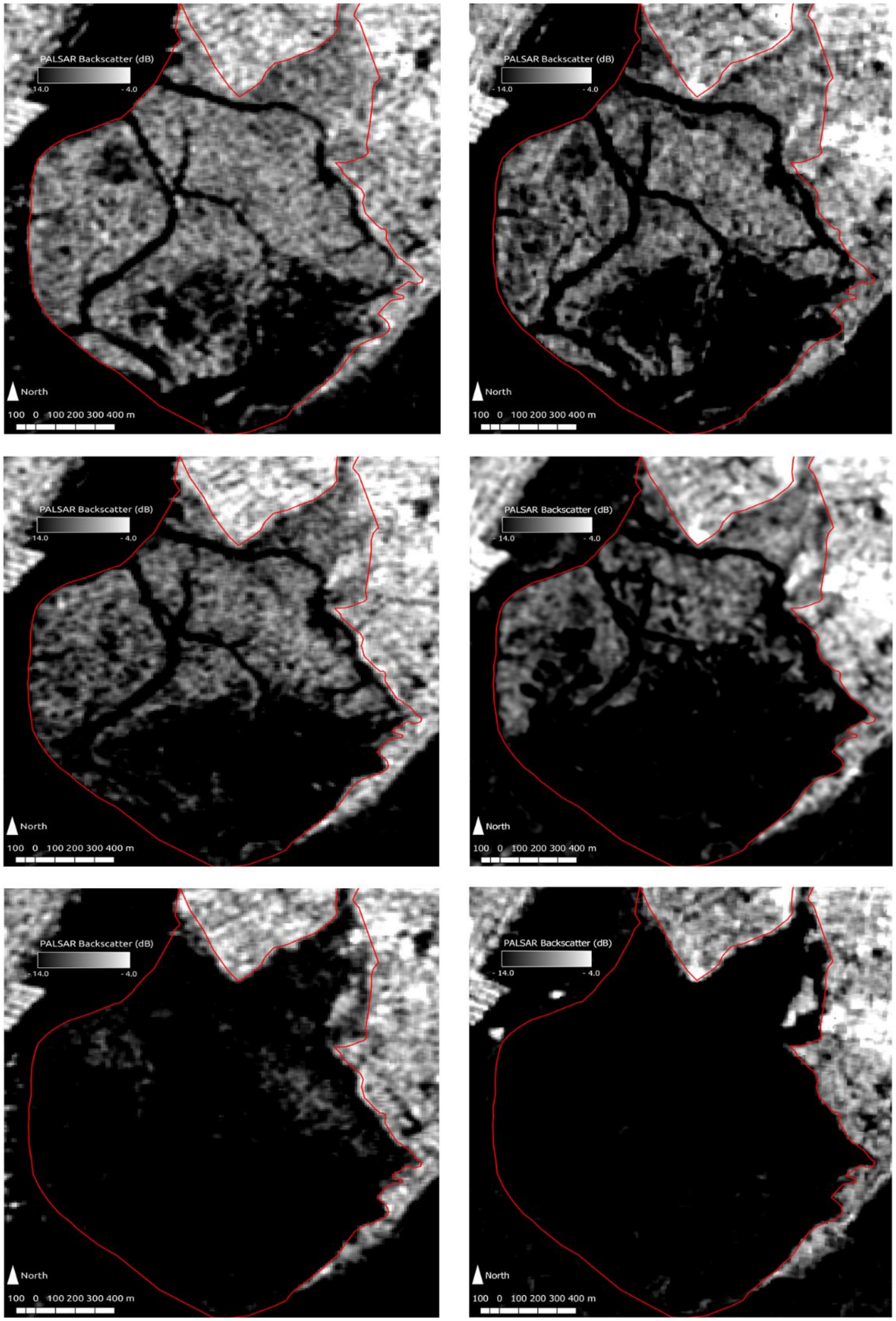

Figure 4.3. Tidally ordered assembly of PALSASR/PALSAR-2 HH imagery over the Wheeler Marsh study site (red outline). Note that backscatter decreases greatly as tidal stage increases (left-right, top-down). Backscatter scaled from -4.0 to -14.0 dB.

4.2.4 Previous Inundation Products Developed (rationale for part 1)

The inundation products we established in previous studies utilized change detection and threshold-based approaches. We developed a change detection approach for timeseries Sentinel-1a C-band imagery over Kirkpatrick Marsh, and a threshold-based approach for PALSAR L-band low tide-high tide image pairs over Blackwater NWR (Lamb et al. 2019). We then applied a similar threshold-based approach to a PALSAR/PALSAR-2 image timeseries over Wheeler Marsh (Lamb et al. 2020). One of the primary findings of this effort was that similar responses between high tide and low tide were observed in backscatter distributions in L-band imagery comparing Blackwater NWR to Wheeler Marsh, in spite of pronounced differences in tidal range between the sites. Over the Wheeler Marsh site, regressing spatial mean marsh backscatter against tidal stage showed a strong inverse relationship (shown in results section). The boxplot results reproduced from Lamb et al. (2019) in Figure 4.4 also showcase this response over Blackwater NWR.

4.2.5 Quad Polarimetric-Based Inundation Products (rationale for part 2)

We acquired quad-polarimetric (HH, HV, VH, VV) complex quad-pol PALSAR-2 imagery for Wheeler Marsh and Blackwater NWR, including a high tide-low tide image pair for Blackwater NWR. Several quad-polarimetric UAVSAR scenes were acquired over the Wax Lake, White Lake, and Port Arthur regions. We performed two forms of inundation classifications on these images, the first were polarimetric decompositions utilizing image phase information, which offer some of the best performance in assessing emergent wetland inundation state for single images (Schmitt and Brisco 2013; Hong et al. 2014; Atwood et al. 2020). We performed polarimetric decompositions on these quad-polarimetric images using the van Zyl and

Yamaguchi decompositions, as these polarimetric decompositions best relate to physical scattering mechanisms including surface scattering, double bounce, and volume scattering. Polarimetric decompositions were performed on complex quad-polarimetric imagery as dual-polarimetric decompositions cannot as effectively resolve these three scattering mechanisms (Ji and Hong 2015). In addition to performing these polarimetric decompositions, we also utilized threshold-based approaches on the same quad-polarimetric images to assess performance comparison between backscatter-based and polarimetric decomposition-based approaches for tidal marsh inundation state characterization. The quad-polarimetric decompositions and threshold-based decompositions were compared to the previously classified inundation products with similar tidal stages.

4.3. Results

4.3.1. Empirical Inundation Product Development and Validation

In the following section we evaluate L-band, C-band, and optical/IR imagery response to tidal marsh inundation state. We do this by assessing image change as it relates to tidal influence. Findings from Lamb et al. (2019) demonstrated that over the Blackwater NWR study site, L-band backscatter distributions shift so drastically that thresholding can be utilized to classify inundation. Reproduction of figures from this research effort are shown in Figure 4.4. Similar response of decreasing backscatter as a function of increasing tidal stage are present in Figure 4.5 which shows that similar responses are present for timeseries imagery over Wheeler Marsh as well. Table 4.3 showcases the correlation between marsh-averaged SAR backscatter and optical water indices/products in terms of their relationship to tidal stage.

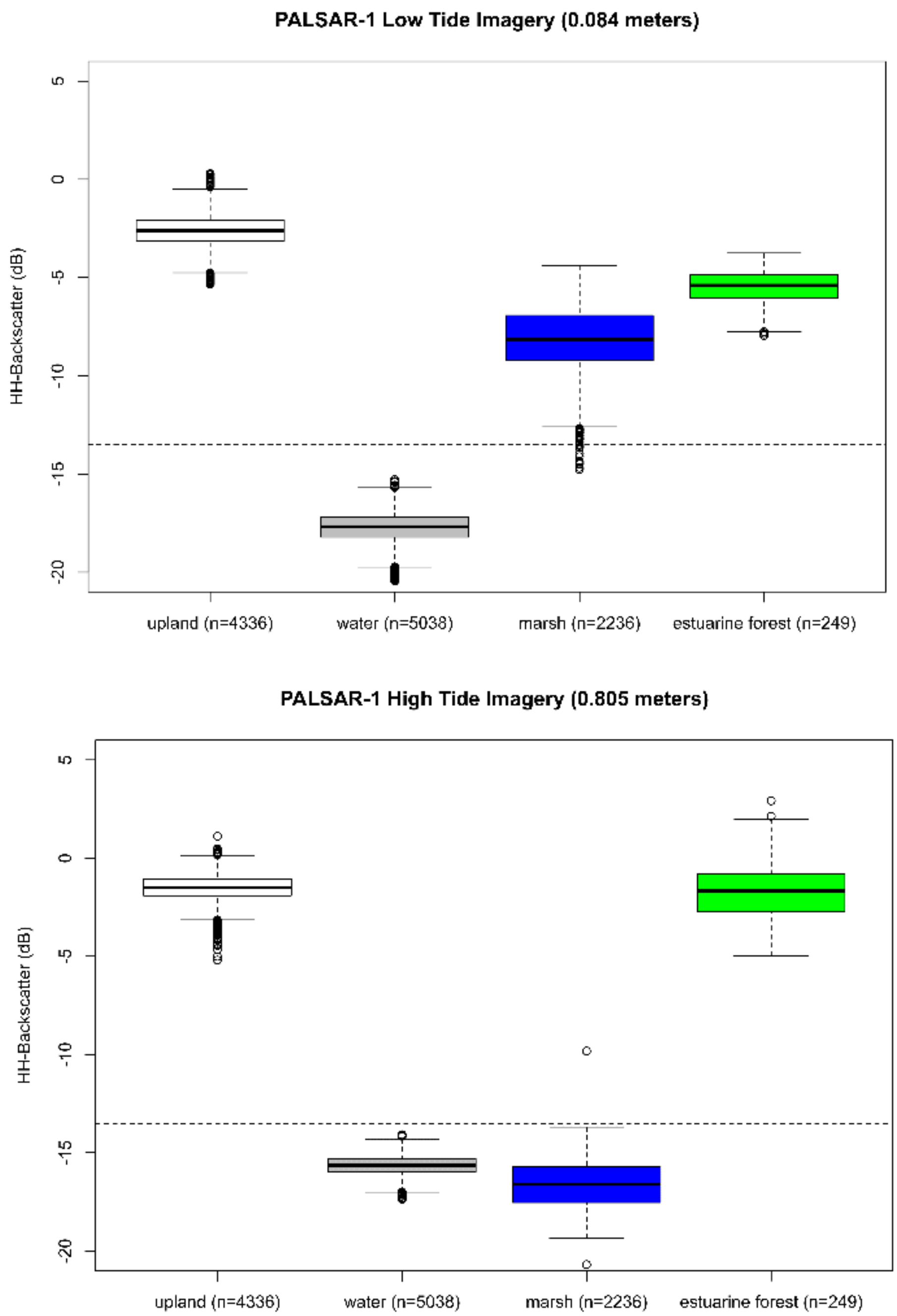

Figure 4.4. Low tide (upper panel) vs. high tide (lower panel) PALSAR backscatter distribution comparison for Blackwater NWR. Threshold of -13.5 dB (dotted horizontal line) effectively separates low tide and high tide marsh (presumably linked to inundation state). The marsh pixels extraction regions dominated by *Spartina alterniflora* vegetation. Figure 4.4 was previously published in Lamb et al. (2019) but was included here to showcase comparison to Figure 4.5. Tidal heights acquired from water level in connected estuary at Bishop's Head NOAA station.

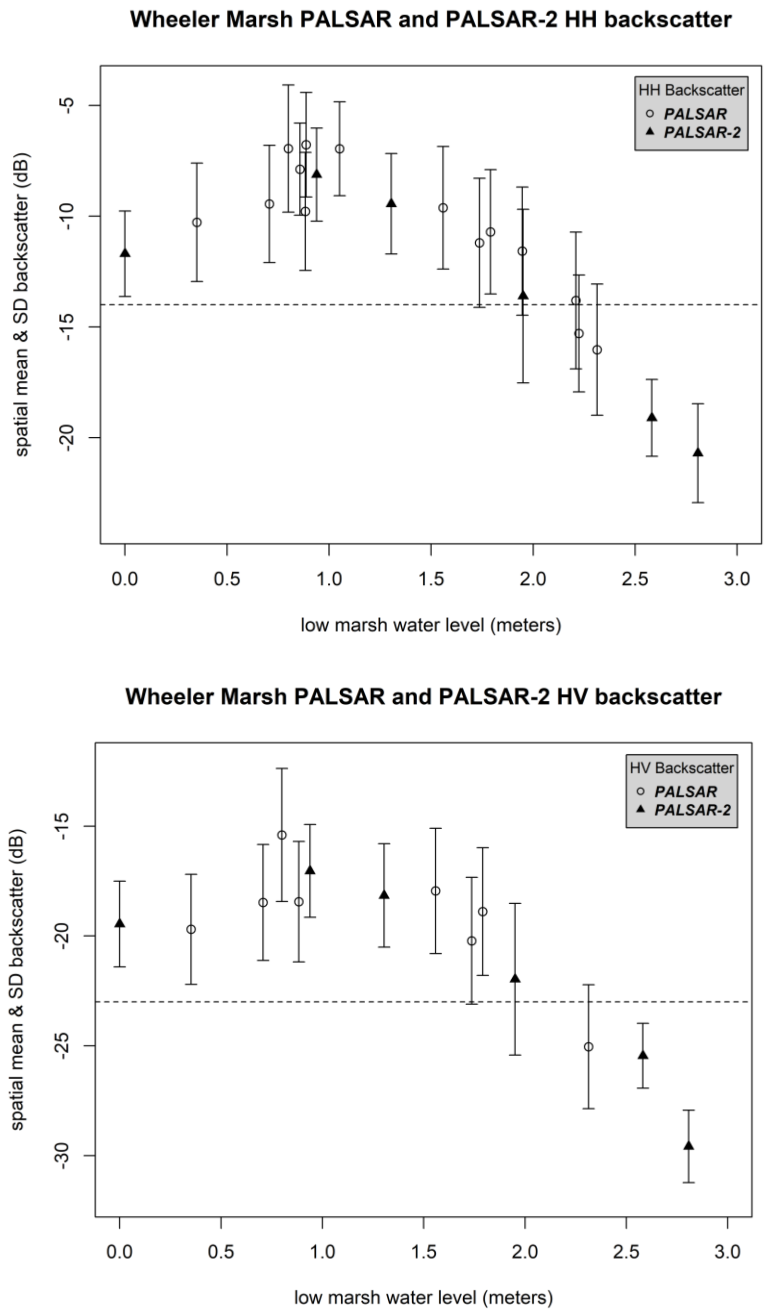

Figure 4.5. Comparison of full PALSAR/PALSAR-2 timeseries (2006-2017) as a function of Wheeler Marsh tidal stage for HH and HV polarizations (upper and lower panels). Horizontal lines shown at -14.0 dB for HH imagery and -23.0 dB for HV imagery. Pixels were extracted from region dominated by *Spartina alterniflora*. Note that in contrast to Blackwater NWR PALSAR analysis in Figure 4.4, Wheeler Marsh exhibits a far greater range of marsh elevations and a greater tidal range for an average tidal cycle. Water level estimated from time and height adjusted Bridgeport NOAA station to capture in-marsh water levels.

Table 4.5. Sentinel-1 (S1) and PALSAR/PALSAR-2 correlation with tidal stage (shown as R-values). This analysis includes all available satellite imagery up to 2018. OLS represents linear least squares fit between marsh-averaged backscatter and tidal stage. Poly represents a 2nd order polynomial fit. R-values greater than 0.8 have been bolded. Note that because only one PALSAR high tide-low tide image pair was available for Blackwater NWR analysis, no correlation assessment was performed. The B, W, GM, and N terms after the NWI classes correspond to Blackwater NWR, Wheeler Marsh, Great Meadows Marsh, and Nissequogue River, respectively.

NWI Class	S1-VH OLS	S1-VH Poly	S1-VV OLS	S1-VV Poly	S1-VV/VH OLS	S1-VV/VH Poly	NDWI OLS	NDWI Poly	mNDWI OLS	mNDWI Poly	PALSAR-HH OLS	PALSAR-HH Poly	PALSAR-HV OLS	PALSAR-HV Poly
E2EM1N-B	−0.638	0.757	0.374	0.575	−0.705	**0.889**	0.314	0.378	0.460	0.468	--	--	--	--
E2EM1P-B	−0.689	0.761	0.581	0.666	−0.765	**0.856**	0.352	0.393	0.471	0.515	--	--	--	--
E2EM1P6-B	−0.450	0.541	0.368	0.378	−0.530	0.567	0.192	0.283	0.001	0.235	--	--	--	--
E2EM1Pd-B	−0.646	0.725	0.457	0.539	−0.684	0.772	0.407	0.412	0.560	0.669	--	--	--	--
E2SS4P-B	−0.189	0.422	0.395	0.403	−0.456	0.457	0.047	0.303	−0.065	0.080	--	--	--	--
E2FO4P-B	−0.089	0.357	0.360	0.381	−0.401	0.401	0.006	0.236	0.108	0.142	--	--	--	--
E2EM1N-W	**-0.833**	**0.875**	-0.779	0.787	0.452	0.474	**0.911**	--	**0.912**	--	**-0.845**	**0.878**	**-0.917**	**0.978**
E2EM1P-W	-0.395	0.430	0.014	0.274	-0.290	0.500	0.562	--	0.701	--	**-0.806**	**0.955**	-0.625	**0.924**
E2EM1N-GM	-0.671	0.733	-0.430	0.430	-0.251	0.413	--	--	--	--	**-0.817**	**0.937**	-0.717	**0.897**
E2EM1P-GM	-0.472	0.555	-0.082	0.107	-0.376	0.497	--	--	--	--	-0.716	**0.872**	-0.666	**0.824**
E2EM1N-N	**-0.833**	**0.875**	-0.759	0.764	--	--	--	--	--	--	-0.670	0.744	**-0.843**	**0.947**
E2EM1P-N	-0.395	0.430	-0.075	0.299	--	--	--	--	--	--	-0.544	0.684	-0.446	**0.854**

In Figures 4.6-4.8 below, tidal image series have been updated to include imagery through 2020. Note the table above only includes imagery up to 2018. The correlation between backscatter and tidal stage improves for the longer timeseries Sentinel-1 C-band imagery, however the separability between high tide and low tide backscatter distributions are less apparent than for the L-band tidal series in Figure 4.5. Figure 4.8 shows an analysis for the Kirkpatrick Marsh site (not shown in Table 4.3).

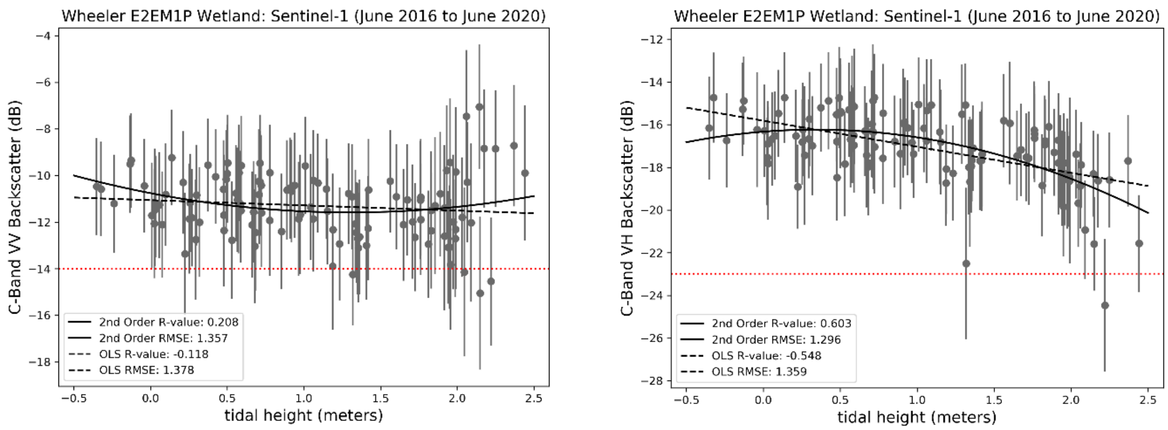

Figure 4.6. Comparison of full Sentinel-1 timeseries as a function of Wheeler Marsh tidal stage for VV (left) and VH (right) polarizations. Horizontal lines shown at -14.0 dB for VV imagery and -23.0 dB for VH imagery. Pixels were extracted from region dominated by *Spartina alterniflora*. Note that in contrast to L-band analysis in Figure 4.5, the polarimetric responses vary between the VV and VH polarizations, with VV backscatter generally increasing and VH backscatter decreasing as a function of tidal stage. Water level estimated from time and height adjusted Bridgeport NOAA station to capture in-marsh water levels. Error bars on points represent +/-1 SD

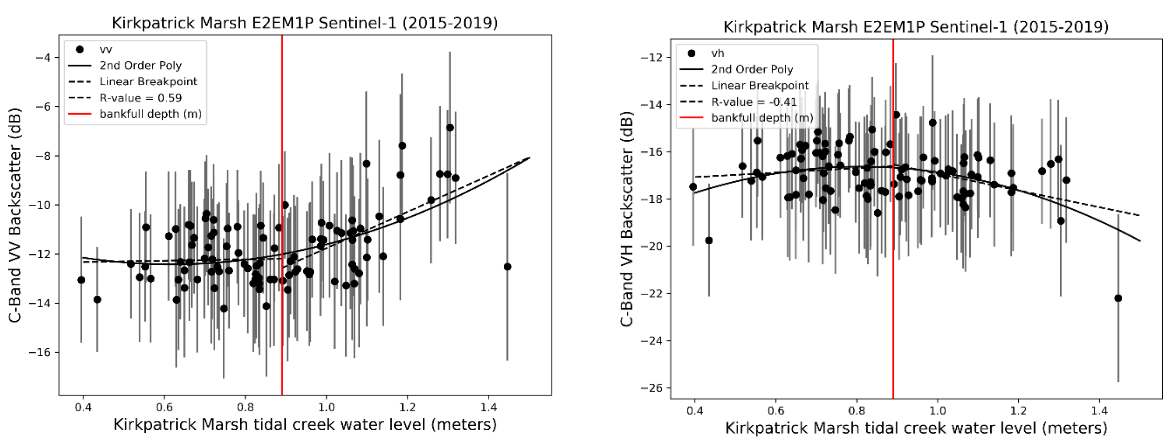

Figure 4.7. Comparison of full Sentinel-1 timeseries as a function of Kirkpatrick Marsh tidal stage for VV (left) and VH (right) polarizations. Pixels were extracted from regions dominated by *Spartina patens*, *Schoenoplectus americanus*, *Iva frutescens*, and *Phragmites australis*. Error bars represent +/-1 SD in backscatter. Vertical red line represents marsh bankfull depth from Nelson et al. (2017). R-value is from above bankfull depth linear regression.

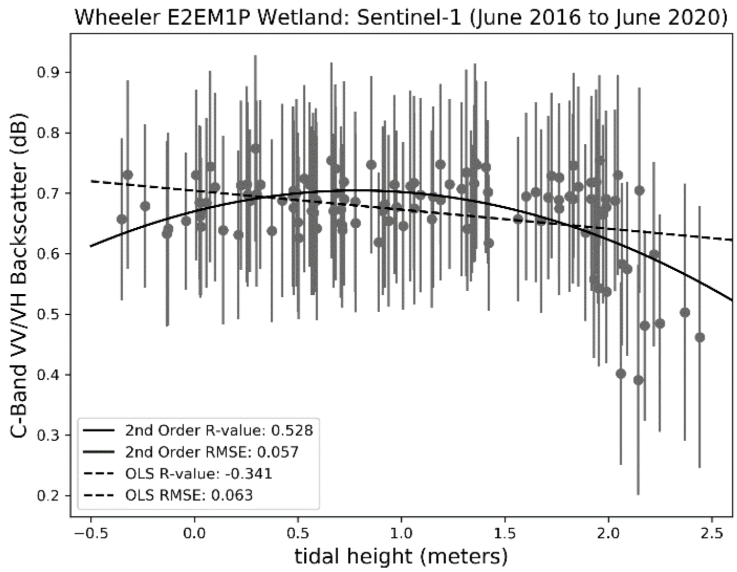

Figure 4.8. Wheeler Marsh Sentinel-1 VV/VH-tidal stage comparison scatter plot. Error bars represent +/-1 SD.

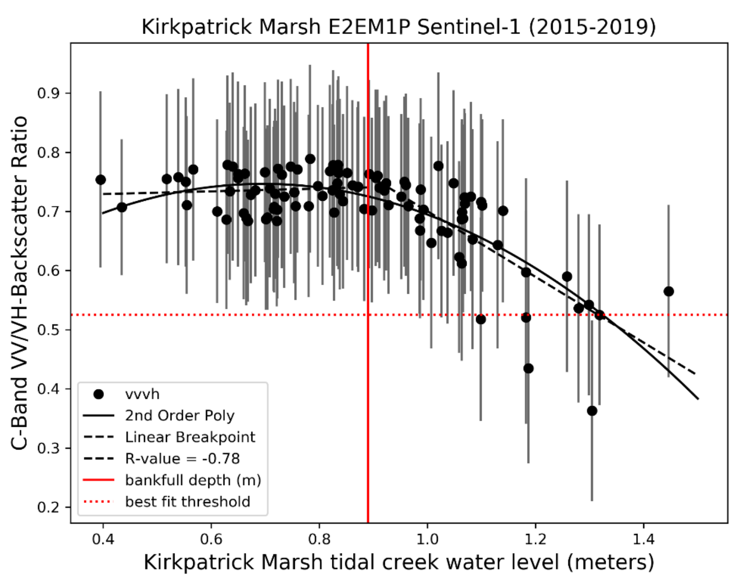

Figure 4.9. Kirkpatrick Marsh Sentinel-1 VV/VH-tidal stage comparison scatter plot. Error bars represent +/-1 SD. Vertical red line represents marsh bankfull depth from Nelson et al. (2017).

Between Kirkpatrick Marsh, Wheeler Marsh, and Blackwater NWR, the Sentinel-1 C-band VV/VH ratio generally provided the most sensitivity to tidal stage compared to the VV and VH polarizations alone. In comparing Kirkpatrick Marsh to Wheeler Marsh backscatter distributions, no consistent separability was observed for this C-band polarimetric ratio as was observed for HH and HV channels in L-band imagery. Thus, absolute thresholding approaches could not be effectively applied to C-band imagery, and instead change detection approaches were utilized. Lamb et al. (2019) had originally tested confidence interval-based change detection approaches for producing inundation products over the Kirkpatrick Marsh site. This approach had defined these confidence intervals based on a temporal standard deviation calculation for all 2016-2017 imagery acquired at low tide (below bankfull depth). The confidence intervals for detection of inundation were tested at 1, 2, and 3 standard deviations (Lamb et al. 2019). In this effort we selected a 1.5 SD threshold for classification of inundation above bankfull depth.

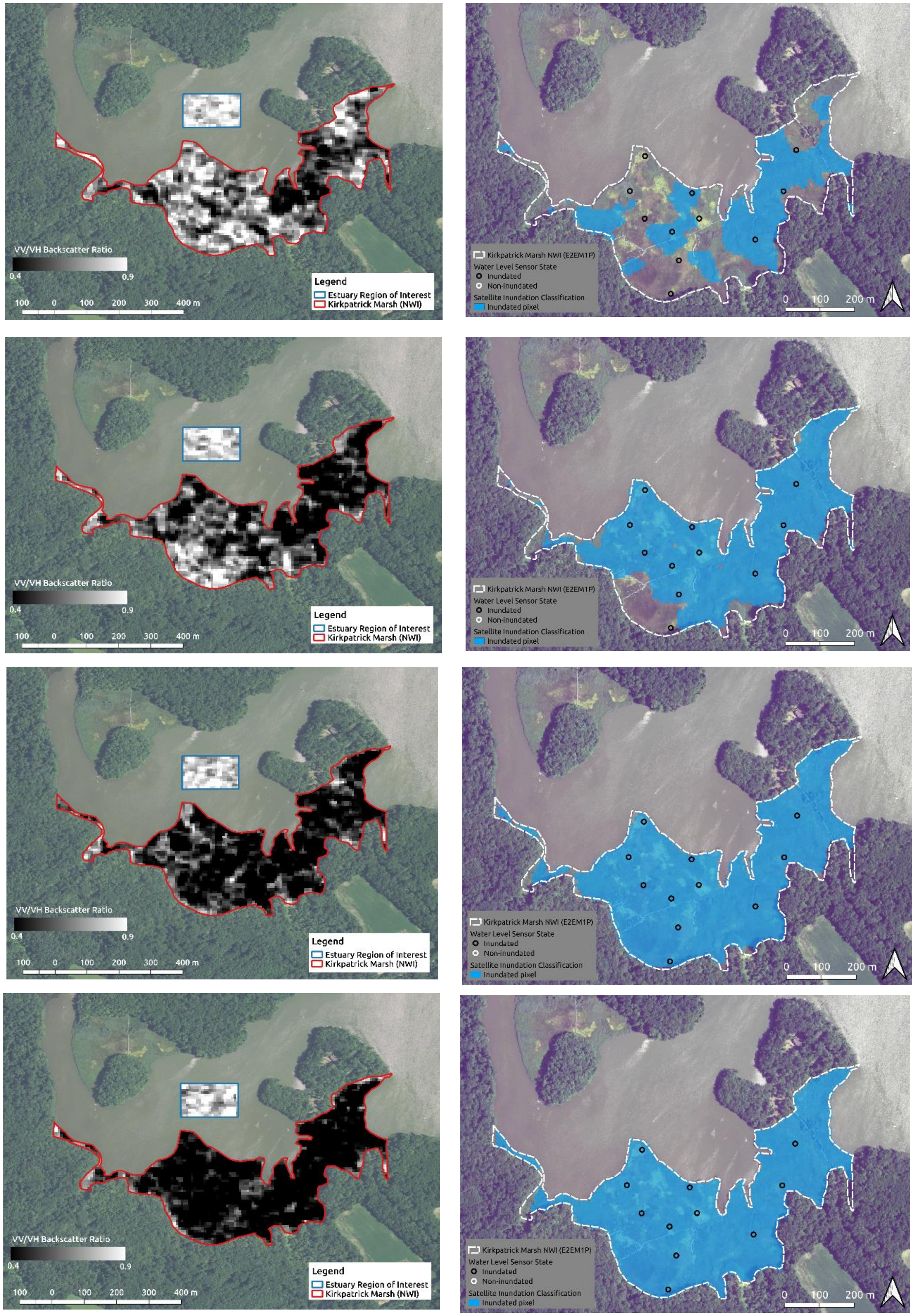

Figure 4.10. 2016 and 2017 example high tide VV/VH ratio imagery (left) and classified inundation with 1.5 SD low tide VV/VH confidence interval (right).

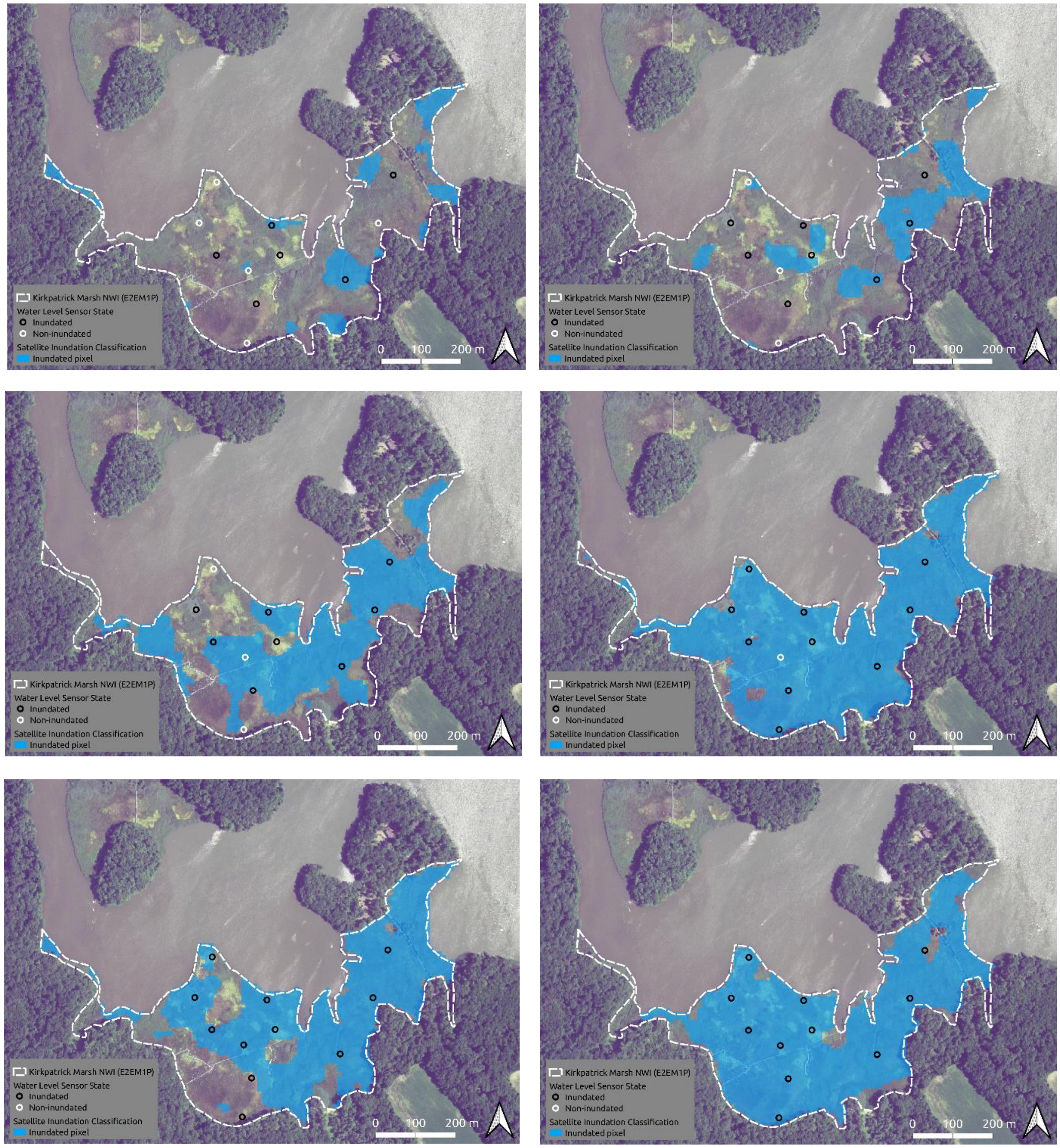

Figure 4.11. 2017-2019 Imagery classified with 1.5 SD change detection approach. For the full above bankfull depth high tide classified imagery, agreement between estimated water level and classified inundation products was 84/110 (76.4%).

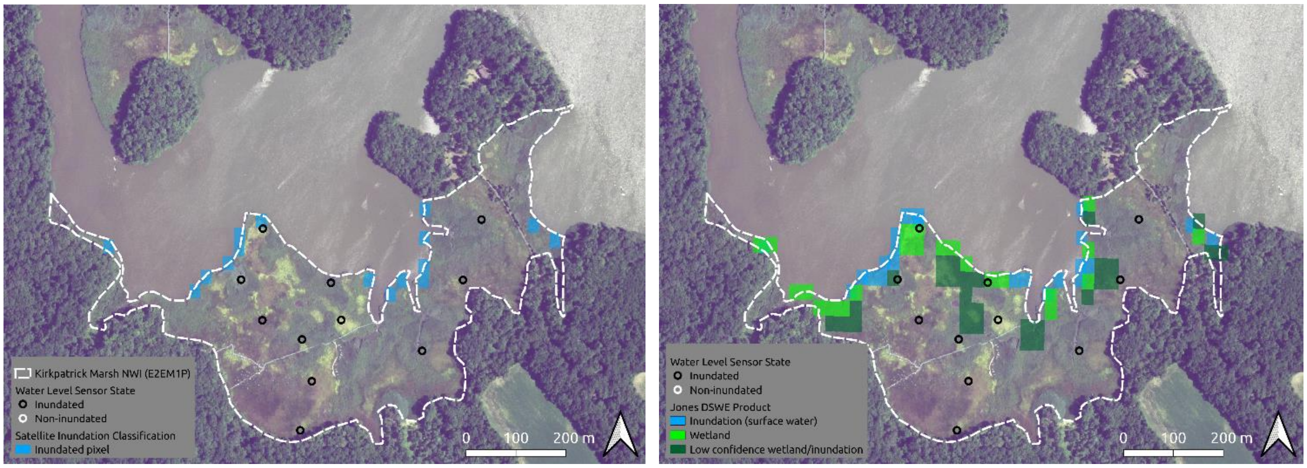

Figure 4.12. High tide optical surface water/inundation products at Kirkpatrick Marsh creek tidal stage >= 1.106 m. JRC maximum surface water extent from Landsat 5-8 record (1985-2019) Pekel et al. (2016) on left. No sensors that detected inundation were classified as inundated by the JRC product. USGS DSWE product on right features a more complex classification with wetland classification in addition to surface water. DSWE product achieves accuracy of 3/11.

The VV/VH change detection products were validated over a range of high tide imagery. This validation yielded a 78.5% accuracy. Comparatively, existing high tide optical inundation products were also validated against water level sensors. Although the Sentinel-1 C-band products did not yield high accuracies, those of optical surface water/inundation products accuracies were far lower for the Kirkpatrick Marsh high marsh site.

The performance of the Kirkpatrick Marsh change detection approach in Figures 4.10 and 4.11 is contrasted by a similar change detection approach incorporated over Wheeler Marsh in Figure 4.13. A key distinction between these approaches is that the Wheeler Marsh inundation product is produced with both VV/VH and VH channel change detection layers.

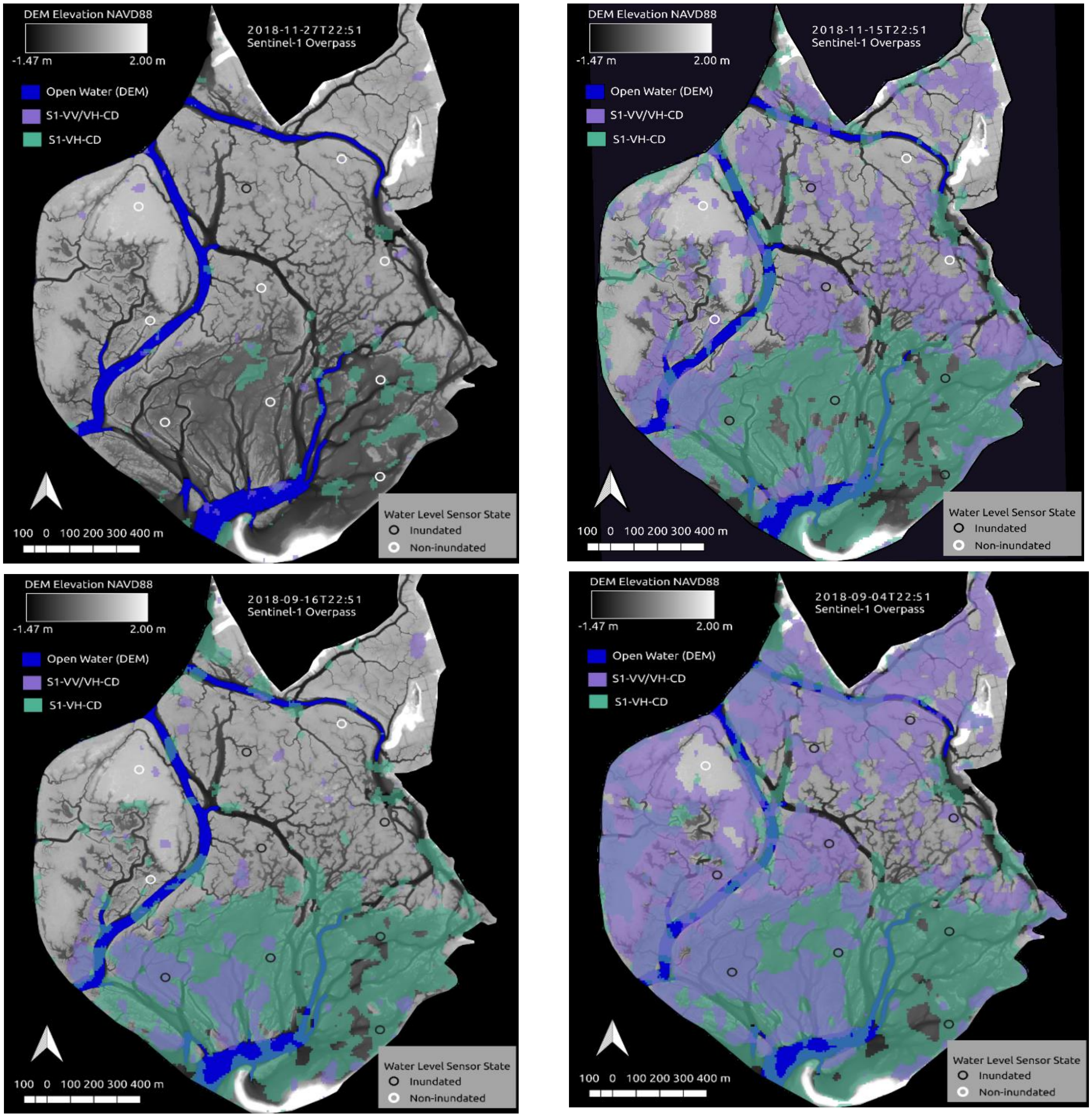

Figure 4.13. Sentinel-1 change detection classified inundation combining VV/VH and VH change detection at a 1.5 SD level. Low tide VV/VH and VH layers were computed for all Sentinel-1 imagery from 2016-2019 below 0.3048 meters time-adjusted Bridgeport NOAA station tidal stage. Classified inundation is validated directly by water level sensors during 2018 deployment. Overall accuracy for tidal series, including low tide classifications (not shown in figure) was 87.5% (71/80) from 8 total Sentinel-1 scenes.

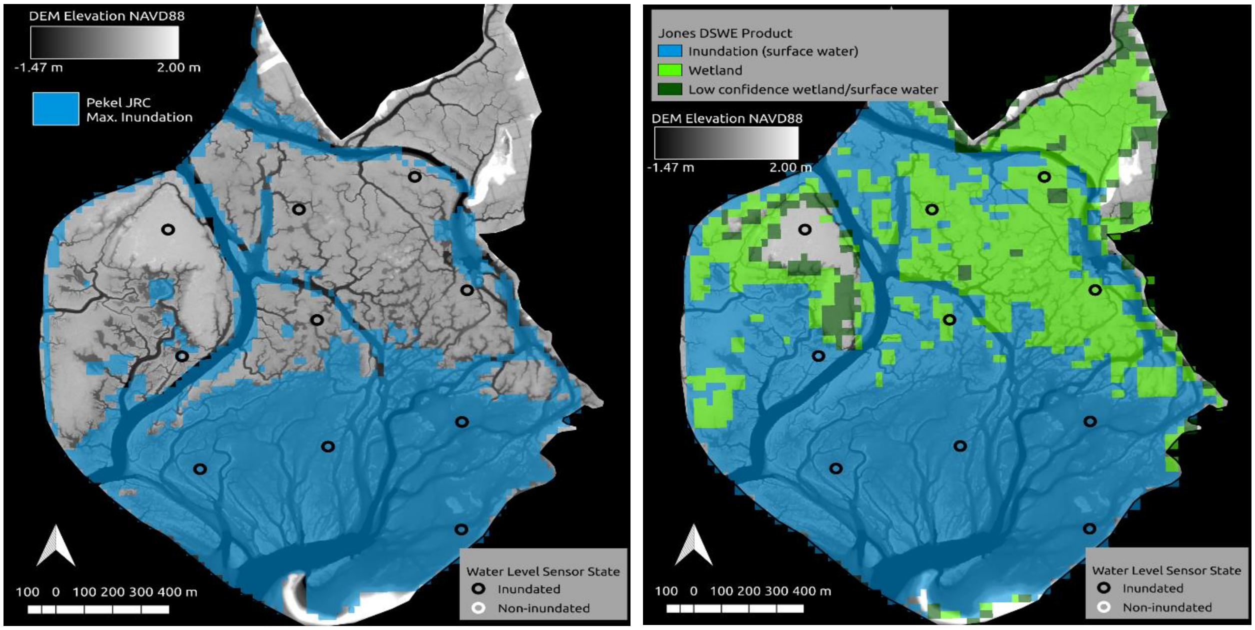

Figure 4.14. High tide optical surface water/inundation products at Wheeler Marsh (tidal stage >= 2.124 m. JRC maximum surface water extent from Landsat 5-8 record (1985-2019) Pekel et al. (2016) on left. 4/10 sensors detected inundation from the JRC product. USGS DSWE product on right features a more complex classification with wetland classification in addition to surface water. DSWE product achieves accuracy of 5/10 if considering only inundation classification, but 9/10 if also considering wetland classification as inundated.

Overall, both the C-band SAR inundation products and optical inundation products performed much better over the Wheeler Marsh site compared to Kirkpatrick Marsh in terms of inundation detection. This is expected given that the *Spartina alterniflora*, the dominant species of vegetation at Wheeler Marsh, has much more open canopy than the high marsh species of Kirkpatrick Marsh. It is possible that the degree of canopy closure combined with the larger degree of canopy submergence during high tide combines in a manner such that both optical/IR reflectance and C-band SAR backscatter respond to marsh hydrologic state. If comparative performance is any indication, the lack of inundation detection at Kirkpatrick Marsh suggests that optical/IR products do not perform well in densely vegetated marsh. High tide L-band imagery did not exist for Kirkpatrick Marsh, but did for Wheeler Marsh where performance is assessed in Figure 4.15.

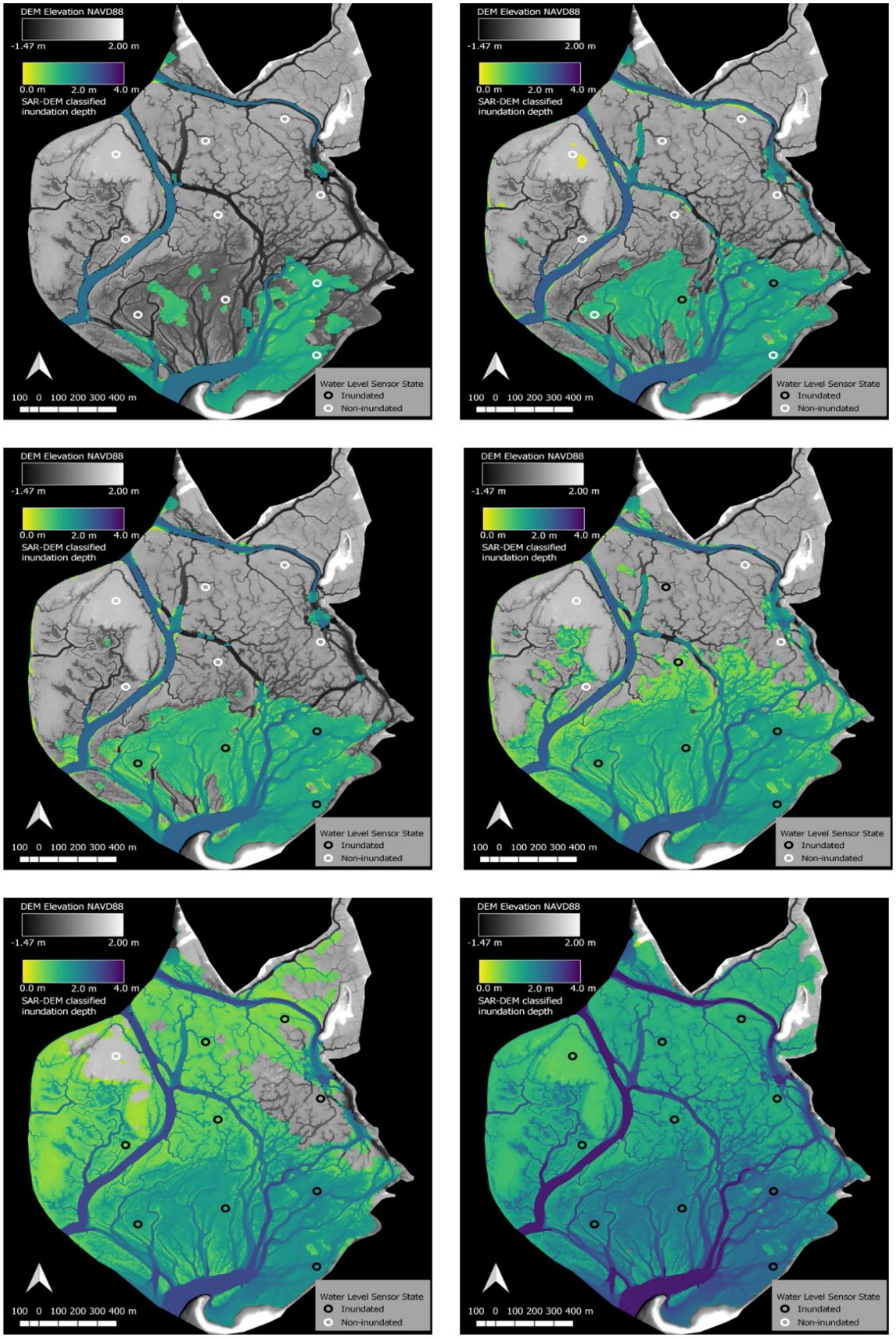

Figure 4.15. PALSAR/PALSASR-2 threshold-based inundation products over Wheeler Marsh. 90% classification accuracy comparing SAR inundation products to *in situ* water level sensor inundation state (54/60).

Comparing the C-band change detection-based inundation product development to the L-band threshold-based inundation product development over the Wheeler Marsh site yielded similar performance in total classification accuracy (87.5% vs. 90%). However, a key distinction needs to be drawn based on the fact that the L-band thresholding approach does not require prior satellite-based assessment of the site (i.e. calculating a normal range of low tidal marsh variability) as the C-band change detection approaches did. This difference was due to the fact that L-band backscatter showed a completely separable distribution change between high and low tide, while C-band did not exhibit this separability. Thus, even when inundation classification performance may be comparable, the threshold-based approaches prove a more effective method with broader applicability outside of a given study region. The USGS DSWE product performed well in inundation mapping at Wheeler Marsh. Although we were not able to test an extensive set of DSWE products, it should be noted that nadir-view optical products do provide potential capabilities in assessing inundation state provided that vegetated canopies retain some degree of openness. However, in tidal marsh systems that lack some degree of canopy openness, like Kirkpatrick Marsh, optical/IR products cannot detect sub-canopy hydrologic state as SAR does. Further, a more extensive validation of DSWE performance at the Wheeler Marsh site is needed, especially considering multiple DSWE classes need to be merged to provide an inundation mapping performance accuracy comparable to L-band SAR at 90% accuracy.

The fact that L-band SAR imagery provided more clearly defined responses to marsh inundation state than C-band SAR is consistent with previous literature (Ramsey et al. 2013; Kim et al. 2014). This difference is likely attributable to C-band backscatter being most responsive to marsh vegetation variability. This is evidenced by variability in C-band polarimetric response comparing Kirkpatrick Marsh and Wheeler Marsh. The Kirkpatrick Marsh site showed a strong positive correlation between VV backscatter and tidal stage, compared to Wheeler Marsh that showed a strong negative correlation between VH backscatter and tidal stage. Fairly consistent decreases in VV/VH ratio was observed over both sites which motivated the use of the VV/VH ratio change detection for both Kirkpatrick Marsh and Wheeler Marsh for inundation mapping. However, Wheeler Marsh also required the use of the VH channel to map inundation regimes accurately. These differences in backscatter responses at the varying C-band polarizations may be attributed to vegetation differences at the two sites (a high elevation marsh vs. low elevation marsh). In the next section we implement radiometric modeling efforts to help elucidate casual factors leading to differing polarimetric and frequency-based response to tidal inundation. Namely the role that marsh vegetation, hydrologic state, and SAR sensor attributes play in influencing observed backscatter responses.

4.3.2 Radiometric Modeling Results

It is critical to establish mechanistic understanding of SAR scattering mechanisms in being able to produce and interpret wetland inundation products. In previous efforts by Lamb et al. (2019) inundation products were established using empirical methods that had not been validated or tested against theoretical analyses (i.e. radiometric modeling efforts). The following results from our MIMICS simulations show backscatter response for a range of vegetation canopy heights and marsh surface hydrologic states and assesses whether the backscatter range for the HH channel < -13.5 to -14 dB and HV channel < -23 is sufficient for detecting sub-canopy inundation state. Figures 4.16-4.18 represent changes in starting canopy height at 0.5, 1.0, and 2.0 meters with growing season vegetation water contents (66.57%).

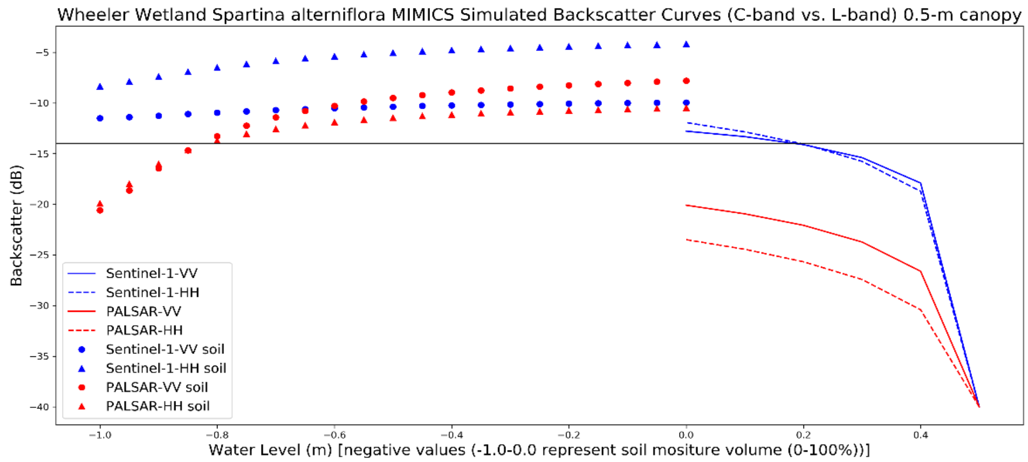

Figure 4.16. MIMICS simulated scattering response for PALSAR and Sentinel-1 for a 0.5 meter vegetated canopy during growing season. Negative x-axis values correspond to % soil moisture (-1.0 = 0.0% soil moisture, 0.0 = 100% soil moisture). Note the step function between wet soil and standing water shows distinct break in backscatter for both Sentinel-1 and PALSAR for HH channel, while VV shows a less distinct break. Defined PALSAR HH inundation classification threshold (-14 dB) shows effective separation only at soil moisture values greater than 20%. Sentinel-1 VV shows less sensitivity to soil moisture variability than PALSAR, but does show a backscatter decrease when inundated that completely separates between moist soil and standing water, albeit at a less drastic backscatter decrease than HH. Note that Sentinel-1 HH polarization provides the best performance in inundation detection, although we obtained no Sentinel-1 HH imagery over our study sites.

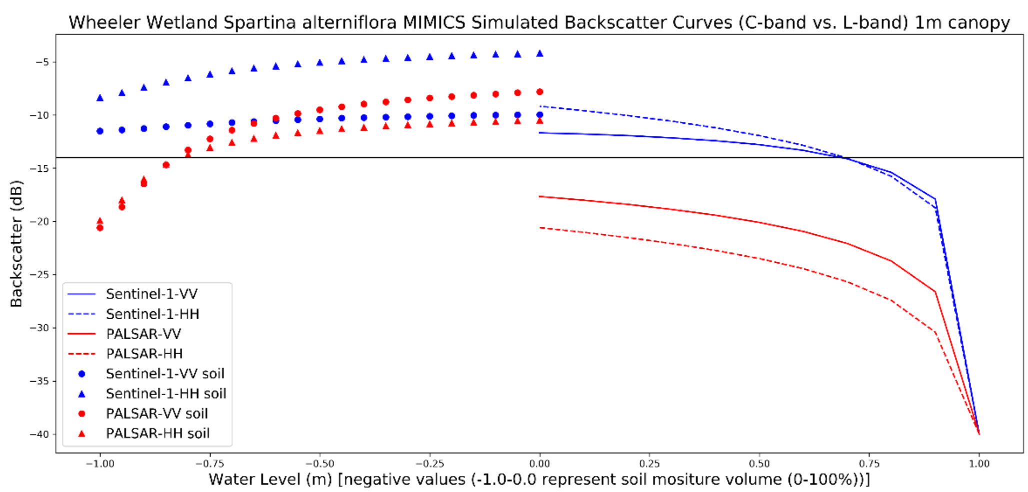

Figure 4.17. MIMICS simulated scattering response for PALSAR and Sentinel-1 for a 1.0 meter vegetated canopy during growing season. Like the 0.5 meter canopy simulation in the preceding figure, PALSAR HH backscatter step function decrease was drastic comparing wet soil to standing water. However, non-inundated soils could only be distinguished from standing water at values above 20% for PALSAR.

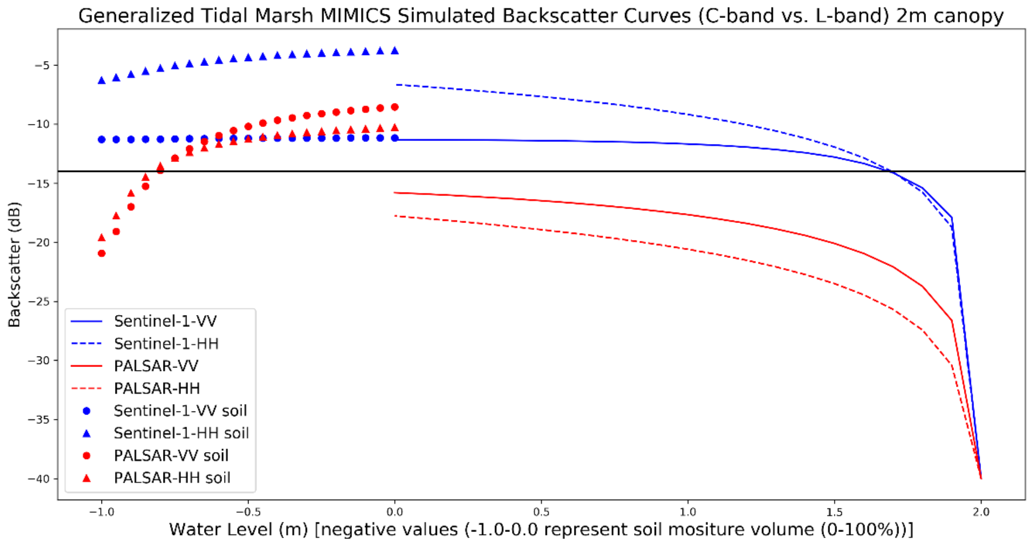

Figure 4.18. MIMICS simulated scattering response for PALSAR and Sentinel-1 for a 2.0 meter vegetated canopy during growing season. Sentinel-1 VV backscatter has almost no sensitivity to changes in soil moisture or water level until canopy was submerged up 1.5 meters. This demonstrates that C-band VV backscatter saturates in vertically-structured higher biomass marsh canopies and is far less effective than Sentinel-1 VH or L-band channels for assessing marsh hydrologic state.

The previous three figures demonstrate that with co-polarized backscatter, L-band produces drastic backscatter decreases in response to change in inundation state for a growing season vertically structured canopy of various total heights. As expected with the longer wavelength L-band signals, there is more sensitivity to sub-canopy hydrologic state than for C-band signals. Importantly, simulated Sentinel-1 C-band HH signals had a far greater degree of sensitivity to hydrologic state change than VV signals. This is an important finding when considering SAR polarimetric operating mode for wetland studies. Unfortunately, the Sentinel-1 satellite has only acquired VV and VH imagery over our Mid-Atlantic study sites. In the following three figures we evaluate backscatter response from a growing season canopy with simulated cross-polarimetric signals and evaluate backscatter responses from non-growing season canopies.

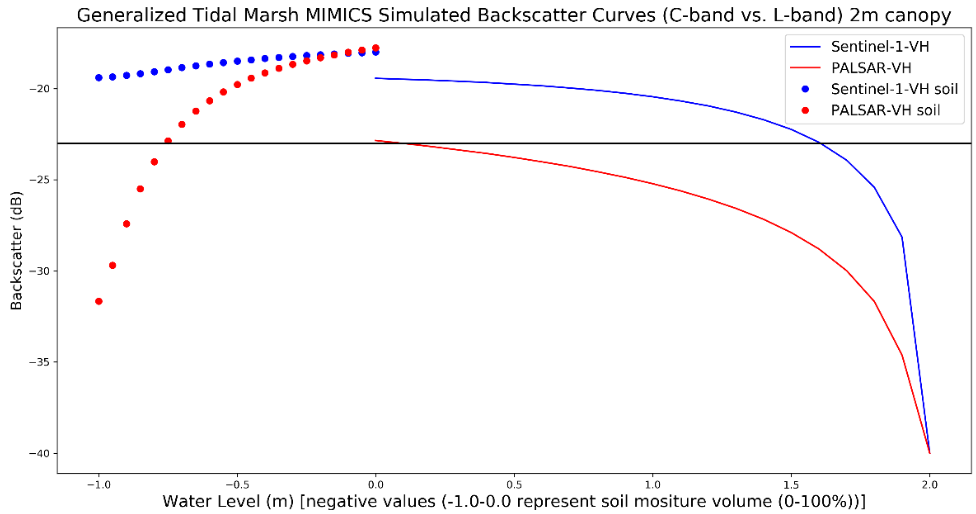

Figure 4.19. MIMICS simulated scattering response for PALSAR HV and Sentinel-1 VH for a 2.0 meter vegetated canopy. For the PALSAR HV channel, in order to distinguish between soil and inundation, a soil moisture value greater than 25% was needed to separate between hydrologic states with the threshold of -23 dB (black horizontal line). The Sentinel-1 VH channel shows a much greater sensitivity to the change in hydrologic state than the VV channel shown in the preceding figure. However, the step change in backscatter is not nearly as drastic as the L-band HV response.

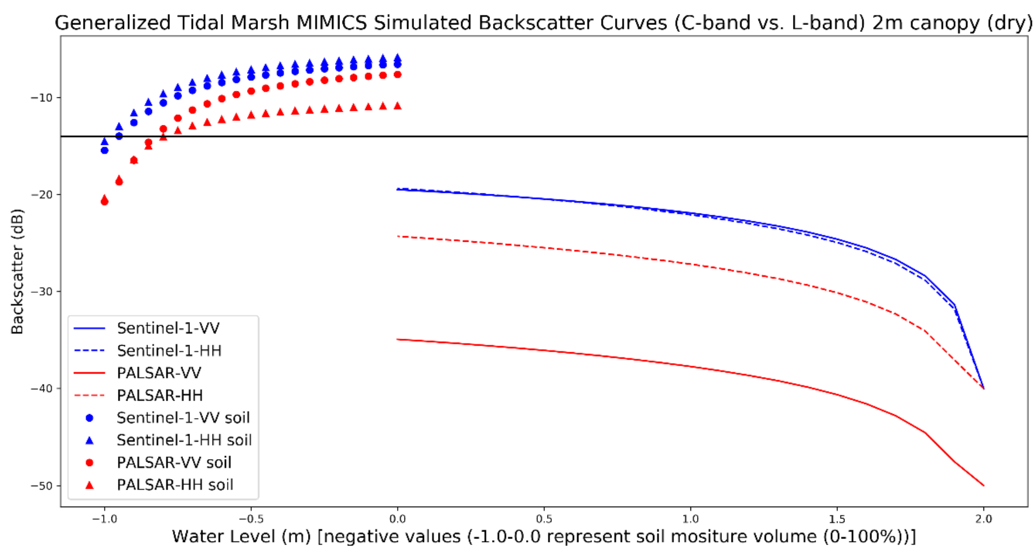

Figure 4.20. MIMICS simulated scattering response for PALSAR and Sentinel-1 for a 2.0 meter dry vegetated canopy (non-growing season). Compared to the case of growing season canopy in figure 4.18, the Sentinel-1 and PALSAR VV and HH channels show backscatter decrease as a function of hydrologic state change. Like previous figures, L-band only shows separation beyond 20% soil moisture.

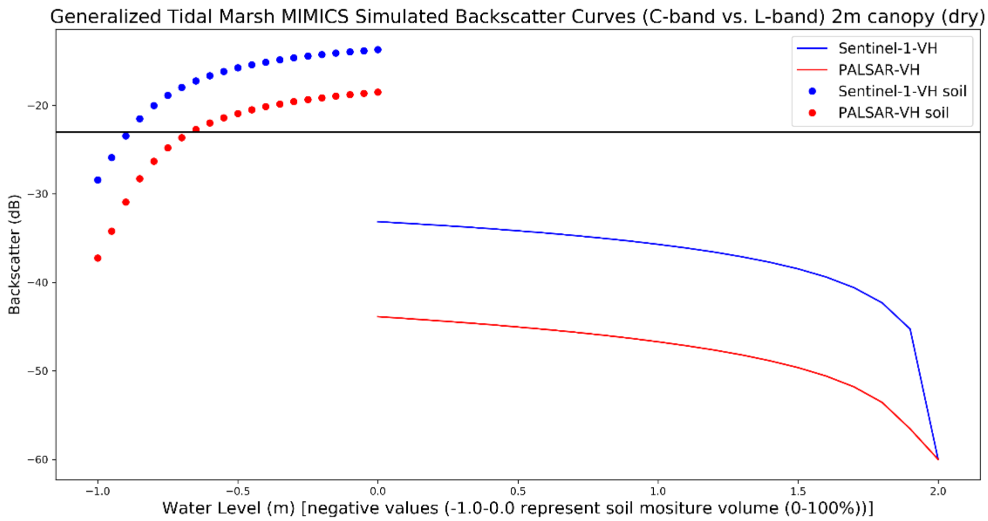

Figure 4.21. MIMICS simulated scattering response for PALSAR HV and Sentinel-1 VH for a 2.0 meter dry vegetated canopy (non-growing season). For the PALSAR HV channel, in order to distinguish between soil and inundation, a soil moisture value greater than 30% was needed to separate between hydrologic states with the threshold of -23 dB (black horizontal line). The Sentinel-1 VH channel shows comparable sensitivity to the change in hydrologic state compared to the VV channel shown in the preceding figure. The simulated inundated backscatter values were not observed in any imagery and are near or lower than the noise floor of most SAR sensors.

The results from the MIMICS simulations demonstrate that in general both C-band and L-band SAR backscatter responds to sub-canopy hydrologic state. For both 0.5 meter and 1.0 meter growing season canopies, Sentinel-1 and PALSAR simulations both showed backscatter step change decrease that was responsive to change between saturated soil and an inundated surface. In terms of the MIMICS model's representation of reality, this step change essentially represents a change from a rough water surface (at a soil moisture of 100%) to a smooth water surface. This calls attention to the importance of water's roughness impacting backscatter. Under marsh canopies, water surfaces are generally smooth as a result of stems and leaves attenuating water's movement from wind, waves, and tides (Leonard and Luther 1995). Thus, the general form of this model's hydrologic change does approximate marsh hydrologic conditions fairly well. Although this abrupt backscatter step change is in reality slightly more continuous as soils saturate and partially inundate transitioning from a surface of high roughness to moderate surface to low roughness.

The differences in C-band and L-band response are most apparent in the 2.0 meter canopy simulations. With the Sentinel-1 VV channel, there was very little response to increasing soil moisture and inundation depth. The Sentinel-1 VH channel in contrast showed fairly well-defined response to the moist soil-inundation transition for all canopy heights during the growing season and non-growing season. According to these simulations, Sentinel-1 VH channel would ideally present a more ideal form of imagery for inundation detection than PALSAR HH or HV channels. However, it was apparent in all MIMICS simulations that the greater magnitude of step change for the L-band PALSAR simulations was likely necessary for separating moist soils from inundated states unambiguously as there are likely uncertainties and errors in attempting to simulate marsh canopy structure and hydrologic state with this modeling effort. The greater step change for the L-band signals was likely drastic enough to negate modeling errors and uncertainties and is likely why a comparison to the empirical L-band image analysis shows similarly well-defined backscatter decreases in response to inundation. The radiometric modeling effort findings were corroborated by the empirical findings in Figures 4.5 and 4.6 comparing PALSAR HH and HV tidal series to Sentinel-1 VH tidal series, where the +/- 1 standard deviation backscatter distributions were separable for the PALSAR images comparing low tide and high tide, while this was not true for Sentinel-1 VH images. It should be noted, however, that in spite of the general correspondence between the MIMICS modeling efforts and L-band empirical assessments in earlier sections, that threshold-based approaches may have limited utility in marshes that have lower soil moisture values (< 20-30%). However, these lower moisture conditions are somewhat atypical for tidal marshes, for instance Moffett et al. (2015) reported average soil volumetric moisture contents of 0.83 (sd = 0.15) in San Francisco tidal marshes. Nonetheless, this is still an important limitation of the threshold-based classification approach that must be clarified. Up to this point, we have discussed total backscatter response to various marsh vegetation and hydrologic states, in the following section we provide a separation of the scattering mechanisms associated with the MIMICS simulations for C-band VV, HH, VH and L-band HH, VV, HV responses. In the figures that follow, backscatter contributions are shown in values of σ rather than dB. In the following plots, total backscatter includes scattering contributions from surface backscatter, direct crown backscatter, crown-ground-crown backscatter, and crown-grown backscatter as described earlier in equation 1. The crown-ground term used in the following plots represents the additions of both crown-ground and ground-crown scattering.

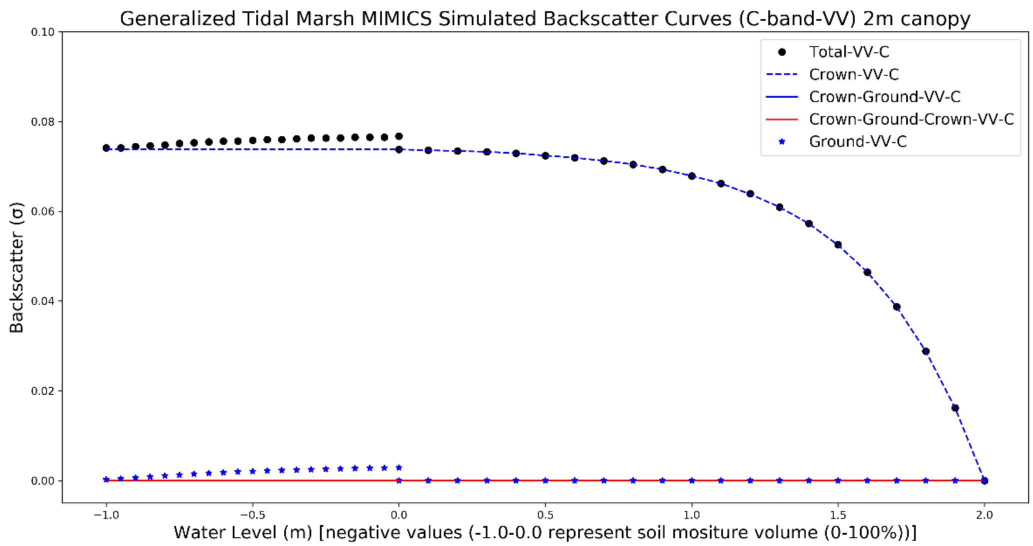

Figure 4.22. MIMICS simulated Sentinel-1 C-band VV scattering contributions from tidal marsh. This includes total backscatter, direct crown scattering, crown-ground scattering, crown-ground-crown scattering, and ground scattering. Note that crown-ground scattering and crown-ground-crown scattering overlap at ~0.00 σ. Direct crown scattering dominates total scattering response. σ scaled between 0.00 to 0.10.

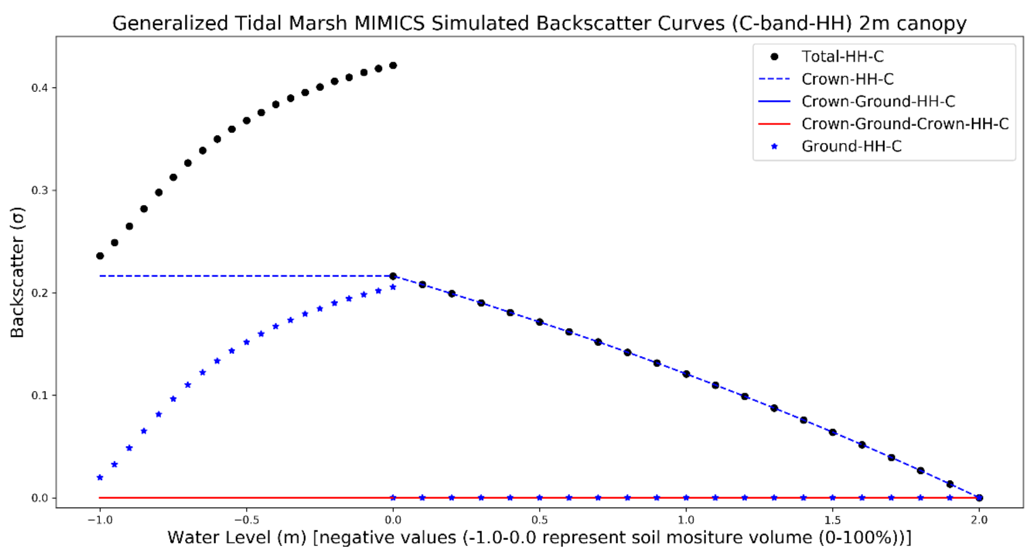

Figure 4.23. MIMICS simulated Sentinel-1 C-band HH scattering contributions from tidal marsh. This includes total backscatter, direct crown scattering, crown-ground scattering, crown-ground-crown scattering, and ground scattering. Note that ground scattering and crown scattering dominate total scattering response when soil is moist, and crown scattering dominates total scattering when marsh surface is inundated. σ scaled between 0.00 to 0.45.

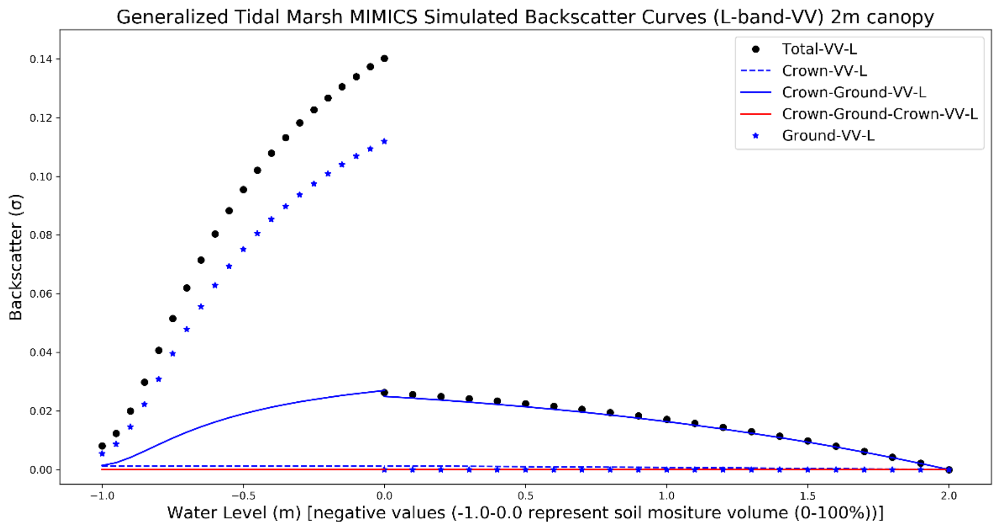

Figure 4.24. MIMICS simulated PALSAR L-band VV scattering contributions from tidal marsh. This includes total backscatter, direct crown scattering, crown-ground scattering, crown-ground-crown scattering, and ground scattering. Note that majority of total scattering response is from ground scattering with lesser amounts of crown-ground scattering when soil is moist. Crown-ground scattering dominates total scattering when marsh surface is inundated. σ scaled between 0.00 to 0.15.

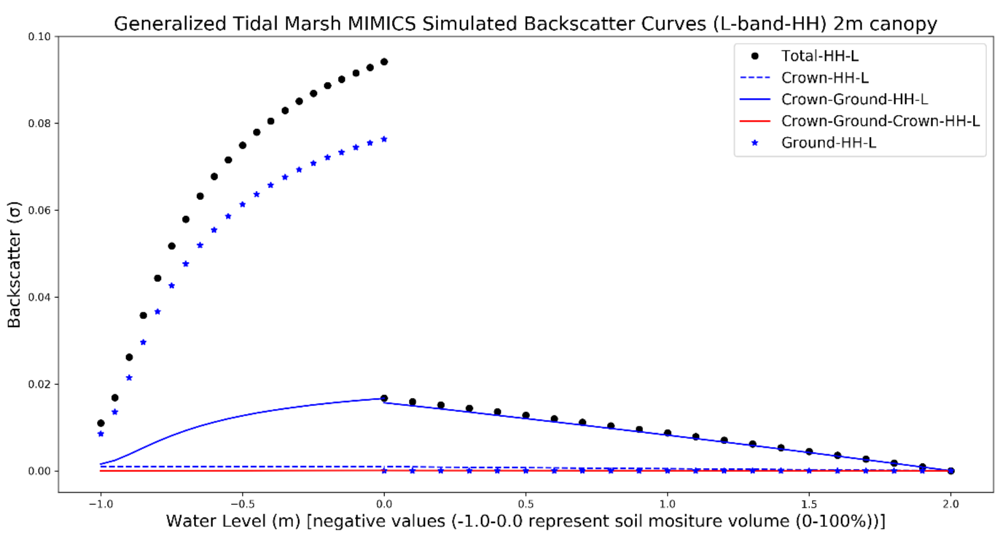

Figure 4.25. MIMICS simulated PALSAR L-band HH scattering contributions from tidal marsh. This includes total backscatter, direct crown scattering, crown-ground scattering, crown-ground-crown scattering, and ground scattering. Note that majority of total scattering response is from ground scattering with lesser amounts of crown-ground scattering when soil is moist. Crown-ground scattering dominates total scattering when marsh surface is inundated. σ scaled between 0.00 to 0.10.

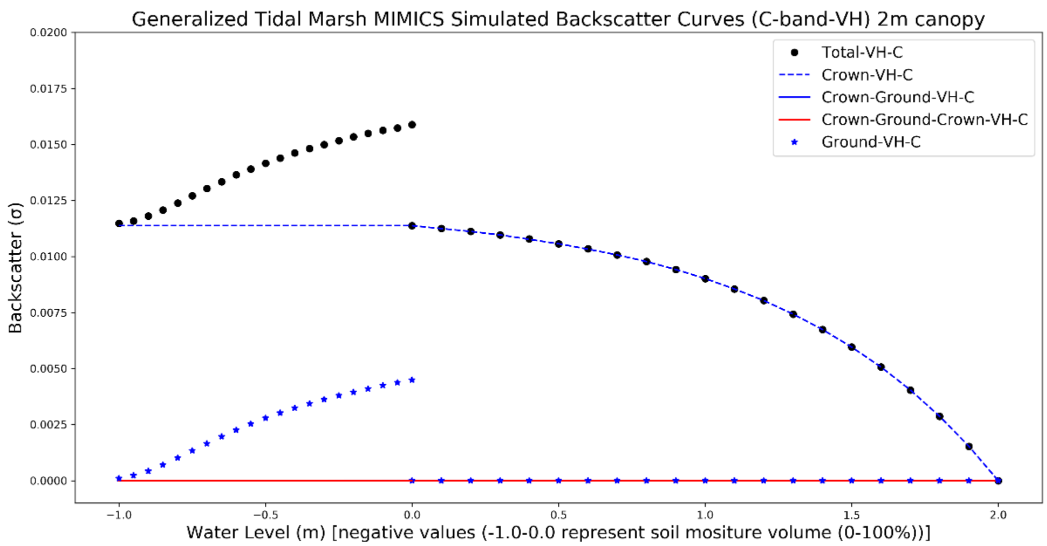

Figure 4.26. MIMICS simulated Sentinel-1 C-band VH scattering contributions from tidal marsh. This includes total backscatter, direct crown scattering, crown-ground scattering, crown-ground-crown scattering, and ground scattering. Note that direct crown and ground scattering dominate total scattering response. Direct crown scattering dominates total scattering response when marsh surface is inundated. σ scaled between 0.00 to 0.020.

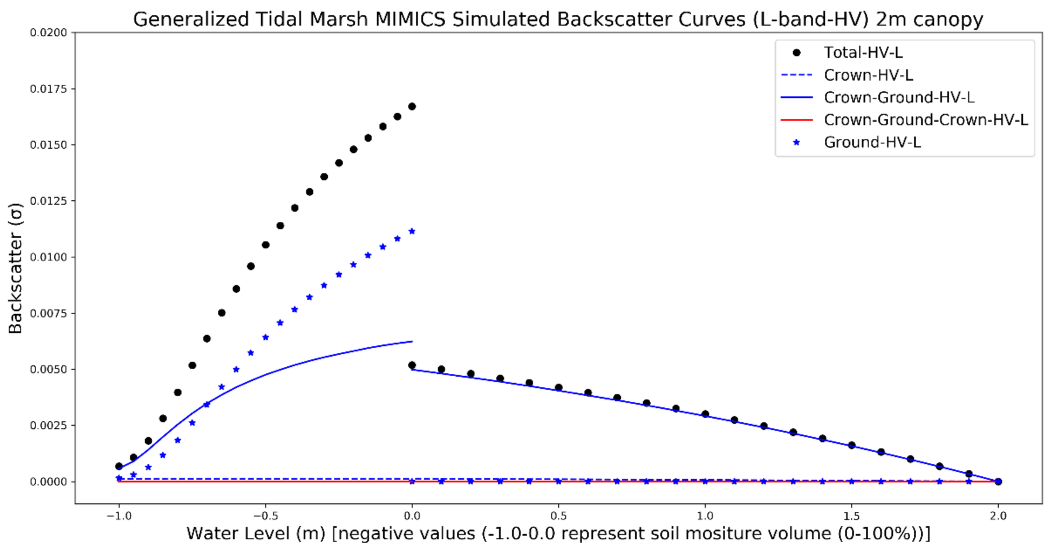

Figure 4.27. MIMICS simulated PALSAR L-band HV scattering contributions from tidal marsh. This includes total backscatter, direct crown scattering, crown-ground scattering, crown-ground-crown scattering, and ground scattering. Note that majority of total scattering response is from ground scattering and crown-ground scattering when soil is moist. Crown-ground scattering dominates total scattering when marsh surface is inundated. σ scaled between 0.00 to 0.020.

One of the general findings from the MIMICS efforts was that double bounce scattering was not a dominant form of scattering in terms contribution to total backscatter intensity in response to hydrologic state change. This was evidenced by the fact that in all MIMICS simulations (SAR wavelengths, SAR polarizations, canopy heights, vegetation moistures, etc.), total backscatter decreased in response to change from saturated soil to an inundated surface, and further decreased in response to increasing inundation depth. If the double bounce mechanism were dominating total backscatter response compared to volume and surface scattering variability, an increase in backscatter intensity in response to inundation would be expected. This is especially true considering the MIMICS radiometric model was parameterized with a smooth inundated surface that would have theoretically led to maximization of double corner scattering from the water surface and vegetation. Figures 4.16-4.21 all showed decreases in total backscatter intensity when transitioning to an inundated state. This decrease was especially prominent for L-band signals showing large decreases in backscatter, indicating that the combination of the surface roughness and dielectric properties have a strong influence on backscatter intensity.

Assessment of individual scattering mechanisms in Figures 4.22-4.27 provided important insights on differences between tidal marsh scattering mechanisms comparing C-band and L-band signals. A very prominent distinction between C-band and L-band signals was the fact that direct crown scattering dominated the total scattering response from inundated marshes at C-band frequencies (Figures 4.22 and 4.23) while crown-ground (and ground-crown) responses dominated total scattering at L-band frequencies (Figures 4.24 and 4.25). This finding suggests that even when marsh vegetation canopies are relatively high biomass, L-band signals still effectively interact with the underlying surface. Additionally, the dominance of the crown-ground scattering demonstrates that double bounce scattering provides a substantial contribution to total scattering at L-band frequencies when marshes inundate. This is a crucial point; while total backscatter intensity may decrease as marshes become inundated due to reductions in surface and volume scattering, double bounce scattering may remain, or become, the primarily mechanism contributing to total backscatter. These findings highlight a key technical advantage of using a radiometric modeling to identify different scattering contributions and highlights a key technical weakness of performing analyses using only SAR backscatter imagery to assess tidal marsh inundation state. While one could surmise reasons for backscatter decrease in response to inundation state change in an empirical image analysis, the MIMICS simulations were essential for resolving changes in scattering contributions.

These radiometric modeling efforts helped point to the fact that multiple scattering beyond double bounce is generally negligible in terms of total backscatter contributions. This is demonstrated by the fact that crown-ground-crown scattering is negligible compared to crown-ground scattering. Volume scattering from vegetated canopies was not a dominant form of backscatter at L-band frequencies. This was evidenced by the fact that L-band HV channel crown-ground backscatter response shown in Figure 4.27 is approximately three times lower than the L-band HH backscatter response shown in Figure 4.25 indicates that the depolarizing impact of crown volume scattering is not playing a significant role in total scattering response. These findings point to the fact that double bounce scattering mechanism is dominant at L-band frequencies when marshes inundate. In the next section we assess the presence of double bounce scattering in inundated tidal marshes utilizing SAR image polarimetric phase information, guided by the findings of the modeling effort that help elucidate expected physical responses.

4.3.3 Polarimetric Decompositions and Threshold-Based Classifications Comparisons

In the following section we perform van Zyl polarimetric decompositions on quad-polarimetric PALSAR-2 imagery acquired over Wheeler Marsh at high tide (2.582 m) and over Blackwater NWR at high tide (0.777 m) and low tide (0.302 m). The van Zyl decomposition utilizes polarimetric phase information in the coherency matrix to derive scattering intensity for odd-bounce scattering (which single bounce surface scattering dominates), even-bounce scattering (which double bounce scattering dominates), and volume scattering intensity. From this information, dominant scattering processes can be directly inferred. The findings from the MIMICS modeling effort indicate that as marshes inundate, they should exhibit lower total backscatter intensity, while the double bounce mechanism becomes more prominent than surface and volume scattering in a relative sense. When marshes reach near submergence, all backscatter should be reduced substantially. For the three PALSAR-2 images we performed polarimetric decompositions on, we also compare to the threshold-based backscatter products that utilize the HH backscatter and HV backscatter intensity. Utilization of the same imagery provides a direct performance comparison between polarimetric decomposition and thresholding approaches. Further, the three PALSAR-2 images we selected cover a range of tidal stages as previously stated. Because the tidal marsh canopies at Wheeler Marsh often nearly or completely submerge during high tide while Blackwater NWR tidal marshes do not, this comparative assessment of scattering mechanisms with the polarimetric decompositions serves to highlight potential differences in scattering response.

Figure 4.28 provides direct evidence that when marshes are sufficiently submerged, L-band scattering may be nearly identical to that of open water. Note that the Long Island Sound estuary in the southern most portion of the image and tidal marshes have nearly identical scattering contributions from each channel. The very dark polarimetric decomposition image indicates that surface, double bounce, and volume scattering are all minimal. Likely because specular forward scattering is dominating total scattering response. In Figure 4.29 that follows, the scattering contributions over Blackwater NWR differ greatly due to lack of canopy submergence compared to Wheeler Marsh. However, the high tide images still show successful classification of inundation extent using threshold-based approaches at both Blackwater NWR and Wheeler Marsh.

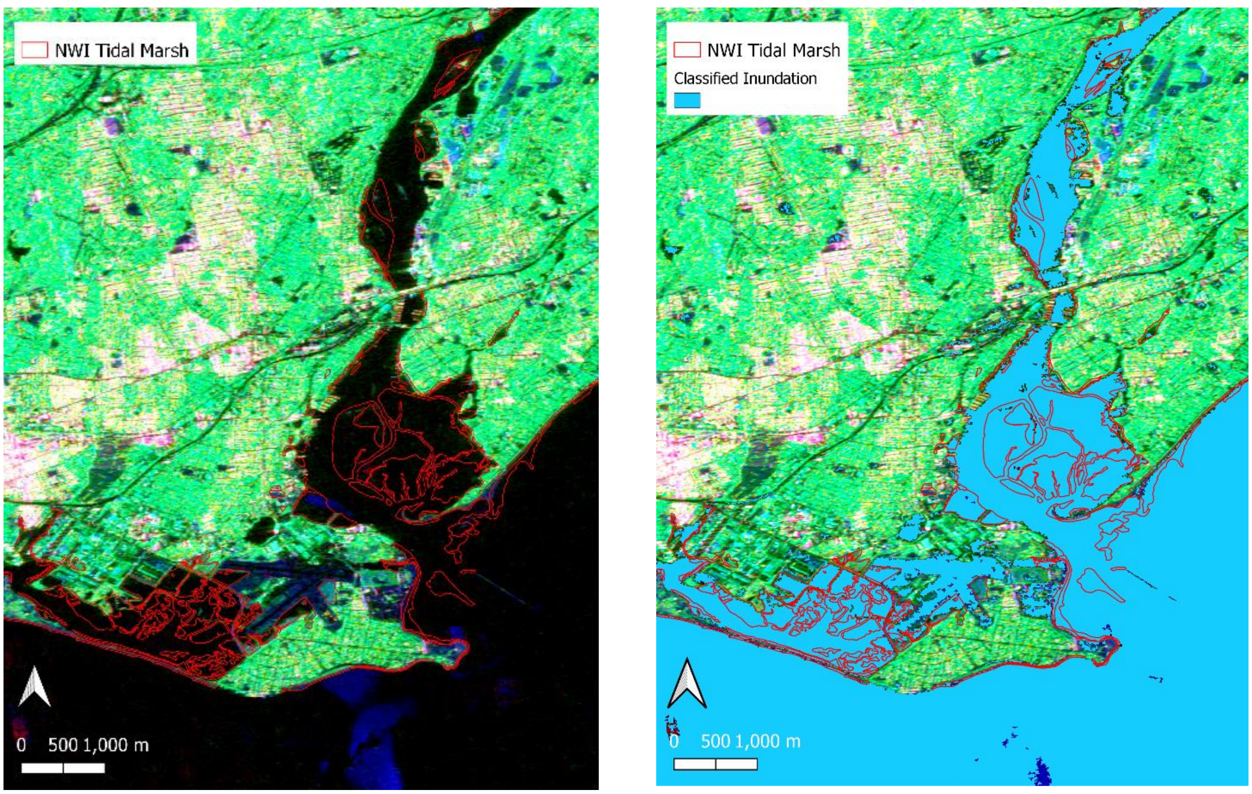

Figure 4.28. Wheeler Marsh high tide (2.582 m) comparison between van Vyl polarimetric decomposition (left) and threshold-based inundation classification (right). In van Zyl RGB channels correspond to double bounce, volume, and surface scattering, respectively, with all channels scaled between -4 to -20 dB. Note that nearly all tidal marsh dominated areas including the Great Meadows system to the southwest and the Housatonic River wetlands to the north of Wheeler Marsh show majority inundated in the threshold-based classification. The van Zyl decomposition shows nearly identical scattering between inundated marshes and permanent open water.

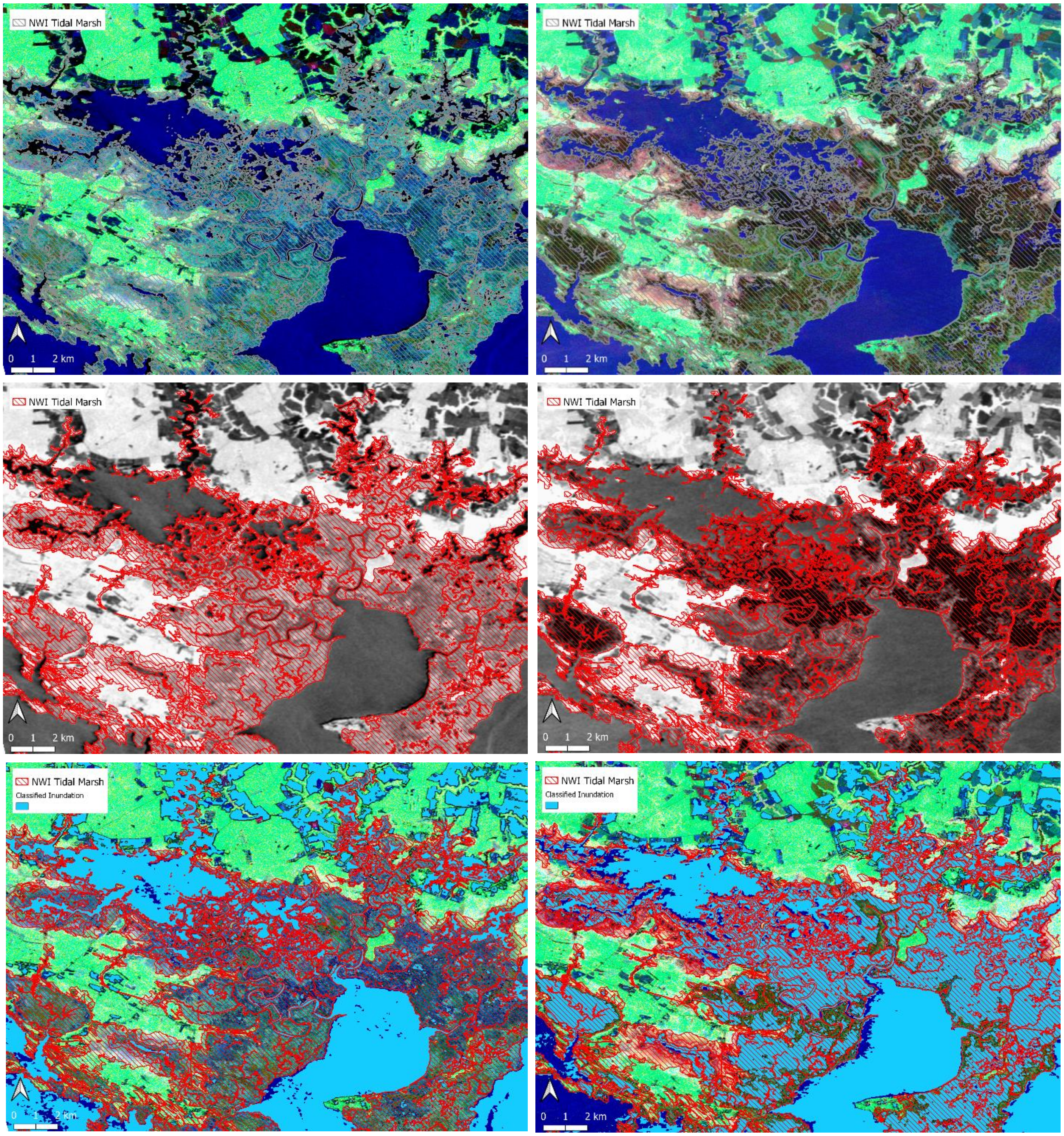

Figure 4.29. Comparison of van Zyl decompositions for low tide image over Blackwater NWR (left) and high tide (right). Vertically descending panels correspond to van Zyl decomposition, HH backscatter, and classified inundation extent from top to bottom. van Zyl RGB channels correspond to double bounce, volume scattering, and surface scattering, respectively. All SAR images scaled between -20 and -4 dB. Note that tidal marsh inundated area increases greatly comparing the low tide classification (left) to the high tide classification (right). In the van Zyl decompositions surface scattering dominates at low tide indicating a primary backscatter response from a rough, moist soil surface. While high tide shows a decrease in total backscatter magnitude for all scattering types and a relative shift from surface scattering (cyan) to a combination of volume and double bounce (brown) consistent with greater inundated area.

4.3.4 Development of UAVSAR Inundation Products

We selected scenes from the UAVSAR AM/PM Campaign from 2019 that captured hydrologic variability over Gulf Coast study sites. CRMS station wetland water level observations were used to assess the ability of UAVSAR imagery and classified UAVSAR inundation products in effectively capturing variability in inundation extent. The three Gulf Coast study sites we selected are associated with large river systems, and thus, influenced strongly by freshwater hydrologic variability in addition to tidal influence. Below we provide comparisons of classified wetlands from Lamb et al. (2020) and overlay UAVSAR imagery and classified inundation products using the approach of thresholding imagery where HH < -14.0 dB and HV < -23.0 dB.

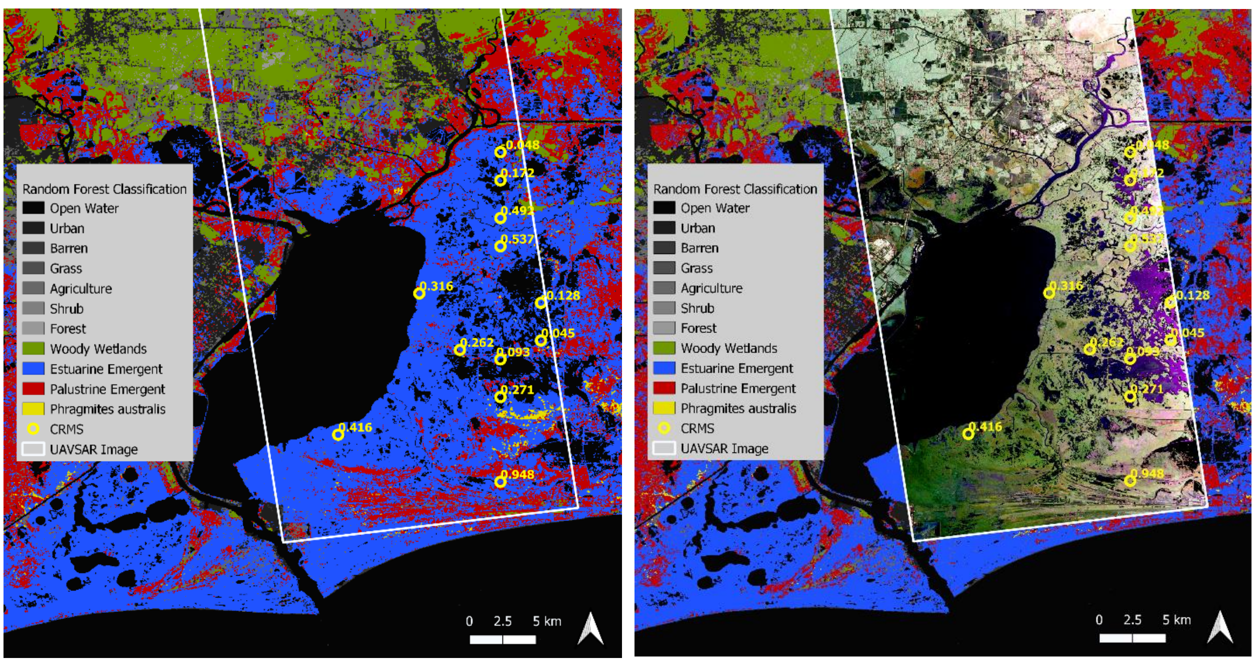

Figure 4.30. Sabine River region classified wetlands within UAVSAR image and CRMS sites with water level height on left. UAVSAR image with HH-HV-VV RGB false-color composite on right. HH and VV channels scaled between -4.0 and -20.0 dB, HV channel scaled between -10.0 and -30.0 dB.

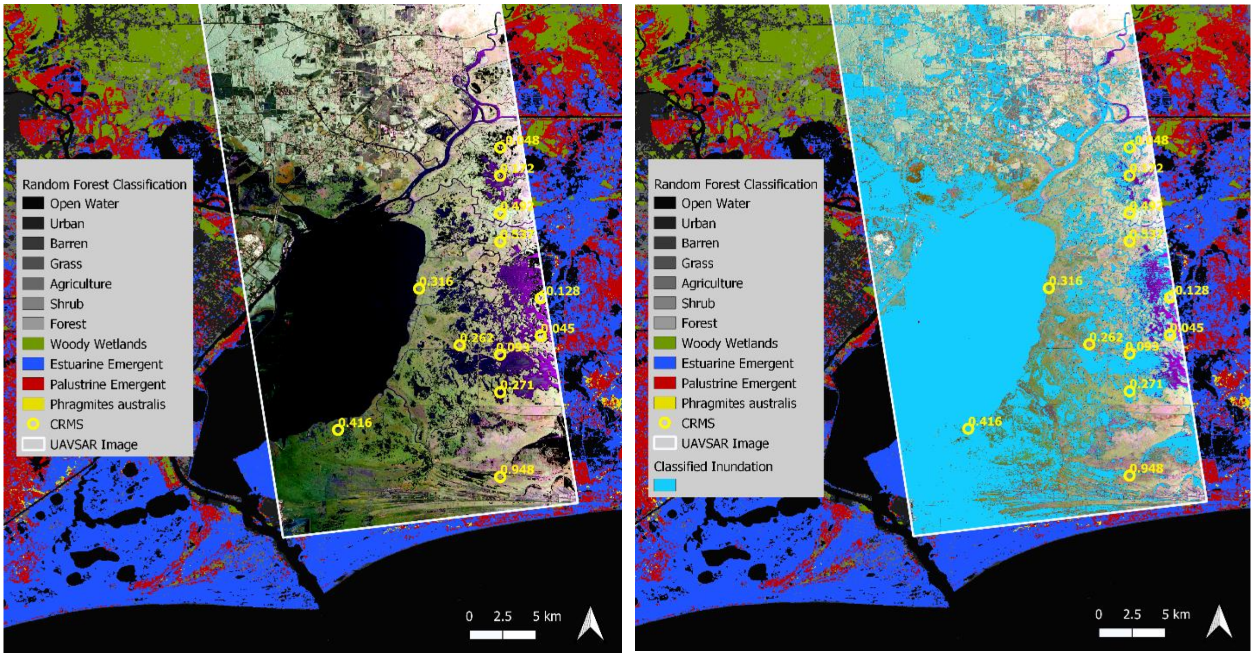

Figure 4.31. Sabine River region August 12th 2019 UAVSAR Image (HH = Red, HV = Green, VV = Blue) (left) and classified inundation extent (includes surface waters and inundated wetlands) (right). Note that CRMS water level values (feet) associated with each station are relatively low and inundation is not detected over marsh areas. 6/12 CRMS stations are classified as majority inundated.

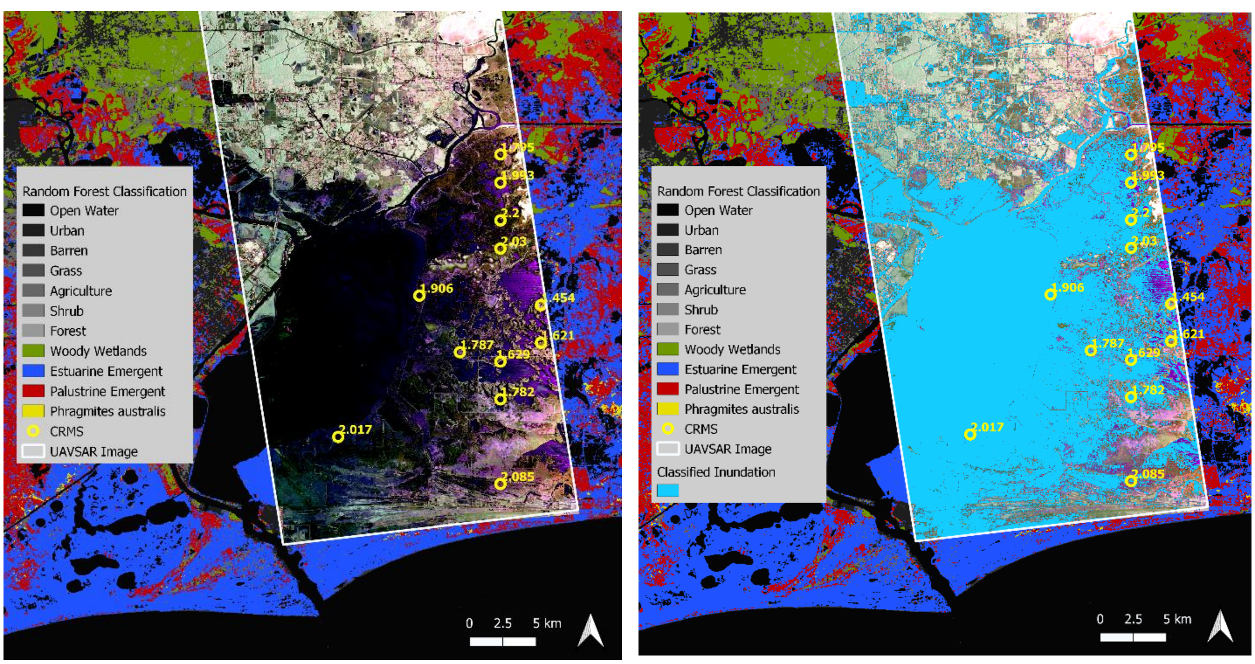

Figure 4.32. Sabine River region September 23rd 2019 UAVSAR Image (HH = Red, HV = Green, VV = Blue) (left) and classified inundation extent (includes surface waters and inundated wetlands) (right). Note that CRMS water level values (feet) associated with each station are high and classified inundation extends into marsh dominated regions. 10/12 CRMS stations are classified as majority inundated.

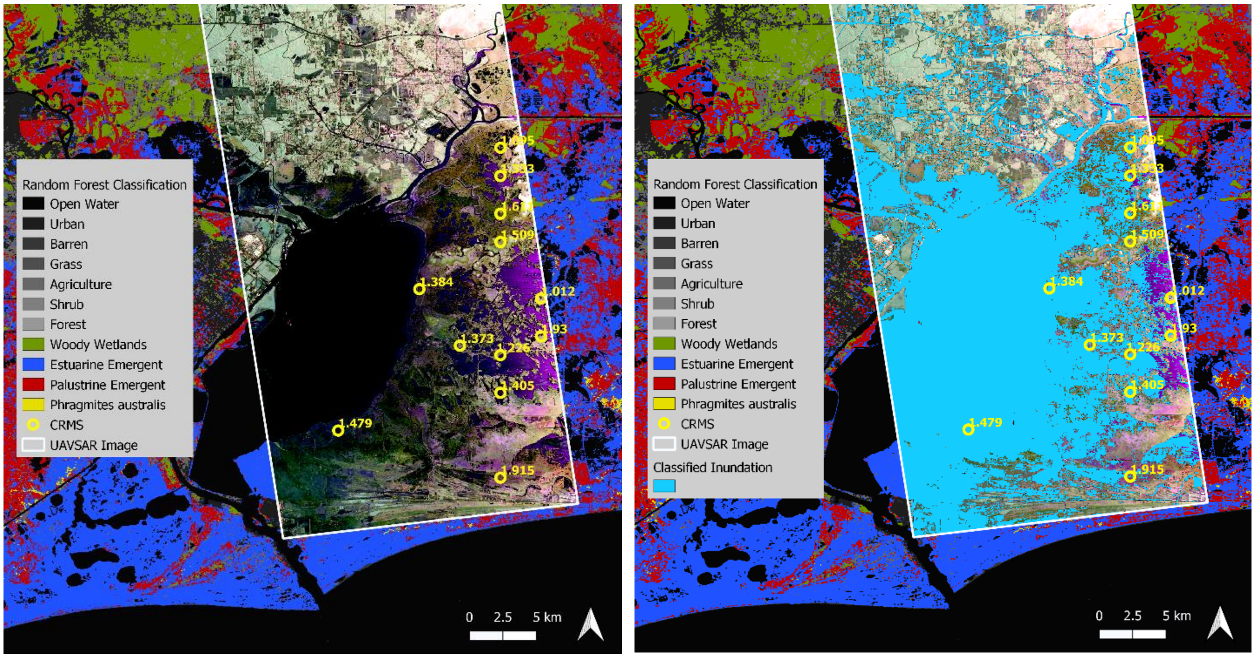

Figure 4.33. Sabine River region September 30th 2019 UAVSAR Image (HH = Red, HV = Green, VV = Blue) (left) and classified inundation extent (includes surface waters and inundated wetlands) (right). Note that CRMS water level values (feet) associated with each station are relatively high and classified inundation extends into marsh dominated regions. 8/12 CRMS stations are classified as majority inundated.

Comparing the three classified inundation products above shows that they effectively capture variability in marsh inundation extent and provide a stable classification over open water. However, it is somewhat challenging to robustly validate these products. The CRMS stations marsh water level values showed varying water levels between stations in the August image that did not coincide with differences in classified inundation. These station differences may be problematic in providing direct inundation product performance assessment. However, the CRMS stations do provide the important indication that every station that was classified as inundation in the low water image was also classified as inundated in the moderate water level image. The same was true comparing the moderate water level image to the high water level image. This demonstrates that the inundation product is responding accurately to hydrological change.

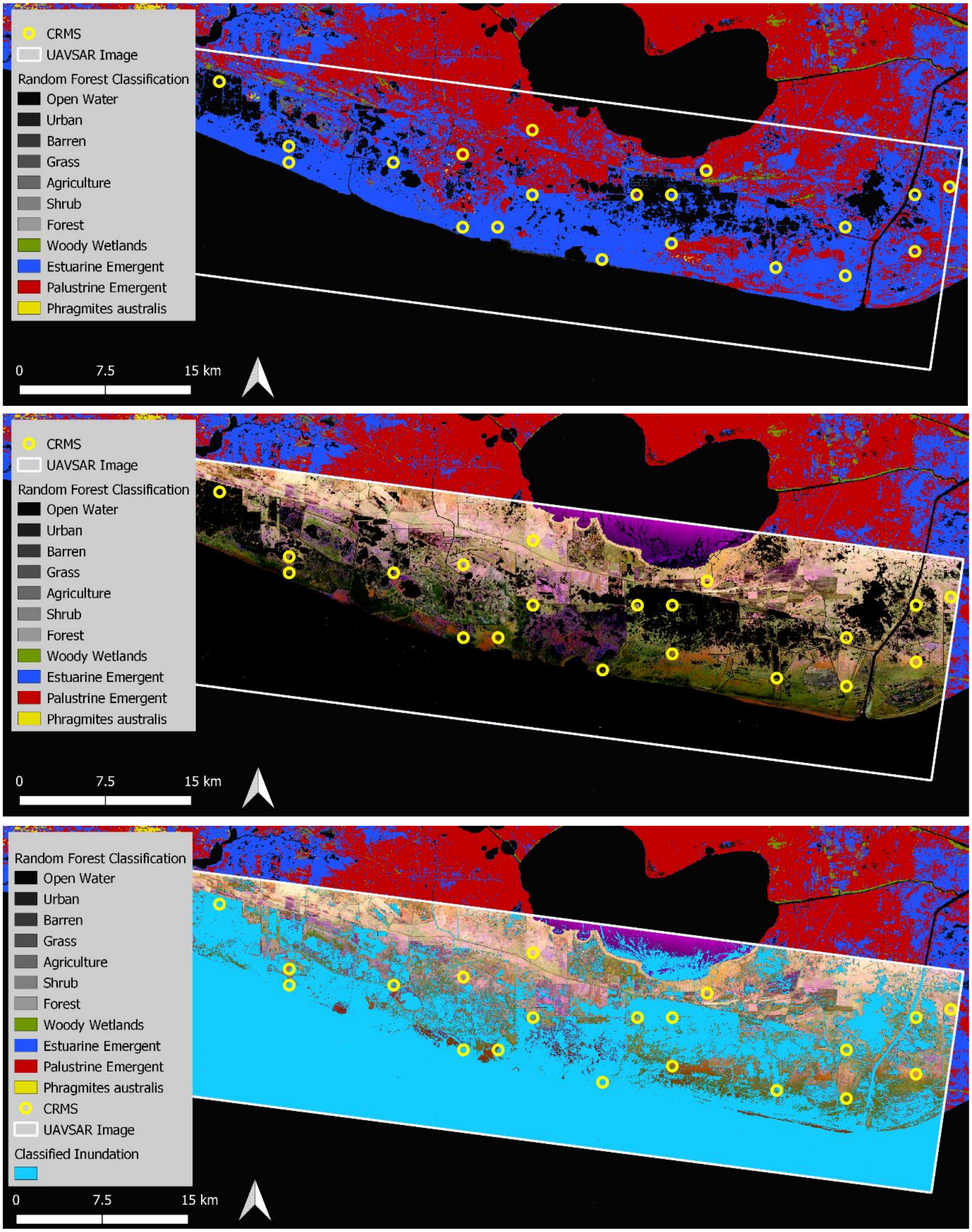

Figure 4.34. White Lake region classified wetlands within UAVSAR image and CRMS sites (upper panel). UAVSAR image with HH-HV-VV RGB false-color composite (middle panel). HH and VV channels scaled between -4.0 and -20.0 dB, HV channel scaled between -10.0 and -30.0 dB. Classified inundation extent shown in lower panel for July 1st 2019. 9/20 CRMS stations inundated.

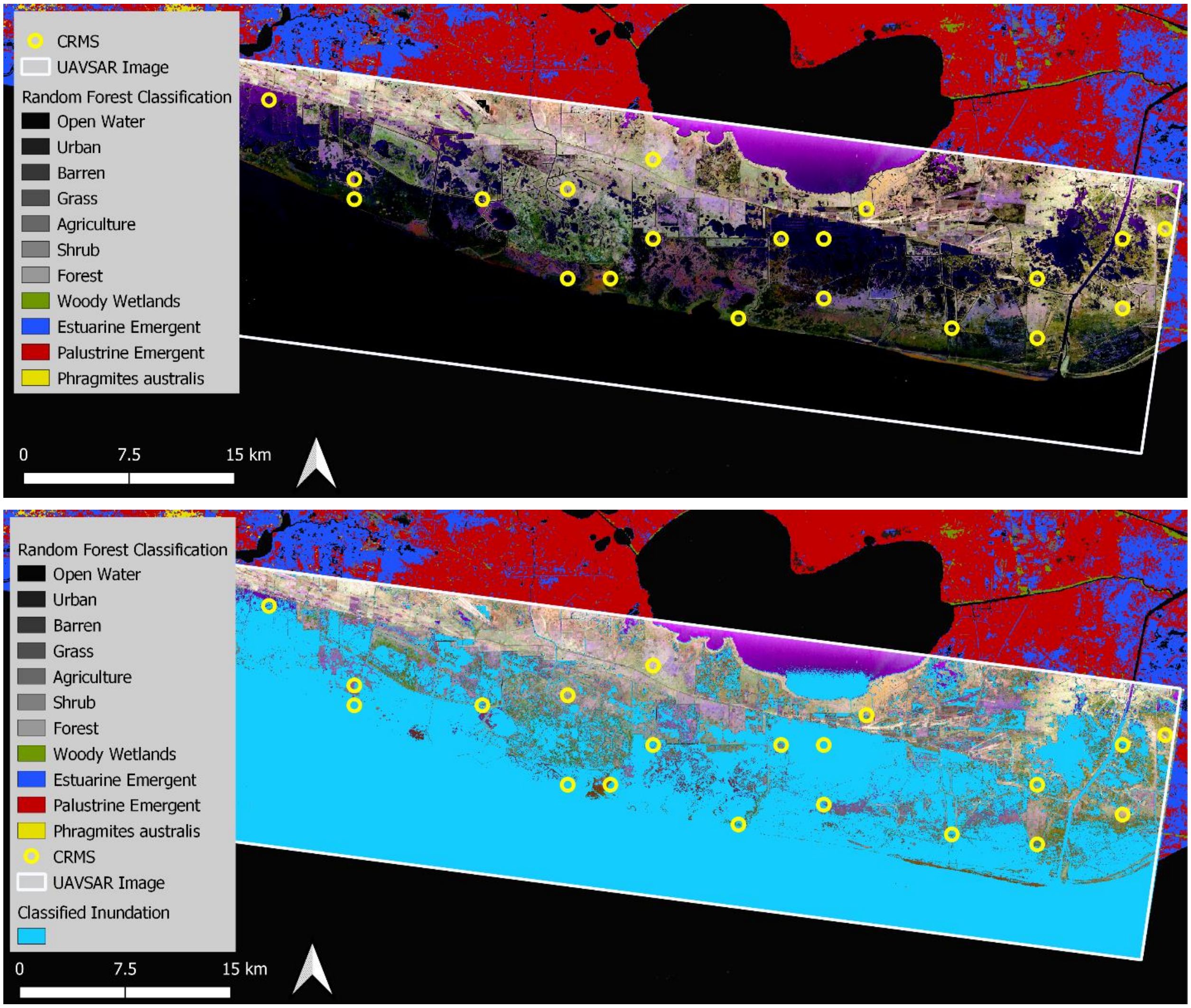

Figure 4.35. White Lake region July 16th 2019 classified inundation product. 13/20 CRMS stations showed classified inundation.

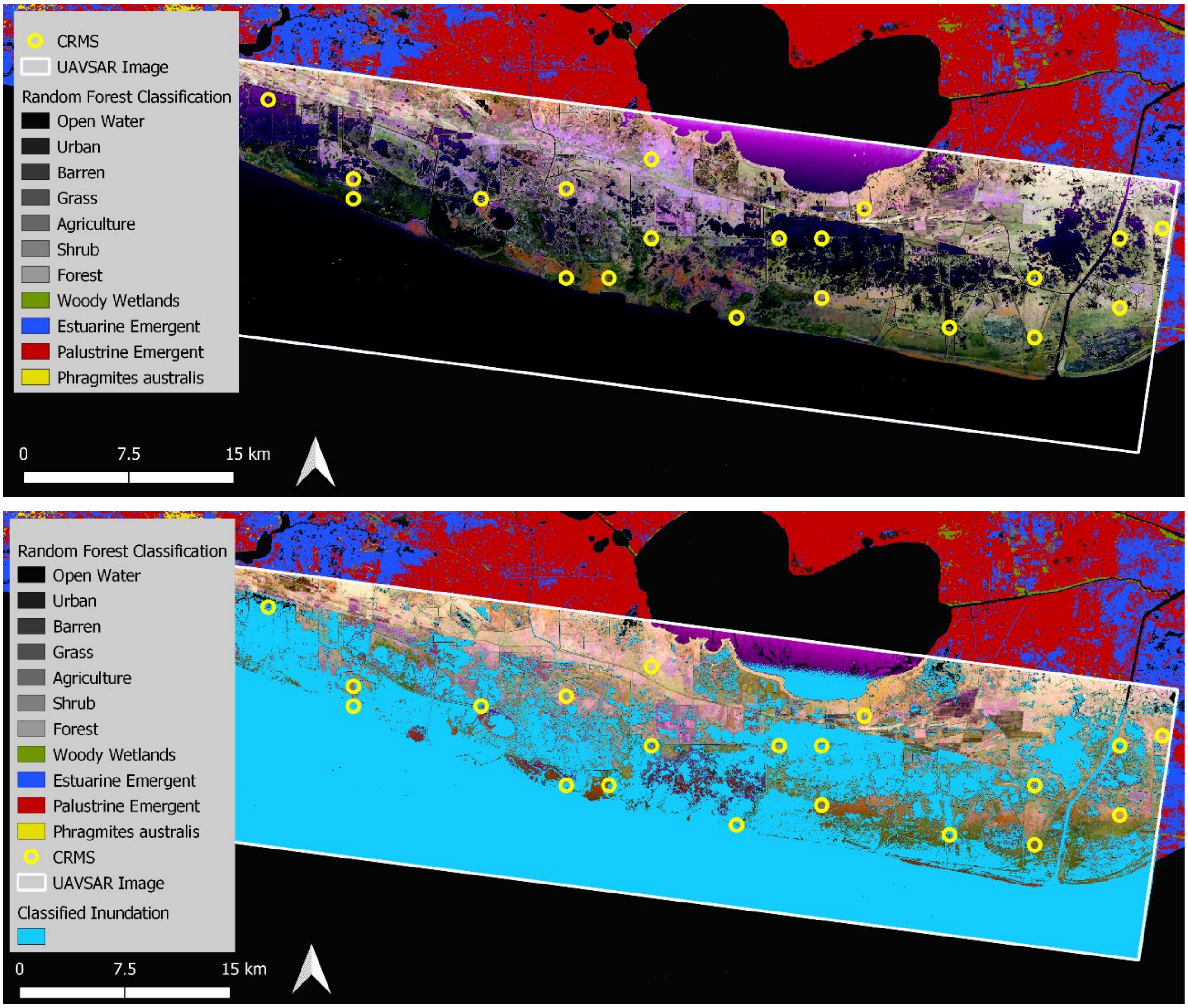

Figure 4.36. White Lake region July 25th 2019 classified UAVSAR inundation image. 10/20 CRMS stations show detected inundation.

The results from the White Lake area did not show substantial variations in inundated extent as the Sabine River analysis did. A key exception was in the July 16th 2019 image which showed increased inundation in the eastern portion of the image. This increased inundation area largely agrees with the NOAA tidal gauge observations from the Freshwater Canal Locks station that observed a very high water event two days prior. It is highly plausible that the marshes surrounding this area remained inundated after this high water event. All of the White Lake images showed that the inundation classification was not effective for the open water in the near range portion of the UAVSAR images. All three images showed a lack of proper classification in the northern portion of the image along the near range swath.

4.4. Discussion and Conclusions

The inundation products that were previously developed in Lamb et al. (2019) for the Chesapeake Bay and expanded to sites in the Long Island Sound in this effort, were validated against *in situ* water level sensors. The C-band based inundation product accuracy for a high marsh system with a low tidal range at Kirkpatrick Marsh was 76.4% when using a VV/VH ratio change detection-based approach. C-band inundation product classification accuracy improved when using both VV/VH and VH imagery in a change detection-based approach for the Wheeler Marsh site where inundation classification had an 87.5% accuracy. Use of L-band imagery showed the greatest inundation classification accuracy at 90%. The ability of Sentinel-1 C-band imagery and PALSAR/PALSAR-2 L-band imagery to detect tidal inundation state was also assessed through radiometric modeling efforts. One of the clear distinctions between C-band and L-band response was the fact that during a transition from moist soil to an inundated surface, L-band backscatter decreases were much more drastic. Our modeling efforts also indicate that L-band signals produce a much stronger ground response from tidal marshes, and overall more effective characterization of marsh surface hydrologic state. This was especially true for the HH channel which was used to derive inundation products over the VV channel. Although the findings from our radiometric modeling efforts indicated that Sentinel-1 VH and HH channels would be effective for detecting a moist soil to inundated surface transition, a sufficiently separable change in backscatter distribution was not observed for the VH channel at Wheeler Marsh in our empirical image analysis. This finding highlights the importance of the magnitude of backscatter decrease when using L-band imagery for characterizing tidal marsh inundation state which showed a much more pronounced decrease in backscatter.

The findings that backscatter decreased in response to the presence of tidal marsh inundation in both the theoretical modeling efforts and empirical image analysis largely agree with previous literature (Tannis et al. 1994; Kaiskchke and Bougier-Chavez 1997; Slatton et al. 2008). These results point the fact that the backscatter response is dominated by a shift to forward scattering in tidal marshes as water levels rise. Our radiometric modeling efforts point to the fact that the double bounce scattering mechanism is still present, and is likely the dominant scattering mechanism when marshes are inundated, but is best characterized by polarimetric phase information as opposed to backscatter intensity information. This is also highlighted by studies like Brisco et al. (2017), Kim et al. (2014), and Hong et al. (2013) that found that phase information, whether used in InSAR-based coherence or polarimetric analyses, provided the best isolation of this scattering mechanism characterizing wetland inundation state. However, the findings in this research effort illustrate that identification of specific scattering mechanisms may not be necessary to classify marsh inundation state effectively. Our radiometric modeling efforts clearly demonstrated that at L-band frequencies, backscatter intensity unambiguously decreases as marshes inundate. Our threshold-based inundation products, which leverage this backscatter decrease, produced relatively high accuracies in mapping inundation with L-band imagery. An additional advantage of this threshold approach is the fact that when wetlands are nearly submerged, only forward scattering dominates, yet threshold-based approaches still provide effective assessments of hydrologic state as they would for open water. An example of this was shown in the polarimetric decomposition analysis in this effort where a high tide image from Wheeler Marsh showed minimal double bounce, surface, and volume scattering, whereas a high tide image from Blackwater NWR showed moderate amounts of double bounce scattering when inundated. Given the Wheeler Marsh vegetation has been observed to completely submerge at high tide, whereas Blackwater NWR does not, this difference in response is expected. However, in spite of these differences in scattering mechanisms, the threshold-based inundation classification proved effective in both systems.

The findings in this analysis demonstrate that backscatter intensity and phase information provide complementary information when assessing tidal marsh inundation state. And that one approach may serve as a useful support for the other. The UAVSAR analysis showed promising capabilities in classifying tidal marsh inundation when using backscatter threshold approaches with multiple polarimetric channels. This has promising implications for the NISAR satellite as well. One of the biggest flaws of the UAVSAR inundation product development was a lack of capability in classifying inundation at incidence angles of 25-27 degrees off-nadir. Because NISAR will operate with an off-nadir view angle ranging from 32 to 47 degrees, this is unlikely to be an issue. A larger technical challenge that emerges with the NISAR satellite is the fact that the quasi-quad polarimetric nature of the instrument makes it so the phase in each polarimetric channel is not readily comparable. This means that true quad-polarimetric decompositions like the van Zyl decomposition used here will not be possible. This means that single date image inundation product development will most likely rely on backscatter-based approaches for multi-polarimetric analyses. However, the NISAR satellite is designed with robust InSAR capabilities, meaning that phase in multiple images with the same polarization can be computed to derive interferograms with associated coherence estimates. With a coherence layer computed between two high tide images, the high coherence areas represent the minimum area that both images where experiencing coherent scattering. In tidal marshes, this coherent scattering would primarily be due to the double bounce effect. In either case, InSAR coherence layers serve as a conservative estimate of total inundated area. These conservative inundated area estimates can be combined with the less restrictive threshold-based inundation products to develop robust fused inundation products for both backscatter intensity and phase information. In Chapter 5, the concluding chapter of this thesis, more details on the NISAR mission are discussed.

CHAPTER 5

SUMMARY OF RESEARCH AND FUTURE DIRECTIONS

5.1. Summary of Findings

Chapters 2-4 each cover a unique concept in the field of remote sensing-based wetland observation and characterization. Chapter 2 highlights the importance of technological evaluation and empirical assessments of remote sensing imagery. This chapter illustrates that empirical assessments often serve as starting points in remote sensing-based research efforts, with observations (i.e. satellite imagery) leading scientific investigations. The findings from Chapter 2 yielded some unanticipated results. One especially surprising finding was how varied C-band backscatter responses were between different wetland sites with only slightly different vegetation communities and hydrological characteristics. Chapter 2's thematic coverage of the importance of empirical analysis ties into another thematically important concept of technological assessment of satellite sensor/platform capabilities. The Sentinel-1 SAR that was used extensively in Chapter 2 was a relatively new satellite at the time this thesis research began (2014 launch). Using empirical image analyses to assess Sentinel-1 image capabilities indicated that the technological advancement of a 12-day revisit time provided unprecedented capabilities in wetland monitoring, with the most comparable operational C-band satellite, RADARSAT-2, having a 24-day revisit. Sentinel-1's 12-day repeat observations also featured a very consistent dual polarization operating mode (VV, VH) that provided a dense timeseries for tidal wetland inundation assessment. The primary challenge in characterizing hydrologic variability in tidal wetlands is the fact that inundated areas can change significantly on even minutely timescales with approximately six hours between high and low tide. Although no polar orbiting satellite can directly resolve hydrologic change during a single tidal cycle, the more frequently a tidal wetland can be observed (or sampled), the more likely a given satellite is to resolve the dominant modes of tidal variability through a sufficient number of observations. This was a clear technical advance provided by the Sentinel-1 satellite which acquired imagery over a narrow interval and wide range of tidal stages. The advantages of a 12-day revisit are also apparent in characterizing the hydrology of wetlands dominated by seasonal hydrologic variability as this variability can be resolved directly with 12-day repeat imagery. In addition to tidal inundation assessment, the frequent revisit of Sentinel-1 provided an accurate characterization of wetland vegetation senescence and identified different forms of senescence comparing persistent and non-persistent emergent vegetation. This technological assessment of Chapter 2 findings served as the foundation for Chapter 3.

The ecological science theme in Chapter 3 built on many of the technological assessments and empirical findings of Chapter 2. Chapter 3's expansion of wetlands mapping and vegetation characterization approaches to larger regional scales outside of the Chesapeake Bay to the Mid-Atlantic and Gulf Coast regions yielded similar, but slightly improved accuracies for the mapping of emergent wetlands, including tidal marshes. This indicated that SAR-optical/IR fusion may be an effective approach for mapping emergent wetlands globally. The addition of invasive *Phragmites australis* to the expanded classification effort for the Mid-Atlantic region did not greatly impact the accuracy of the mapping of tidal marshes and freshwater marshes with native vegetation as all three classes were mapped with greater than 80% accuracy. The approaches used for this mapping effort present a potentially useful tool for natural resource managers in monitoring the spread of this invasive species. A random forest-based classification experiment in Chapter 2 demonstrated that Sentinel-1 C-band SAR annual backscatter variability (i.e. standard deviation) was one of the most statistically important layers for mapping non-persistent marsh vegetation. Building on the findings from Chapter 2 with a Sentinel-1 C-band backscatter analysis covering 2016-2017, we expanded these efforts to include 2017-2019 in Chapter 3. All four years of the Sentinel-1a timeseries showed very consistent tracking of vegetation phenological change. We leveraged these findings and utilized Sentinel-1 standard deviation layers to map non-persistent emergent marsh vegetation with an accuracy greater than 93%. An unexpected direction of this research was the finding that the invasive water chestnut (*Trapa natans*) which is extremely prolific in the Hudson River, was classified similarly as rooted native non-persistent emergent wetland species initially. While carrying out the research effort in Chapter 3, it became apparent that separation between invasive *Trapa natans* and native non-persistent marsh vegetation was critical for assessing wetland and deepwater ecological status. To accomplish this objective, we employed a decision-tree approach that provided a straightforward separation between *Trapa natans* and rooted non-persistent emergents which were mapped with >93% accuracy and >96% accuracy, respectively. The development of this split between these vegetation types was critically dependent on Sentinel-1's frequent 12-day revisit time, as a short time period in spring was used to distinguish the phenology of *Trapa natans* from other non-persistent species. Linking to the theme of Chapter 2, this technical improvement (e.g. more frequent imagery) likely provides improved capabilities for any number of wetland observation and characterization studies that require the detection of short timescale processes.

In Chapter 3, specific Gulf Coast emergent wetland classes were not classified as accurately as they were in the Mid-Atlantic, likely because complex salinity gradients, which influence wetland vegetation community composition, made the split between freshwater marshes and tidal marshes difficult. However, the combined emergent wetland class was mapped with greater than 91% accuracy. Combined with the fact that open water was mapped with greater than 93% accuracy, this presents an important tool for natural resource managers in the Gulf Coast tracking conversion of emergent wetlands to permanent open water, which is a continued issue in the region as a result of sea level rise and sediment budget deficits.

Chapter 4 also builds on several of the findings in Chapter 2 that evaluated tidal inundation mapping capabilities. This chapter thematically carries an engineering focus as inundation detection algorithm development was the primary objective. A number of the inundation products that were developed over study sites in Chapter 2 (Kirkpatrick Marsh, Wheeler Marsh, and Blackwater NWR) were assessed rigorously in Chapter 4 through both *in situ* validation and radiometric modeling efforts. As Chapter 1.5 had illustrated, the degree to which SAR surface scattering, double bounce scattering, and volume scattering respond to emergent wetland inundation state is somewhat debated. Part of the motivation behind the radiometric modeling effort was to evaluate the presence of these scattering mechanisms in marshes with varying hydrologic conditions. In all radiometric modeling runs, C-band and L-band backscatter decreases were observed in response to inundation for simulated marshes with vertically oriented vegetation. This indicates that the variability in total backscatter intensity may not be dominated by double bounce scattering, which would increase backscatter, but instead dominated by decreases in surface and volume scattering contributions to total backscatter. Polarimetric decompositions that make use of the multi-polarization and relative phase information in SAR imagery showed pronounced differences in dominant scattering mechanisms comparing images acquired at low tide and high tide. For example, for the Blackwater NWR site there was a relative shift from surface scattering to double bounce scattering as tidal stage increased, even though total backscatter intensity decreased. It should be noted that backscatter intensity may decrease as marshes inundate, as forward surface scattering away from the sensor dominates total scattering response, while double bounce scattering still has the primary impact on backscattered signal returning to the sensor. This means that phase information (polarimetric phase differences or repeat pass interferometry) may provide alternative and complementary information on wetland inundation state compared to approaches that utilize backscatter intensity information. Some of the most high-quality SAR wetland inundation assessment studies rely on phase-based approaches (Brisco et al. 2017; Schmitt and Brisco 2013; Hong and Wdowinski 2013; Kim et al. 2014). However, in the findings of Chapter 4, we clearly demonstrate that L-band backscatter intensity thresholding can be applied to imagery for accurate inundation mapping, especially over a range of tidal stages. Further, our polarimetric decomposition results largely corroborated backscatter thresholding results with respect to detecting inundation over similar spatial extents. It should also be noted that when marsh vegetation is not of excessively high biomass, the backscatter thresholding approaches we developed may work more effectively than polarimetric decompositions which may show varying scattering mechanism classifications as a function of vegetation submergence level, while backscatter thresholding shows consistent detection of inundation. Further, the thresholding approaches developed in this thesis are not dependent on multi-pass interferometric information which requires two or more SAR images of the similar tidal stage for accurate assessment of inundation extent. Obtaining multiple images of a similar tidal stage can be very challenging when also considering the need to maintain short temporal and perpendicular image baselines when implementing InSAR approaches. Alternatively, the threshold-based approaches we developed here can be applied to single-date imagery. Further, it is much more common for SAR satellites to operate in dual-polarimetric mode than true quad-polarimetric mode. A central focus of Chapter 4 was to provide tidal marsh inundation mapping approaches relevant to the upcoming NISAR satellite mission. Because this mission will generally operate in L-band dual-polarimetric mode (HH, HV) and quasi-quad-polarimetric mode (without fully comparable polarimetric phase channels), the use of a dual-polarimetric backscatter intensity threshold-based approaches for tidal marsh inundation mapping presents an alternative to true polarimetric decomposition-based approaches which are not feasible.

5.2. Future Directions

The launch of the Sentinel-1a satellite in 2014 proved invaluable to this thesis research effort. Ongoing measurements from Sentinel-1a and the recently launched Sentinel-1b satellite will only continue to improve wetland observation and characterization with C-band SAR imagery. Landsat 8 imagery also served as a foundation for this research effort. This is especially true considering that Chapters 2-3 clearly demonstrate just how important the fusion of SAR and optical/IR imagery are for the accurate mapping of wetlands and characterizing wetland vegetation. It's clear that Landsat 8 and Sentinel-1 imagery provide highly complementary observations due to similar spatial resolutions, revisit times, and radiometric quality, while also offering distinct spectral and polarimetric capabilities. Landsat 8's radiometric quality is noticeably higher than its predecessors Landsat 5 and Landsat 7. Seldom were striping patterns or artifacts observed in Landsat 8 imagery over wetlands sites. This was critical for effectively computing vegetation and water indices which often rely on visible, near infrared (NIR), and shortwave infrared (SWIR) bands. SWIR bands are especially prone to artifacts due to sensor design limitations in achieving ample signal to noise ratios in the SWIR EM region. Of all the higher spatial resolution optical sensors operating (30-m or finer), Landsat 8 has some of the highest signal to noise ratios (SNRs). Landsat 8 has been widely regarded as the first high resolution optical satellite with SNR values capable of acquiring science-quality imagery for aquatic/ocean color remote sensing studies (Franz et al. 2015; Pahlevan et al. 2017). Wetland remote sensing may not have the strict SNR requirements of ocean color remote sensing, but having higher SNRs are always advantageous, especially for improving the accuracy of atmospheric correction and cloud masking. The recent launch of Sentinel-2a and Sentinel-2b optical/IR satellites provides comparable observations to Landsat 8, albeit at a higher spatial resolution and slightly lower radiometric quality (Pahlevan et al. 2019; Kuhn et al. 2019). Still, the radiometric quality is more than sufficient for wetland-based studies. The terrestrial remote sensing community has even developed products that harmonize Landsat 8 and Sentinel-2 (HLS) observations, producing a combined product with common spectral properties, but at improved temporal resolutions (Claverie et al. 2017). With the anticipated launch of Landsat 9 in 2021, which will have spectral bands almost identical to Landsat 8, but with slightly higher SNRs, optical/IR image temporal revisit continues to improve. Although cloud cover always remains an issue for optical/IR imagery, the virtual constellation of two Landsat and two Sentinel-2 satellites will provide far greater potential in matching the effective revisit of Sentinel-1 C-band SAR imagery, and will far exceed the effective revisit of Sentinel-1 SAR in areas that are not significantly impacted by cloud cover. Chapters 2-3 largely found that optical/IR vegetation and water indices were much more useful in multitemporal wetlands classifications than the use of individual spectral bands, and improved classification accuracies to a much greater extent in initial testing. Further, these spectral indices proved far more parsimonious in achieving accurate wetlands classifications with as input layers as possible compared to classifications with individual spectral bands. This finding was likely attributed to the fact that temporal compositing of Landsat 8 may have produced higher levels of variability in individual band reflectance within seasonal temporal windows compared to the spectral indices which are often normalized by several spectral bands, and thus, likely provide more stability. When considering issues with spatially and temporally varying cloud cover, this stability becomes even more important. The fact that Landsat 8 was the only optical/IR imagery used in this thesis research is certainly a limitation, and while use of vegetation and water indices do prove advantageous over individual bands in terms of performing wetlands classifications over large scales, this may not be true in all cases. For instance, several wetlands mapping studies have found that individual spectral bands are very useful when utilizing single date imagery, or individual image scenes that are not temporally composited (Hurd et al. 2005; Klemas 2013; Campbell et al. 2015). With more frequent high spatial resolution optical/IR observations from Landsat and Sentinel-2, wetlands classifications incorporating multitemporal optical/IR imagery will likely improve, whether utilizing indices or individual bands.

Another technical area of optical/IR wetland remote sensing where capabilities are expected to greatly improve is in terms of spectral resolution. The upcoming Surface Biology and Geology (SBG) Designated Observable will provide high-spatial resolution hyperspectral imagery, which will greatly aid in wetland remote sensing, especially in accurately classifying vegetation (NAS 2017). Utilization of this imagery allows for matching of satellite spectra to known spectra measured in the field or laboratory, providing far greater opportunities for classifying vegetation at the species level, which is somewhat challenging with multispectral imagery. Hyperspectral imagery also presents the opportunity to not only classify dominant vegetation in a single image pixel but classify relative percentages of different species in an image pixel by utilizing spectral unmixing techniques. Although hyperspectral imagery is most useful for vegetation classification, it also presents additional opportunities for assessing inundation state and potentially even soil moisture state with hyperspectral NIR and SWIR imagery. Thesis Chapters 2 and 4 demonstrated that water indices like the mNDWI and optically-based surface water products like the USGS DWSE perform relatively well for assessing tidal marsh inundation state in sparsely vegetation low marsh regions. Yet these indices and products still rely on spectrally coarse multispectral imagery. Being able to assess changes in NIR-SWIR spectral slope, rather than spectral angles, provides improved opportunities in optically-based tidal marsh hydrologic assessments.

The current and anticipated technological advancements in optical/IR remote sensing will enhance wetland observation in terms of temporal resolution (revisit) and spectral resolution. However, Landsat, Sentinel-2, and SBG satellites are all polar-orbiting. These polar-orbiting satellites cannot directly resolve variability in inundation state over a tidal cycle. The anticipated launch of the Geosynchronous Littoral Imaging and Monitoring Radiometer (GLIMR) instrument in 2026-2027 will however provide this capability for multiple measurements per day while acquiring hyperspectral imagery. Although the exact mission and instrument specifications are still under development, GLIMR's geosynchronous orbit will undoubtedly acquire imagery at a temporal resolution far finer than is currently capable with polar orbiting satellites. Combined with hyperspectral capabilities, and at 300-350 m resolution, this instrument will provide potential inundation extent assessments throughout a given tidal cycle, which will be critical in directly assessing tidal marsh hydrologic variability. GLIMR will focus primarily over the Gulf of Mexico region of the United States (with more than 7 primary science scans per day) but will also cover (with fewer scans per day) other coastal regions of the United States (e.g., 2 scans per day over the Caribbean Sea, East/West CONUS, Amazon plume, and Equatorial Pacific). This is a necessary trade-off consideration with satellite specifications, you can have high temporal resolution, high spatial resolution, and global coverage, but never all three together.

The NISAR satellite, which has already been discussed in Chapter 4, will produce high spatial resolution L-band imagery with near-global coverage. While NISAR will not acquire imagery as frequently as GLIMR, it will do so with a 12-day revisit time, that is unprecedented by spaceborne L-band SAR with similar spatial resolutions. Comparatively, PALSAR/PALSAR-2 have a 46-day revisit. NISAR's projected acquisition scheme will feature primarily dual-polarimetric (HH, HV) and some quasi-quad polarimetric (HH, HV, VH, VV) observations over coastal regions of the United States (and globally) according to the NASA-ISRO SAR (NISAR) Mission Science Users' Handbook (NASA 2018). The dual-polarimetric and quasi-quad polarimetric modes are projected to be fairly stable as an acquisition scheme, meaning NISAR will acquire comparable observations every 12 days, which is very similar to Sentinel-1, but with more optimal frequency and polarizations for tidal marsh inundation mapping. The expanded possibilities that exist with this acquisition scheme at an L-band frequency are great. If there is a single point that this thesis has hopefully demonstrated, it is that Sentinel-1's frequent revisit time was absolutely critical in tidal marsh mapping, monitoring, and characterization. The findings in Chapter 4, however, found that difficulties can exist with C-band imagery in accurately assessing tidal marsh inundation state with single date imagery. L-band imagery in contrast had improved performance and allowed the use of single date image inundation classifications when using PALSAR/PALSAR-2 and UAVSAR imagery. Having L-band inundation products at a 12-day repeat would represent a significant advance in characterizing tidal marsh hydrology, especially as it relates to the study of coastal processes including carbon cycling, biogeochemistry, and sedimentology. NISAR's 12-day repeat L-band imagery provides the potential for great improvements in mapping tidal marsh inundation patterns with single date L-band imagery, but also in combining this global coverage L-band imagery with NISAR S-band image acquisitions over India and globally distributed calibration/validation sites. Further, the combination of NISAR L-band imagery and Sentinel-1 C-band imagery may present a highly effective tool for assessing tidal marsh inundation state and for mapping tidal marshes at the global scale. The empirical findings in Chapters 2 and 4, and the radiometric modeling findings in Chapter 4 clearly demonstrate that C-band scattering responds primarily to marsh vegetation structure while L-band scattering responds to sub-canopy inundation state. Fusing C-band and L-band observations presents a tool of tremendous potential utility in tidal marsh mapping and monitoring. In regions where C-band, S-band, and L-band imagery are acquired this presents further improvements in assessing wetlands characteristics and great opportunities for improving radar-based ecological science in general.

The recent and anticipated advances in remote sensing technologies relevant to the monitoring and characterization of wetlands should be cause for optimism, especially in the context of characterization of wetland hydrology as well as vegetation phenology and community composition within wetlands systems. However, this optimism should be tempered by the fact that defining the extent of wetlands and effectively mapping them at large scales remains challenging. It is quite feasible that the science of wetland process studies has advanced well beyond the science of wetland distribution studies. There are several examples in previous research, and this thesis, that illustrate that very point. It's helpful to again highlight two important datasets that are used to define tidal marsh distributions, the Mcowen et al. (2017) product which aggregates national-scale tidal marsh inventories into a global inventory and the

National Wetlands Inventory (NWI) which attempts to map all wetlands and deepwaters of the United States. In the United States, wetlands are defined legally and scientifically as areas possessing hydric soils, hydrophilic vegetation, and unique hydrology. This wetland definition and the origination of the term "hydric soils" comes from the Cowardin classification, upon which the NWI is based (Cowardin et al. 1979; Tiner 1997). However, actual development of the NWI is carried out via photo interpretation of aerial imagery with visible and NIR bands which makes the assessment of soil hydrologic characteristics challenging, especially compared to SWIR and microwave-based approaches. Further, vegetation community composition simply cannot be assessed by aerial photography at the class or species level, especially with single date aerial photography. Perhaps identification of hydrology is the only wetland definitional criterion that can be effectively assessed with visible and NIR aerial photography (provided vegetated canopies remain open). These technical limitations need to be viewed in the context of the NWI's original intended purpose, which is to serve as a reasonably accurate reference dataset for resource managers, landowners, regulatory agencies, and scientists needing information on wetlands distributions in the United States (Tiner 1997). In the United States, wetlands that are considered jurisdictional (subject to federal regulation) need to be defined by highly scientifically rigorous field studies that require species-level hydrophilic vegetation identifications, sub-surface hydric soil indicators, and evidence of a water table at or near the soil surface. Neither the NWI, nor any other remote sensing-based dataset, can assess these requirements, and the intended purpose of the NWI was never to provide an inventory of jurisdictional wetlands (Tiner 1997). Although the NWI is intended to map all probable wetlands, not just legally defined jurisdictional wetlands, it still underestimates total wetland extent, as it errs on the side of omission rather than commission. Another limitation with the

NWI dataset is that wetlands classes are often classified incorrectly in addition to the fact that NWI accuracy has not been rigorously assessed. A limited number of independent field surveys have suggested good accuracy (> 90%) for NWI mapping of inland wetlands (Nichols 1994; Kudray and Gale 2000; Handley and Wells 2009). However, it is unclear what accuracy can be expected for coastal wetlands as almost no validation studies exist, and the accuracy of this NWI class is noted as "considered approximate based on available reports or limited checking" (Tiner 1997). Considering that the NWI serves as the U.S. tidal marsh survey used in the Mcowen et al. (2017) global tidal marsh product, these limitations need to be noted.

In this thesis research effort, we noted several cases where NWI errors were present over coastal wetland study sites. For instance, at Jug Bay, a low marsh system with non-persistent vegetation was incorrectly identified as a mix of low marsh with persistent vegetation and non-persistent aquatic beds. In this system, use of radar imagery proved much more useful than aerial photography in assessing wetland vegetation. At the Wheeler Marsh site, a high marsh system with herbaceous vegetation was defined scrub-shrub by the NWI. Although the NWI's spatial delineation of this system was highly accurate, the classification was incorrect, which suggest a limitation of the photointerpretation approach. When this system was classified with a SAR-optical remote sensing approach in thesis Chapter 3, the high marsh was correctly classified as tidal marsh. The inclusion of multitemporal SAR imagery was likely critical for the accurate classification of high marsh at the Wheeler Marsh because the Jug Bay site indicated fairly temporally invariant C-band scattering for ground verified scrub-shrub wetland while emergent herbaceous species all showed significant amounts of backscatter variability. It is important to note these areas where NWI inaccuracies exist as they will inventively be ingested into the Mcowen tidal marsh product that integrates NWI and data from other national surveys. However, the findings in this thesis should call into question how accurate any number of those surveys truly are.

The overarching objective of this thesis was to improve the monitoring and characterization of tidal marshes with remote sensing observations. While a number of new approaches were developed that vastly improved characterization of wetland vegetation and wetland hydrology, the goal of achieving more accurate tidal marsh assessments was only carried out for two regions of the United States, the Mid-Atlantic and the Gulf Coast. Clearly much more research is needed to reach a point of having an accurate tidal marsh inventory for the United States let alone globally. For the United States, it's clear that satellite remote sensing datasets and the NWI have relative strengths that can be leveraged to produce an improved synergized wetlands product. The NWI's strengths clearly lie in the spatial detail. Seldom in this thesis research effort did we encounter a wetlands system that was not digitized in a highly accurate manner. The spatial accuracy of the NWI delineations is unmatched by publicly available satellite imagery with resolutions at 10-m or coarser. The weaknesses of the NWI are classification accuracy and its static nature, which in contrast are strengths of satellite imagery which more accurately detects wetland biophysical properties and is collected much more frequently than NWI updates. Satellite capabilities will continue to improve in this way as more frequent multispectral imagery, hyperspectral imagery, and L-band SAR imagery become more available. A suggested initial research effort would be a validation of NWI polygons with a simplified satellite-based classification that separating open water, vegetated deepwaters, emergent tidal marsh, palustrine marsh, forested wetlands, and upland forest, and even specific vegetation types where possible. This would be similar to the classification developed in Chapters 2 and 3, but could feature a decision tree-based classification rather than a mixed machine learning-decision tree classification. Critical to this effort would be the inclusion of L-band NISAR imagery which would much better allow the distinction between forested wetlands and upland forest. Although this satellite wetlands product would be less spatially detailed than the NWI polygons, it would serve as an accuracy check by using the classified pixels lying within the NWI polygons bounds as a validation. NWI classes could be re-assigned if the satellite product and NWI did not correspond throughout the majority of the NWI polygon. The identification of non-correspondence between the satellite product and NWI would also be critical for identifying wetlands that may have been lost due to human modification, sea level rise, or other factors.

Rigorous and informative satellite-based wetland monitoring is now clearly feasible at an annual or sub-annual resolution. One of the keys for these types of research efforts would be the identification of training sites where wetlands were known to be classified accurately by the NWI and additional studies, such as those that were identified in Chapter 3 of this thesis. These sites would allow for the development of both decision tree and machine learning-based satellite wetlands products, which in turn could be used to validate the NWI in areas where additional ground validation studies do not exist. At this point, such recommendations are general, but the approaches used in each of these thesis chapters represents a piece of the roadmap that arrives at more accurate wetlands mapping efforts in general, and for tidal marshes in particular. The capabilities that satellites provide in characterization of wetland processes also need to be leveraged for wetlands identification and mapping, even if it's for validating existing products like NWI. After all, it is the wetland processes that provide the very definition of wetlands. The evolving satellite capabilities that continue to improve in assessing wetlands vegetation and hydrologic state present a way forward in wetlands mapping as well. Although the satellites may never characterize sub-surface soil redox state, the characterization of hydrology with SAR and vegetation mapping at the species level with hyperspectral imagery will greatly advance wetland science at a scale unrivaled by field studies.

References

Ágoston-Szabó, Edit, and Mária Dinka. 2008. "Decomposition of Typha Angustifolia and Phragmites Australis in the Littoral Zone of a Shallow Lake." *Biologia* 63 (6): 1104–10. https://doi.org/10.2478/s11756-008-0154-4.

Arnold, D.W.D, et al. 2017. "Solid Earth Decaying Lava Extrusion Rate at El Reventador Volcano, Ecuador, Measured Using High-Resolution Satellite Radar," *Journal of Geophysical Research*. 9966–88. https://doi.org/10.1002/2017JB014580

Allen, Allison L, and Stephen K Gill. 2003. "Tidal Characteristics of Blackwater National Wildlife Refuge." *U.S. Army Corps of Engineers (USACE) and National Oceanic and Atmospheric Administration (NOAA).*

Anderson, Frank E, Brian Bergamaschi, Cove Sturtevant, Sara Knox, Lauren Hastings, Lisamarie Windham-Myers, Matteo Detto, et al. 2016. "Variation of Energy and Carbon Fluxes from a Temperate Freshwater Wetland and Implications for Carbon Market Verification Protocols." *Journal of Geophysical Research: Biogeoscienceal of Geophysical Research: Biogeoscience* 121: 1–19. https://doi.org/10.1002/2015JG003083

Anthony Bloom, A., W. Kevin Bowman, Meemong Lee, J. Alexander Turner, Ronny Schroeder, R. John Worden, Richard Weidner, C. Kyle McDonald, and J. Daniel Jacob. 2017. "A Global Wetland Methane Emissions and Uncertainty Dataset for Atmospheric Chemical Transport Models (WetCHARTs Version 1.0)." *Geoscientific Model Development* 10 (6): 2141–56. https://doi.org/10.5194/gmd-10-2141-2017.

Atkins, Rowland J, Morgan Tidd, and Gord Ruffo. 2016. "Coastal Education & Research Foundation, Inc." 27 (75): 661–71. https://doi.org/10.2112/SI63-011.1.

Atwood, Don, Michael Battaglia, Laura Bourgeau-Chavez, Frank Ahern, Kevin Murnaghan, and Brian Brisco. 2020. "Exploring Polarimetric Phase of Microwave Backscatter from Typha Wetlands." *Canadian Journal of Remote Sensing* 46 (1): 49–66. https://doi.org/10.1080/07038992.2020.1726736.

Audubon Society of the United States. 2018. "Important Bird Areas. Active Delta (Mississippi River Birdsfoot Delta)." https://www.audubon.org/important-bird-areas/active-delta-mississippi-river-birdsfoot-delta. Accessed 2020.

Barbier, Edward B., Sally D. Hacker, Chris Kennedy, Evamaria W. Koch, Adrian C. Stier, and Brian R. Silliman. 2011. "The Value of Estuarine and Coastal Ecosystem Services." *Ecological Monographs* 81 (2): 169–93. https://doi.org/10.1890/10-1510.1.

Bartlett, D. S., and V. Klemas. 1981. "In Situ Spectral Reflectance Studies of Tidal Wetland Grasses." *Photogrammetric Engineering and Remote Sensing* 47 (12): 1695–1703.

Baute, Kurtis, Laura L. Van Eerd, Darren E. Robinson, Peter H. Sikkema, Maryam Mushtaq, and Brandon H. Gilroyed. 2018. "Comparing the Biomass Yield and Biogas Potential of Phragmites Australis with Miscanthus X Giganteus and Panicum Virgatum Grown in Canada." *Energies* 11 (9). https://doi.org/10.3390/en11092198.

Beckett, Leah H, Andrew H Baldwin, and Michael S Kearney. 2016. "Tidal Marshes across a Chesapeake Bay Subestuary Are Not Keeping up with Sea-Level Rise." *PLoS ONE* 11 (7): 1–12. https://doi.org/10.1371/journal.pone.0159753.

Behnamian, Amir, Sarah Banks, Lori White, Brian Brisco, Koreen Milard, Jon Pasher, Zhaohua Chen, Jason Duffe, Laura Bourgeau-Chavez, and Michael Battaglia. 2017. "Semi-Automated Surface Water Detection with Synthetic Aperture Radar Data: A Wetland Case Study." *Remote Sensing* 9 (12): 1–21. https://doi.org/10.3390/rs9121209.

Benner, Ronald, Mary Ann Moran, and Robert E. Hodson. 1986. "Biogeochemical Cycling of Lignocellulosic Carbon in Marine and Freshwater Ecosystems: Relative Contributions of Procaryotes and Eucaryotes." *Limnology and Oceanography* 31 (1): 89–100. https://doi.org/10.4319/lo.1986.31.1.0089.

Bertness, M D, P J Ewanchuk, and B R Silliman. 2002. "Anthropogenic Modification of New England Salt Marsh Landscapes." *Proceedings of the National Academy of Sciences* 99 (3): 1395–98. https://doi.org/10.1073/pnas.022447299.

Bertness, Mark D. 1991. "Zonation of Spartina Patens and Spartina Alterniflora in New England Salt Marsh." *Ecological Society* 72 (1): 138–48.

Bioresita, Filsa, Anne Puissant, André Stumpf, and Jean Philippe Malet. 2018. "A Method for Automatic and Rapid Mapping of Water Surfaces from Sentinel-1 Imagery." *Remote Sensing* 10 (2). https://doi.org/10.3390/rs10020217.

Bourgeau-Chavez, Laura L, Kurt P Kowalski, Martha L Carlson, Kirk A Scarbrough, Richard B Powell, Colin N Brooks, Brian Huberty, et al. 2013. "Mapping Invasive Phragmites Australis in the Coastal Great Lakes with ALOS PALSAR Satellite Imagery for Decision Support." *Journal of Great Lakes Research* 39: 65–77. https://doi.org/10.1016/j.jglr.2012.11.001.

Bourgeau-Chavez, Laura, Sarah Endres, Michael Battaglia, Mary Ellen Miller, Elizabeth Banda, Zachary Laubach, Phyllis Higman, Pat Chow-Fraser, and James Marcaccio. 2015. "Development of a Bi-National Great Lakes Coastal Wetland and Land Use Map Using Three-Season PALSAR and Landsat Imagery." *Remote Sensing* 7 (7): 8655–82. https://doi.org/10.3390/rs70708655.

Breiman, Leo. 2001. "Breiman 2001 - Random Forests," 1–33.

Brisco, Brian, M. Kapfer, T. Hirose, B. Tedford, and J Liu. 2011. “Evaluation of C-Band Polarization Diversity and Polarimetry for Wetland Mapping.” *Canadian Journal of Remote Sensing* 37 (1): 82–92. https://doi.org/10.5589/m11-017.

Brisco, Brian, Frank Ahern, Kevin Murnaghan, Lori White, Francis Canisus, and Philip Lancaster. 2017. “Seasonal Change in Wetland Coherence as an Aid to Wetland Monitoring.” *Remote Sensing* 9 (2): 1–19. https://doi.org/10.3390/rs9020158.

Brown, Ian, Simon Mwansasu, and Lars Ove Westerberg. 2016. “L-Band Polarimetric Target Decomposition of Mangroves of the Rufiji Delta, Tanzania.” *Remote Sensing* 8 (2). https://doi.org/10.3390/rs8020140.

Bunting, Pete, Ake Rosenqvist, Richard M. Lucas, Lisa Maria Rebelo, Lammert Hilarides, Nathan Thomas, Andy Hardy, Takuya Itoh, Masanobu Shimada, and C. Max Finlayson. 2018. “The Global Mangrove Watch - A New 2010 Global Baseline of Mangrove Extent.” *Remote Sensing* 10 (10). https://doi.org/10.3390/rs10101669.

Byrd, Kristin B., Laurel Ballanti, Nathan Thomas, Dung Nguyen, James R. Holmquist, Marc Simard, and Lisamarie Windham-Myers. 2018. “A Remote Sensing-Based Model of Tidal Marsh Aboveground Carbon Stocks for the Conterminous United States.” *ISPRS Journal of Photogrammetry and Remote Sensing* 139: 255–71. https://doi.org/10.1016/j.isprsjprs.2018.03.019.

C.N. Koyama, K. Schneider. 2010. “A Novel Approach To Estimate Soil Moisture Under Vegetation Using Partial Polarimetric Alos Palsar Data.” *International Archives of the Photogrammetry, Remote Sensing and Spatial Information Science* XXXVIII: 421–26.

Cable, Jeffrey, John Kovacs, Xianfeng Jiao, and Jiali Shang. 2014. “Agricultural Monitoring in Northeastern Ontario, Canada, Using Multi-Temporal Polarimetric RADARSAT-2 Data.” *Remote Sensing* 6 (3): 2343–71. https://doi.org/10.3390/rs6032343.

Campbell, Anthony, Yeqiao Wang, Mark Christiano, and Sara Stevens. 2017. “Salt Marsh Monitoring in Jamaica Bay, New York from 2003 to 2013: A Decade of Change from Restoration to Hurricane Sandy.” *Remote Sensing* 9 (2): 1–20. https://doi.org/10.3390/rs9020131.

Cao, Fang and Maria Tzortziou. 2020. “Capturing dissolved organic carbon dynamics with Landsat-8 and Sentinel-2 in tidally influenced wetland-estuarine systems” *Remote Sensing of Environment*. In Review.

Carle, Melissa V, Charles E. Sasser, and Harry H. Roberts. 2015. “Accretion and Vegetation Community Change in the Wax Lake Delta Following the Historic 2011 Mississippi River Flood”. *Journal of Coastal Research*. https://doi.org/10.2112/JCOASTRES-D-13-00109.1

Clewley, Daniel, Jane Whitcomb, Mahta Moghaddam, Kyle McDonald, Bruce Chapman, and Peter Bunting. 2015. “Evaluation of ALOS PALSAR Data for High-Resolution Mapping of

Vegetated Wetlands in Alaska." *Remote Sensing* 7 (6): 7272–97. https://doi.org/10.3390/rs70607272.

Cloude, Shane Robert. 2007. "The Dual Polarisation Entropy / Alpha Decomposition." *Proceedings of the 3rd International Workshop on Science and Applications of SAR Polarimetry and Polarimetric Interferometry*, 1–6.

Collins, Alan R., and Neil Gillies. 2014. "Constructed Wetland Treatment of Nitrates: Removal Effectiveness and Cost Efficiency." *Journal of the American Water Resources Association* 50 (4): 898–908. https://doi.org/10.1111/jawr.12145.

Connor, R., and G. L. Chmura. 2000. "Dynamics of Above- and Belowground Organic Matter in a High Latitude Macrotidal Saltmarsh." *Marine Ecology Progress Series* 204 (Gallagher 1983): 101–10. https://doi.org/10.3354/meps204101.

Costa, M, O Niemann, E Novo, and F Ahern. 2002. "Biophysical Properties and Mapping of Aquatic Vegetation during the Hydrological Cycle of the Amazon …." *International Journal of Remote Sensing* 23 (7): 1401–26.

Dabrowska-Zielinska, Katarzyna, Maria Budzynska, Monika Tomaszewska, Alicja Malinska, Martyna Gatkowska, Maciej Bartold, and Iwona Malek. 2016. "Assessment of Carbon Flux and Soil Moisture in Wetlands Applying Sentinel-1 Data." *Remote Sensing* 8 (9). https://doi.org/10.3390/rs8090756.

Dahl, Kristina A, Melanie F Fitzpatrick, and Erika Spanger-Siegfried. 2017. "Sea Level Rise Drives Increased Tidal Flooding Frequency at Tide Gauges along the U.S. East and Gulf Coasts: Projections for 2030 and 2045." *PLoS ONE* 12 (2): 1–23. https://doi.org/10.1371/journal.pone.0170949.

Du, Yun, Yihang Zhang, Feng Ling, Qunming Wang, Wenbo Li, and Xiaodong Li. 2016. "Water Bodies' Mapping from Sentinel-2 Imagery with Modified Normalized Difference Water Index at 10-m Spatial Resolution Produced by Sharpening the Swir Band." *Remote Sensing* 8 (4). https://doi.org/10.3390/rs8040354.

Duan, Xueyang, and Cathleen E. Jones. 2017. "Coherent Microwave Scattering Model of Marsh Grass." *Radio Science* 52 (12): 1578–95. https://doi.org/10.1002/2017RS006325.

Duke, Shawn Trevor. 2012. "Effects of Invasion by the Common Reed (Phragmites Australis) on Carbon Transformations in a Great Lakes Marsh," no. 2012: 56.

Duman, T., and K. V.R. Schäfer. 2017. "Partitioning Net Ecosystem Carbon Exchange of Native and Invasive Plant Communities by Vegetation Cover in an Urban Tidal Wetland in the New Jersey Meadowlands (USA)." *Ecological Engineering*, no. May: 0–1. https://doi.org/10.1016/j.ecoleng.2017.08.031.

Ellison, Candice, Murat Sean McKeown, Samir Trabelsi, and Dorin Boldor. 2017. "Dielectric Properties of Biomass/Biochar Mixtures at Microwave Frequencies." *Energies* 10 (4): 1–11. https://doi.org/10.3390/en10040502.

Elliton, Courtney Erin. 2013. "Interactions among Hydrology, Sediment and Vegetation in Accreting Wax Lake Delta: Physical and Biogeochemical Implications for Coastal Louisiana Restoration." *Masters Thesis*. Louisiana State University

Elmore, Annette Hall. 2008. "Remote sensing of tidal freshwater marsh elevation, channels, and vegetation structure." *Masters Thesis*. University of Maryland.

Environmental Protection Agency (EPA). 1996. "Beyond the Estuary: The Importance of Upstream Wetlands in Estuarine Processes". EPA904-B-96-002.

Feagin, R. A., I. Forbrich, T. P. Huff, J. G. Barr, J. Ruiz-Plancarte, J. D. Fuentes, R. G. Najjar, et al. 2020. "Tidal Wetland Gross Primary Production Across the Continental United States, 2000–2019." *Global Biogeochemical Cycles* 34 (2): 1–25. https://doi.org/10.1029/2019GB006349.

Franz, Bryan A., Sean W. Bailey, Norman Kuring, and P. Jeremy Werdell. 2015. "Ocean Color Measurements with the Operational Land Imager on Landsat-8: Implementation and Evaluation in SeaDAS." *Journal of Applied Remote Sensing* 9 (1): 096070. https://doi.org/10.1117/1.JRS.9.096070.

Frohn, Robert C, Molly Reif, Charles Lane, and Brad Autrey. 2009. "Satellite Remote Sensing of Isolated Wetlands Using Object-Oriented Classification of Landsat-7 Data." *Wetlands* 29 (3): 931–41. https://doi.org/10.1672/08-194.1.

Ganju, Neil K, Zafer Defne, Matthew L Kirwan, Sergio Fagherazzi, Andrea D'Alpaos, and Luca Carniello. 2017. "Spatially Integrative Metrics Reveal Hidden Vulnerability of Microtidal Salt Marshes." *Nature Communications* 8. https://doi.org/10.1038/ncomms14156.

Ganju, Neil K, Nicholas J Nidzieko, and Matthew L Kirwan. 2013. "Inferring Tidal Wetland Stability from Channel Sediment Fluxes: Observations and a Conceptual Model." *Journal of Geophysical Research: Earth Surface* 118 (4): 2045–58. https://doi.org/10.1002/jgrf.20143.

Gatkowska, Martyna, Iwona Malek, Konrad Turlej, and Milena Napiorkowska. 2014. "Monitoring Wetlands Ecosystems Using ALOS PALSAR (L-Band, HV) Supplemented by Optical Data: A Case Study of Biebrza Wetlands in Northeast Poland," 1605–33. https://doi.org/10.3390/rs6021605.

Gilmore, Martha S., Emily H. Wilson, Nels Barrett, Daniel L. Civco, Sandy Prisloe, James D. Hurd, and Cary Chadwick. 2008. "Integrating Multi-Temporal Spectral and Structural Information to Map Wetland Vegetation in a Lower Connecticut River Tidal Marsh."

Remote Sensing of Environment 112 (11): 4048–60. https://doi.org/10.1016/j.rse.2008.05.020.

Gorelick, Noel, Matt Hancher, Mike Dixon, Simon Ilyushchenko, David Thau, and Rebecca Moore. 2017. "Google Earth Engine: Planetary-Scale Geospatial Analysis for Everyone." *Remote Sensing of Environment* 202: 18–27. https://doi.org/10.1016/j.rse.2017.06.031.

Graven, H D, R F Keeling, S C Piper, P K Patra, B B Stephens, S C Wofsy, L R Welp, et al. 2013. "Enhanced Seasonal Exchange of CO2 by Northern Ecosystems since 1960." *Science (New York, N.Y.)* 341 (6150): 1085–89. https://doi.org/10.1126/science.1239207.

Halevy, Abraham H., and A. H. Pieterse. 2020. "Eichhornia Crassipes." *CRC Handbook of Flowering*, 462–65. https://doi.org/10.1201/9781351072540-69.

Hamann, Elena, and Sara Puijalon. 2013. "Biomechanical Responses of Aquatic Plants to Aerial Conditions." *Annals of Botany* 112 (9): 1869–78. https://doi.org/10.1093/aob/mct221.

Handley, Larry, and Chris Wells. 2009. "Comparison of NLCD with NWI Classifications of Baldwin and Mobile Counties, Alabama." *U.S. Geological Survey Open-File Report 2009-1058*, 11 pp.

Hänsch, Ronny, and Olaf Hellwich. 2016. "Random Forests." *Handbuch Der Geodäsie*, 1–42. https://doi.org/10.1007/978-3-662-46900-2.

Herbert, Ellen R, Joseph Schubauer-berigan, Christopher B Craft, Environmental Affairs, Environmental Protection Agency, and National Risk. 2019. "Intrusion on Tidal Freshwater Marsh Carbon Cycling." https://doi.org/10.1007/s10533-018-0436-z.

Hestir, Erin Lee, Vittorio E. Brando, Mariano Bresciani, Claudia Giardino, Erica Matta, Paolo Villa, and Arnold G. Dekker. 2015. "Measuring Freshwater Aquatic Ecosystems: The Need for a Hyperspectral Global Mapping Satellite Mission." *Remote Sensing of Environment* 167: 181–95. https://doi.org/10.1016/j.rse.2015.05.023.

Hinson, Audra L., Rusty A. Feagin, Marian Eriksson, Raymond G. Najjar, Maria Herrmann, Thomas S. Bianchi, Michael Kemp, Jack A. Hutchings, Steve Crooks, and Thomas Boutton. 2017. "The Spatial Distribution of Soil Organic Carbon in Tidal Wetland Soils of the Continental United States." *Global Change Biology* 23 (12): 5468–80. https://doi.org/10.1111/gcb.13811.

Hird, Jennifer N, Evan R DeLancey, Gregory J McDermid, and Jahan Kariyeva. 2017. "Google Earth Engine, Open-Access Satellite Data, and Machine Learning in Support of Large-Area Probabilistic Wetland Mapping." *Remote Sensing* 9 (12). https://doi.org/10.3390/rs9121315.

Holmquist, James R., Lisamarie Windham-Myers, Blanca Bernal, Kristin B. Byrd, Steve Crooks, Meagan Eagle Gonneea, Nate Herold, et al. 2018. "Uncertainty in United States Coastal

Wetland Greenhouse Gas Inventorying.” *Environmental Research Letters* 13 (11). https://doi.org/10.1088/1748-9326/aae157.

Hong, Sang Hoon, and Shimon Wdowinski. 2010. “Rotated Dihedral and Volume Scattering Behavior in Cross-Polarimetric SAR.” *International Geoscience and Remote Sensing Symposium (IGARSS)* 1 (d): 3138–41. https://doi.org/10.1109/IGARSS.2010.5654326.

Hong, Sang Hoon, and Shimon Wdowinski. 2014. “Double-Bounce Component in Cross-Polarimetric SAR from a New Scattering Target Decomposition.” *IEEE Transactions on Geoscience and Remote Sensing* 52 (6): 3039–51. https://doi.org/10.1109/TGRS.2013.2268853.

Hong, Sang-Hoon, Hyun-Ok Kim, Shimon Wdowinski, and Emanuelle Feliciano. 2015. “Evaluation of Polarimetric SAR Decomposition for Classifying Wetland Vegetation Types.” *Remote Sensing* 7 (7): 8563–85. https://doi.org/10.3390/rs70708563.

Howard, Jennifer, Ariana Sutton-Grier, Dorothée Herr, Joan Kleypas, Emily Landis, Elizabeth Mcleod, Emily Pidgeon, and Stefanie Simpson. 2014. “Clarifying the Role of Coastal and Marine Systems in Climate Mitigation.” https://doi.org/10.1002/fee.1451.

Howes, Nick C., Duncan M. FitzGerald, Zoe J. Hughes, Ioannis Y. Georgiou, Mark A. Kulp, Michael D. Miner, Jane M. Smith, and John A. Barras. 2010. “Hurricane-Induced Failure of Low Salinity Wetlands.” *Proceedings of the National Academy of Sciences of the United States of America* 107 (32): 14014–19. https://doi.org/10.1073/pnas.0914582107.

Hunt, E. Raymond Jr., Lingli Wang, John J. Qu, and Xianjun Hao. 2012. “Remote Sensing of Fuel Moisture Content from Canopy Water Indices and Normalized Dry Matter Index.” *Journal of Applied Remote Sensing* 6. https://doi.org/10.1117/1.JRS.6.061705.

Hurd, James D, Daniel L Civco, Martha S Gilmore, Sandy Prisloe, and Emily H Wilson. 2005. “Coastal Marsh Characterization Using Satellite Remote Sensing and in Situ Radiometry Data: Preliminary Results.” *Geospatial Goes Global: From Your Neighborhood to the Whole Planet*.

Jensen, Daniel, Kyle C. Cavanaugh, Marc Simard, Gregory S. Okin, Edward Castañeda-Moya, Annabeth McCall, and Robert R. Twilley. 2019. “Integrating Imaging Spectrometer and Synthetic Aperture Radar Data for Estimating Wetland Vegetation Aboveground Biomass in Coastal Louisiana.” *Remote Sensing* 11 (21). https://doi.org/10.3390/rs11212533.

Jensen, Katherine, Kyle McDonald, Erika Podest, Nereida Rodriguez-Alvarez, Viviana Horna, and Nicholas Steiner. 2018. “Assessing L-Band GNSS-Reflectometry and Imaging Radar for Detecting Sub-Canopy Inundation Dynamics in a Tropical Wetlands Complex.” *Remote Sensing* 10 (9). https://doi.org/10.3390/rs10091431.

Ji, Kefeng, and Yonghui Wu. 2015. “Scattering Mechanism Extraction by a Modified Cloude-Pottier Decomposition for Dual Polarization SAR.” *Remote Sensing* 7 (6): 7447–70. https://doi.org/10.3390/rs70607447.

Jin, S.; Yang, L.; Danielson, P.; Homer, C.; Fry, J.; Xian, G. 2013. “A comprehensive change detection method for updating the National Land Cover Database to circa 2011” *Remote Sensing of Environment*. 132: 159–175.

Jones, John W. 2019. “Improved Automated Detection of Subpixel-Scale Inundation-Revised Dynamic Surface Water Extent (DSWE) Partial Surface Water Tests.” *Remote Sensing* 11 (4). https://doi.org/10.3390/rs11040374.

Jordan, E. 1991. “Continuous Exchanges Marshes Automated of Nutrients Sampling of Tidal by Brackish.” *Water*, 527–45.

Kasischke, Eric S., and Laura L. Bourgeau-Chavez. 1997. “Monitoring South Florida Wetlands Using ERS-1 SAR Imagery.” *Photogrammetric Engineering and Remote Sensing* 63 (3): 281–91.

Kasischke, Eric S, Kevin B Smith, Laura L Bourgeau-Chavez, Edwin A Romanowicz, Suzy Brunzell, and Curtis J Richardson. 2003. “Effects of Seasonal Hydrologic Patterns in South Florida Wetlands on Radar Backscatter Measured from ERS-2 SAR Imagery.” *Remote Sensing of Environment* 88 (4): 423–41. https://doi.org/10.1016/j.rse.2003.08.016.

Kearney, Michael S, Andrew S Rogers, John R G Townshend, Eric Rizzo, David Stutzer, J Court Stevenson, and Karen Sundborg. 2002. “Landsat Imagery Shows Decline of Coastal Marshes in Chesapeake and Delaware Bays.” *Eos, Transactions American Geophysical Union* 83 (16): 173. https://doi.org/10.1029/2002EO000112.

Kearney, William S., Giulio Mariotti, Linda A. Deegan, and Sergio Fagherazz. 2017. “Stage-Discharge Relationship in Tidal Channels.” *Limnology and Oceanography: Methods* 15 (4): 394–407. https://doi.org/10.1002/lom3.10168.

Keenan, Trevor F., David Y. Hollinger, Gil Bohrer, Danilo Dragoni, J. William Munger, Hans Peter Schmid, and Andrew D. Richardson. 2013. “Increase in Forest Water-Use Efficiency as Atmospheric Carbon Dioxide Concentrations Rise.” *Nature* 499 (7458): 324–27. https://doi.org/10.1038/nature12291.

Kemp, Andrew C., Troy D. Hill, Christopher H. Vane, Niamh Cahill, Philip M. Orton, Stefan A. Talke, Andrew C. Parnell, Kelsey Sanborn, and Ellen K. Hartig. 2017. “Relative Sea-Level Trends in New York City during the Past 1500 Years.” *Holocene* 27 (8): 1169–86. https://doi.org/10.1177/0959683616683263.

Kim, Jin-Woo, Zhong Lu, John W. Jones, C.K. Shum, Hyongki Lee, and Yuanyuan Jia. 2014. “Monitoring Everglades Freshwater Marsh Water Level Using L-Band Synthetic Aperture

Radar Backscatter." *Remote Sensing of Environment* 150: 66–81. https://doi.org/10.1016/j.rse.2014.03.031.

Kirwan, Matthew L, Stijn Temmerman, Emily E Skeehan, Glenn R Guntenspergen, and Sergio Fagherazzi. 2016. "Overestimation of Marsh Vulnerability to Sea Level Rise." *Nature Climate Change* 6 (3): 253–60. https://doi.org/10.1038/nclimate2909.

Klemas, Victor. 2013. "Using Remote Sensing to Select and Monitor Wetland Restoration Sites: An Overview." *Journal of Coastal Research* 289 (July 2013): 958–70. https://doi.org/10.2112/JCOASTRES-D-12-00170.1.

Knight, J F, B P Tolcser, J M Corcoran, and L P Rampi. 2013. "The Effects of Data Selection and Thematic Detail on the Accuracy of High Spatial Resolution Wetland Classifications." *Photogrammetric Engineering and Remote Sensing* 79 (7): 613–23. https://doi.org/http://dx.doi.org/10.14358/PERS.79.7.613.

Koch, Benjamin J., Catherine M. Febria, Muriel Gevrey, Lisa A. Wainger, and Margaret A. Palmer. 2014. "Nitrogen Removal by Stormwater Management Structures: A Data Synthesis." *Journal of the American Water Resources Association* 50 (6): 1594–1607. https://doi.org/10.1111/jawr.12223.

Kovacic, David A., Mark B. David, Lowell E. Gentry, Karen M. Starks, and Richard A. Cooke. 2000. "Effectiveness of Constructed Wetlands in Reducing Nitrogen and Phosphorus Export from Agricultural Tile Drainage." *Journal of Environmental Quality* 29 (4): 1262. https://doi.org/10.2134/jeq2000.00472425002900040033x.

Kudray, Gregory and Margaret Gale. 2000. "Evaluation of National Wetland Inventory maps in a heavily forested region in the upper Great Lakes" *Wetlands* 20(4):581-587 https://doi.org/10.1672/0277-5212(2000)020%5B0581:EONWIM%5D2.0.CO;2

Kuenzer, Claudia, Igor Klein, Tobias Ullmann, Efi Foufoula Georgiou, Roland Baumhauer, and Stefan Dech. 2015. "Remote Sensing of River Delta Inundation: Exploiting the Potential of Coarse Spatial Resolution, Temporally-Dense MODIS Time Series." *Remote Sensing* 7 (7): 8516–42. https://doi.org/10.3390/rs70708516.

Kuhn, Catherine, Aline de Matos Valerio, Nick Ward, Luke Loken, Henrique Oliveira Sawakuchi, Milton Kampel, Jeffrey Richey, et al. 2019. "Performance of Landsat-8 and Sentinel-2 Surface Reflectance Products for River Remote Sensing Retrievals of Chlorophyll-a and Turbidity." *Remote Sensing of Environment* 224 (July 2018): 104–18. https://doi.org/10.1016/j.rse.2019.01.023.

Kulawardhana, R W, P S Thenkabail, J Vithanage, C Biradar, Md.A. a Islam, S Gunasinghe, and R Alankara. 2007. "Evaluation of the Wetland Mapping Methods Using Landsat ETM+ and SRTM Data." *Journal of Spatial Hydrology* 7 (2): 62–96.

Lamb, Brian T., Maria A. Tzortziou, Kyle C. McDonald. 2019. "Evaluation of Approaches for Mapping Tidal Wetlands of the Chesapeake and Delaware Bays" *Remote Sensing* 11(20) 2366. https://doi.org/10.3390/rs11202366

Lamb, Brian T., Maria A. Tzortziou, Kyle C. McDonald. 2020. "Satellite-based characterizations of tidal wetland hydrology to provide volumetric water measurements in support of wetland-estuary biogeochemical exchange characterization" *American Geophysical Union Ocean Sciences Meeting.* Abstract ID: CP43B-05

Lamb, Brian T., Maria A. Tzortziou, Kyle C. McDonald. 2020. "A fused radar-optical remote sensing approach for mapping tidal marshes and marsh vegetation characteristics in coastal wetlands and deepwater habitats: Application to the Gulf of Mexico and Mid-Atlantic Coasts of the U.S." *Remote Sensing*. In Preparation.

Land, Magnus, Wilhelm Granéli, Anders Grimvall, Carl Christian Hoffmann, William J. Mitsch, Karin S. Tonderski, and Jos T.A. Verhoeven. 2016. "How Effective Are Created or Restored Freshwater Wetlands for Nitrogen and Phosphorus Removal? A Systematic Review." *Environmental Evidence* 5 (1): 1–26. https://doi.org/10.1186/s13750-016-0060-0.

Lang, Megan W., Philip A. Townsend, and Eric S. Kasischke. 2008. "Influence of Incidence Angle on Detecting Flooded Forests Using C-HH Synthetic Aperture Radar Data." *Remote Sensing of Environment* 112 (10): 3898–3907. https://doi.org/10.1016/j.rse.2008.06.013.

Lang, Megan W, and Eric S Kasischke. 2008. "Using C-Band Synthetic Aperture Radar Data to Monitor Forested Wetland Hydrology in Maryland's Coastal Plain, USA." *IEEE Transactions on Geoscience and Remote Sensing* 46 (2): 535–46. https://doi.org/10.1109/TGRS.2007.909950.

Langley, J. Adam, and J. Patrick Megonigal. 2012. "Field-Based Radiometry to Estimate Tidal Marsh Plant Growth in Response to Elevated CO 2 and Nitrogen Addition." *Wetlands* 32 (3): 571–78. https://doi.org/10.1007/s13157-012-0292-x.

Leck, Mary Allessio, Andrew H Baldwin, V Thomas Parker, Lisa Schile, and Dennis F Whigham. 2009. "Plant Communities of Tidal Freshwater Wetlands of the Continental USA and Canada." *Tidal Freshwater Wetlands*, 41–58.

Legault, Rene, Gregory P. Zogg, and Steven E. Travis. 2018. "Competitive Interactions between Native Spartina Alterniflora and Non-Native Phragmites Australis Depend on Nutrient Loading and Temperature." *PLoS ONE* 13 (2): 1–12. https://doi.org/10.1371/journal.pone.0192234.

Leonard, Lynn A., and Alexander L. Croft. 2006. "The Effect of Standing Biomass on Flow Velocity and Turbulence in Spartina Alterniflora Canopies." *Estuarine, Coastal and Shelf Science* 69 (3–4): 325–36. https://doi.org/10.1016/j.ecss.2006.05.004.

Leonard, Lynn A., and Mark E. Luther. 1995. “Flow Hydrodynamics in Tidal Marsh Canopies.” *Limnology and Oceanography* 40 (8): 1474–84. https://doi.org/10.4319/lo.1995.40.8.1474.

Logozzo L., Tzortziou M., Neale P., Clark B.. 2020. “Photochemical and Microbial Degradation of Chromophoric Dissolved Organic Matter Exported from Tidal Marshes.” *Journal of Geophysical Research - Biogeosciences*. In Revision.

Lopes, Carina L., Renato Mendes, Isabel Caçador, and João M. Dias. 2020. “Assessing Salt Marsh Extent and Condition Changes with 35 Years of Landsat Imagery: Tagus Estuary Case Study.” *Remote Sensing of Environment* 247 (April): 111939. https://doi.org/10.1016/j.rse.2020.111939.

Loudermilk, Erica. 2015. “Correlating Elevation to Vegetation Communities and Investigating Operator Error of an Electronic Level and RTK-GPS in a Tidal Freshwater Marsh,” no. August: 1–13.

Lovelock, Catherine E., Maria Fernanda Adame, Vicki Bennion, Matthew Hayes, Julian O’Mara, Ruth Reef, and Nadia S. Santini. 2014. “Contemporary Rates of Carbon Sequestration through Vertical Accretion of Sediments in Mangrove Forests and Saltmarshes of South East Queensland, Australia.” *Estuaries and Coasts* 37 (3): 763–71. https://doi.org/10.1007/s12237-013-9702-4.

Lu, Yuehan, James E. Bauer, Elizabeth A. Canuel, Youhei Yamashita, R. M. Chambers, and Rudolf Jaff. 2013. “Photochemical and Microbial Alteration of Dissolved Organic Matter in Temperate Headwater Streams Associated with Different Land Use.” *Journal of Geophysical Research: Biogeosciences* 118 (2): 566–80. https://doi.org/10.1002/jgrg.20048.

Marsh, Amanda, Linda K. Blum, Robert R. Christian, Elijah Ramsey, and Amina Rangoonwala. 2016. “Response and Resilience of Spartina Alterniflora to Sudden Dieback.” *Journal of Coastal Conservation* 20 (4): 335–50. https://doi.org/10.1007/s11852-016-0445-9.

McDonald, Kyle C, C Science Team Member, Erika Podest, Bruce Chapman, Ronny Schroeder, and Sarah Flores. “K & C Science Report – Phase 2: Mapping Boreal Wetlands and Open Water for Supporting Assessment of Land-Atmosphere Carbon Exchange.”

McFeeters, Stuart K. 1996. “The use of the Normalized Difference Water Index (NDWI) in the delineation of open water features”. *Remote Sensing Letters*. 1425-1432. https://doi.org/10.1080/01431169608948714.

McFeeters, Stuart K. 2013. “Using the Normalized Difference Water Index (Ndwi) within a Geographic Information System to Detect Swimming Pools for Mosquito Abatement: A Practical Approach.” *Remote Sensing* 5 (7): 3544–61. https://doi.org/10.3390/rs5073544.

McLeod, Elizabeth, Gail L Chmura, Steven Bouillon, Rodney Salm, Mats Bjork, Carlos M Duarte, Catherine E Lovelock, William H Schlesinger, and Brian R Silliman. 2011. “A Blueprint for Blue Carbon: Toward an Improved Understanding of the Role of Vegetated

Coastal Habitats in Sequestering CO2.” *Frontiers in Ecology and the Environment* 9 (10): 552–60. https://doi.org/10.1890/110004.

Mcowen, Chris, Lauren Weatherdon, Jan-Willem Bochove, Emma Sullivan, Simon Blyth, Christoph Zockler, Damon Stanwell-Smith, et al. 2017. “A Global Map of Saltmarshes.” *Biodiversity Data Journal* 5: e11764. https://doi.org/10.3897/BDJ.5.e11764.

Milligan, Gailynn, Helen M. Poulos, Martha S. Gilmore, Graeme P. Berlyn, Joseph Milligan, and Barry Chernoff. 2019. “Estimation of Short-Term C-Fixation in a New England Temperate Tidal Freshwater Wetland.” *Heliyon* 5 (5): e01782. https://doi.org/10.1016/j.heliyon.2019.e01782.

Mitsch, William J. and James G. Gosselink. 2007. “Wetlands”. 4th Edition, *John Wiley & Sons, Inc.*, Hoboken.

Montalto, Franco A., Tammo S. Steenhuis, and J. Yves Parlange. 2006. “The Hydrology of Piermont Marsh, a Reference for Tidal Marsh Restoration in the Hudson River Estuary, New York.” *Journal of Hydrology* 316 (1–4): 108–28. https://doi.org/10.1016/j.jhydrol.2005.03.043.

Moser, Linda, Andreas Schmitt, Anna Wendleder, and Achim Roth. 2016. “Monitoring of the Lac Bam Wetland Extent Using Dual-Polarized X-Band SAR Data”. *Remote Sensing*. Vol. 8. https://doi.org/10.3390/rs8040302.

National Academy of Sciences (NAS). 2017. “THRIVING ON OUR CHANGING PLANET. A Decadal Strategy for Earth Observation from Space”.

National Aeronautics and Space Administration (NASA). 2018. “NASA-ISRO SAR (NISAR) Mission Science Users’ Handbook”.

Nelson, N.G.; Munoz-Carpena, R.; Neale, P.J.; Tzortziou, M.; Megonigal, P.J. 2017. “Temporal variability in the importance of hydrologic, biotic, and climatic descriptors of dissolved oxygen dynamics in a shallow tidal marsh creek”. *Water Resources*. 00000, 5974–5997

Neubauer, Scott C. 2000. “Carbon Dynamics in a Tidal Freshwater Marsh,” 220. https://doi.org/10.25773/v5-z4ar-j180. *PhD Dissertation*. William and Mary.

Nichols, Christine. 1994. “Map Accuracy of National Wetlands Inventory Maps for Areas Subject to Maine Land Use Regulation Commission Jurisdiction”. *U.S. Department of the Interior, Northeast Region*.

Nieto, C;, DA; Dos Santos, AE; Izquierdo, JS; Rodriguez, and HR Grau. 2017. “Mesohabitat Mosaic in Lowland Braided Rivers: Short-Term Variability of Macroinvertebrate Metacommunities Mesohabitat Mosaic in Lowland Braided Rivers : Short-Term Variability of Gemma BURGAZZI , * Alex LAINI , Erica RACCHETTI , Pierluigi VIAROLI Departm.” *Journal of Limnology*, no. April. https://doi.org/10.4081/jlimnol.2017.

Novo, E M L M, M P F Costa, J E Mantovani, and I B T Lima. 2002. "Relationship between Macrophyte Stand Variables and Radar Backscatter at L and C Band, Tucuruí Reservoir, Brazil." *International Journal of Remote Sensing* 23 (7): 1241–60. https://doi.org/10.1080/01431160110092885.

O'Connell, Jessica L., Deepak R. Mishra, David L. Cotten, Li Wang, and Merryl Alber. 2017. "The Tidal Marsh Inundation Index (TMII): An Inundation Filter to Flag Flooded Pixels and Improve MODIS Tidal Marsh Vegetation Time-Series Analysis." *Remote Sensing of Environment* 201 (October 2016): 34–46. https://doi.org/10.1016/j.rse.2017.08.008.

O'Connor, Michael T., and Kevan B. Moffett. 2015. "Groundwater Dynamics and Surface Water-Groundwater Interactions in a Prograding Delta Island, Louisiana, USA." *Journal of Hydrology* 524: 15–29. https://doi.org/10.1016/j.jhydrol.2015.02.017.

Odum, William E. 1988. "Comparative Ecology of Tidal Freshwater and Salt Marshes" 19 (d): 147–76.

Odum, William E, Thomas J Smith III, John K Hoover, and Carole C McIvor. 1984. "The Ecology of Tidal Freshwater Marshes of the U.S. East Coast: A Community Profile," no. U.S. Fish and Wildlife Service FWS/obs-83/17: 177.

Oldak, A, T J Jackson, P Starks, and R Elliott. 2003. "Mapping Near-Surface Soil Moisture on Regional Scale Using ERS-2 SAR Data." *International Journal of Remote Sensing* 24 (22): 4579–98. https://doi.org/10.1080/0143116031000070463.

Oliver-Cabrera, Talib, and Shimon Wdowinski. 2016. "InSAR-Based Mapping of Tidal Inundation Extent and Amplitude in Louisiana Coastal Wetlands." *Remote Sensing* 8 (5). https://doi.org/10.3390/rs8050393.

Olliver, E. A., D. A. Edmonds, and J. B. Shaw. 2020. "Influence of Floods, Tides, and Vegetation on Sediment Retention in Wax Lake Delta, Louisiana, USA." *Journal of Geophysical Research: Earth Surface* 125 (1): 1–21. https://doi.org/10.1029/2019JF005316.

Ornes, WH, and DI Kaplan. 1989. "Macronutrient Status of Tall and Short Forms of Spartina Alterniflora in a South Carolina Salt Marsh." *Marine Ecology Progress Series* 55: 63–72. https://doi.org/10.3354/meps055063.

Ouarzeddine, Mounira, Boularbah Souissi, and Aichouche Belhadj-Aissa. 2007. "Unsupervised Classification Using Wishart Classifier." *European Space Agency, (Special Publication) ESA SP*, no. SP-644: 1–6.

Ozesmi, Stacy L, and Marvin E Bauer. 2002. "Satellite Remote Sensing of Wetlands." *Wetlands Ecology and Management* 10 (5): 381–402. https://doi.org/10.1023/A:1020908432489.

Pahlevan, Nima, Sandeep K. Chittimalli, Sundarabalan V. Balasubramanian, and Vincenzo Vellucci. 2019. "Sentinel-2/Landsat-8 Product Consistency and Implications for Monitoring

Aquatic Systems." *Remote Sensing of Environment* 220 (October 2017): 19–29. https://doi.org/10.1016/j.rse.2018.10.027.

Pahlevan, Nima, John R. Schott, Bryan A. Franz, Giuseppe Zibordi, Brian Markham, Sean Bailey, Crystal B. Schaaf, Michael Ondrusek, Steven Greb, and Christopher M. Strait. 2017. "Landsat 8 Remote Sensing Reflectance (Rrs) Products: Evaluations, Intercomparisons, and Enhancements." *Remote Sensing of Environment* 190: 289–301. https://doi.org/10.1016/j.rse.2016.12.030.

Parkinson, Hilary, Monica Pokorny, Plant Materials Specialist, Jane Mangold, Extension Invasive, and Plant Specialist. 2017. "Invasive Species Technical Note," no. May: 1–13.

Pekel, Jean-François, Andrew Cottam, Noel Gorelick, and Alan S. Belward. 2016. "High-Resolution Mapping of Global Surface Water and Its Long-Term Changes." *Nature* 540 (7633): 418–22. https://doi.org/10.1038/nature20584.

Pendleton, Linwood, Daniel C Donato, Brian C Murray, Stephen Crooks, W Aaron Jenkins, Samantha Sifleet, Christopher Craft, et al. 2012. "Estimating Global 'Blue Carbon' Emissions from Conversion and Degradation of Vegetated Coastal Ecosystems." *PLoS ONE* 7 (9). https://doi.org/10.1371/journal.pone.0043542.

Pope, K O, E Rejmankova, J F Paris, and R Woodruff. 1997. "Detecting Seasonal Cycle of the Yucatan Peninsula with SIR-C Polarmetric Radar Imagery." *Remote Sensing of Environment* 59 (96): 157–66.

Pope, Robin M, and Edward S Fry. 1997. "Absorption spectrum (380-700 nm) of Pure Water" *Applied Optics* 36: 8710-8723.

Prabhakara, Kusuma, W. Dean Hively, and Gregory W. McCarty. 2015. "Evaluating the Relationship between Biomass, Percent Groundcover and Remote Sensing Indices across Six Winter Cover Crop Fields in Maryland, United States." *International Journal of Applied Earth Observation and Geoinformation* 39: 88–102. https://doi.org/10.1016/j.jag.2015.03.002.

Prakash, Rishi, Dharmendra Singh, and Nagendra P. Pathak. 2012. "A Fusion Approach to Retrieve Soil Moisture with SAR and Optical Data." *IEEE Journal of Selected Topics in Applied Earth Observations and Remote Sensing* 5 (1): 196–206. https://doi.org/10.1109/JSTARS.2011.2169236.

Prisloe, S, E Wilson, D L Civco, J D Hurd, and M S Gilmore. 2006. "Use of Lidar Data to Aid in Discriminating and Mapping Plant Communities in Tidal Marshes of the Lower Connecticut River: Preliminary Results." *American Society for Photogrammetry and Remote Sensing - Annual Conference of the American Society for Photogrammetry and Remote Sensing 2006: Prospecting for Geospatial Information Integration* 2: 1108–15. http://www.scopus.com/inward/record.url?eid=2-s2.0-84869030119&partnerID=40&md5=b5266569903327c15fa1768b8bad7a2b.

Quegan, Shaun, and Jiong Jiong Yu. 2001. “Filtering of Multichannel SAR Images.” *IEEE Transactions on Geoscience and Remote Sensing* 39 (11): 2373–79. https://doi.org/10.1109/36.964973.

R Core Team. “R: A Language and Environment for Statistical Computing.” R Core Team: Vienna, Austria, 2017.

Ramsey, Elijah, Amina Rangoonwala, and Terri Bannister. 2013. “Coastal Flood Inundation Monitoring with Satellite C-Band and L-Band Synthetic Aperture Radar Data.” *Journal of the American Water Resources Association* 49 (6): 1239–60. https://doi.org/10.1111/jawr.12082.

Ramsey, Elijah, Amina Rangoonwala, Zhaohui Chi, Cathleen E. Jones, and Terri Bannister. 2014. “Marsh Dieback, Loss, and Recovery Mapped with Satellite Optical, Airborne Polarimetric Radar, and Field Data.” *Remote Sensing of Environment* 152: 364–74. https://doi.org/10.1016/j.rse.2014.07.002.

Ramsey, Elijah, Amina Rangoonwala, and Cathleen E. Jones. 2015. “Structural Classification of Marshes with Polarimetric SAR Highlighting the Temporal Mapping of Marshes Exposed to Oil.” *Remote Sensing* 7 (9): 11295–321. https://doi.org/10.3390/rs70911295.

Ramsey, Elijah, Amina Rangoonwala, and Cathleen E. Jones. 2016. “Marsh Canopy Structure Changes and the Deepwater Horizon Oil Spill.” *Remote Sensing of Environment* 186: 350–57. https://doi.org/10.1016/j.rse.2016.08.001.

Ramsey, Elijah, Dirk Werle, Yukihiro Suzuoki, Amina Rangoonwala, and Zhong Lu. 2012. “Limitations and Potential of Satellite Imagery to Monitor Environmental Response to Coastal Flooding.” *Journal of Coastal Research* 280 (2): 457–76. https://doi.org/10.2112/JCOASTRES-D-11-00052.1.

Rangoonwala, Amina, Nicholas M. Enwright, Elijah Ramsey, and Joseph P. Spruce. 2016. “Radar and Optical Mapping of Surge Persistence and Marsh Dieback along the New Jersey Mid-Atlantic Coast after Hurricane Sandy.” *International Journal of Remote Sensing* 37 (7): 1692–1713. https://doi.org/10.1080/01431161.2016.1163748.

Rangoonwala, Amina, Cathleen E. Jones, and Elijah Ramsey. 2016. “Wetland Shoreline Recession in the Mississippi River Delta from Petroleum Oiling and Cyclonic Storms.” *Geophysical Research Letters* 43 (22): 11,652-11,660. https://doi.org/10.1002/2016GL070624.

Reay, William G., and Kenneth A. Moore. 2009. “Introduction to the Chesapeake Bay National Estuarine Research Reserve in Virginia.” *Journal of Coastal Research* 10057: 1–9. https://doi.org/10.2112/1551-5036-57.sp1.1.

Reschke, Julia, Annett Bartsch, Stefan Schlaffer, and Dmitry Schepaschenko. 2012. "Capability of C-Band SAR for Operational Wetland Monitoring at High Latitudes" 1: 2923–43. https://doi.org/10.3390/rs4102923.

Rooth, J E, and J C Stevenson. 2000. "Sediment Deposition Patterns in Phragmites Australis Communities: Implications for Coastal Areas Threatened by Rising Sea-Level." *Wetlands Ecology and Management* 8 (2–3): 173–83. https://doi.org/10.1023/a:1008444502859.

Rosenqvist, Ake. 1999. "International Journal of Remote Sensing Temporal and Spatial Characteristics of Irrigated Rice in JERS-1 L-Band SAR Data Temporal and Spatial Characteristics of Irrigated Rice in JERS-1 L-Band SAR Data." *Int. J. Remote Sensing* 20 (8): 1567–87. https://doi.org/10.1080/014311699212614.

Rosenqvist, Jessica, Ake Rosenqvist, Katherine Jensen, and Kyle McDonald. 2020. "Mapping of Maximum and Minimum Inundation Extents in the Amazon Basin 2014–2017 with ALOS-2 PALSAR-2 ScanSAR Time-Series Data". *Remote Sensing* 12 (8) 1326.

Ross, Pauline, and Paul Adam. 2013. *Climate Change and Intertidal Wetlands*. *Biology*. Vol. 2. https://doi.org/10.3390/biology2010445.

Schmitt, Andreas, and Brian Brisco. 2013. "Wetland Monitoring Using the Curvelet-Based Change Detection Method on Polarimetric SAR Imagery." *Water* 5 (3): 1036–51. https://doi.org/10.3390/w5031036.

Schoelynck, Jonas, Kris Bal, Veerle Verschoren, Ellis Penning, Eric Struyf, Tjeerd Bouma, Dieter Meire, Patrick Meire, and Stijn Temmerman. 2014. "Different Morphology of Nuphar Lutea in Two Contrasting Aquatic Environments and Its Effect on Ecosystem Engineering." *Earth Surface Processes and Landforms* 39 (15): 2100–2108. https://doi.org/10.1002/esp.3607.

Sciance, Ben, Christopher Patrick, Donald Weller, Meghan Williams, Melissa McCormick, and Eric Hazelton. "Local and regional disturbances associated with the invasion of Chesapeake Bay marshes by the common reed Phragmites australis". *Biological Invasions*. https://doi.org/10.1007/s10530-016-1136-z

Segelstein, David. 1981. "The Complex Refractive Index of Water." *Masters Thesis*. University of Missouri-Kansas City.

Shan, Zili, Chao Wang, Hong Zhang, and Jiehong Chen. 2011. "H-α Decomposition and Alternative Parameters for Dual Polarization SAR Data." *PIERS Proc.*, 1386–90.

Shelestov, Andrii, Mykola Lavreniuk, Nataliia Kussul, Alexei Novikov, and Sergii Skakun. 2017. "Exploring Google Earth Engine Platform for Big Data Processing: Classification of Multi-Temporal Satellite Imagery for Crop Mapping." *Frontiers in Earth Science* 5 (February): 1–10. https://doi.org/10.3389/feart.2017.00017.

Sinha, E., AM Michalak, and V Balaji. 2017. “Eutrophication Will Increase during the 21st Century as a Reult of Precipitation Changes.” *Science*, no. July: 1–4.

Slatton, K Clint, Melba M Crawford, and Li-der Chang. 2008. “Modeling Temporal Variations in Multipolarized Radar Scattering from Intertidal Coastal Wetlands” 63: 559–77. https://doi.org/10.1016/j.isprsjprs.2008.07.003.

Small, Ernest. 2011. “Water Chestnut.” *Top 100 Exotic Food Plants* 2600 (October): 601–8. https://doi.org/10.1201/b11391-99.

Smith, Joseph A M. 2013. “The Role of Phragmites Australis in Mediating Inland Salt Marsh Migration in a Mid-Atlantic Estuary.” *PLoS ONE* 8 (5). https://doi.org/10.1371/journal.pone.0065091.

Subcommittee, Wetlands, Federal Geographic, and Data Committee. 2013. “Classification of Wetlands and Deepwater Habitats of the United States,” no. August.

Subsystem, Marine, Intertidal Class, Subclass Rb, Rock Bottom, Rubble Ub, Unconsolidated Bottom, Mud Ab, et al. 2015. “NWI Wetlands and Deepwater Map Code Diagram NWI Wetlands and Deepwater Map Code Diagram,” 1–2.

Sutter, Lori A., James E. Perry, and Randy M. Chambers. 2014. “Tidal Freshwater Marsh Plant Responses to Low Level Salinity Increases.” *Wetlands* 34 (1): 167–75. https://doi.org/10.1007/s13157-013-0494-x.

Swarth, Christopher W., Patricia Delgado, and Dennis F. Whigham. 2013. “Vegetation Dynamics in a Tidal Freshwater Wetland: A Long-Term Study at Differing Scales.” *Estuaries and Coasts* 36 (3): 559–74. https://doi.org/10.1007/s12237-012-9568-x.

Tabak, Nava M., Magdeline Laba, and Sacha Spector. 2016. “Simulating the Effects of Sea Level Rise on the Resilience and Migration of Tidal Wetlands along the Hudson River.” *PLoS ONE* 11 (4): 1–25. https://doi.org/10.1371/journal.pone.0152437.

Tanis, F J, L L Bourgeau-Chavez, and M C Dobson. 1994. “Application of ERS-1 SAR for Coastal Inundation.” *Proceedings of IGARSS ’94 - 1994 IEEE International Geoscience and Remote Sensing Symposium* 3: 1481–83. https://doi.org/10.1109/IGARSS.1994.399475.

Teutschbein, Claudia, Tomas Grabs, Reinart Karlsen, H Laudon, and Kevin Bishop. 2015. “Water Resources Research.” *Water Resources Research* 00000 (51): 5974–97. https://doi.org/10.1002/2015WR017408.Received.

Thomas, Nathan, Richard Lucas, Peter Bunting, Andrew Hardy, Ake Rosenqvist, and Marc Simard. 2017. “Distribution and Drivers of Global Mangrove Forest Change, 1996-2010.” *PLoS ONE* 12 (6): 1–14. https://doi.org/10.1371/journal.pone.0179302.

Tiner, Ralph W. 1997. “NWI Maps: What They Tell Us.” *National Wetlands Newsletter* 19 (2): 7–12. http://www.fws.gov/wetlands/Documents/NWI-Maps-What-They-Tell-Us.pdf.

Tobias, C, and Sc Neubauer. 2009. *Chapter 16 - Salt Marsh Biogeochemistry - An Overview*. *COASTAL WETLANDS: An Integrated Ecosystem Approach*. Vol. 76. https://doi.org/10.1016/B978-0-444-53103-2.00016-8.

Tobias, V. D., and J. A. Nyman. 2017. “Leaf Tissue Indicators of Flooding Stress in the Above- and Belowground Biomass of Spartina Patens.” *Journal of Coastal Research* 33 (2): 309–20. https://doi.org/10.2112/JCOASTRES-D-15-00142.1.

Tripathee, R., and K. V.R. Schäfer. 2014. “Above- and Belowground Biomass Allocation in Four Dominant Salt Marsh Species of the Eastern United States.” *Wetlands* 35 (1): 21–30. https://doi.org/10.1007/s13157-014-0589-z.

Tucker, C.J. 1979. “Red and photographic infrared linear combinations for monitoring vegetation.” *Remote Sensing of Environment* (8): 127–150

Tulbure, Mirela G., Dana M. Ghioca-Robrecht, Carol A. Johnston, and Dennis F. Whigham. 2012. “Inventory and Ventilation Efficiency of Nonnative and Native Phragmites Australis (Common Reed) in Tidal Wetlands of the Chesapeake Bay.” *Estuaries and Coasts* 35 (5): 1353–59. https://doi.org/10.1007/s12237-012-9529-4.

Turner, R. Eugene, Michael Layne, Yu Mo, and Erick M. Swenson. 2019. “Net Land Gain or Loss for Two Mississippi River Diversions: Caernarvon and Davis Pond.” *Restoration Ecology* 27 (6): 1231–40. https://doi.org/10.1111/rec.13024.

Tyler, Anna Christina, and Joseph C. Zieman. 1999. “Patterns of Development in the Creekbank Region of a Barrier Island Spartina Alterniflora Marsh.” *Marine Ecology Progress Series* 180: 161–77. https://doi.org/10.3354/meps180161.

Tzortziou, Maria, Patrick J Neale, J Patrick Megonigal, Crystal Lee Pow, and Megan Butterworth. 2011. “Spatial Gradients in Dissolved Carbon Due to Tidal Marsh Outwelling into a Chesapeake Bay Estuary.” *Marine Ecology Progress Series* 426: 41–56. https://doi.org/10.3354/meps09017.

Tzortziou, Maria, Patrick J Neale, Christopher L Osburn, J Patrick Megonigal, Nagamitsu Maie, and Rudolf Jaffe. 2008. “Tidal Marshes as a Source of Optically and Chemically Distinctive Colored Dissolved Organic Matter in the Chesapeake Bay” *Limnology and Oceanography* 53 (1): 148–59.

Uddin, Md Nazim, and Randall William Robinson. 2017. “Responses of Plant Species Diversity, Soil Physical-Chemical-Microbial Properties to Phragmites Australis Invasion along a Density Gradient.” *Scientific Reports* 7 (1): 1–13. https://doi.org/10.1038/s41598-017-11205-0.

Ulaby, Fawwaz, El-Rayes, Mohammed. 1987 “Microwave Dielectric Spectrum of Vegetation - Part II: Dual-Dispersion Model” *IEEE Transactions on Geoscience and Remote Sensing* (Volume: GE-25, Issue: 5, Sept. 1987). https://doi.org/10.1109/TGRS.1987.289833

Ulaby, Fawwaz, David Long, et. al. 2015. “Microwave Radar and Radiometric Remote Sensing.” ISBN-13: 978-0472119356.

UNEP. 2017. “Global Distribution of Saltmarsh,” 1–4. https://doi.org/10.3897/BDJ.5.e11764.

United States Department of Agriculture (USDA) NRCS Plant Materials Program. 2006. “Plant Fact Sheet – Yellow Pond Lily – *Nuphar lutea*” *The U.S. Department of Agriculture*, 2. https://plants.usda.gov/factsheet/pdf/pg_nulu.pdf.

United States Department of Agriculture (USDA) NRCS Plant Materials Program. 2002. “Plant Fact Sheet – Smooth Cordgrass – *Nuphar lutea*” *The U.S. Department of Agriculture*, 2. https://plants.usda.gov/factsheet/pdf/fs_spal.pdf.

United States Geological Survey (USGS), Department of Interior. “USGS Landsat 8 Surface Reflectance Code (LaSRC).” *USGS*. Washington, DC, USA, 2018; pp. 1–3

Vaccaro, L E, B L Bedford, and C A Johnston. 2009. “Litter Accumulation Promotes Dominance of Invasive Species of Cattails (Typha Spp.) in Lake Ontario Wetlands.” *Wetlands* 29 (3): 1036–48. https://doi.org/10.1672/08-28.1.

Vachon, Paris W., and John Wolfe. 2011. “C-Band Cross-Polarization Wind Speed Retrieval.” *IEEE Geoscience and Remote Sensing Letters* 8 (3): 456–59. https://doi.org/10.1109/LGRS.2010.2085417.

Vanderhoof, Melanie K., Jay Christensen, Yen Ju G. Beal, Ben DeVries, Megan W. Lang, Nora Hwang, Christine Mazzarella, and John W. Jones. 2020. *Isolating Anthropogenic Wetland Loss by Concurrently Tracking Inundation and Land Cover Disturbance across the Mid-Atlantic Region, U.S. Remote Sensing*. Vol. 12. https://doi.org/10.3390/RS12091464.

Vermote, Eric, Chris Justice, Martin Claverie, and Belen Franch. 2016. “Preliminary Analysis of the Performance of the Landsat 8/OLI Land Surface Reflectance Product.” *Remote Sensing of Environment* 185: 46–56. https://doi.org/10.1016/j.rse.2016.04.008.

Villa, Paolo, Mariano Bresciani, Rossano Bolpagni, Monica Pinardi, and Claudia Giardino. 2015. “A Rule-Based Approach for Mapping Macrophyte Communities Using Multi-Temporal Aquatic Vegetation Indices.” *Remote Sensing of Environment* 171: 218–33. https://doi.org/10.1016/j.rse.2015.10.020.

Wainger, Lisa A., Nathan E. Harms, Cedric Magen, Dong Liang, Genevieve M. Nesslage, Anna M. McMurray, and Al F. Cofrancesco. 2018. “Evidence-Based Economic Analysis Demonstrates That Ecosystem Service Benefits of Water Hyacinth Management Greatly

Exceed Research and Control Costs." *PeerJ* 2018 (5): 1–23. https://doi.org/10.7717/peerj.4824.

Whitcomb J.A., Moghaddam, M.A., McDonald K.B., Kellndorfer J.B., Podest E.C. 2009. "Mapping Vegetated Wetlands of Alaska Using L-Band Radar Satellite Imagery." *Canadian Journal of Remote Sensing* 35 (1): 54–72. https://doi.org/10.1109/IGARSS.2007.4423348.

White, Lori, Brian Brisco, Mohammed Dabboor, Andreas Schmitt, and Andrew Pratt. 2015. "A Collection of SAR Methodologies for Monitoring Wetlands." *Remote Sensing* https://doi.org/10.3390/rs70607615.

Woodhouse, Iain. 2006. "Introduction to Microwave Remote Sensing" 1st Edition. *Francis & Taylor*. ISBN-13: 978-0415271233.

Windham, L. 2001. "Comparison of Biomass Production and Decomposition between Phragmites Australis (Common Reed) and Spartina Patens (Salt Hay Grass) in Brackish Tidal Marshes of New Jersey, USA." *Wetlands* 21 (2): 179–88. https://doi.org/10.1672/0277-5212(2001)021[0179:COBPAD]2.0.CO;2.

Windham, Lisamarie. 1999. "Microscale Spatial Distribution of Phragmites Australis (Common Reed) Invasion into Spartina Patens (Salt Hay)-Dominated Communities in Brackish Tidal Marsh." *Biological Invasions* 1 (2–3): 137–48. https://doi.org/10.1023/a:1010016319074.

Yamaguchi, Yoshio, Yuki Yajima, and Hiroyoshi Yamada. 2006. "A Four-Component Decomposition of POLSAR Images Based on the Coherency Matrix." *IEEE Geoscience and Remote Sensing Letters* 3 (3): 292–96. https://doi.org/10.1109/LGRS.2006.869986.

Yamazaki, Dai, Daiki Ikeshima, Ryunosuke Tawatari, Tomohiro Yamaguchi, Fiachra O'Loughlin, Jeffery C. Neal, Christopher C. Sampson, Shinjiro Kanae, and Paul D. Bates. 2017. "A High-Accuracy Map of Global Terrain Elevations." *Geophysical Research Letters* 44 (11): 5844–53. https://doi.org/10.1002/2017GL072874.

Yang, Limin, Suming Jin, Patrick Danielson, Collin Homer, Leila Gass, Stacie M. Bender, Adam Case, et al. 2018. "A New Generation of the United States National Land Cover Database: Requirements, Research Priorities, Design, and Implementation Strategies." *ISPRS Journal of Photogrammetry and Remote Sensing* 146 (September): 108–23. https://doi.org/10.1016/j.isprsjprs.2018.09.006.

Zhu, Zhe, Shixiong Wang, and Curtis E. Woodcock. 2015. "Improvement and Expansion of the Fmask Algorithm: Cloud, Cloud Shadow, and Snow Detection for Landsats 4-7, 8, and Sentinel 2 Images." *Remote Sensing of Environment* 159: 269–77. https://doi.org/10.1016/j.rse.2014.12.014.